frontiers | Research Topics

# Near-earth electromagnetic environment and natural hazards disturbances

**Edited by**
Zeren Zhima, Angelo De Santis, Mirko Piersanti,
Xuhui Shen, Chao Xiong and Lin Jian

**Published in**
Frontiers in Earth Science
Frontiers in Environmental Science

ISSN 1664-8714
ISBN 978-2-8325-5000-7
DOI 10.3389/978-2-8325-5000-7

## About Frontiers

Frontiers is more than just an open access publisher of scholarly articles: it is a pioneering approach to the world of academia, radically improving the way scholarly research is managed. The grand vision of Frontiers is a world where all people have an equal opportunity to seek, share and generate knowledge. Frontiers provides immediate and permanent online open access to all its publications, but this alone is not enough to realize our grand goals.

## Frontiers journal series

The Frontiers journal series is a multi-tier and interdisciplinary set of open-access, online journals, promising a paradigm shift from the current review, selection and dissemination processes in academic publishing. All Frontiers journals are driven by researchers for researchers; therefore, they constitute a service to the scholarly community. At the same time, the *Frontiers journal series* operates on a revolutionary invention, the tiered publishing system, initially addressing specific communities of scholars, and gradually climbing up to broader public understanding, thus serving the interests of the lay society, too.

## Dedication to quality

Each Frontiers article is a landmark of the highest quality, thanks to genuinely collaborative interactions between authors and review editors, who include some of the world's best academicians. Research must be certified by peers before entering a stream of knowledge that may eventually reach the public - and shape society; therefore, Frontiers only applies the most rigorous and unbiased reviews. Frontiers revolutionizes research publishing by freely delivering the most outstanding research, evaluated with no bias from both the academic and social point of view. By applying the most advanced information technologies, Frontiers is catapulting scholarly publishing into a new generation.

## What are Frontiers Research Topics?

Frontiers Research Topics are very popular trademarks of the *Frontiers journals series*: they are collections of at least ten articles, all centered on a particular subject. With their unique mix of varied contributions from Original Research to Review Articles, Frontiers Research Topics unify the most influential researchers, the latest key findings and historical advances in a hot research area.

Find out more on how to host your own Frontiers Research Topic or contribute to one as an author by contacting the Frontiers editorial office: frontiersin.org/about/contact

# Near-earth electromagnetic environment and natural hazards disturbances

**Topic editors**

Zeren Zhima — National Institute of Natural Hazards, Ministry of Emergency Management, China

Angelo De Santis — National Institute of Geophysics and Volcanology (INGV), Italy

Mirko Piersanti — University of L'Aquila, Italy

Xuhui Shen — National Institute of Natural Hazards, Ministry of Emergency Management, China

Chao Xiong — Wuhan University, China

Lin Jian — National Institute of Natural Hazards, Ministry of Emergency Management, China

**Citation**

Zhima, Z., De Santis, A., Piersanti, M., Shen, X., Xiong, C., Jian, L., eds. (2024). *Near-earth electromagnetic environment and natural hazards disturbances*. Lausanne: Frontiers Media SA. doi: 10.3389/978-2-8325-5000-7

# Table of contents

frontiers | Frontiers in Environmental Science

TYPE Editorial
PUBLISHED 06 November 2023
DOI 10.3389/fenvs.2023.1307941



OPEN ACCESS

EDITED AND REVIEWED BY
Alexander Kokhanovsky,
German Research Centre for Geosciences, Potsdam

*CORRESPONDENCE
Angelo De Santis,
angelo.desantis@ingv.it

RECEIVED 05 October 2023
ACCEPTED 16 October 2023
PUBLISHED 06 November 2023

CITATION
De Santis A, Jian L, Piersanti M, Shen X, Xiong C and Zhima Z (2023), Editorial: Near-earth electromagnetic environment and natural hazards disturbances.
*Front. Environ. Sci.* 11:1307941.
doi: 10.3389/fenvs.2023.1307941



# Editorial: Near-earth electromagnetic environment and natural hazards disturbances

Angelo De Santis[1]*, Lin Jian[2], Mirko Piersanti[3], Xuhui Shen[2], Chao Xiong[4] and Zeren Zhima[2]

[1]Istituto Nazionale di Geofisica e Vulcanologia, Roma, Italy, [2]National Institute of Natural Hazards, Ministry of Emergency Management, Beijing, China, [3]Department of Physical and Chemical Sciences, University of L'Aquila, L'Aquila, Italy, [4]Electronic Information School, Faculty of Information Sciences, Wuhan University, Wuhan, China

KEYWORDS

**natural hazards, satellite, electromagnetic environment, data analysis, LAIC**

Editorial on the Research Topic
Near-earth electromagnetic environment and natural hazards disturbance

Throughout history, human communities have faced consistent threats from natural hazards like earthquakes, volcanic eruptions, and tsunamis. Yet, scientists strive to understand the process behind hazard formation and to predict their occurrences. Since the 1980s, space technology has allowed satellites to capture abnormal electromagnetic (EM) emissions, plasma density irregularities, and energetic particle precipitations near seismic fault zones, volcanic belts, and tsunami-prone coasts. Extensive efforts have been dedicated to rock-rupture processing experiments and ground-space comparative studies. EM precursors have shown promising potential for short-term earthquake prediction. In 2004, France launched the DEMETER satellite, operational until 2010, followed by China's China Seismo-Electromagnetic Satellite (CSES) in February 2018, focusing on earthquake monitoring from space.

This Research Topic serves two main purposes. Firstly, it validates and calibrates data from ground-based instruments and satellite platforms to explore the space's EM environment including the EM field, plasma parameters, energetic particle flux, and distributions. Secondly, it emphasizes cross-disciplinary studies of natural hazard monitoring, including earthquakes, volcanoes, etcetera. By combining modeling and observation, the goal is to develop innovative methodologies for studying natural hazards and the interconnected mechanisms of the Lithosphere-Atmosphere-Ionosphere system.

This first volume includes nine contributions which will be excellent references to the future works focused on the Research Topic.

Liu et al. proposed a spatial analysis method to extract the disturbances of CSES electron density (Ne) before earthquakes. An example was taken from the 5 August 2018 Indonesia Mw6.9 earthquake. A superposed epoch and space approach was applied to the Ne anomalies during Mw ≥ 6.0 global earthquakes for more than 2 years. It was found that 1) relative to the epicenters, seismo-ionospheric disturbances are more obvious in the equator direction than those in the polar direction; 2) the anomalies within 300 km distance from the epicenter are significant 11, 3, and 2 days before earthquakes; 3) the influence region of the anomalies associated with earthquakes enlarges with the magnitude increase, and the stronger magnitude is, the earlier disturbance appears. The results would support the electric field pathway as the main channel of lithosphere–atmosphere–ionosphere coupling.

He et al. examined ionospheric total electron content (TEC) anomalies before the 2011 Mw9.0 Tohoku-oki earthquake in Japan using Global Navigation Satellite System data from northern Australia. They found that TEC anomalies in Australia began approximately 41.5 min before the earthquake, closely matching the timing observed in Japan. These anomalies appeared on the same longitude as northeastern Japan, supporting the theory that ionospheric electric fields redistributed electrons before significant earthquakes. However, the anomaly in Australia was shifted about 500 km southward, indicating differences in the underlying physical mechanisms between the two hemispheres.

Chu et al. simulated the variation of geomagnetic cutoff rigidities from 1965 to 2025, which quantify Earth's magnetic field's shielding effect on energetic particles with data from the International Geomagnetic Reference Field model and energetic particles' windows (EPWs). Results revealed a relationship between cutoff latitude and the background magnetic field intensity, but it's not a simple linear one. Changes in cutoff rigidities and the geomagnetic field are asymmetric on the global scale. The weakening of the geomagnetic field shifts cutoff latitudes toward the equatorial region in the southern hemisphere, while the situation in the northern hemisphere is less predictable. In the northern hemisphere, EPWs decrease by about 0.03% per year, while in the southern hemisphere, they increase by approximately 0.05%–0.12% per year. The positions of EPWs do not align precisely with geomagnetic poles or magnetic dip poles, being closer to geomagnetic poles.

Yan et al. analyzed the correlation between electron density (Ne) and temperature (Te) in the ionosphere, by using simultaneous observations from four satellites: CSES, Swarm A, Swarm B, and the CHAMP satellite. Results from all four satellites indicated a generally consistent negative correlation between Ne and Te. However, The negative correlation between Ne and Te becomes weaker or even reverses into a positive correlation after Ne exceeds a certain threshold. The slope of the correlation also varies with season and magnetic latitude, reflecting the seasonal and MLat-dependent features.

Jianing et al. studied the in-orbit magnetic field data from CSES and Swarm satellites, aiming to assess data consistency through cross-comparison. Their approach involved analyzing data from two satellites passing close to each other in a relatively short timeframe within a specific spatial location, with criteria for geomagnetic quiet periods based on the Kp index. The study visualized differences between in-orbit data and model values, examining variations in data over time and with changes in geomagnetic latitude.

Huang et al. analyzed CSES data to investigate the characteristics of artificial source signals that are transmitted from ground-based artificial source stations. The research aimed to pinpoint the position and intensity of the strongest points within these two regions by examining the power-spectrum density of the electric field recorded by CSES over the NWC transmitter. The analysis focused on a specific frequency of 19.8 kHz with a bandwidth of 200 Hz. The "strongest point" was defined as the location with the highest power spectral density within a range of ± 10° around the NWC transmitter. The study uncovered several noteworthy statistical characteristics related to these strongest points, with variations influenced by factors such as day/night, location, and different components of electric field vectors.

Wang et al. based on CSES observations, reported three notable disturbing steps in the space environment: Electromagnetic radiation from solar flares reaches Earth at the speed of light, followed by solar energetic charged particles, and finally, coronal mass ejections (CMEs) and geomagnetic storms. The analyzed disturbance cases are all associated with solar proton events (SPEs). The observations confirm that the data quality of the high-energy particle package (HEPP) from CSES is highly reliable and accurate and is highly advantageous to monitor the variation of energetic particles and X-rays in the radiation belt of the Earth during solar activities.

Wu et al. studied high-resolution electromagnetic field intensity data from the DEMETER satellite to detect harmonic electromagnetic radiations in the ionosphere, specifically above extra-high voltage and ultra-high voltage power plants in China. The highest frequency recorded was around 8,850 Hz. The origins of these radiations are likely associated with nonlinear devices such as converters or geomagnetic disturbances. A simple physical model explains how these radiations propagate from the Earth's surface to the ionosphere.

Yang et al. address the critical Research Topic of "communication blackout" during reentry for sharp-coned vehicles. While previous research mainly focused on EHF (extremely high frequency) communication for blunt-coned vehicles, this study explores EHF communication for sharp-coned vehicles. The study models the EHF communication system, considering modulation modes (2ASK, 2PSK, and 2FSK). Key findings indicate that transmission coefficient increases with carrier frequency, channel gap decreases over time, phase shift stabilizes with higher carrier frequency, and bit error rate (BER) varies based on factors like antenna placement, carrier frequency, and modulation mode.

## Author contributions

ADS: Writing–original draft, Writing–review and editing. LJ: Writing–review and editing. MP: Writing–review and editing. XS: Writing–review and editing. ZZ: Writing–review and editing.

## Funding

The author(s) declare that no financial support was received for the research, authorship, and/or publication of this article.

## Conflict of interest

The authors declare that the research was conducted in the absence of any commercial or financial relationships that could be construed as a potential conflict of interest.

## Publisher's note

frontiers in Earth Science

ORIGINAL RESEARCH
published: 22 February 2022
doi: 10.3389/feart.2022.811658

# Using a Spatial Analysis Method to Study the Seismo-Ionospheric Disturbances of Electron Density Observed by China Seismo-Electromagnetic Satellite

*Jing Liu*[1]*, *Xiaoling Qiao*[1], *Xuemin Zhang*[1], *Zhuangkai Wang*[2], *Chen Zhou*[2] and *Yu Zhang*[1]

[1]Institute of Earthquake Forecasting, China Earthquake Administration, Beijing, China, [2]Wuhan University, Wuhan, China

Due to the complex processes of earthquake preparation, the observations and studies associated with earthquakes have attracted the attention of geophysicists for many years. The CSES was successfully launched on 2 February 2018. This satellite can provide global data of the electromagnetic field, plasma, and energetic particles in the ionosphere to monitor and study the ionospheric perturbations associated with earthquakes. Focusing on the characteristics of CSES, a spatial analysis method was proposed to extract the disturbances of electron density prior to earthquakes. Taking Indonesia Mw6.9 earthquake that occurred on 5 August 2018 as an example, the spatial method was illustrated and verified by another analysis method also using the data of electron density and GPS TEC data with the same analysis method. Based on the electron density of CSES for more than 2 years, this method was applied to carry out the statistical study prior to Mw ≥ 6.0 global earthquakes using the superposed epoch and space approach (SESA) method. It was found that 1) relative to the epicenters, seismo-ionospheric disturbances are more obvious in the equator direction than those in the polar direction; 2) the anomalies within 300 km distance from the epicenter are significant 11, 3, and 2 days prior to Mw ≥ 6.0 earthquakes; 3) the influence region of perturbances associated with earthquakes enlarges with the magnitude increase, and the stronger magnitude is the earlier disturbance appears. These statistical characteristics were not detected for the random earthquakes. Comparing the statistical result with the simulation output, the electric field pathway could be considered as the main channel of lithosphere–atmosphere–ionosphere coupling.

**Keywords: CSES, analysis method, electron density, ionospheric disturbance, earthquake**

OPEN ACCESS

***Edited by:***
*Mirko Piersanti,*
*National Institute of Astrophysics (INAF), Italy*

***Reviewed by:***
*Angelo De Santis,*
*Istituto Nazionale di Geofisica e Vulcanologia (INGV), Italy*
*Saioa A. Campuzano,*
*Institute of Geosciences (CSIC), Spain*

***Correspondence:**
*Jing Liu*
*liujingeva@163.com*

***Specialty section:***
*This article was submitted to Geohazards and Georisks, a section of the journal Frontiers in Earth Science*

***Received:*** *09 November 2021*
***Accepted:*** *26 January 2022*
***Published:*** *22 February 2022*

***Citation:***
*Liu J, Qiao X, Zhang X, Wang Z, Zhou C and Zhang Y (2022) Using a Spatial Analysis Method to Study the Seismo-Ionospheric Disturbances of Electron Density Observed by China Seismo-Electromagnetic Satellite. Front. Earth Sci. 10:811658. doi: 10.3389/feart.2022.811658*

## 1 INTRODUCTION

The abnormal ionospheric plasma density variations before and/or after earthquakes have attracted much attention from the geophysicists for many years (e.g., Pulinets and Legen'ka, 2003; Pulinets and Boyarchuk, 2004; Le et al., 2015). In general, ionospheric measuring techniques are categorized as ground and space observations to obtain the ionospheric parameters (Xiong et al., 1999). The former one includes the ground-based ionosonde, global position system (GPS) or global navigation satellite system (GNSS) receivers, and incoherent scatter radar (Rishbeth and Garriott 1969; Schunk and Nagy 2009). The latter involves topside ionospheric sounding and *in situ* observation by satellites and

rockets (Pulinets, 1998; Pulinets, 2006). The total electron content (TEC) of time series and global ionosphere map (GIM) has been widely used to detect seismo-ionospheric anomalies. Focused on the earthquakes that occurred at Taiwan, Liu et al. (2000) found the critical frequency of the F2 layer (*fo*F2) which fell below the lower threshold 1–6 days prior to Mw ≥ 6.0 earthquakes, and Liu et al. (2004a) also detected *fo*F2 and TEC both decreased 4 days before M ≥ 5.0 earthquakes. The GPS TEC data for 11 Sulawesi earthquakes from 1993 to 2002 were analyzed by Saroso et al. (2008), and they reported the negative anomalies of TEC within 2–7 days before earthquakes. Liu et al. (2009) found the GPS TEC at the epicenters decreased 3–5 days before 17 M ≥ 6.3 earthquakes among 35 M ≥ 6.0 earthquakes in China. Kon et al. (2011) indicated the TEC-positive anomalies 1–5 days before M ≥ 6.0 earthquakes in Japan and within 1,000 km from the epicenters by analyzing GIM TEC data. Combining the observation data of GNSS ground receivers and ionosondes, Liu et al. (2018) constructed a three-dimensional tomography of ionospheric electron density to further understand the structure and dynamics of seismo-ionospheric precursors.

The first report mentioned the seismo-ionospheric perturbations detected by a satellite could be attributed to the beginning of 1980s (Larkina et al., 1983; Gokhberg et al., 1983a; Gokhberg et al., 1983b). With the continuous launch of low-Earth orbital (LEO) satellites, studies about topside electron density (*Ne*) disturbances related to earthquakes have been reported, which makes the major contribution toward understanding the nature of the seismo-ionospheric coupling. Based on Cosmos-1809 satellite data, Chmyrev et al. (1997) found the *Ne* disturbances with d*Ne*/*Ne* ≈ 3%–8% from minutes to hours before 5 aftershocks of Spitak earthquakes that occurred on December 7, 1988. Using the topside sounding of Alouette, AE-C, and Interkosmos-19 satellites, Pulinets and Legen'ka (2003) and Pulinets et al. (2003) established major features of the ionospheric precursors for topside *fo*F2 or *Ne*, including the occurrence time of anomaly between 5 days to a few hours and the disturbance position shifting equatorward. Sarkar et al. (2007) analyzed the data of the Detection of Electro-Magnetic Emissions Transmitted from Earthquake Regions (DEMETER) satellite and found the anomalies of electron and ion densities several days before some earthquakes. Parrot (2012) used automatic software to detect the abrupt enhancement of ion density observed by the DEMETER satellite. Based on the statistical analysis of 17,366 M > 4.8 earthquakes, Parrot (2012) found that perturbations in ionospheric ion density before earthquakes are more obvious than those prior to randomly selected pseudo-earthquake events. By analyzing the electron density and temperature data from the DEMETER satellite, Liu et al. (2014) extracted the disturbances of plasma parameters before 49 earthquakes among 82 Ms ≥ 7.0 earthquakes during 2005–2010. Ryu et al. (2014) reported the equatorial ionization anomaly (EIA) enhancements prior to M > 5.0 earthquakes in the low-latitude region based on the statistical analysis of *Ne* measured by the DEMETER satellite. Yan et al. (2017) applied the statistics method to analyze the ion density of the DEMETER satellite and found that perturbations occur around 200 km from the epicenters in 5 days before the earthquakes. De Santis et al. (2019) carried out a statistical study of 1,312 M > 5.5 earthquakes and found that the *in situ* ionospheric precursors are significant from a few days to 80 days before earthquakes by analyzing the electron density and magnetic field data of Swarm constellation.

The China Seismo-Electromagnetic Satellite (CSES), which is also called ZhangHeng-1 (ZH-1), was successfully launched on 2 February 2018. CSES can provide global electromagnetic data to study the seismo-ionospheric perturbations, especially those due to the strong earthquakes (Shen et al., 2018a). From the comparisons between CSES *Ne* and other observations/models (Wang et al., 2019; Yan et al., 2020; Liu et al., 2021), it confirms that the *Ne* data can reliably reveal the ionospheric characteristics at the satellite altitude of 507 km. So far, using the CSES data, some case studies of seismo-ionospheric disturbances have been reported (e.g., Yan et al., 2018; Piersanti et al., 2020; Song et al., 2020; Zhang et al., 2020). A statistical study was carried out by Li et al. (2020) based on 1-year *Ne* data. Using *Ne* data of CSES during 10 non-contiguous months, De Santis et al. (2021) analyzed the statistical correlation between ionospheric anomalies and M5.5 + shallow earthquakes. However, different analysis methods, long time data, and more cases studies are also needed to detect the characteristics of seismo-ionospheric disturbances. In this work, according to the characteristics of CSES, a spatial analysis method for identifying the seismo-ionospheric disturbances was proposed. Then, taking Indonesia Mw6.9 earthquake that occurred on 5 August 2018 as an example, this method was verified using other methods and observations. Finally, a statistical study prior to Mw ≥ 6.0 global earthquakes was carried out to investigate the characteristics of seismo-ionospheric anomalies using the CSES *Ne* data from 1 May 2018 to 30 September 2020.

## 2 DATA

The CSES, with a circular orbit, is a Sun-synchronous satellite. The altitude of this satellite is 507 km, and its inclination is 97.4°. The ascending and descending nodes are 02:00 LT (local time) and 14:00 LT, respectively. The revisiting cycle of CSES is 5-day, so the global electromagnetic environment in the topside ionosphere can be obtained every 5 days. CSES is equipped with eight scientific payloads (Shen et al., 2018b), including a high-precision magnetometer (HPM), an electric field detector (EFD), a search coil magnetometer (SCM), a plasma analyzer package (PAP), a Langmuir probe (LAP), a high energetic particle package (HEPP), high energetic particle detector (HEPD), a GNSS occultation receiver (GOR), and a tri-band beacon (TBB).

In this work, the *Ne* data observed by a LAP payload were downloaded from the website http://www.leos.ac.cn/. The *Ne* range of LAP measurement is $5 \times 10^2$–$1 \times 10^7$ $cm^{-3}$, with the relative accuracy of 10% (Liu et al., 2019). Two sensors are equipped on the LAP payload. Sensor 1 is a larger one with the diameter of 5 cm, and the diameter of sensor 2 is 1 cm, which is designed as a backup. All the data used in this study were derived from sensor 1. CSES includes two operation modes, survey and burst modes. When the satellite flies over China, the Circum-Pacific, and Eurasia seismic belts, the burst mode will

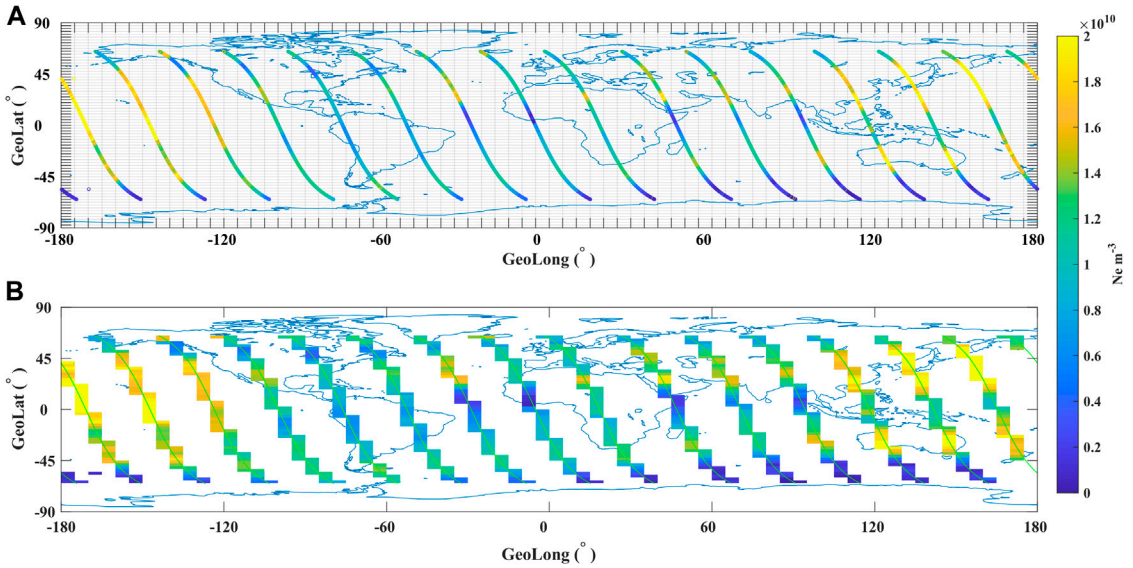


**FIGURE 1 |** *Ne* distribution of global data in the nighttime on 28 July 2018 from CSES. **(A)** Raw data along the orbits and the 2.5°(latitude)×5°(longitude) cells. **(B)** Median values in each cell, which is utilized to exhibit the *Ne* distribution in 1 day.

be automatically triggered with higher time resolution—1.5 s. In other places, the satellite works in the survey mode with a 3-s sampling rate.

## 3. METHOD: SPATIAL ANALYSIS

The time and location of satellite data are both changing along the flight orbit. Unlike the ionospheric observation by remote sensing on the ground, such as TEC or *fo*F2 data, some well-known analytical methods (e.g., running mean method) cannot be applied to analyze the satellite data. Based on the characteristics of CSES data, a spatial analysis method was proposed in this study.

The local time of descending and ascending nodes for CSES is 14:00 (LT) and 02:00 (LT), which represent the daytime and nighttime observations. In a certain local time, the global *Ne* distribution can be considered as within the same spatial environment; thus, the satellite observations in each day were divided into two groups (daytime and nighttime data) to carry out the spatial analysis. Three steps were taken to extract *Ne* disturbances before earthquakes. First, the dataset was divided into 2.5° (latitude)×5° (longitude) cells, selecting a geomagnetically quiet day as an example (the nighttime data on 29 July 2018 shown in **Figure 1A**). The median value of the data falling into each cell was calculated to represent the observational values in every day (**Figure 1B**). We used median value, instead of mean value, to exclude some eventual spikes from the data. Regarding the number of data to calculate the median value, the cell is 2.5° in latitude, which means a number of survey and burst mode data in each cell is about 13 and 26, respectively. Second, the relative change (*Rc*) was obtained using the following expression:

$$Rc = \frac{Od - Bd}{Bd} \times 100, \quad (1)$$

where *Od* is observation data calculated according to the first step, and *Bd* represents the background, which is the median value of 27-day data before *Od*. Due to the solar rotation, the ionospheric parameters, for example, topside *Ne*, also show variations with a 27-day period (Brace et al., 1987; Rich et al., 2003; Min et al., 2009). Therefore, a 27-day window was selected to obtain the ionospheric background. Finally, maximum or minimum values of *Rc* for 1 day were considered as disturbances potentially related to earthquakes if:

- far from high latitudes (excluding disturbances from the polar region);
- occurring in the geomagnetically quiet day ($F_{10.7}$ < 160 and *Kp* < 3 and |*D*st|<30nT); and
- just appearing near the epicenter, exhibiting the local characteristics.

The ionosphere is a complex system affected by many sources, such as the solar, geomagnetic storms, substorms, planetary waves, and tides. The disturbances caused by these aforementioned sources usually cover a large scale (Schunk and Sojka, 1996; Tsurutani, 2004; Liu et al., 2011), which means the extrema of *Ne* relative change may not only appear in the seismic region; thus, local anomalies just around the epicenters may have a potential relationship with earthquakes (Pulinets et al., 2021).

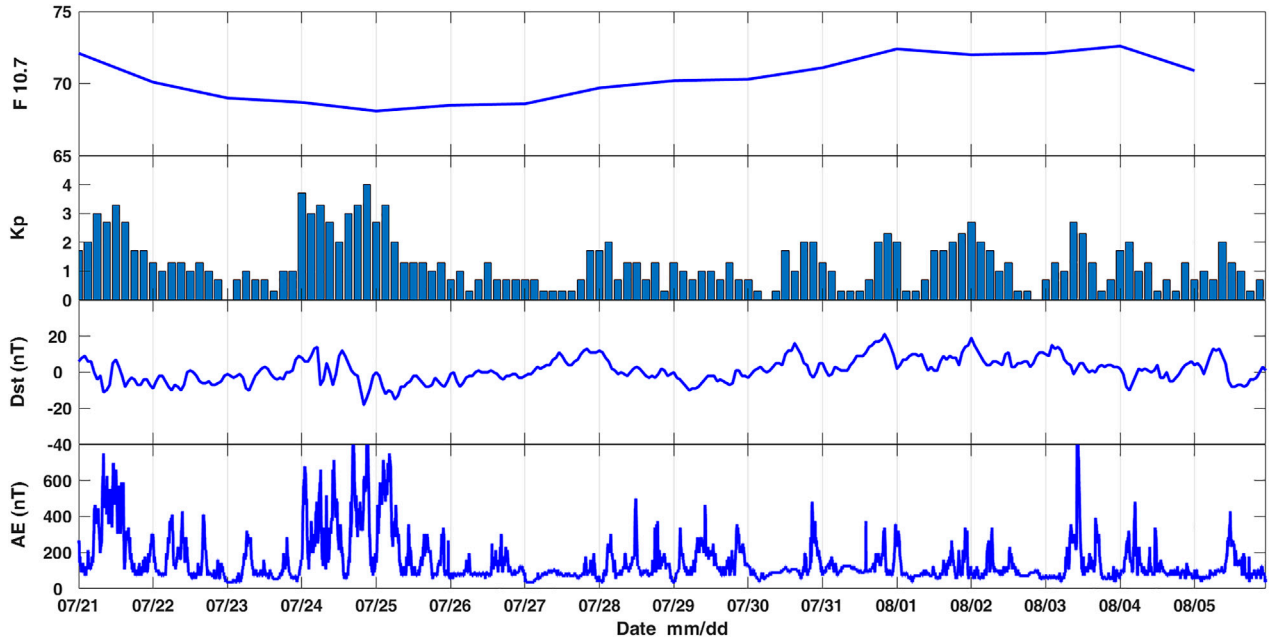


**FIGURE 2 |** $F_{10.7}$, *Kp*, *Dst*, and *AE* indices from 21 July to 5 August 2018.

## 4 A CASE STUDY

At the southwest of Loloan, Indonesia, a Mw6.9 earthquake with the location of 8.258°S, 116.438°E occurred at 11:46:38 (UT, universal time) on 5 August 2018. Focused on this earthquake, some research studies have been made by analyzing CSES data. Zhang et al. (2020) found the signal-to-noise ratio (SNR) for VLF transmitters of NWC and JJI stations reduced around the epicenter within 10 days prior to the earthquake. Song et al. (2020) extracted the *Ne* disturbances in the daytime and nighttime on 31 July. Based on atmospheric temperature, GPS TEC, EFD, and LAP data of CSES, Piersanti et al. (2020) reported the existence of atmospheric gravity waves (AGWs) 6 h before the earthquake and the co-seismic phase. We also selected this earthquake as an example to verify the spatial analysis method.

### 4.1 Spatial Analysis

Before the analysis, the 10.7-cm solar radio flux ($F_{10.7}$), *Kp*, *Dst*, and *AE* indices were checked to analyze the active solar and geomagnetic environment, which is shown in **Figure 2**. The level of solar activity was low, and the geomagnetic environment was relatively quiet during this period, except for some magnetic perturbations on 21, 24, and 25 July for *Kp* more than 3 and *AE* more than 500 nT. Using the spatial analysis method, relative changes of *Ne* data observed by CSES in the daytime and nighttime were analyzed from 21 July to 5 August 2018, which includes 15 days before and the occurrence day of Indonesia Mw6.9 earthquake. During geomagnetically quiet days, there were 2 days for daytime data, in which the maximum of *Ne* relative change just occurred around the epicenter. On 31 July (**Figure 3A**), the maximum of relative *Ne* was found in the northeastern direction of the epicenter, while the value decreased at the northwest. The enhancements at the west of the epicenter and its conjugate point were detected on 4 August (**Figure 3B**), and the maximum of *Ne* relative change reached up to 120%. Marchetti et al. (2020) analyzed the ionospheric data before Mw7.5 Indonesia earthquake (0.258°S, 119.845°E) occurred on 28 September 2018 and detected magnetic field anomalies in the *Y*-component by Swarm constellation on 31 July and CSES HPM payload on 4 August. Although they were different earthquakes, the locations of the two cases were not far. The magnetic field anomalies in the 2 days may have some relationships with disturbances of electron density detected by our study. The synchronous anomalies of magnetic field, electron field, and plasma parameters prior to earthquakes were also reported using the DEMETER satellite (Zhang et al., 2010; Zhang et al., 2011) and CSES (Piersanti et al., 2020) observation data.

Among these 16-day data in the nighttime, one disturbance was found using the spatial analysis method during geomagnetically quiet days. At the east of epicenter, the maximum of *Ne* relative change was located around the magnetic equator on 31 July, and the highest value was about 270% (**Figure 3C**). On the other side, the electron density decreased at the northwest of epicenter. In the nighttime, the equatorial plasma bubble (EPB) is another phenomenon of local disturbances. Based on the study of Kil and Heelis (1998), the EPB mainly occurs during 19:00 (LT)–21:00 (LT) and its occurrence decays after midnight. Furthermore, besides the large density depletion for EPB, the density in the depletion region is irregular (Hanson and Urquhart, 1994; Xiong et al., 2010). The local time of CSES ascending node is 02:00 LT, when the occurrence of EPB decays. An example of EPB for CSES (red line in **Figure 4**) was shown to compare with the disturbances in the nighttime on 31

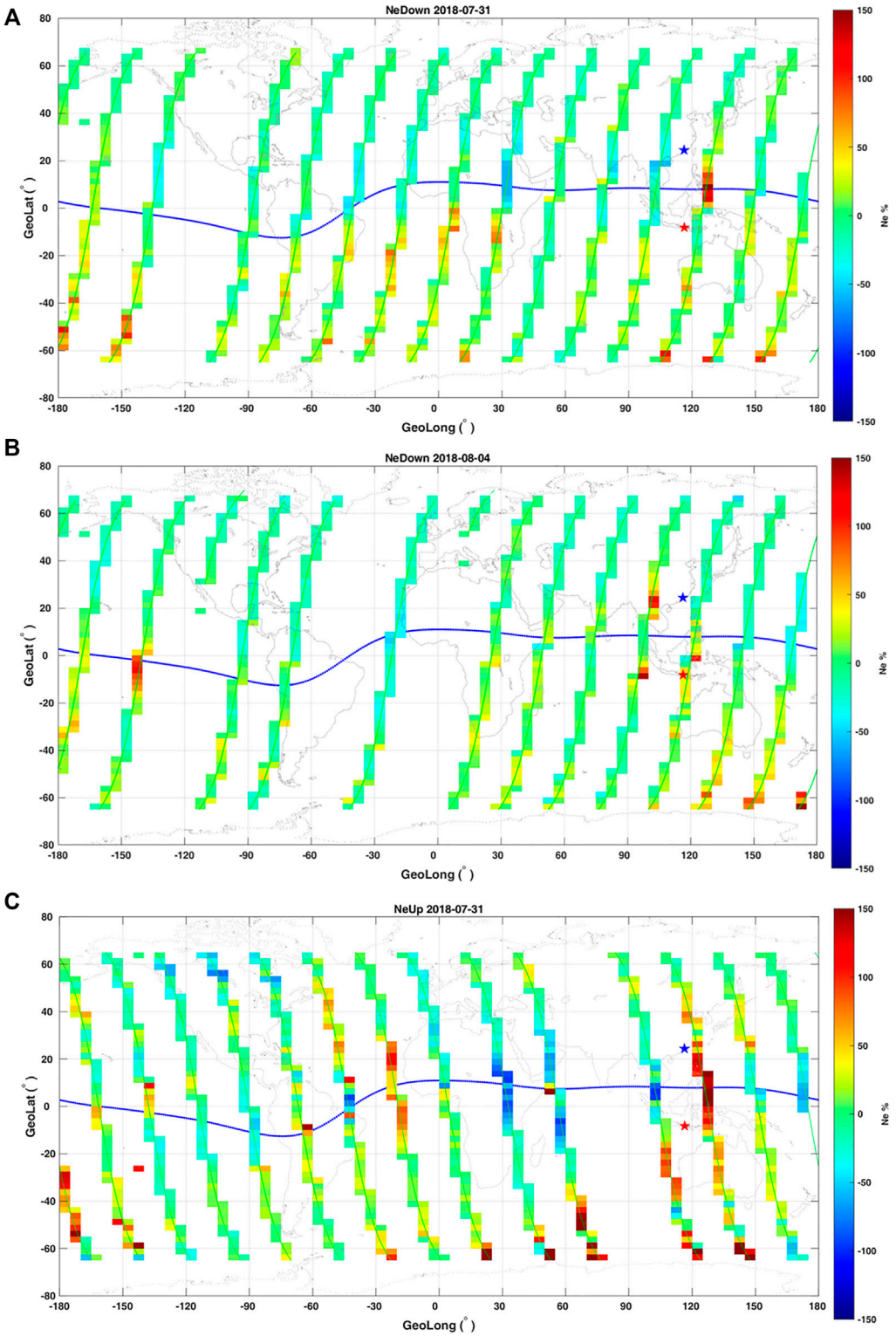


**FIGURE 3 |** Relative change of *Ne* data observed by CSES in the daytime on 31 July **(A)**, August 4 **(B)**, and in the nighttime on 31 July **(C)**. Blue line represents the magnetic equator. Green lines are the flight orbits of CSES. Red star shows the epicenter, and blue one indicates its conjugate point.

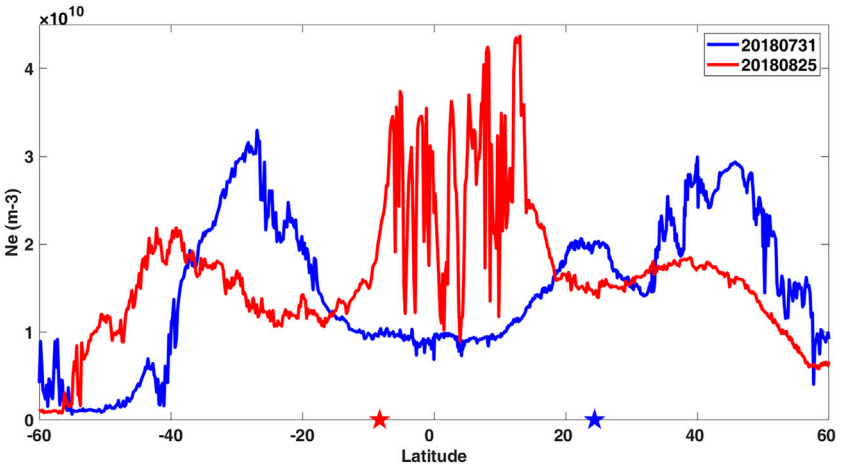


**FIGURE 4 |** Electron densities distribute along the latitude for two orbits in the nighttime. Blue line is on 31 July 2018. Red line is on 25 August 2018. Note that the *Ne* change around the magnetic equator for the orbit on 25 August 2018 is affected by EPB. Red and blue stars represent the epicenter of Indonesia Mw6.9 earthquake and its conjugate point, respectively.

July (blue line in **Figure 4**). The electron density slightly increased around the latitude of epicenter, and a peak emerged around the latitude of epicenter conjugate point on 31 July (above the blue star). The irregular shape like the EPB was not detected from the pattern of *Ne*. Therefore, the source of local anomaly in the nighttime on 31 July was different from that of EPB. The positive anomalies of *Ne* deviation during the daytime and nighttime on 31 July were also detected by Song et al. (2020), while the disturbance on 4 August was not reported by them. Although both of us paid attention to the *Ne* deviation, the different periods of background and different resampling resolution brought differences in detected anomalies.

## 4.2 Revisiting Data Analysis

The CSES strictly revisits previous orbits, so observation data in the same place can be obtained for each 5 days. In order to confirm the anomalies extracted using the spatial analysis method, revisiting data analysis was carried out to check if the observation data of extracted anomalies have some differences in the value and pattern from those of other revisiting orbits over the same place. The data of three revisiting orbits before and two after the anomalies were selected, which means that the time range of analyzing data can cover almost 1 month.

**Figures 5A,B** show the *Ne* distribution along the latitude in the daytime on 31 July, 4 August, and their revisiting dates which are marked in the legend. The red and blue stars represent the epicenter and its conjugate point, respectively, and the latitude of two blue lines has 20° distance from that of epicenter. The electron density in the northern direction of epicenter on 31 July exceeded the data of other revisiting orbits during 1 month (**Figure 5A**). The *AE* values on 16 July were higher than 500 nT. It was considered that in this day, the *Ne* enhancement around the magnetic equator and the ionospheric irregularities at the high and middle latitudes in the southern hemisphere may have a potential relationship with the substorm. On 4 August (**Figure 5B**), the *Ne* value near the epicenter was slightly higher than that of other orbits, except the data on 14 August. The *Ne* pattern on 14 August exhibited the spreading of equator crests, which may be caused by an eastward electric field around the magnetic equator, just like the phenomenon of ionospheric fountain effect (Anderson, 1981; Walker et al., 1994). The obvious enhancement around the conjugate point was detected compared with the other revisiting data. As the season of August is local summer for the northern hemisphere, the content of electron density is higher in the northern hemisphere than that in the southern hemisphere. If there were some disturbance sources, the change of electron density may be stronger in the northern hemisphere for the relative high value of background data. However, the influence of seasonal variation can be reduced by subtracting the background for the spatial analysis method; thus, the enhancements of electron density were both obvious for the epicenter and its conjugate point on 4 August. The enhancement of *Ne* close to the equator on 9 August may be caused by day-to-day variation in the ionosphere, for a little high $F_{10.7}$ index. **Figure 5C** shows the electron density change of revisiting orbits in the nighttime on 31 July. Except for the jumps on 16 July (*AE* more than 500 nT), the *Ne* data on 31 July were higher than those of other revisiting orbits above the epicenter and its conjugate point. Possibly affected by the influence of seasonal variation, the anomaly of conjugate point was more obvious than that of the epicenter. In a word, disturbances detected by the spatial analysis method also exhibited some differences from the revisiting data around the epicenter and its conjugate point, which means the spatial analysis method proposed by this study could be used to extract seismo-ionospheric anomalies.

## 4.3 Global Ionosphere Map Data Analysis

From the previous analyses, some seismo-ionospheric disturbances were detected by analyzing the CSES *Ne* data. Except for the same observation data studied by different methods, GIM TEC data were also applied to check the synchronous perturbations.

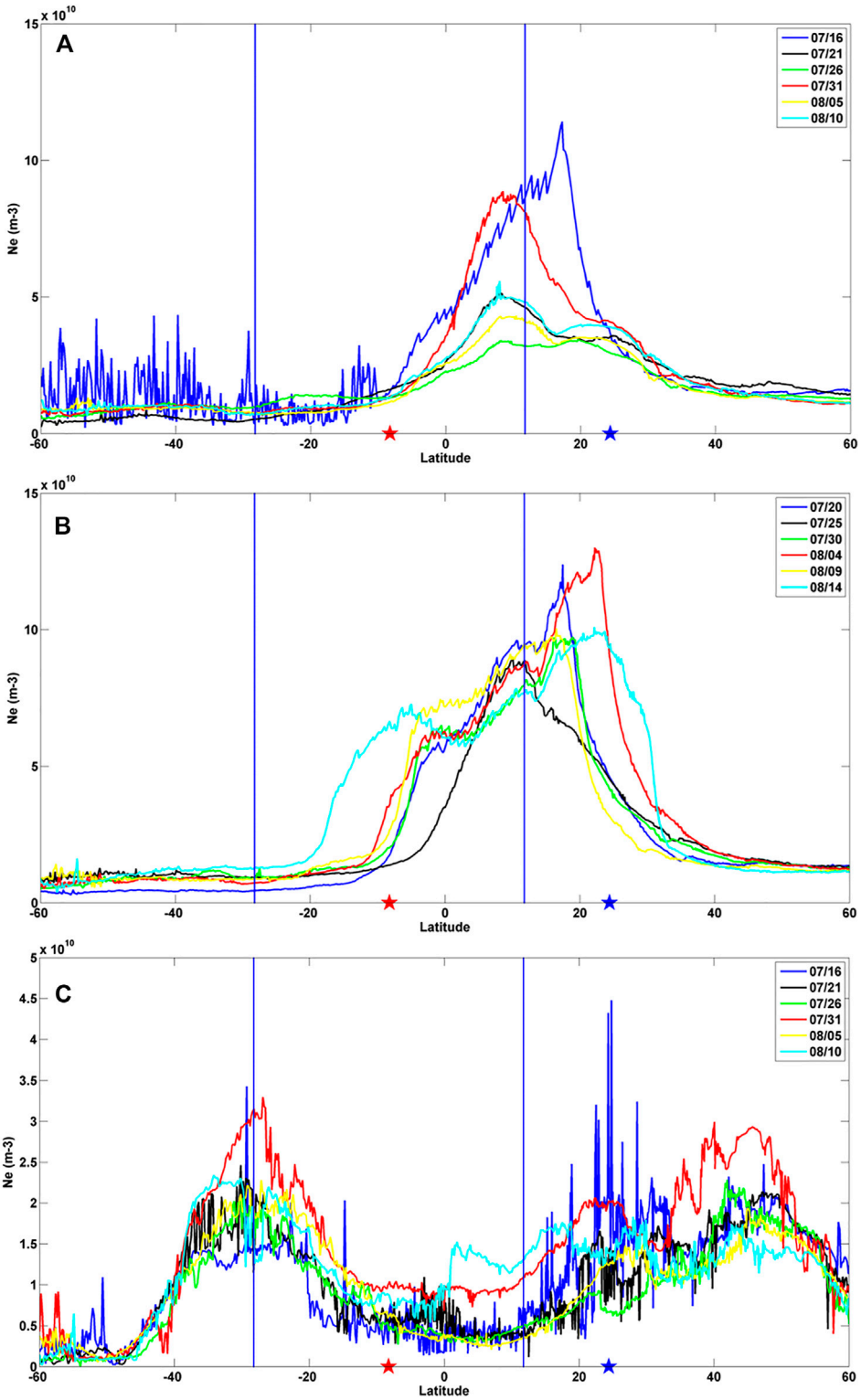


**FIGURE 5 |** Electron densities distribute along the latitude for the revisiting orbits in the daytime on 31 July **(A)**, 4 August **(B)**, and in the nighttime on 31 July **(C)**. The red curve represents the orbit with detected anomalies, and the other color curves represent its revisiting orbits whose dates are marked in the legend. The red and blue stars represent epicenter and its conjugate point, and two blue lines have the distance of 20° away from the latitude of epicenter.

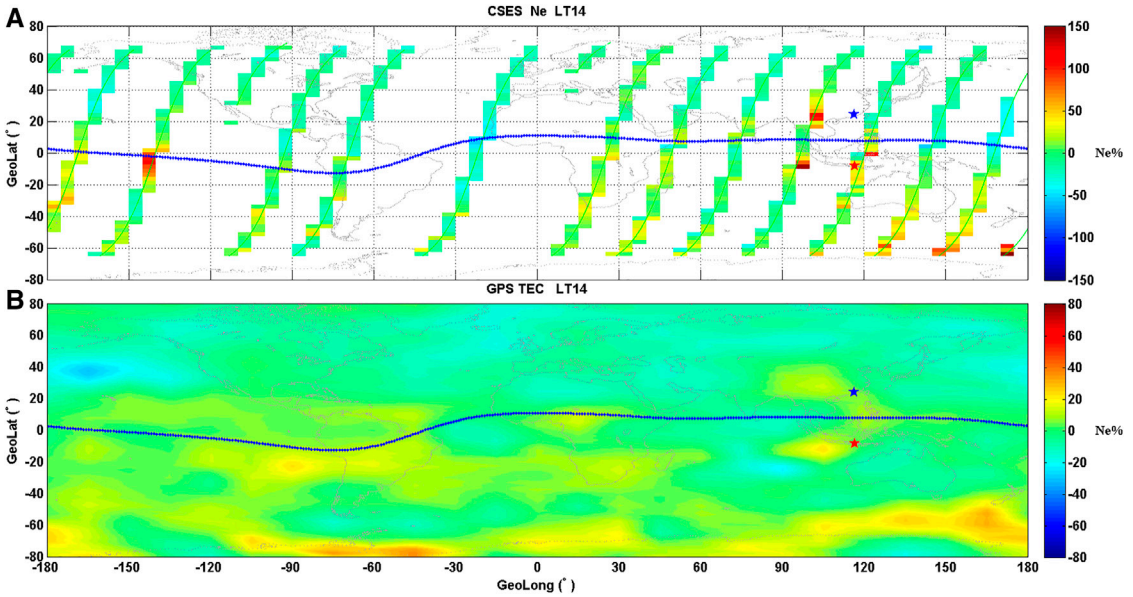


**FIGURE 6 |** Relative change of CSES *Ne* **(A)** and GIM TEC **(B)** in the daytime on 4 August 2018. Blue line represents magnetic equator. Red star shows the epicenter and blue one indicates its conjugate point.

Global/local ionospheric maps using GNSS observation data can be traced back to 1992, when Wilson and Mannucci of Jet Propulsion Laboratory (JPL) first mapped the global ionosphere with 8th order spherical harmonics (Wilson et al., 1992; Mannucci et al., 1998). The GIM TEC of JPL is supported by about 150 stations of IGS (International GNSS Service) and other organizations, with the spatial resolution of 2.5° in latitude and 5° in longitude for each 2 h, which can be downloaded from the website ftp://cddis.gsfc.nasa.gov/pub/gps/products/ionex.

In order to compare the TEC data with the electron density of CSES, GIM TEC at UT was converted to that at LT. Relative changes of GIM TEC data in the whole world at 14:00 (LT) and 02:00 (LT) were obtained using the same spatial analysis method (described in **Section 3**). Checking relative changes of GIM TEC when *Ne* disturbances occurred, the GIM TEC synchronous anomalies with *Ne* data were found in the daytime on 4 August, shown in **Figure 6**. The enhancements of TEC data were detected at the west of epicenter and its conjugate region at 14:00 (LT) on 4 August (**Figure 6B**), which was almost the same as the result of CSES *Ne* (**Figure 6A**). All cells in the whole world have data for GIM TEC, while the *Ne* median data can be obtained just for cells that the CSES flies over. Possibly affected by this reason, the region of GIM TEC anomaly was larger than that of CSES.

## 5 A WORLDWIDE ANALYSIS: STATISTICAL STUDY

Through the same observation with different analysis methods and different data with the same analysis method, the case study showed that disturbances associated with earthquakes can be detected by the spatial analysis. Therefore, the statistical study prior to strong earthquakes was carried out using the spatial analysis method, in order to find some characteristics of seismo-ionospheric disturbances.

For the 27-day background data that will be used to extract the disturbance, the time range of selected earthquakes in the statistical study is from 1 June 2018 to 30 September 2020. The list of global Mw ≥ 6.0 earthquakes that occurred during this period was downloaded from the website of the U.S. Geological Survey (USGS, https://earthquake.usgs.gov/earthquakes/search/), which is usually considered as strong earthquakes. The earthquakes with the geomagnetic latitude exceeding ±40° were excluded to avoid the influence at the high latitude. To exclude the post-seismic effect, the earthquakes were omitted if they were within 15 days and ±10° away from the previous one. At last, 206 Mw ≥ 6.0 earthquakes were selected, and the locations of epicenters are shown in **Figure 7**. The summarized information of earthquakes is listed in **Table 1**, including the magnitude and location.

A dataset of *Ne* from 30 days before the selected earthquakes to the occurrence day was created, which includes the daytime and nighttime data during 31 days for each earthquake. According to the study of Kon et al. (2011), Hattori et al. (2013), and De Santis et al. (2021), the superposed epoch and space approach (SESA) analysis method is accepted in this statistical study. The processing procedure involves four steps. First, for each earthquake, the area within ±20° away from the epicenter was selected as the study region, which means the cell data have 17 lines with the 2.5° latitude resolution and 9 columns with the 5° longitude resolution each day. Second, if the *Ne* relative changes in each cell were maximum or minimum compared to the values of the rest of cells out of ±20° away from the epicenter, from which

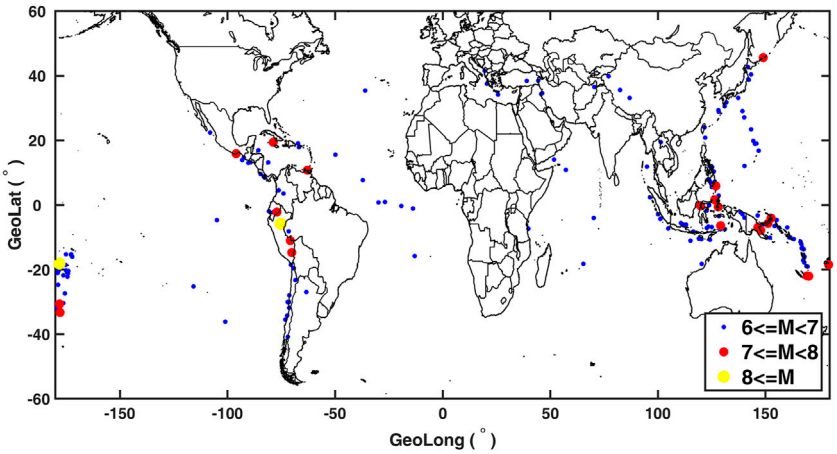


**FIGURE 7 |** Epicenters locations of global Mw ≥ 6.0 earthquakes from 1 June 2018 to 30 September 2020. Blue points represent the earthquakes with magnitude greater than 6 but less than 7. Red points represent the earthquakes with magnitude greater than 7 but less than 8. Yellow points represent the earthquakes with magnitude greater than 8.

**TABLE 1 |** Summarized information of 206 Mw ≥ 6.0 earthquakes.

| **Magnitude (M)** | | | **Location** | | | |
|---|---|---|---|---|---|---|
| 6 ≤ M < 7 | 7 ≤ M < 8 | 8 ≤ M | Geo-South | Geo-North | Mag-South | Mag-North |
| 183 | 21 | 2 | 129 | 77 | 140 | 66 |

the disturbances with the latitude greater than 40° were also excluded, the observation data were considered as potential seismo-ionospheric anomalies and were automatically marked as "1" (positive anomaly) or "−1" (negative anomaly). The other data which were not the extrema were marked as "0." We suppose that disturbances around the epicenter are significant after excluding the background and some known perturbation sources (e.g., solar activity and magnetic storm), same as the opinions of Liu et al. (2010) and Le et al. (2012). Therefore, if the *Ne* relative change is not the extremum around the epicenter (e.g., another higher value exists in another region), it will not be considered as a seismo-ionospheric anomaly in our study. Third, to exclude the disturbances induced by solar activity and magnetic storm, the anomalies that occurred in the day with an $F_{10.7} \geq 160$ or $Kp \geq 3$ or $|Dst| \geq$-30 nt or AE ≥ 500 nT were omitted and were also marked as "0." Finally, the markers ("−1," "0," and "−1") for 206 earthquakes during the daytime and nighttime were superposed together to obtain the SESA result.

The distributions of disturbances were exhibited in equator-polar direction for earthquakes locating in the geomagnetically southern or northern hemispheres. The summed result from 15 days before earthquakes to the occurrence day is shown in **Figure 8**. Both the positive and negative anomalies in the equator direction of epicenters were more obvious than those in the poleward direction of epicenters. The depletion of electron density was obvious near the epicenter 11 days before earthquakes. Around the locations of earthquakes, the positive disturbances enhanced 7 days before earthquakes and negative disturbances emerged 4 days prior to earthquakes. Three days before earthquakes, the electron density increased and decreased in the eastern and western directions, respectively. Near the occurrence of earthquakes, the anomalies around the epicenter were mainly positive in 1 day before earthquakes.

The distance between the center of each cell and epicenter was calculated to analyze the relationship of the distance from the epicenter, seismic magnitude, and occurrence time of the anomalies based on the statistical study. Meanwhile, similar to studies by Parrot (2012) and Ouyang et al. (2020), a random dataset with 206 Mw ≥ 6.0 earthquakes was obtained to carry out comparative analysis with real earthquakes. De Santis et al. (2019) compared their real results between real earthquakes and random anomalies. Although there is a little difference between De Santis et al. (2019) and our study for random events, their purpose and ours are to verify the statistical significance of real earthquakes with pseudo disturbances which have no relationship with real earthquakes. Same as real earthquakes, the spatial analysis method, anomalies excluded in the days of magnetic disturbances, and SESA statistical method were also applied to analyze random earthquakes. Through the statistical analysis of real and random earthquakes, **Figures 9**, **11**, **12** gave out the results of seismo-ionospheric disturbances with three parameters, including the occurrence time of anomalies, seismic magnitude, and distance from the epicenter. The increase and depletion of electron density were not distinguished in these figures, and numbers of positive and negative anomalies were summed together to show the number of anomalies, which means "1" and "−1" were both counted as "1." In order to avoid the difference brought by the sample size of distance and

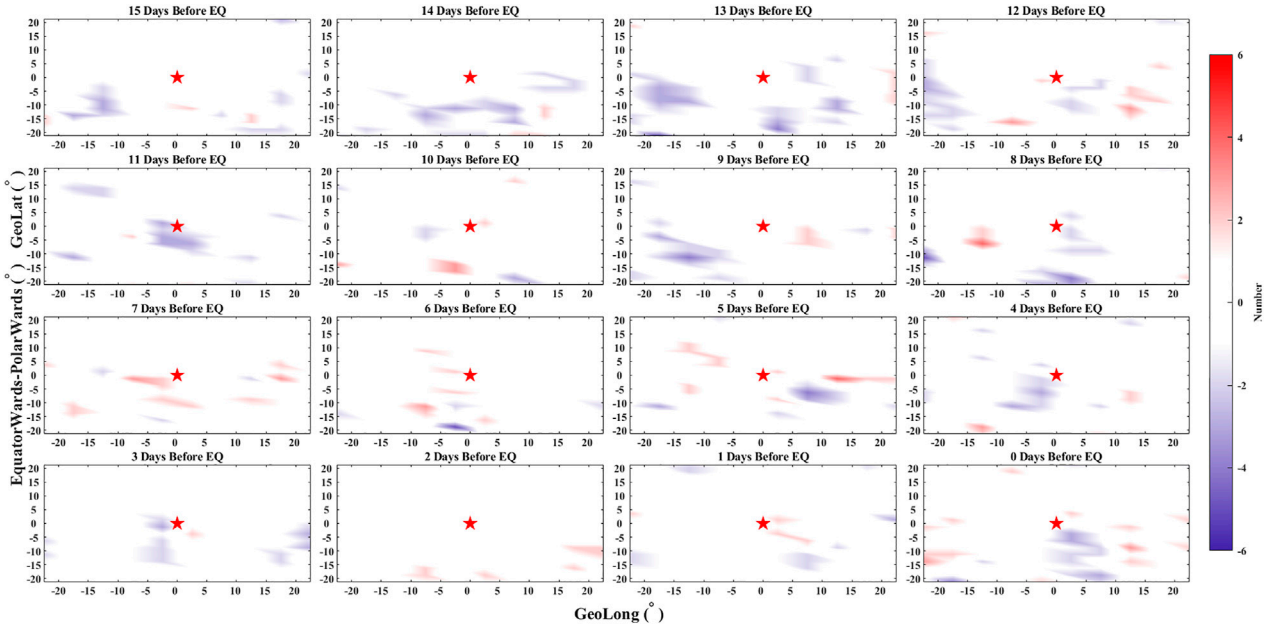


**FIGURE 8 |** Distributions of *Ne* anomalies from 15 days before earthquakes to the occurrence day. The red star represents the epicenter. In each subplot, *X* and *Y* axes are degrees from the epicenter in the geographic longitude and geographic latitude, respectively. The days before earthquakes are marked on the top of each panel.

magnitude, the numbers of anomalies were normalized. **Figures 9A,B**, **11A,B**, **12A,B** represent statistical results of real and random earthquakes, respectively, and the colors mean normalized number by SESA.

A time–distance diagram is constructed in **Figure 9** with 1-day step for *X*-axis and 100-km step for *Y*-axis, where the origin (0, 0) was set as the location and the temporal occurrence of each earthquake. The normalized number is the ratio between the counted number of anomalies and the number of cells with the same distance. The horizontal white band of the picture means that there is no data in this distance. In panel (A), although there are some seismo-ionospheric disturbances in other distances and days, those anomalies within 300 km from the epicenter are more obvious. De Santis et al. (2021) found the anomalies of electron density were concentrating within 380 km from epicenters by analyzing CSES data before M ≥ 5.5 shallow earthquakes. In the time, the anomalies are more in 11, 3, and 2 days prior to earthquakes. While in the result of random earthquakes (**Figure 9B**), anomalies randomly distribute along with the days and distances and do not exhibit the potential relationship with the distance to epicenter and occurrence time of real earthquake. It is supposed that seismo-ionospheric anomalies cannot be detected for random earthquakes, which could be considered as the background to assess the significance of real earthquakes statistics (He et al., 2021). The numbers within 300 km from the epicenter were summed in each day for real and random earthquakes. The data of real earthquakes results were plotted along with the days before earthquakes, as shown in **Figure 10**. The mean value (*M*) and standard deviation (*std*) of random earthquakes results in all 31 days were calculated, and $M \pm 2^{*}std$ was selected as the upper and lower thresholds, which possess a 95% confidence interval. The numbers of anomalies in 11, 3, and 2 days prior to earthquakes all exceeded the upper threshold. According to the study of De Santis et al. (2019), the parameter *d* was calculated, as illustrated in Supplementary **Supplementary Appendix S1**. The *d* value of statistical result within 300 km distance from the epicenter is 1.42, and that with the distance from 300 to 3,000 km is 0.93, which verifies the statistical significance of the former one.

To analyze the anomaly characteristics with the time and magnitude, the numbers of cells with ±20° away from the epicenter were all counted in each day for the same magnitude, which is shown in **Figure 11**. The normalized number represents the ratio between the counted number in 1 day and the number of earthquakes with the same magnitude. The statistical result in **Figure 11A** is not comprehensive for the limited sample size of Mw ≥ 8.0 earthquakes, while it can still be seen that the stronger the magnitude is, the earlier the disturbance appears. Based on the analysis of ground magnetic observations for Japan earthquakes, Rikitake (1987) proposed the general empirical law between precursor time (*T*) and magnitude (*M*) with the equation $logT = a+bM$, which also represents the linear relationship between the occurrence of anomalies and the magnitude of earthquakes, as confirmed by De Santis et al. (2019) for satellite data. In **Figure 11**, the occurrence time of disturbances prior to Mw ≥ 8.0 earthquakes can reach to 29 days. The maximum for Mw ≥ 8.0 earthquakes is earlier than that for 7.5 ≤ Mw < 8.0 earthquakes. A similar phenomenon is also exhibited for 7.5 ≤ Mw < 8.0 and 7.0 ≤ Mw < 7.5 earthquakes. Furthermore, the number of anomalies for earthquakes with a magnitude greater than 7 is larger than that for earthquakes with a magnitude less than 7. While in the result of random

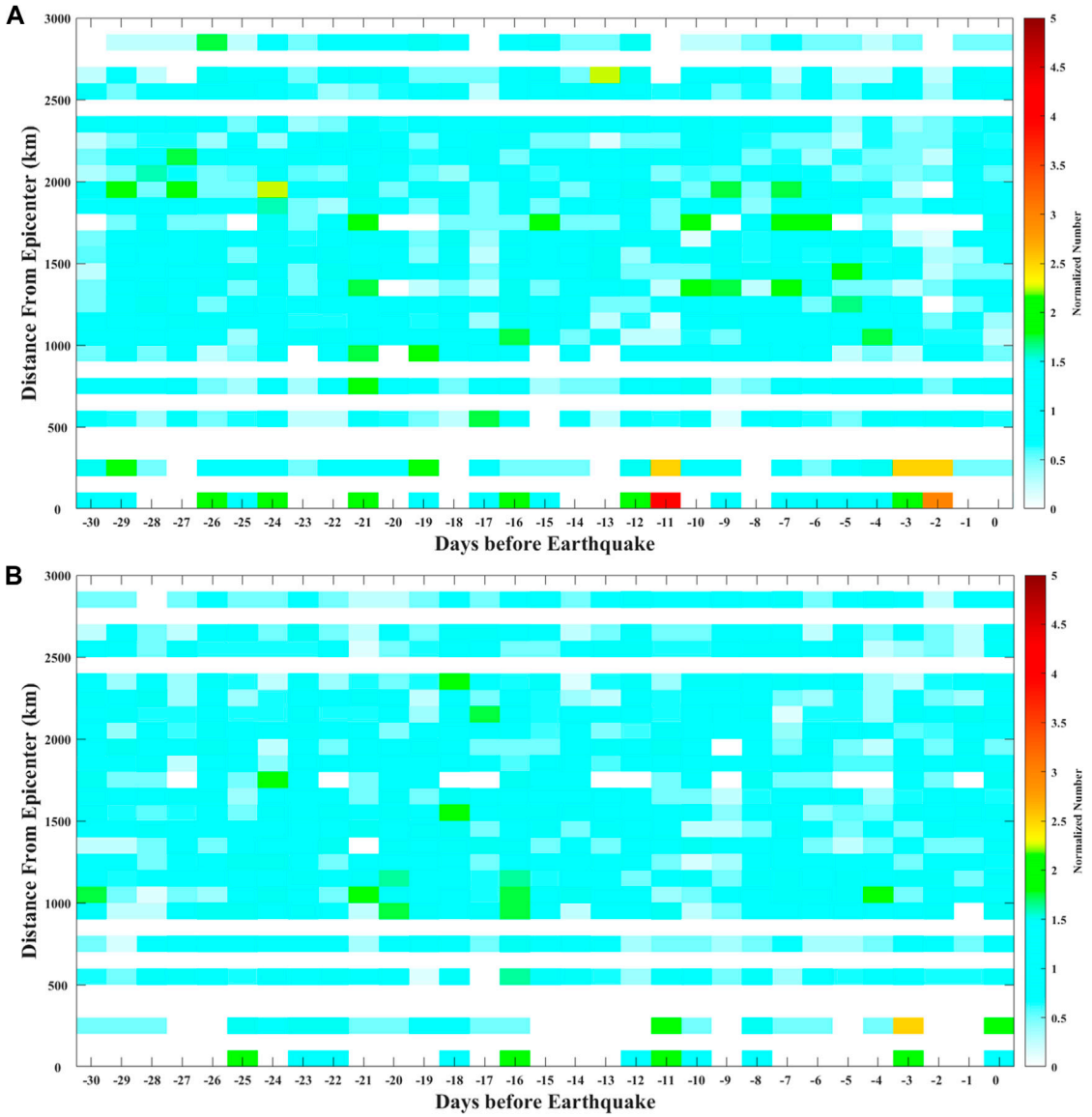


**FIGURE 9 |** Statistical result of seismo-ionospheric disturbances with the days before earthquake (*X* axis) and distance from the epicenter (*Y*-axis) by SESA. **(A,B)** Statistical results of real and random earthquakes, respectively. The color represents the normalized number by SESA, which is illustrated in the text. The horizontal white band of the picture means there is no data in this distance.

earthquakes (**Figure 11B**), normalized numbers are almost at the same level for all the days and magnitudes. The statistical characteristics of real earthquakes were not detected in the analysis of random earthquakes.

The numbers in all 31 days were summed together to analyze the anomaly characteristics with the magnitude and distance, which is shown in **Figure 12**. The normalized number represents the ratio between the counted number and the number of earthquakes with the same magnitude and the number of cells with the same distance. In **Figure 12A**, with the enhancement of seismic magnitude, the influence region of the seismo-ionospheric disturbances gradually enlarges. The maximum value can be found in 2,900–3,000 km distance from the epicenter for earthquakes with the magnitude between 7.5 and 8. In the lithosphere, the preparation region of earthquakes can be estimated by the formula $R = 10^{0.43M}$, where $R$ is the radius of the seismic effect zone and $M$ is the seismic magnitude (Dobrovolsky et al., 1979). For the earthquake with a magnitude of 8.0, the $R$ is 2,754 km, which is almost the same as the distance of statistical result. Unlike the statistical characteristics of real earthquakes, the relationship between the distance and earthquake magnitude is not obvious for random earthquakes, shown in **Figure 12B**.

The earthquakes were divided into shallow and deep ones according to the depth greater than 60 km or not. If the counted number of all cells in the 31-day dataset was larger than 1, the anomaly associated with the earthquake was considered as

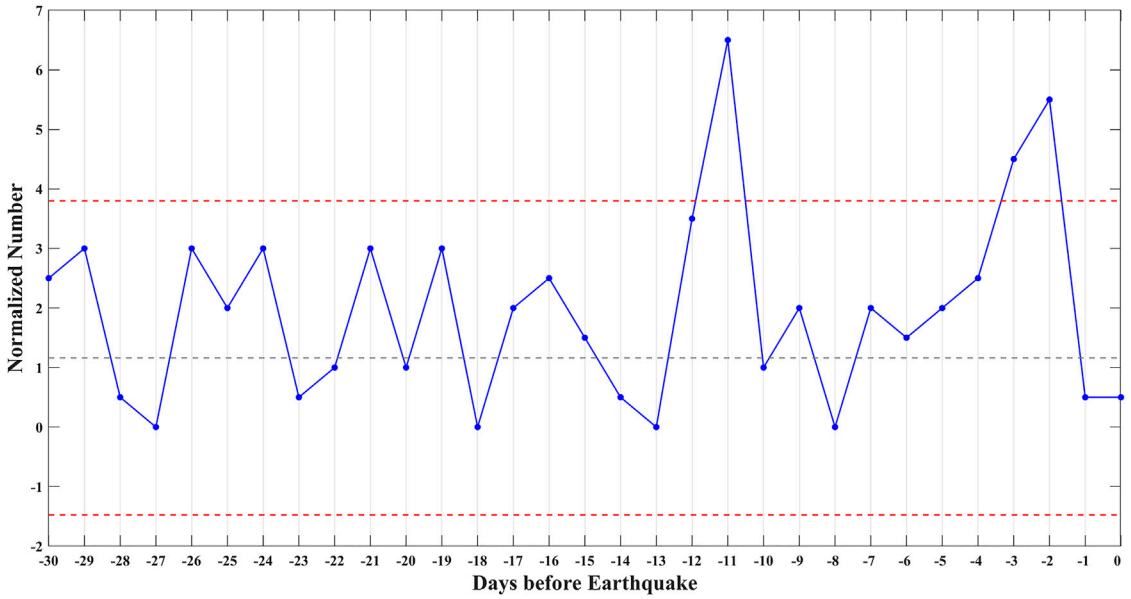


**FIGURE 10 |** Summed number of anomalies with 300 km distance from epicenter for real earthquakes. *X*-axis represents the days before earthquakes. *Y*-axis represents the total number of the data in first three lines in **Figure 9**. The gray dash line is the mean value (*M*) of random earthquakes results in all 31 days. Red dash lines are the upper and lower thresholds with $M \pm 2^{*}std$, where *M* and *std* are the mean value and standard deviation of random earthquakes results in all 31 days, respectively.

successfully detected. After the calculation, the probabilities of detected anomalies are 86.03% and 91.43% for shallow and deep earthquakes, respectively. For differences between the two probabilities are not significant, it is considered that the depth of earthquake is not the main factor for detecting anomalies. Whether the disturbance can propagate to the Earth's surface around the earthquake may mainly depend on the underground structure and material composition.

# 6 DISCUSSION

## 6.1 Location of Disturbances

From the previous analyses, not only the case study but also the statistical result shows that the seismo-ionospheric disturbances are more obvious in the equatorward direction for earthquakes located in the geomagnetically southern or northern hemispheres. Due to $\boldsymbol{E}\times\boldsymbol{B}$ drifts induced by the penetration of the ground anomalous electric field into the ionosphere, researchers reported that the location of the seismo-ionospheric anomalies might shift equatorward (Pulinets and Boyarchuk, 2004; Kuo et al., 2011; Liu et al., 2014; Kuo et al., 2015). Taking Indonesia Mw6.9 earthquake as an example, a simulation study using electric field penetration and the thermosphere–ionosphere–electrodynamics general circulation model (TIEGCM, Richmond et al., 1992) was carried out, and the comparison between the output and observation was applied to further understand the seismo-ionospheric coupling mechanism.

According to Zhou et al.'s (2017) study, ionospheric electric potential equations can be obtained in spherical coordinates based on the external electric current theory. The simulation results indicate that a vertical current generated by an additional vertical electric field at the ground can flow into the ionosphere without divergence in the neutral atmosphere and consequently induce the abnormal electric field in the ionosphere. This model can be used to calculate the additional lithosphere–atmosphere–ionosphere coupling (LAIC) electric field penetration at different altitudes by taking into account the inhomogeneous conductivity. Not only the laboratory experiment but also the real observation, an upward electric field in atmosphere before earthquakes, was reported by scientists (Smirnov, 2008; Choudhury et al., 2013); thus, a vertical upward electric current was added around the epicenter (8.258°S, 116.438°E) on 31 July 2018 when the anomalies can be detected both in the daytime and nighttime. According to the observation, the magnitude of atmospheric vertical electric field before earthquakes almost reaches to the level of kV/m (Hao et al., 1998; Smirnov, 2008; Choudhury et al., 2013). The disturbed atmospheric conductivity before earthquakes was assumed as $10^{-12}$–$10^{-11}$ S/m near the ground in the model for Schumann resonance (Nickolaenko et al., 2006; Galuk et al., 2020; Hayakawa et al., 2020). From the calculation using the formula $J = \sigma^{*}E$, the magnitude of disturbed electric current near the Earth's surface is $10^{-9}$–$10^{-8}$ A/m$^2$. Therefore, in this simulation, the maximum value of electric current was set as $8 \times 10^{-9}$ A/m$^2$. Pulinets and Boyarchuk (2004) pointed out that when the diameter of anomalous field on the ground exceeds 200 km, the vertical electric field can effectively penetrate from the ground into the ionosphere. To obtain obvious disturbance of electron density in the ionosphere,

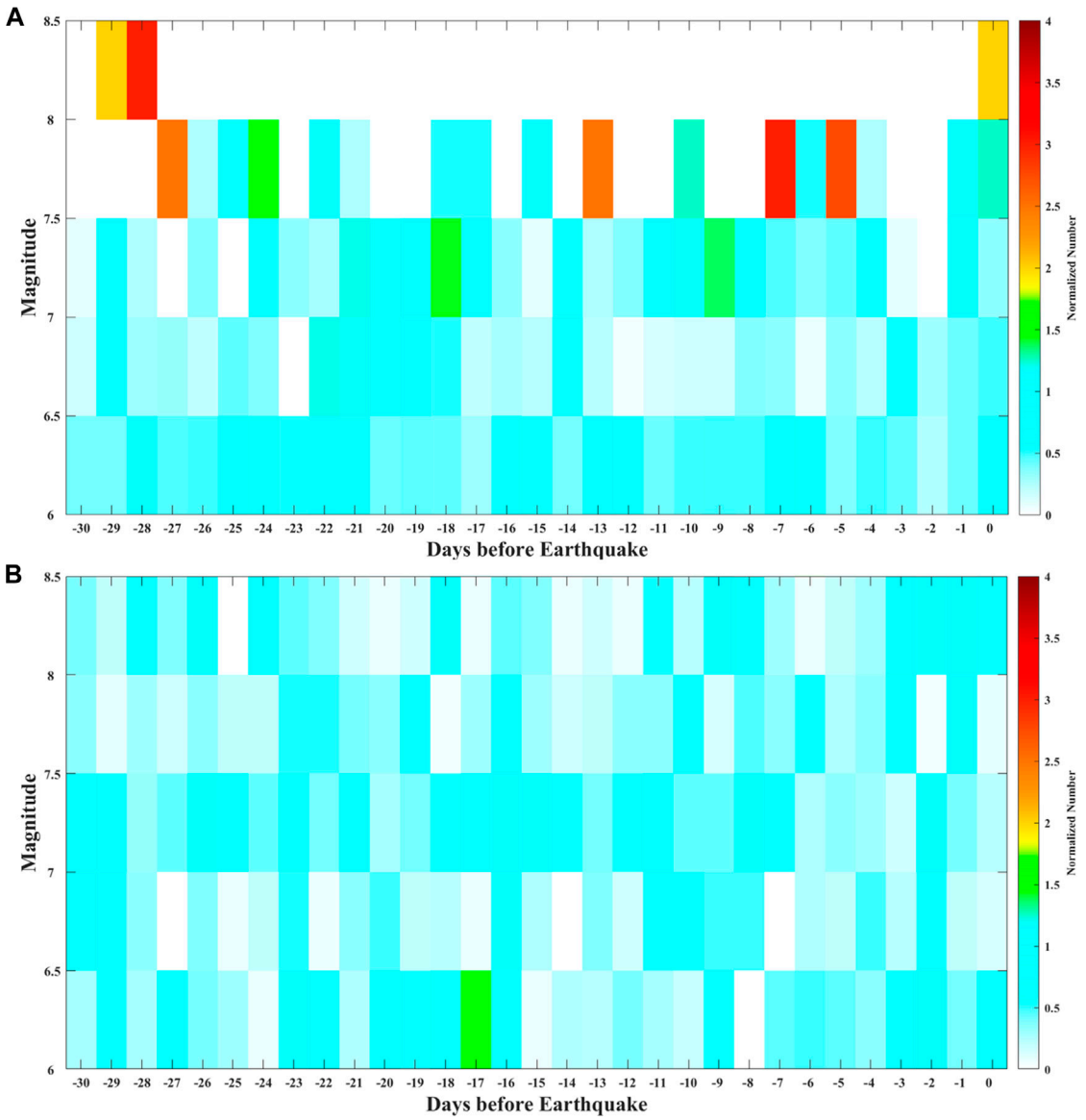


**FIGURE 11 |** Statistical result of seismo-ionospheric disturbances with the days before earthquakes (*X*-axis) and seismic magnitude (*Y*-axis) by SESA. **(A,B)** Statistical results of real and random earthquakes, respectively. The color represents the normalized number by SESA, which is illustrated in the text.

the radius of the current near the Earth's surface was assumed as 200 km with a Gaussian distribution, which is the same as the input of Zhou et al.'s (2017) study. Through the calculation using the detailed formulations given in **Supplementary Appendix S2**, the distribution of electric field at the bottom of ionosphere (~90 km) in a different direction is shown in **Figure 13**, which was induced by the additional electric current.

The National Center for Atmospheric Research (NCAR) TIEGCM is a time-dependent, three-dimensional model of the coupled thermosphere and ionosphere system. The model self-consistently solves the energy, momentum, and continuity equations of the neutral gas (Richmond et al., 1992). The horizontal resolution of the TIEGCM is 2.5°(latitude)×2.5°(longitude), and the vertical resolution is a quarter scale height from 97 to ~500 km (Wu et al., 2012). The code of TIEGCM is open, which is available at the High Altitude Observatory website (http://www.hao.ucar.edu/modeling/tgcm/download.php). The penetrated electric field calculated from the previous simulation (**Figure 13**) was applied to drive the TIEGCM, in order to check the *Ne* anomalies at the satellite altitude. To compare the modeling output with the observation data, the *Ne* relative change with and without the penetrated electric field was also obtained by **Eq. 1**, where *Od* represents the modeling *Ne* with the penetrated electric field and *Bd* is the simulation *Ne* without this electric field.

**Figure 14** shows the *Ne* relative change at 14:00 (LT) on 31 July 2018 at about 500 km altitude (with the same atmospheric pressure). Disturbed by the penetrating electric field, the electron

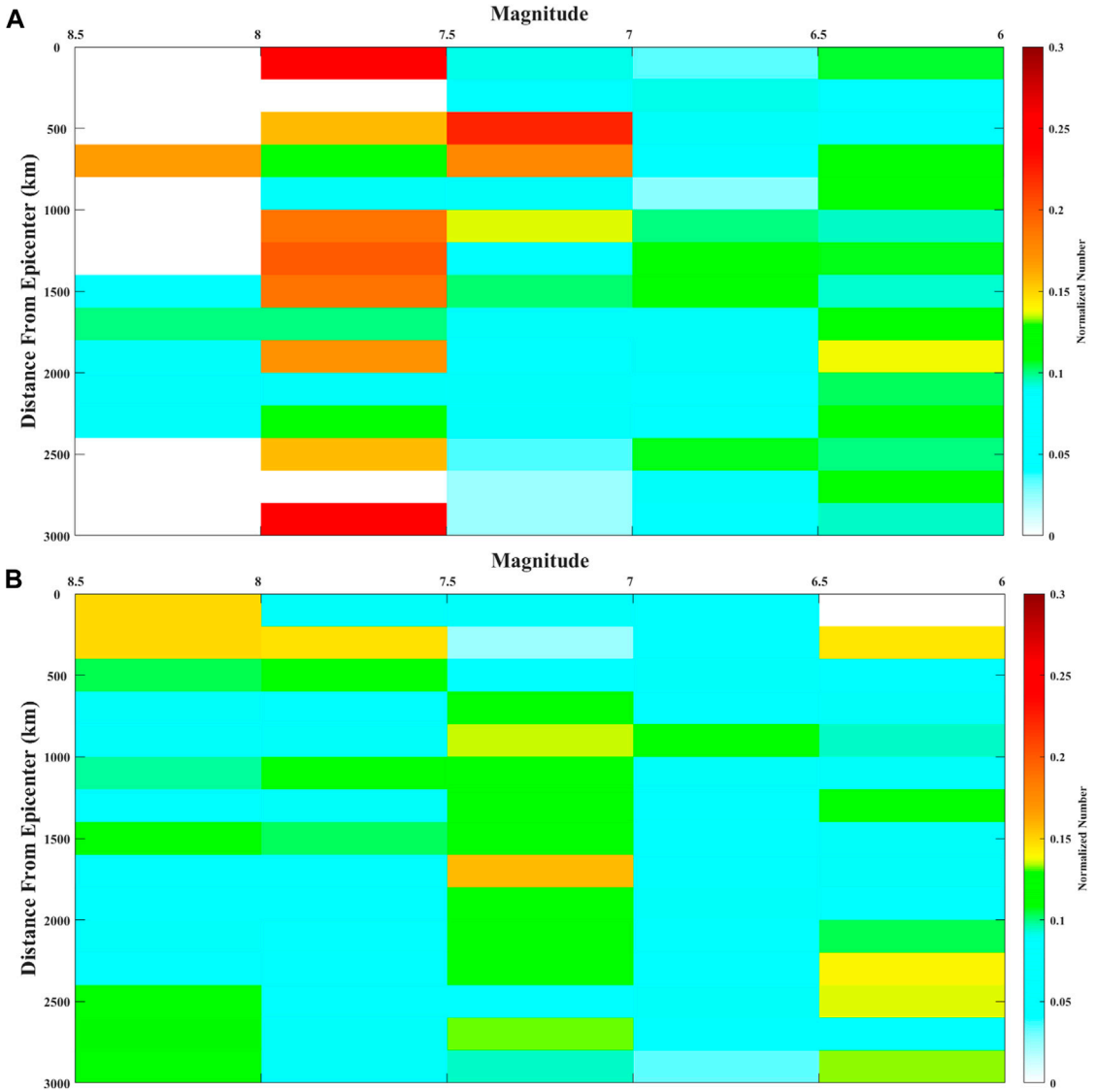


**FIGURE 12 |** Statistical result of seismo-ionospheric disturbances with the seismic magnitude (*X*-axis) and distance from the epicenter (*Y*-axis) by SESA. **(A,B)** Statistical results of real and random earthquakes, respectively. The color represents the normalized number by SESA, which is illustrated in the text.

density increases and decreases in the northeast and northwest directions of the epicenter, respectively. In the northern hemisphere, the location of the enhancement and depletion is symmetric with the epicenter region along the magnetic equator, which also situates in the equator direction of conjugate point. No matter in the daytime or nighttime (**Figures 3A,C**), the *Ne* disturbance on 31 July for Indonesia Mw6.9 earthquake was almost the same as the simulation output, with the patterns of increasing in the northeast and decreasing in the northwest of the earthquake locating in the geomagnetic southern hemisphere. The disturbed electric field in the ionosphere drives the electron density to move from one side to another side and makes the positive and negative anomalies exhibit the characteristics of right–left symmetry. Limited by the resolution of satellite, the circular morphology of simulation was not detected by the observation. Both positive and negative anomalies of ionospheric electron densities before earthquakes have been reported in previous studies (Liu et al., 2000; Kon et al., 2011). According to the simulation, the enhancement and depletion of electron density situate on different sides of the epicenter. Same as our result, Zhao et al. (2010) also showed that TEC positive and negative anomalies occurred on the east and west sides of the epicenter on 9 May before the Wenchuan earthquake on 12 May 2008. In addition to that, the occurrence of positive or negative anomalies can also depend on the altitude and time of observations. For the same Wenchuan earthquake, Zhang et al. (2009) reported that the oxygen-ion density at 660 km altitude decreased around the epicenter on 9 May using the

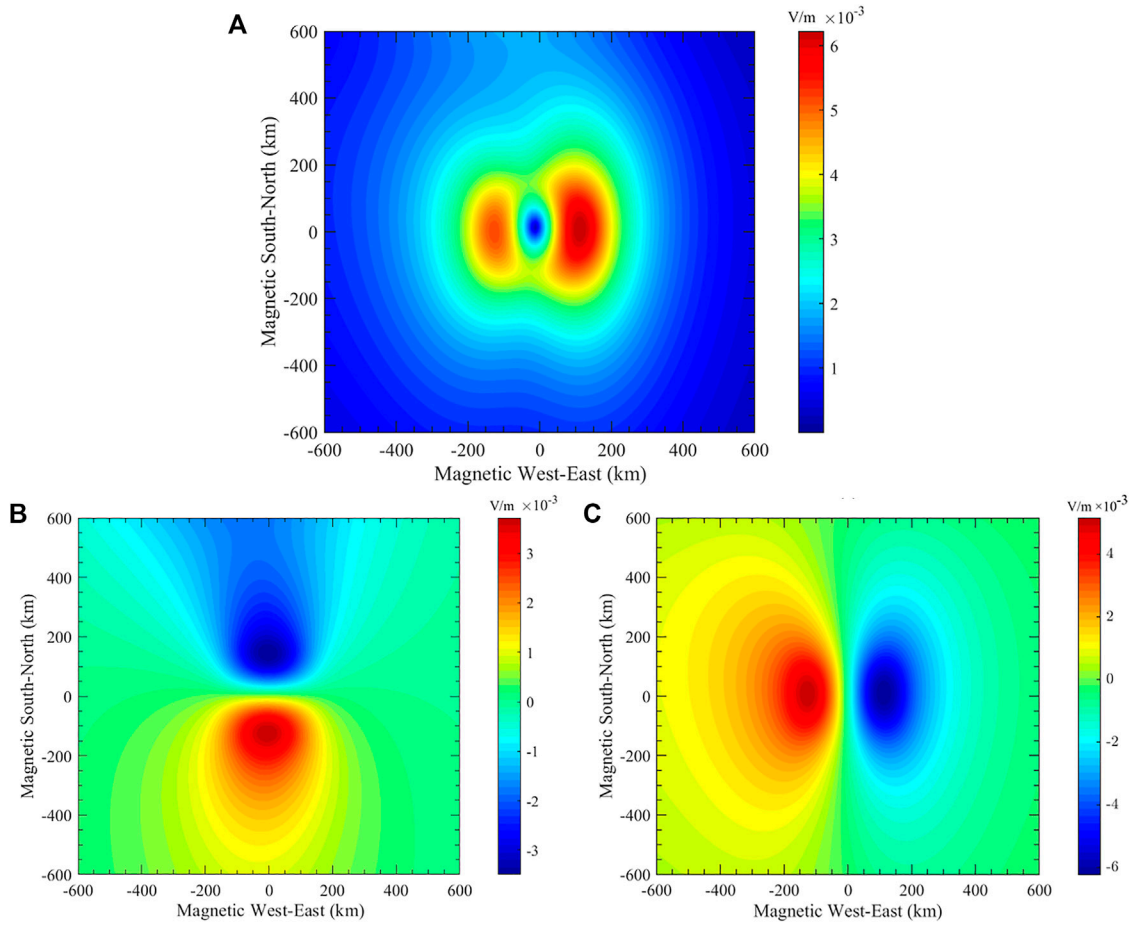


**FIGURE 13 |** Distribution of penetrating electric field at the bottom of ionosphere (~90 km) by LAIC simulation. **(A)** Total horizontal electric field. **(B)** Horizontal electric field in the south–north direction. **(C)** Horizontal electric field in the west–east direction. In each panel, *X* and *Y* coordinate axes represent magnetic west–east and south–north direction, respectively.

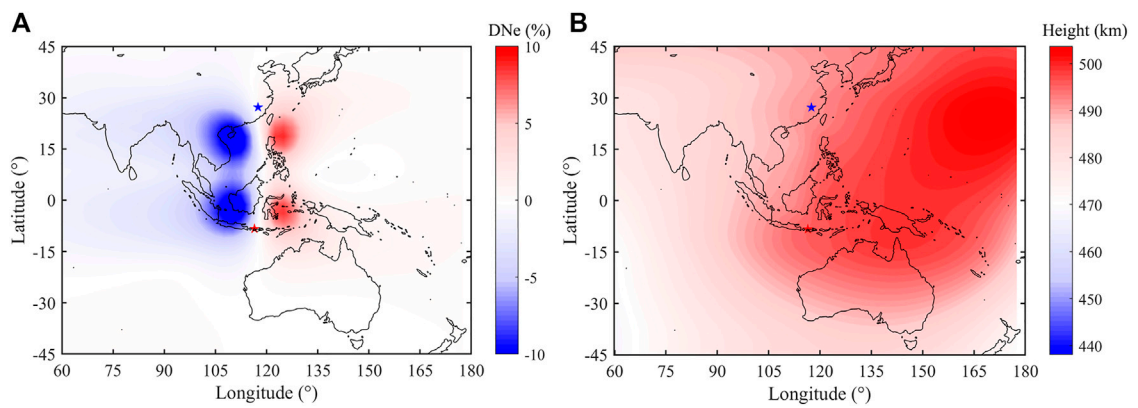


**FIGURE 14 |** Simulation result at 14:00 (LT) on 31 July 2018. **(A)** Distribution of *Ne* relative change with and without penetrating the electric field, and **(B)** altitude of *Ne* in **(A)**. Red and blue stars represent epicenter and its conjugate point, respectively.

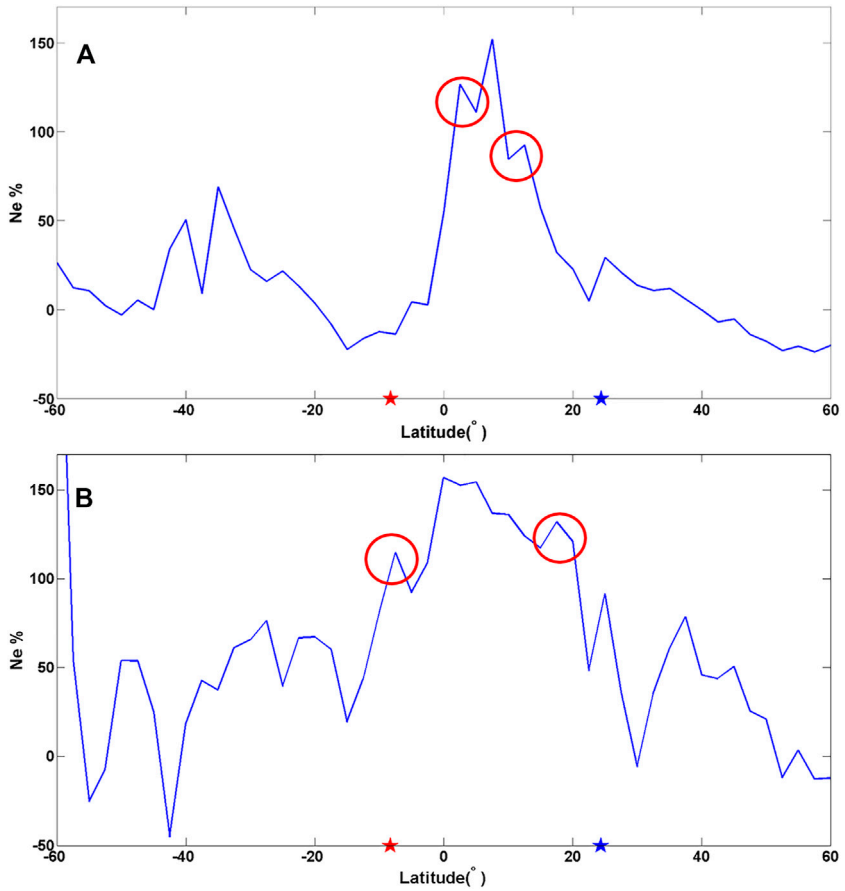


**FIGURE 15 |** *Ne* relative change along orbit in the daytime **(A)** and nighttime **(B)** on 31 July 2018. The red and blue stars represent the epicenter and its conjugate point, respectively.

DEMETER data, and Liu et al. (2009) found the negative anomalies of GIM TEC on 6 May.

In the simulation, *Ne* disturbance shows two peaks in the north and south of the magnetic equator. *Ne* relative changes in the daytime and nighttime on 31 July were plotted along the satellite orbits, as shown in **Figures 15A,B**. Like the simulation, there are also two peaks in the observation data, which is denoted by the red circle. Different from the simulation, no matter the daytime or nighttime, there is another strong peak around the magnetic equator. There may be two reasons that induce the differences between observations and simulations. First, limited by one satellite, the spatial resolution of CSES observation is lower than that of TIEGCM, indicating that there are no observation data in some regions. Second, in the topside of ionosphere, the ionospheric models have some differences from observation data (Bilitza et al., 2007; Lühr and Xiong, 2010; Lomidze et al., 2017). *Ne* usually exhibits a single peak around the magnetic equator in the topside of ionosphere (Zhang, 2014; Yan et al., 2020), while the ionospheric model (e.g., IRI model) shows two peaks in this region (Liu et al., 2021). The enhancement on August 4 was located in the west (**Figure 3B**), which was reversed with the simulation. The additional electric field was set in the upward direction in this simulation, which means the negative anomaly of electrostatic field around the epicenter, while some researchers also reported the positive variation of electric field prior to earthquakes in real observations (Mikhailov et al., 2006; Kachakhidze et al., 2009; Jin et al., 2020). The different directions of additional electric field may make the enhancement and depletion of electron density appear in different directions of epicenters. Affected by magnetic lines of the Earth, the disturbed electric field makes the electron density fluctuate in the equator direction, which is shown in the modeling simulation. The disturbances detected by CSES prior to Indonesia Mw6.9 earthquake were shifting equatorward. Furthermore, the *Ne* anomalies obtained by statistical analysis (**Figure 8**) were also obvious in the equator direction as the simulation, and the phenomenon of one side enhancing and the other side reducing was found in 3 days before earthquakes. The location consistency of anomalies between observation and simulation proposes that the electric field pathway may be the main channel of LAIC.

## 6.2 Time of Disturbances

From the statistical analysis, the seismo-ionospheric disturbances within 300 km distance from the epicenter are relatively obvious

11, 3, and 2 days prior to Mw ≥ 6.0 earthquakes. De Santis et al. (2019) suggested that ionospheric *Ne* anomalies may occur from a few days to 80 days before earthquakes, which is related to the earthquake magnitude. Some researchers considered the advance time of precursors may depend on the regions of earthquakes. By analyzing the GPS TEC and *fo*F2 data, Liu et al. (2004b), Liu et al. (2006) detected that the ionospheric anomalies appear within 5 days before strong earthquakes in the Taiwan area. In Greece, Davidenko and Pulinets (2019) found the majority of precursors appear 1 day before M ≥ 6.0 earthquakes by analyzing vertical sounding data and TEC data. Pulinets et al. (2021) detected the precursory phenomena of ionospheric parameters 5–7 days before two strong earthquakes occurred in California.

In this study, we found that the occurrence time of disturbances has a relationship with the seismic magnitude. The stronger magnitude is the earlier disturbance appears. In the statistical study of Le et al. (2011), the occurrence time of abnormal GPS TEC rates prior to Mw > 7.0 earthquakes is earlier than that of other magnitudes. Based on case studies of earthquakes in China, Wang et al. (2018) reported that the duration of pre-earthquake phenomena have a positive relationship with the magnitude of future earthquake.

Another question is that why the anomalies are not continuous after their emergence. From the previous simulation, we consider the penetrating electric field is the main channel of LAIC. The anomalies of electric field near the ground have been found 3–16 days (Myachkin et al., 1972) and 2–40 days (Hao et al., 1998) prior to earthquakes, and these anomalies are not persistent till the occurrence of earthquakes. It is currently not clear why an anomaly of electric field occurs at a particular day or time before an earthquake. Furthermore, for the solar-synchronized orbit of CSES, the satellite can just support observations in two local times (ascending and descending nodes), whereas the ionospheric precursors strongly depend on the local time (Pulinets and Davidenko, 2018; Liu et al., 2000). Therefore, the observation data not in continuous time may reduce the detected probability of seimo-ionospheric disturbances. In addition to that, there may be other factors that the anomalies are not observed prior to earthquakes: the abnormal electric field on the ground does not penetrate into the ionosphere subject to the transition pathway; due to the limitation of the observation, including the time and location, the anomalies are not detected in the ionospheric topside. In a word, integration of ionospheric observation from both ground and space can support more comprehensive data to investigate disturbances prior to earthquakes.

## 7 CONCLUSION

Based on the characteristics of CSES, a spatial analysis method was applied to extract *Ne* disturbances prior to strong earthquakes. Focused on the Indonesia Mw6.9 earthquake, the anomalies were found in the daytime and nighttime on 31 July, and in the daytime on 4 August, the location of which almost shifted equatorward. Furthermore, these anomalies can also be detected by the revisiting orbit method using CSES *Ne* and GIM TEC data with the same analyzing method, which verifies the spatial analysis method, is effective to extract the seismo-ionospheric disturbances.

Through the statistical study prior to 206 Mw ≥ 6.0 global earthquakes using CSES *Ne* data from 1 May 2018 to 30 September 2020, some conclusions were obtained as follows: 1) Both the positive and negative anomalies in the equator direction are more obvious than those in the polar direction of earthquakes; 2) the anomalies within 300 km distance from the epicenter are more obvious than those at longer distances, and the number of anomalies in this distance exceeds 2*std threshold of random case in 11, 3, and 2 days prior to Mw ≥ 6.0 earthquakes; 3) with the enhancement of seismic magnitude, the influence region of seismo-ionospheric disturbances gradually enlarges and the occurrence time of anomalies associated with earthquakes becomes early. In the comparitive analysis of random earthquakes, these statistical characteristics were not detected. Through the modeling of electric field LAIC and TIEGCM, the simulation result supports the *Ne* anomalies induced by the disturbed electric field will shift equatorward and exhibit the characteristics of magnetic conjugate effect. Comparing the statistical result with the simulation output, the electric field pathway could be considered as the main channel of LAIC.

Although we identified some characteristics of ionospheric anomalies associated with strong earthquakes by analyzing the electron density observed by CSES, more studies are needed in the future, including more cases for improving the statistics and more observations analyses (such as Swarm dataset in the same period), in order to fully understand the physical mechanism of the seismo-ionospheric coupling.

## DATA AVAILABILITY STATEMENT

The original contributions presented in the study are included in the article/**Supplementary Material**; further inquiries can be directed to the corresponding author.

## AUTHOR CONTRIBUTIONS

JL analyzed the data and wrote the manuscript. XQ analyzed the data and wrote some programs. XZ proposed the topic and conceived the study. ZW and CZ completed the simulation work. YZ collected the data and did some analyses. All authors read and approved the final manuscript.

## FUNDING

This work is supported by the National Key R&D Program of China (2018YFC1503506, 2018YFF01013705), the Specialized Research Funds of the National Key Laboratory of Electromagnetic Environment (202001002), and APSCO Earthquake Research Project Phase II and ISSI-Beijing (2019-IT33).

## ACKNOWLEDGMENTS

The authors acknowledge CSES mission for providing the electron density, JPL for providing the GIM TEC data and USGS for the earthquake list. The websites for downloading these data are as follows: CSES data from http://www.leos.ac.cn/, JPL TEC data from ftp://cddis.gsfc.nasa.gov/pub/gps/products/ionex and earthquake list from https://earthquake.usgs.gov/earthquakes/search/. The authors also acknowledge the World Data Center for Geomagnetism, Kyoto for supplying *AE* and *Dst* indices, GFZ for providing *Kp* index, and Space Weather Canada for supporting $F_{10.7}$ index. The authors acknowledge the High Altitude Observatory for supporting the model of TIEGCM, which is available at the website (http://www.hao.ucar.edu/modeling/tgcm/download.php).

## SUPPLEMENTARY MATERIAL

The Supplementary Material for this article can be found online at: https://www.frontiersin.org/articles/10.3389/feart.2022.811658/full#supplementary-material

## REFERENCES

Anderson, D. N. (1981). Modeling the Ambient, Low Latitude F-Region Ionosphere-A Review. *J. Atmos. Terr. Phys.* 43, 753–762. doi:10.1016/0021-9169(81)90051-9

Bilitza, D., Truhlik, V., Richards, P., Abe, T., and Triskova, L. (2007). Solar Cycle Variations of Mid-latitude Electron Density and Temperature: Satellite Measurements and Model Calculations. *Adv. Space Res.* 39, 779–789. doi:10.1016/j.asr.2006.11.022

Brace, L. H., Theis, R. F., and Hoegy, W. R. (1987). Ionospheric Electron Temperature at Solar Maximum. *Adv. Space Res.* 7 (6), 99–106. doi:10.1016/0273-1177(87)90281-X

Chmyrev, V. M., Isaev, N. V., Serebryakova, O. N., Sorokin, V. M., and Sobolev, Y. P. (1997). Small-scale Plasma Inhomogeneities and Correlated ELF Emissions in the Ionosphere over an Earthquake Region. *J. Atmos. solar-Terr. Phys.* 59 (9), 967–974. doi:10.1016/S1364-6826(96)00110-1

Choudhury, A., Guha, A., De, B. K., and Roy, R. (2013). A Statistical Study on Precursory Effects of Earthquakes Observed through the Atmospheric Vertical Electric Field in Northeast India. *Ann. Geophys.* 56 (3), 1861–1867. doi:10.4401/ag-6235

Davidenko, D. V., and Pulinets, S. A. (2019). Deterministic Variability of the Ionosphere on the Eve of Strong (M ≥ 6) Earthquakes in the Regions of Greece and Italy According to Long-Term Measurements Data. *Geomagn. Aeron.* 59 (4), 493–508. doi:10.1134/s001679321904008x

De Santis, A., Marchetti, D., Pavón-Carrasco, F. J., Cianchini, G., Perrone, L., Abbattista, C., et al. (2019). Precursory Worldwide Signatures of Earthquake Occurrences on Swarm Satellite Data. *Sci. Rep.* 9 (1), 20287. doi:10.1038/s41598-019-56599-1

De Santis, A., Marchetti, D., Perrone, L., Campuzano, S. A., Cianchini, G., Cesaroni, C., et al. (2021). Statistical Correlation Analysis of strong Earthquakes and Ionospheric Electron Density Anomalies as Observed by CSES-01. *Il Nuovo Cimento* 44, 119. doi:10.1393/ncc/i2021-21119-1

Dobrovolsky, I. P., Zubkov, S. I., and Miachkin, V. I. (1979). Estimation of the Size of Earthquake Preparation Zones. *Pageoph* 117 (5), 1025–1044. doi:10.1007/BF00876083

Galuk, Y. P., Kudintseva, I. G., Nickolaenko, A. P., and Hayakawa, M. (2020). Modifications of Schumann Resonance Spectra as an Estimate of Causative Earthquake Magnitude: The Model Treatment. *J. Atmos. Solar-Terr. Phys.* 209, 105392. doi:10.1016/j.jastp.2020.105392

Gokhberg, M. B., Pilipenko, V. A., and Pokhotelov, O. A. (1983a). Satellite Observations of Electromagnetic Radiation above the Epicentral Region of an Imminent Earthquake. *Dokl. USSR Acad. Sci.* 268 (1), 53–55.

Gokhberg, M. B., Pilipenko, V. A., and Pokhotelov, O. A. (1983b). Seismic Precursors in the Ionosphere. *Izvestiya Earth Phys.* 19, 762–765.

Hanson, W. B., and Urquhart, A. L. (1994). High Altitude Bottomside Bubbles? *Geophys. Res. Lett.* 21, 2051–2054. doi:10.1029/94GL01580

Hao, J., Tang, T., and Li, D. (1998). Advancement of the Study on Taking the Anomalies of Static Atmospheric Field as index of Short-Term and Imminent Earthquake Prediction. *Earthquake* 18, 245–256. (in Chinese with English abstract).

Hattori, K., Han, P., Yoshino, C., Febriani, F., Yamaguchi, H., and Chen, C.-H. (2013). Investigation of ULF Seismo-Magnetic Phenomena in Kanto, Japan during 2000-2010: Case Studies and Statistical Studies. *Surv. Geophys.* 34, 293–316. doi:10.1007/s10712-012-9215-x

Hayakawa, M., Nickolaenko, A. P., Galuk, Y. P., and Kudintseva, I. G. (2020). Scattering of Extremely Low Frequency Electromagnetic Waves by a Localized Seismogenic Ionospheric Perturbation: Observation and Interpretation. *Radio Sci.* 55, e2020RS007130. doi:10.1029/2020RS007130

He, Y., Zhao, X., Yang, D., Wu, Y., and Li, Q. (2021). A Study to Investigate the Relationship between Ionospheric Disturbance and Seismic Activity Based on Swarm Satellite Data. *Phys. Earth Planet. Interiors*, 106826. doi:10.1016/j.pepi.2021.106826

Jin, X., Zhang, L., Bu, J., Qiu, G., Ma, L., Liu, C., et al. (2020). Discussion on Anomaly of Atmospheric Electrostatic Field in Wenchuan Ms8.0 Earthquake. *J. Electrost.* 104, 103423. doi:10.1016/j.elstat.2020.103423

Kachakhidze, N., Kachakhidze, M., Kereselidze, Z., and Ramishvili, G. (2009). Specific Variations of the Atmospheric Electric Field Potential Gradient as a Possible Precursor of Caucasus Earthquakes. *Nat. Hazards Earth Syst. Sci.* 9, 1221–1226. doi:10.5194/nhess-9-1221-2009

Kil, H., and Heelis, R. A. (1998). Global Distribution of Density Irregularities in the Equatorial Ionosphere. *J. Geophys. Res.* 103, 407–417. doi:10.1029/97JA02698

Kon, S., Nishihashi, M., and Hattori, K. (2011). Ionospheric Anomalies Possibly Associated with M ⩾ 6.0 Earthquakes in the Japan Area during 1998-2010: Case Studies and Statistical Study. *J. Asian Earth Sci.* 41, 410–420. doi:10.1016/j.jseaes.2010.10.005

Kuo, C. L., Huba, J. D., Joyce, G., and Lee, L. C. (2011). Ionosphere Plasma Bubbles and Density Variations Induced by Pre-earthquake Rock Currents and Associated Surface Charges. *J. Geophys. Res.* 116 (A10). doi:10.1029/2011JA016628

Kuo, C.-L., Lee, L.-C., and Heki, K. (2015). Preseismic TEC Changes for Tohoku-Oki Earthquake: Comparisons between Simulations and Observations. *Terr. Atmos. Ocean. Sci.* 26, 63–72. doi:10.3319/tao.2014.08.19.06(grt)

Larkina, V. I., Migulin, V. V., Nalivaiko, A. V., Gershenzon, N. I., Gokhberg, M. B., Liperovsky, V. A., et al. (1983). Observation of VLF Emissions, Related with Seismic Activity, on the Intercosmos-19 Satellite. *Geomagn. Aeronom.* 23, 684–687.

Le, H., Liu, J. Y., and Liu, L. (2011). A Statistical Analysis of Ionospheric Anomalies before 736M6.0+ Earthquakes during 2002-2010. *J. Geophys. Res.* 116 (A2). doi:10.1029/2010JA015781

Le, H., Liu, L., Liu, J.-Y., Zhao, B., Chen, Y., and Wan, W. (2013). The Ionospheric Anomalies Prior to the M9.0 Tohoku-Oki Earthquake. *J. Asian Earth Sci.* 62, 476–484. doi:10.1016/j.jseaes.2012.10.034

Le, H., Liu, J., Zhao, B., and Liu, L. (2015). Recent Progress in Ionospheric Earthquake Precursor Study in China: A Brief Review. *J. Asian Earth Sci.* 114, 420–430. doi:10.1016/j.jseaes.2015.06.024

Li, M., Shen, X., Parrot, M., Zhang, X., Zhang, Y., Yu, C., et al. (2020). Primary Joint Statistical Seismic Influence on Ionospheric Parameters Recorded by the CSES and DEMETER Satellites. *J. Geophys. Res. Space Phys.* 125, e2020JA028116. doi:10.1029/2020JA028116

Liu, J. Y., Chen, Y. I., Pulinets, S. A., Tsai, Y. B., and Chuo, Y. J. (2000). Seismo-ionospheric Signatures Prior to M≥6.0 Taiwan Earthquakes. *Geophys. Res. Lett.* 27 (19), 3113–3116. doi:10.1029/2000GL011395

Liu, J. Y., Chen, Y.-I., Jhuang, H.-K., and Lin, Y.-H. (2004a). Ionospheric foF2 and TEC Anomalous Days Associated with M >= 5.0 Earthquakes in Taiwan during

1997-1999. *Terr. Atmos. Ocean. Sci.* 15, 371–383. doi:10.3319/tao.2004.15.3.371(ep)

Liu, J. Y., Chuo, Y. J., Shan, S. J., Tsai, Y. B., Chen, Y. I., Pulinets, S. A., et al. (2004b). Pre-Earthquake Ionospheric Anomalies Registered by Continuous GPS TEC Measurements. *Ann. Geophys.* 22, 1585–1593. doi:10.5194/angeo-22-1585-2004

Liu, J. Y., Chen, Y. I., Chuo, Y. J., and Chen, C. S. (2006). A Statistical Investigation of Preearthquake Ionospheric Anomaly. *J. Geophys. Res.* 111, A05304. doi:10.1029/2005JA011333

Liu, J. Y., Chen, Y. I., Chen, C. H., Liu, C. Y., Chen, C. Y., Nishihashi, M., et al. (2009). Seismoionospheric GPS Total Electron Content Anomalies Observed before the 12 May 2008Mw7.9 Wenchuan Earthquake. *J. Geophys. Res.* 114, 231–261. doi:10.1029/2008JA013698

Liu, J. Y., Chen, Y. I., Chen, C. H., and Hattori, K. (2010). Temporal and Spatial Precursors in the Ionospheric Global Positioning System (GPS) Total Electron Content Observed before the 26 December 2004 M9.3 Sumatra-Andaman Earthquake. *J. Geophys. Res.* 115. doi:10.1029/2010JA015313

Liu, L., Wan, W., Chen, Y., and Le, H. (2011). Solar Activity Effects of the Ionosphere: A Brief Review. *Chin. Sci. Bull.* 56 (12), 1202–1211. doi:10.1007/s11434-010-4226-9

Liu, J., Huang, J., and Zhang, X. (2014). Ionospheric Perturbations in Plasma Parameters before Global strong Earthquakes. *Adv. Space Res.* 53 (5), 776–787. doi:10.1016/j.asr.2013.12.029

Liu, J.-Y., Hattori, K., and Chen, Y.-I. (2018). "Application of Total Electron Content Derived from the Global Navigation Satellite System for Detecting Earthquake Precursors," in *Pre-Earthquake Processes: A Multidisciplinary Approach to Earthquake Prediction Studies*. Editors . Editors D. Ouzounov, S. Pulinets, K. Hattori, and P. Taylor (Wiley), 305–317. doi:10.1002/9781119156949.ch17

Liu, C., Guan, Y., Zheng, X., Zhang, A., Piero, D., and Sun, Y. (2019). The Technology of Space Plasma *In-Situ* Measurement on the China Seismo-Electromagnetic Satellite. *Sci. China Technol. Sci.* 62, 829–838. doi:10.1007/s11431-018-9345-8

Liu, J., Guan, Y., Zhang, X., and Shen, X. (2021). The Data Comparison of Electron Density between CSES and DEMETER Satellite, Swarm Constellation and IRI Model. *Earth Space Sci.* 8, e2020EA001475. doi:10.1029/2020EA001475

Lomidze, L., Knudsen, D. J., Burchill, J., Kouznetsov, A., and Buchert, S. C. (2018). Calibration and Validation of Swarm Plasma Densities and Electron Temperatures Using Ground-Based Radars and Satellite Radio Occultation Measurements. *Radio Sci.* 53, 15–36. doi:10.1002/2017RS006415

Lühr, H., and Xiong, C. (2010). IRI-2007 Model Overestimates Electron Density during the 23/24 Solar Minimum. *Geophys. Res. Lett.* 37, a–n. doi:10.1029/2010GL045430

Mannucci, A. J., Wilson, B. D., Yuan, D. N., Ho, C. H., Lindqwister, U. J., and Runge, T. F. (1998). A Global Mapping Technique for GPS-Derived Ionospheric Total Electron Content Measurements. *Radio Sci.* 33 (3), 565–582. doi:10.1029/97RS02707

Marchetti, D., De Santis, A., Shen, X., Campuzano, S. A., Perrone, L., Piscini, A., et al. (2020). Possible Lithosphere-Atmosphere-Ionosphere Coupling Effects Prior to the 2018 Mw = 7.5 Indonesia Earthquake from Seismic, Atmospheric and Ionospheric Data. *J. Asian Earth Sci.* 188, 104097. doi:10.1016/j.jseaes.2019.104097

Mikhailov, Y. M., Mikhailova, G. A., Kapustina, O. V., Druzhin, G. I., and Smirnov, S. E. (2006). Electric and Electromagnetic Processes in the Near-Earth Atmosphere before Earthquakes on Kamchatka. *Geomagn. Aeron.* 46 (6), 796–808. doi:10.1134/s0016793206060156

Min, K., Park, J., Kim, H., Kim, V., Kil, H., Lee, J., et al. (2009). The 27-day Modulation of the Low-Latitude Ionosphere during a Solar Maximum. *J. Geophys. Res.* 114. doi:10.1029/2008JA013881

Myachkin, V. I., Sobolev, G. A., Dolbilkina, N. A., Morozow, V. N., and Preobrazensky, V. B. (1972). The Study of Variations in Geophysical fields Near Focal Zones of Kamchatka. *Tectonophysics* 14 (3-4), 287–293. doi:10.1016/0040-1951(72)90077-7

Nickolaenko, A. P., Hayakawa, M., Sekiguchi, M., Ando, Y., and Ohta, K. (2006). Model Modifications in Schumann Resonance Intensity Caused by a Localized Ionosphere Disturbance over the Earthquake Epicenter. *Ann. Geophys.* 24, 567–575. doi:10.5194/angeo-24-567-2006

Ouyang, X. Y., Parrot, M., and Bortnik, J. (2020). ULF Wave Activity Observed in the Nighttime Ionosphere above and Some Hours before Strong Earthquakes. *J. Geophys. Res. Space Phys.* 125 (9), e2020JA028396. doi:10.1029/2020ja028396

Parrot, M. (2012). Statistical Analysis of Automatically Detected Ion Density Variations Recorded by DEMETER and Their Relation to Seismic Activity. *Ann. Geophys.* 55 (1), 149–155. doi:10.4401/527010.4401/ag-5270

Piersanti, M., Materassi, M., Battiston, R., Carbone, V., Cicone, A., D'Angelo, G., et al. (2020). Magnetospheric-Ionospheric-Lithospheric Coupling Model. 1: Observations during the 5 August 2018 Bayan Earthquake. *Remote Sens.* 12, 3299. doi:10.3390/rs12203299

Pulinets, S., and Boyarchuk, K. (2004). *Ionospheric Precursors of Earthquakes*. New York: Springer Berlin Heidelberg.

Pulinets, S. A., and Davidenko, D. V. (2018). The Nocturnal Positive Ionospheric Anomaly of Electron Density as a Short-Term Earthquake Precursor and the Possible Physical Mechanism of its Formation. *Geomagn. Aeron.* 58 (4), 559–570. doi:10.1134/s0016793218040126

Pulinets, S. A., and Legen'ka, A. (2003). Spatial-temporal Characteristics of the Large Scale Disturbances of Electron Concentration Observed in the F-Region of the Ionosphere before strong Earthquakes. *Cosm. Res.* 41, 221–230. doi:10.1023/A:1024046814173

Pulinets, S. A., Legen'ka, A. D., Gaivoronskaya, T. V., and Depuev, V. K. (2003). Main Phenomenological Features of Ionospheric Precursors of strong Earthquakes. *J. Atmos. solar-terrestrial Phys.* 65 (16-18), 1337–1347. doi:10.1016/j.jastp.2003.07.011

Pulinets, S., Tsidilina, M., Ouzounov, D., and Davidenko, D. (2021). From Hector Mine M7.1 to Ridgecrest M7.1 Earthquake. A Look from a 20-Year Perspective. *Atmosphere* 12, 262. doi:10.3390/atmos12020262

Pulinets, S. A. (1998). Strong Earthquake Prediction Possibility with the Help of Topside Sounding from Satellites. *Adv. Space Res.* 21 (3), 455–458. doi:10.1016/S0273-1177(97)00880-6

Pulinets, S. A. (2006). Space Technologies for Short-Term Earthquake Warning. *Adv. Space Res.* 37 (4), 643–652. doi:10.1016/j.asr.2004.12.074

Rich, F. J., Sultan, P. J., and Burke, W. J. (2003). The 27-day Variations of Plasma Densities and Temperatures in the Topside Ionosphere. *J. Geophys. Res.* 108 (A7), 1297. doi:10.1029/2002JA009731

Richmond, A. D., Ridley, E. C., and Roble, R. G. (1992). A Thermosphere/ionosphere General Circulation Model with Coupled Electrodynamics. *Geophys. Res. Lett.* 19, 601–604. doi:10.1029/92GL00401

Rikitake, T. (1987). Earthquake Precursors in Japan: Precursor Time and Detectability. *Tectonophysics* 136, 265–282. doi:10.1016/0040-1951(87)90029-1

Rishbeth, H., and Garriott, O. K. (1969). *Introduction to Ionospheric Physics*. New York: Academic Press, 344.

Ryu, K., Lee, E., Chae, J. S., Parrot, M., and Pulinets, S. (2014). Seismo-ionospheric Coupling Appearing as Equatorial Electron Density Enhancements Observed via DEMETER Electron Density Measurements. *J. Geophys. Res. Space Phys.* 119 (10), 8524–8542. doi:10.1002/2014JA020284

Sarkar, S., Gwal, A. K., and Parrot, M. (2007). Ionospheric Variations Observed by the DEMETER Satellite in the Mid-latitude Region during strong Earthquakes. *J. Atmos. Solar-Terr. Phys.* 69 (13), 1524–1540. doi:10.1016/j.jastp.2007.06.006

Saroso, S., Liu, J.-Y., Hattori, K., and Chen, C.-H. (2008). Ionospheric GPS TEC Anomalies and M ≧ 5.9 Earthquakes in Indonesia during 1993 - 2002. *Terr. Atmos. Ocean. Sci.* 19, 481–488. doi:10.3319/tao.2008.19.5.481(t)

Schunk, R., and Nagy, A. (2009). *Ionospheres: Physics, Plasma Physics, and Chemistry*. England: Cambridge University Press, 628.

Schunk, R. W., and Sojka, J. J. (1996). Ionosphere-thermosphere Space Weather Issues. *J. Atmos. Terr. Phys.* 58 (14), 1527–1574. doi:10.1016/0021-9169(96)00029-3

Shen, X. H., Zhang, X., Yuan, S., Wang, L., Cao, J., Huang, J., et al. (2018a). The State-Of-The-Art of the China Seismo-Electromagnetic Satellite mission. *Sci. China Technol. Sci.* 61, 634–642. doi:10.1007/s11431-018-9242-0

Shen, X. H., Zong, Q. G., and Zhang, X. M. (2018b). Introduction to Special Section on the China Seismo-Electromagnetic Satellite and Initial Results. *Earth Planet. Phys.* 2 (6), 3–7. doi:10.26464/epp2018041

Smirnov, S. (2008). Association of the Negative Anomalies of the Quasistatic Electric Field in Atmosphere with Kamchatka Seismicity. *Nat. Hazards Earth Syst. Sci.* 8 (4), 745–749. doi:10.5194/nhess-8-745-2008

Song, R., Hattori, K., Zhang, X., and Sanaka, S. (2020). Seismic-ionospheric Effects Prior to Four Earthquakes in Indonesia Detected by the China Seismo-Electromagnetic Satellite. *J. Atmos. Solar-Terr. Phys.* 205, 105291. doi:10.1016/j.jastp.2020.105291

Tsurutani, B. (2004). Global Dayside Ionospheric Uplift and Enhancement Associated with Interplanetary Electric fields. *J. Geophys. Res.* 109 (A8), A08302. doi:10.1029/2003ja010342

Walker, G. O., Ma, J. H. K., and Golton, E. (1994). The Equatorial Ionospheric Anomaly in Electron Content from Solar Minimum to Solar Maximum for South East Asia. *Ann. Geophys.* 12, 195–209. doi:10.1007/s00585-994-0195-0

Wang, H., Zhang, Y., Liu, J., Shen, X., Yu, H., Jiang, Z., et al. (2018). "Pre-Earthquake Observations and Their Application in Earthquake Prediction in China," in *Pre-Earthquake Processes: A Multidisciplinary Approach to Earthquake Prediction Studies, Geophysical Monograph 234*. Editors D. Ouzounov, S. Pulinets, K. Hattori, and P. Taylor (United States of America: John Wiley & Sons, Inc. & American Geophysical Union), 19–39. doi:10.1002/9781119156949.ch3

Wang, X., Cheng, W., Yang, D., and Liu, D. (2019). Preliminary Validation of *In Situ* Electron Density Measurements Onboard CSES Using Observations from Swarm Satellites. *Adv. Space Res.* 64 (4), 982–994. doi:10.1016/j.asr.2019.05.025

Wilson, B., Mannucci, A., Edwards, C., and Roth, T. (1992). "Global Ionospheric Maps Using a Global Network of GPS Receivers," in Paper Presented at URSI Beacon Satellite Symposium, Cambridge, MA, July, 1992.

Wu, Q., Ortland, D. A., Foster, B., and Roble, R. G. (2012). Simulation of Nonmigrating Tide Influences on the Thermosphere and Ionosphere with a TIMED Data Driven TIEGCM. *J. Atmos. Solar-Terr. Phys.* 90-91, 61–67. doi:10.1016/j.jastp.2012.02.009

Xiong, N. L., Tang, C. C., and Li, X. J. (1999). *Introduction to the Ionosphere Physics*. Wuhan: Wuhan University press, 354–433. (In Chinese).

Xiong, C., Park, J., Lühr, H., Stolle, C., and Ma, S. Y. (2010). Comparing Plasma Bubble Occurrence Rates at CHAMP and GRACE Altitudes during High and Low Solar Activity. *Ann. Geophys.* 28 (9), 1647–1658. doi:10.5194/angeo-28-1647-2010

Yan, R., Parrot, M., and Pinçon, J.-L. (2017). Statistical Study on Variations of the Ionospheric Ion Density Observed by DEMETER and Related to Seismic Activities. *J. Geophys. Res. Space Phys.* 122, 12,421–12,429. doi:10.1002/2017JA024623

Yan, R., Shen, X. H., Shen, X., Huang, J., Wang, Q., Chu, W., et al. (2018). Examples of Unusual Ionospheric Observations by the CSES Prior to Earthquakes. *Earth Planet. Phys.* 2, 515–526. doi:10.26464/epp2018050

Yan, R., Zhima, Z., Xiong, C., Shen, X., Huang, J., Guan, Y., et al. (2020). Comparison of Electron Density and Temperature from the CSES Satellite with Other Space-Borne and Ground-Based Observations. *J. Geophys. Res. Space Phys.* 125 (10), e2019JA027747. doi:10.1029/2019JA027747

Zhang, X., Shen, X., Liu, J., Ouyang, X., Qian, J., and Zhao, S. (2009). Analysis of Ionospheric Plasma Perturbations before Wenchuan Earthquake. *Nat. Hazards Earth Syst. Sci.* 9, 1259–1266. doi:10.5194/nhess-9-1259-2009

Zhang, X., Shen, X., Liu, J., Ouyang, X., Qian, J., and Zhao, S. (2010). Ionospheric Perturbations of Electron Density before the Wenchuan Earthquake. *Int. J. Remote Sens.* 31 (13), 3559–3569. doi:10.1080/01431161003727762

Zhang, X., Zeren, Z., Parrot, M., Battiston, R., Qian, J., and Shen, X. (2011). ULF/ELF Ionospheric Electric Field and Plasma Perturbations Related to Chile Earthquakes. *Adv. Space Res.* 47 (6), 991–1000. doi:10.1016/j.asr.2010.11.001

Zhang, X., Wang, Y., Boudjada, M., Liu, J., Magnes, W., Zhou, Y., et al. (2020). Multi-Experiment Observations of Ionospheric Disturbances as Precursory Effects of the Indonesian Ms6.9 Earthquake on August 05, 2018. *Remote Sens.* 12, 4050. doi:10.3390/rs12244050

Zhang, X. (2014). Electron Density Comparison between IRI 2007 and DEMETER Satellite Data in Solar Minimum Year. *Terr. Atmos. Ocean. Sci.* 25, 559–571. doi:10.3319/TAO.2014.02.24.0110.3319/tao.2014.02.24.01(aa)

Zhao, B., Wang, M., Yu, T., Xu, G., Wan, W., and Liu, L. (2010). Ionospheric Total Electron Content Variations Prior to the 2008 Wenchuan Earthquake. *Int. J. Remote Sens.* 31 (13), 3545–3557. doi:10.1080/01431161003727622

Zhou, C., Liu, Y., Zhao, S., Liu, J., Zhang, X., Huang, J., et al. (2017). An Electric Field Penetration Model for Seismo-Ionospheric Research. *Adv. Space Res.* 60 (10), 2217–2232. doi:10.1016/j.asr.2017.08.007

**Conflict of Interest:** The authors declare that the research was conducted in the absence of any commercial or financial relationships that could be construed as a potential conflict of interest.

**Publisher's Note:** All claims expressed in this article are solely those of the authors and do not necessarily represent those of their affiliated organizations, or those of the publisher, the editors, and the reviewers. Any product that may be evaluated in this article, or claim that may be made by its manufacturer, is not guaranteed or endorsed by the publisher.

frontiers in Earth Science

ORIGINAL RESEARCH
published: 23 March 2022
doi: 10.3389/feart.2022.818788

# Study on Long-Term Variation Characteristics of Geomagnetic Cutoff Rigidities of Energetic Protons Caused by Long-Term Variation of Geomagnetic Field

*Wei Chu*[1]*, *Yanyan Yang*[1], *Song Xu*[1], *Gang Qin*[1], *Jianping Huang*[1], *Zhima Zeren*[1] and *Xuhui Shen*[1]

[1]Ministry of Emergency Management of China, National Institute of Natural Hazards, Beijing, China, [2]School of Science, Harbin Institute of Technology, Shenzhen, China

As a parameter that quantitatively measures the shielding effect of the Earth's magnetic field on energetic particles, the geomagnetic cutoff rigidities will change significantly with the long-term change of geomagnetic field. In this article, by using the numerical simulation method, combined with the variation trend of the Earth's main field International Geomagnetic Reference Field (IGRF) model and the energetic particles' windows (EPWs), the variation characteristics of the cutoff rigidities of geomagnetic energetic particles in the vertical direction from 1965 to 2025 were studied. The study found that there is a close relationship between the cutoff latitude corresponding to the cutoff rigidities and the background magnetic field intensity, but they are not in a simple linear relationship. The changes of the cutoff rigidities and geomagnetic field in the northern and southern hemispheres are asymmetric. The weakening of the geomagnetic field will push the cutoff latitudes toward the near equatorial region in the southern hemisphere, but for northern hemisphere the phenomenon is not always credible. In the northern hemisphere, the areas of EPWs will decrease at a relative rate of 0.03%/yr, but in the southern hemisphere, it will increase at a rate of about 0.05%/yr to 0.12%/yr. The long-term trajectory of the positions of the EPWs' central points do not correspond to geomagnetic poles, nor the magnetic dip poles, relatively speaking, its position is closer to the geomagnetic poles. The study can be used for a long-term forecasting of cutoff rigidities caused by background geomagnetic field variations.

**Keywords: geomagneticfield, cutoff rigidities, energetic particles, long-term, energetic particles' windows**

OPEN ACCESS

***Edited by:***
*Juergen Pilz,*
*University of Klagenfurt, Austria*

***Reviewed by:***
*F. Javier Pavón-Carrasco,*
*Complutense University of Madrid, Spain*
*Gelvam André Hartmann,*
*Campinas State University, Brazil*

***Correspondence:**
*Wei Chu*
*chuwei4076@126.com*

***Specialty section:***
*This article was submitted to Environmental Informatics and Remote Sensing, a section of the journal Frontiers in Earth Science*

***Received:*** *20 November 2021*
***Accepted:*** *01 March 2022*
***Published:*** *23 March 2022*

***Citation:***
*Chu W, Yang Y, Xu S, Qin G, Huang J, Zeren Z and Shen X (2022) Study on Long-Term Variation Characteristics of Geomagnetic Cutoff Rigidities of Energetic Protons Caused by Long-Term Variation of Geomagnetic Field. Front. Earth Sci. 10:818788. doi: 10.3389/feart.2022.818788*

## 1 INTRODUCTION

Energetic particles play a useful key-role in space weather storms forecasting (Mavromichalaki et al., 2006) and in the specification of magnetic properties of coronal mass ejections (CMEs), shocks, and ground level enhancements (GLEs). Meanwhile, the ionosphere and atmosphere of the Earth can be affected by the energetic particles which enter the magnetosphere at low altitudes (Nesse Tyssøy et al., 2013; Galand, 2001). Furthermore, energetic particles are major space weather phenomena that can produce hazardous effects in the near-Earth space environment. Understanding the physical

processes of the energetic particles has both scientific and practical significance, considering their serious impact on the space environment and space systems (e.g., harming the spacecrafts in the inner magnetosphere) (Koons et al., 1998; Baker and D., 2000). Therefore, the study of the coupling mechanism between interplanetary and magnetospheric energetic particles is an important issue in solar terrestrial space physics.

Energetic protons are the main component of cosmic rays, and the interplanetary energetic particles can penetrate the protective layer of electronic components, resulting in single-event inversion, which poses a threat to the health of astronauts. At the same time, it will also reduce the service life of solar cells and affect polar short wave communication. In serious cases, it will cause damage to electronic components, cause satellite failure, and even completely destroy the satellite (Baker and D, 2000; Koons et al., 1998). Also, the variation of the energetic particle environment can affect the airplane routes across the polar region (Alken et al., 2020). Also, some researchers found that the cosmic rays can affect the climate (Kirkby, 2007), which will have a long-term variation.

The access of energetic protons into the magnetosphere is controlled by the magnetic field. As the first barrier of the Earth, the geomagnetic field can effectively prevent the entry of interplanetary energetic particles and reduce the radiation of energetic particles in near-Earth space. Störmer (1955) first theoretically described the behavior by assuming that the magnetic field is a dipole field. In a pure dipole magnetic field, particles are shielded by a potential barrier from an inner forbidden region whose boundary is defined by the following equation as (Störmer, 1955):

$$r = \sqrt{\frac{Mq}{mvc}}\ \frac{\cos^2\lambda}{1+\sqrt{1+\cos^3\lambda}}, \tag{1}$$

where $M$ is the dipole moment, $\lambda$ is the geomagnetic latitude, $r$ is the radial distance from the center of the dipole with the unit of $r$ being Re (the Earth radii), $m$ is the mass, $c$ is the speed of light, $q$ is the charge of particles, and $v$ is the particle speed. In order to predict the energetic particles transporting to a specific location through the magnetosphere, the concept of geomagnetic rigidity is used. The geomagnetic rigidity is defined as $R = mvc/q$. As a parameter that quantitatively measures the shielding effect of the Earth's magnetic field on energetic particles, the geomagnetic cutoff rigidity describes the rigidities threshold of energetic charged particles when they pass through the geomagnetic shielding effect and reach the observation points (Smart and Shea, 2005). From **Eq. 1**, the cutoff rigidity at any point in space can be expressed as

$$R(\mathrm{GV}) = \frac{C}{r^2}\ \frac{\cos^4\lambda}{\left(1+\sqrt{1+\cos^3\lambda}\right)^2}, \tag{2}$$

where constant $C = 60$ is derived by the dipole model (Kress et al., 2010), and GV is the unit of the rigidity.

This equation can give the global cutoff rigidities simply and quickly, but because the dipole magnetic field cannot completely and accurately describe the real Earth's background magnetic field, especially in the period of intense magnetospheric activity, such as magnetic storm and substorm, the Earth's magnetic field will be compressed or stretched, resulting in the reduction of the effectiveness of the geomagnetic field described by the dipole magnetic field. With the continuous improvement of numerical simulation calculation, the global cutoff rigidities distribution image is given. At the same time, with the continuous progress of satellite observation technology and the continuous improvement of numerical simulation calculation, it is found that the cutoff rigidities of energetic particles corresponding to latitude should be calculated by more complex formulas (Dmitriev et al., 2010). Meanwhile, due to the long-term variation of the geomagnetic field, especially the geomagnetic change has accelerated significantly in recent years (Alken et al., 2020), the shielding effect of the geomagnetic field on energetic particles will change significantly, resulting in the change of the background energetic particle environment caused by the entry of solar/galactic cosmic rays into the magnetosphere. Therefore, it is necessary to remeasure the cutoff rigidities of energetic particles caused by the change of magnetic field. Although some researchers (Shea, 1971; Bhattacharyya and Mitra, 1997; Kudela and Bobik, 2004; Smart and Shea, 2009; Dorman et al., 2017; Cordaro et al., 2018, 2019) have studied the cutoff rigidities of energetic particles for the long-term variation of the geomagnetic field, their research either used the earlier geomagnetic field model until the year 2000 (Shea and Smart, 2001) or did not give the difference behavior for different hemispheres. Some authors calculated the cutoff rigidities only for one or several stations (Shea and Smart, 2001) or the limited area (Cordaro et al., 2018, 2019). Shea et al. (1987) studied the cosmic ray vertical cutoff rigidities as a function McIlwain L-parameter for different epochs of the geomagnetic field, while the McIlwain L-parameter cannot give the three-dimensional locations exactly. Dorman et al. (2017) studied this problem for the entire global world using the numerical simulation method, but they did not give a parameter relationship to evaluate the background change of high-energy particles.

All studies did not give the overall change of the cutoff latitude, nor the quantitative parameters were used to study its change trend, especially the change of the central point corresponding to the cutoff latitude, which has not even received any research and attention. Since not many articles on the change of the cutoff rigidities are available, we consider this article of utmost importance. This article will study this problem from different aspects, especially the inconsistency between the change of cutoff rigidities and the long-term change of the geomagnetic field. Using the newest IGRF model and more refined grid division (compared with the grid 5 × 15 in latitude and longitude (Bhattacharyya and Mitra, 1997)), this article will focus on the overall change at different times. At the same time, we will study its geometric center point and explore the correlation between them in combination with the change of the position of the magnetic poles.

The following parts of this article will discuss different contents, respectively. The second section will introduce the numerical simulation method. The third section shows the inconsistency of the change trend by analyzing the change of

geomagnetic field and cutoff rigidities. Finally, a brief summary and discussion are made.

## 2 SIMULATION METHOD

The equation of charged particle's motion in the magnetosphere can be written as

$$\frac{d\mathbf{p}}{dt} = q\mathbf{v} \times \mathbf{B}, \tag{3}$$

where **p** is the relativistic momentum of the particle, **v** is the velocity, $q$ is the charge, and **B** is the magnetic field. Here, the electric field is ignored. Following Smart et al. (2000), we calculate charged particle trajectories time backward. If a particle can reach the boundary of the magnetosphere before its total trajectory path length exceeds 1000 Re, the rigidity is considered an allowed rigidity (Kress et al., 2004). However, if the particle intersects the solid Earth or the particle is still moving in the magnetosphere after its total trajectory path length exceeds 1000 Re, the rigidity is considered a forbidden one.

The lowest rigidity above which all rigidities are allowed is denoted as the upper cutoff rigidity $R_{\max}$, and the highest rigidity below which all rigidities are forbidden is denoted as the lower cutoff rigidity $R_{\min}$. From a rigidity much higher than the possible $R_{\max}$ to a rigidity much lower than the possible $R_{\min}$, we scan the rigidity values at the discrete intervals $\delta R = 0.001$ GV. In this way, we obtain the values of $R_{\max}$ and $R_{\min}$, and the allowed and forbidden rigidities between $R_{\max}$ and $R_{\min}$ are denoted as $\delta R_{allowed}$ and $\delta R_{forbidden}$, respectively. Thus, the effective cutoff rigidity, $R_{eff}$, is calculated with the formula

$$R_{eff} = R_{max} - \sum_{R_{min}}^{R_{max}} \delta R_{allowed}. \tag{4}$$

In our numerical method, **Eq. 3** is integrated with the fourth order Runge–Kutta method. The step size in time is set to be equal to 0.01 of particles' gyro-period throughout the trajectory (Kress et al., 2004). We consider that the particles access the position from the vertical direction. So, the initial velocities $v_{x_i}$ ($x_i = x, y, z$) of the particles at the given position $x$, $y$, and $z$ are

$$v_{x_i} = v\frac{x_i}{\sqrt{x^2 + y^2 + z^2}}, \tag{5}$$

where $v$ is the initial velocity of particles, and the altitude of the position is set to be 450 km as the initial position, according to Smart and Shea (2003). In addition, the inner boundary is set to be $1.0R_e$ from the Earth center. The $x$, $y$, and $z$ coordinates are applicable when using the magnetospheric coordinates which are right-handed, orthogonal, and Earth-centered coordinate systems (Smart et al. (2000)). The coordinates we use here are the GEO (geographic coordinate system) and GSM (geocentric solar-magnetospheric).

It should be noted that during the numerical simulation with the main field of International Geomagnetic Reference Field (IGRF) as the background magnetic field, the inner and outer boundaries are set at a radial distance of an Earth radius. At the same time, because IGRF is the Earth's main field, the magnetopause-type given by Tsyganenko (Tsyganenko, 1995, 1996; Tsyganenko and Stern, 1996) is not suitable to describe the simple IGRF magnetopause. Therefore, in the simulation process, we only use the total time and total distance of particle motion and the maximum range of particle motion in three-dimensional, rather than using the magnetopause-type given by Tsyganenko as the outer boundary. At the same time, as the dependence of cutoff rigidities on latitude is significantly greater than that on longitude, but the longitude dependence of geomagnetic field change is obvious, in order to analyze the global spatial change characteristics with high precision, we use the latitude direction interval of 1 degree and longitude direction of 10 degrees to grid the world. The temporal and spatial evolution characteristics of global vertical cutoff rigidities are calculated. For the detailed numerical simulation process of calculating the cutoff rigidities, please refer to Chu and Qin (2016).

Considering the change of the long-term geomagnetic field, here, we only use the main field as the background field for numerical simulation. The main field model we used here is the International Geomagnetic Reference Field (IGRF) model (http://www.ngdc.noaa.gov/IAGA/vmod/igrf.html). The model is a standard mathematical description of the Earth's main magnetic field and its secular variation. The IGRF model is standardized for a particular year, reflecting the most accurate measurements available at that time and indicating a small-scale, slow time variation of the Earth's magnetic field. The model is usually updated every 5 years to make sure the results given by the model are the most accurate at present. In December 2019, the 13th generation of the International Geomagnetic Reference Field (IGRF) was released by the International Association of Geomagnetism and Aeronomy (IAGA) Division V Working Group (V-MOD). This model updates the previous generation with a definitive main field model for epoch 2015, a main field model for epoch 2020, and a predictive linear secular variation for 2020 to 2025 (Alken et al., 2020). Since the moving speed of the pole was accelerated in the 1960s, we set the time range for our study after 1965. Meanwhile, since the dipole point has crossed the primary meridian in recent years and the IGRF 13 model can deduce the magnetic field data in 2025, we will continue our research until 2025. To calculate the main sources contribution of the geomagnetic field and coordinate transformations, we use the source code package GEOPACK-2008 provided by Tsyganenko. All the aforementioned computer codes for magnetospheric field and coordinate transformation calculations are downloaded from the website http://geo.phys.spbu.ru/tsyganenko/modeling.html.

## 3 SIMULATION RESULTS AND DISCUSSION

Since the change of cutoff rigidities is mainly caused by the change of the Earth's magnetic field, the long-term variation characteristics of the IGRF magnetic field are given here first.

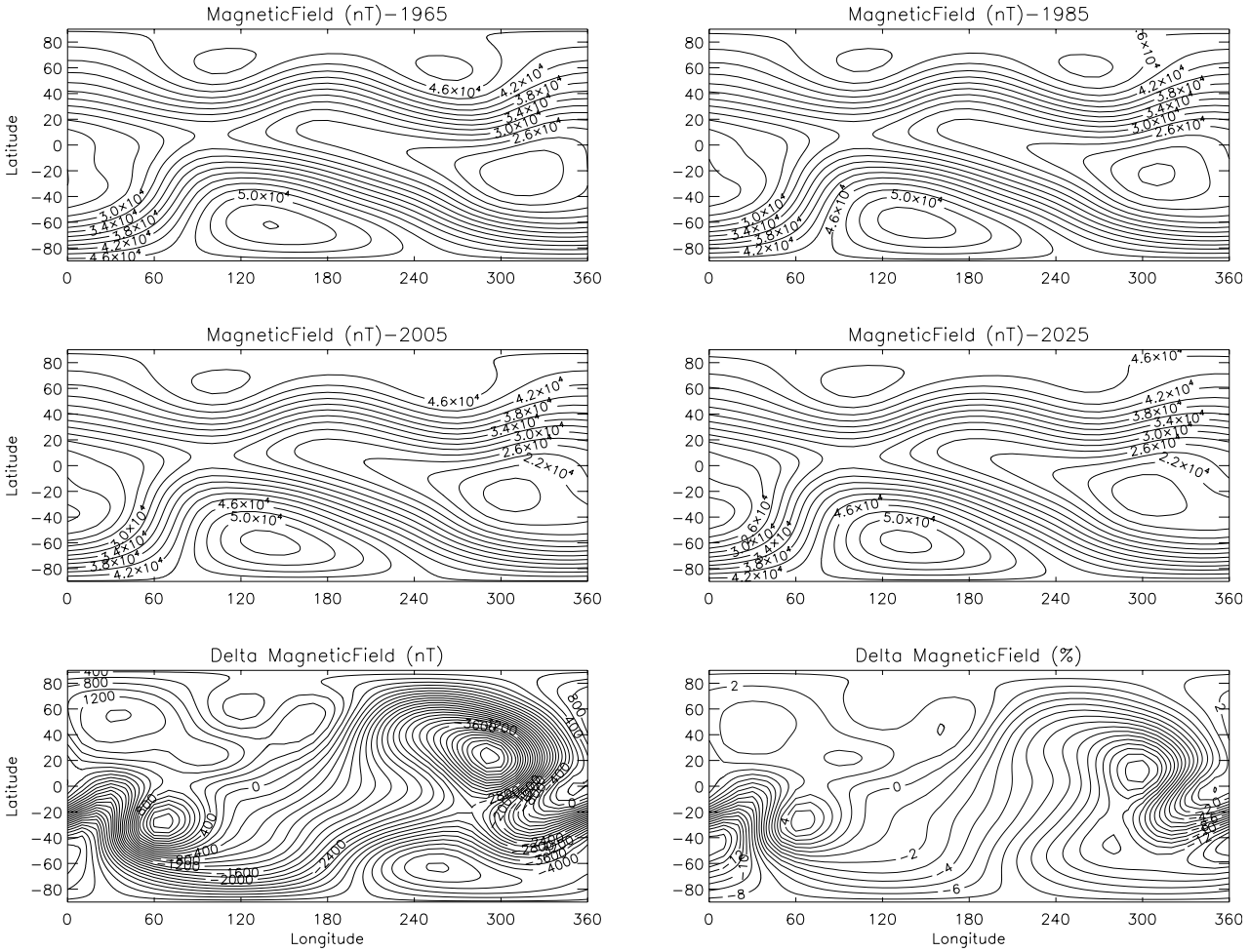


**FIGURE 1 |** Contour of the background magnetic field calculated by the IGRF 13 model from 1965 to 2025 by every 20 years and absolute and relative changes of the magnetic field contour image.

## 3.1 Long-Term Variation of Geomagnetic Field

Here, we will focus on only two aspects: the change of global magnetic field intensity and the movement of magnetic poles. The movement of magnetic poles includes the magnetic dip poles and geomagnetic poles in both northern and southern hemispheres. According to the article by Alken et al. (2020), the geomagnetic poles are calculated from the three dipole Gauss coefficients and correspond to where the magnetic dipole axis intersects a sphere of mean Earth radius 6371.2 km. The magnetic dip poles are defined as the locations where the main magnetic field as a whole is normal to the Earth's surface, represented by the WGS84 reference ellipsoid. They can be defined as the locations where the magnetic field component tangent to the ellipsoid vanishes.

For the convenience of picture expression, we will give the image of background magnetic field in limited years and give the change information. **Figure 1** shows the global contour map of the total field intensity at the altitude of 450 km at an interval of 20 years from 1965 to 2025. The map shows that Siberia and the Southern Ocean between Australia and Antarctic in the southern hemisphere own the largest field intensities. Also, South America, which is known as the South Atlantic Anomaly (SAA), is the region of significantly weaker field. Usually, in this region, because the radiation environment of energetic particles is much higher than that in other areas, many payloads will be shut down in this area to ensure the safety of satellite operation. Interestingly, Terra-Nova et al. (2019) found that a region which is close to SAA minimum longitude has a second minimum intensity. This region can be found at the Earth's surface, but it cannot be found at our simulation height (450 km). The global contour map of variation of the total field intensity is given in **Figure 1**. From the figure, we can find that the global magnetic field intensity has two obvious reduction regions from 1965 to till date. However, the global background magnetic field intensity does not always decrease, especially in the eastern hemisphere, and there is also an obvious enhancement, but the enhancement range is not so large compared with the weakening range.

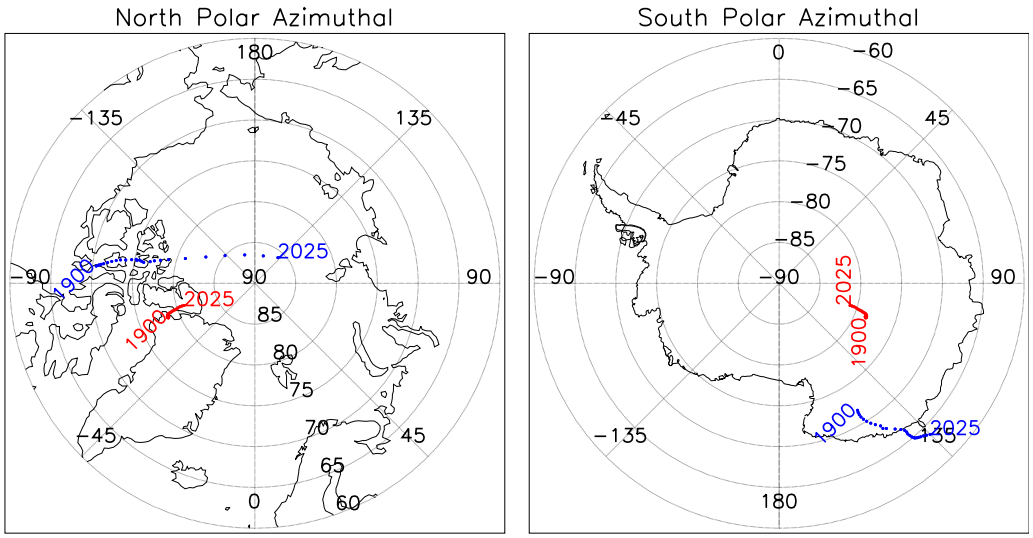


**FIGURE 2 |** Center location of the IGRF magnetic field for different years from 1900 to 2025 with the time resolution of 5 years. The blue dots are the magnetic dip pole centers, and the red ones are the geomagnetic pole centers. The data are from the article by Alken et al. (2020).

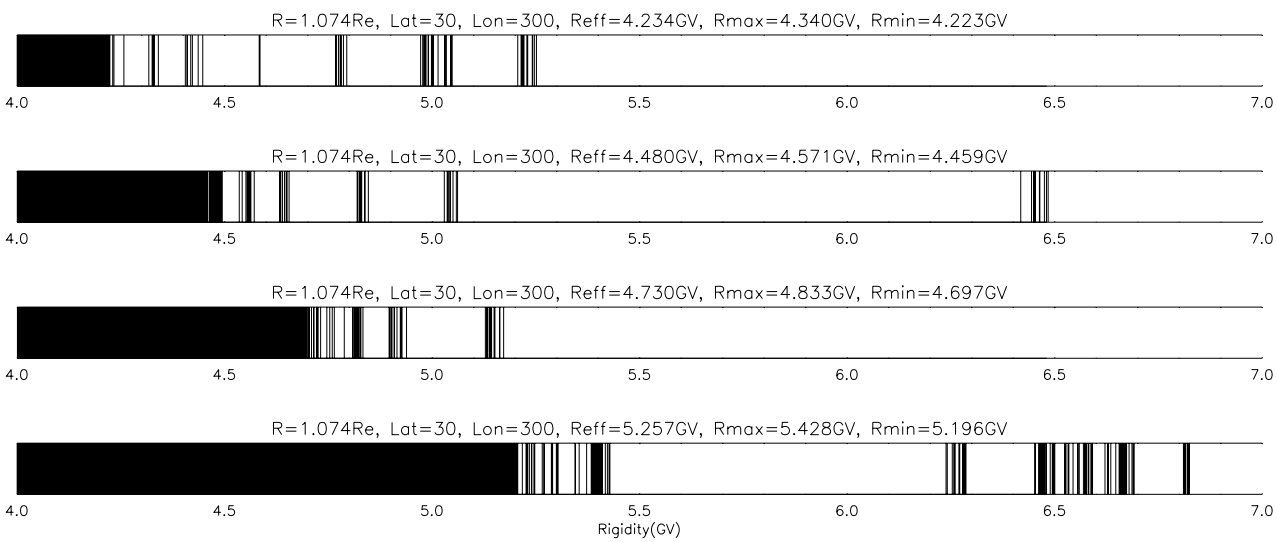


**FIGURE 3 |** Illustration of the geomagnetic cutoff rigidities penumbra. This figure shows the maximum, minimum, and effective cutoff rigidity at an interval of 1 MeV for the calculation of the rigidity at an altitude of 450 km, determined by trajectory calculations. In this illustration, black indicates forbidden rigidities, and white indicates allowed rigidities. Note that the cutoff is not sharp and that as the rigidity is decreased. The transmission of cosmic rays changes from fully allowed at rigidities above the maximum computed cutoff, $R_{max}$, to partly allowed in the cosmic ray penumbra, to totally forbidden at rigidities below the minimum computed cutoff, $R_{min}$. In addition, they are either allowed or forbidden to access with rigidities between $R_{max}$ and $R_{min}$, so it is named the penumbra area. The panel from top to bottom represents the changes of the penumbra of the cutoff rigidities at the same location in 1965, 1985, 2005, and 2025, respectively.

The position with the strongest relative decrease is in the magnetic equatorial regions of North and South America and the outer boundary of the SAA region, in which the outer boundary of the SAA region decreases most strongly, with a relative change of about 15%.

**Figure 2** is the pole positions of the IGRF magnetic field for different years from 1900 to 2025 with the time resolution of 5 years. The blue dots are the magnetic dip poles, and the red ones are the geomagnetic poles. The data are from the article by Alken et al. (2020). There are significant differences between the two due to the non-dipolar structure of the Earth's magnetic field. For more than a century, the change of the dip poles is more obvious than that of the geomagnetic poles. Usually, when the interplanetary and magnetospheric coupling mechanism is studied, the geomagnetic poles are used, as they can be used to specify the relative orientation of the Earth's magnetic field with respect to the Sun.

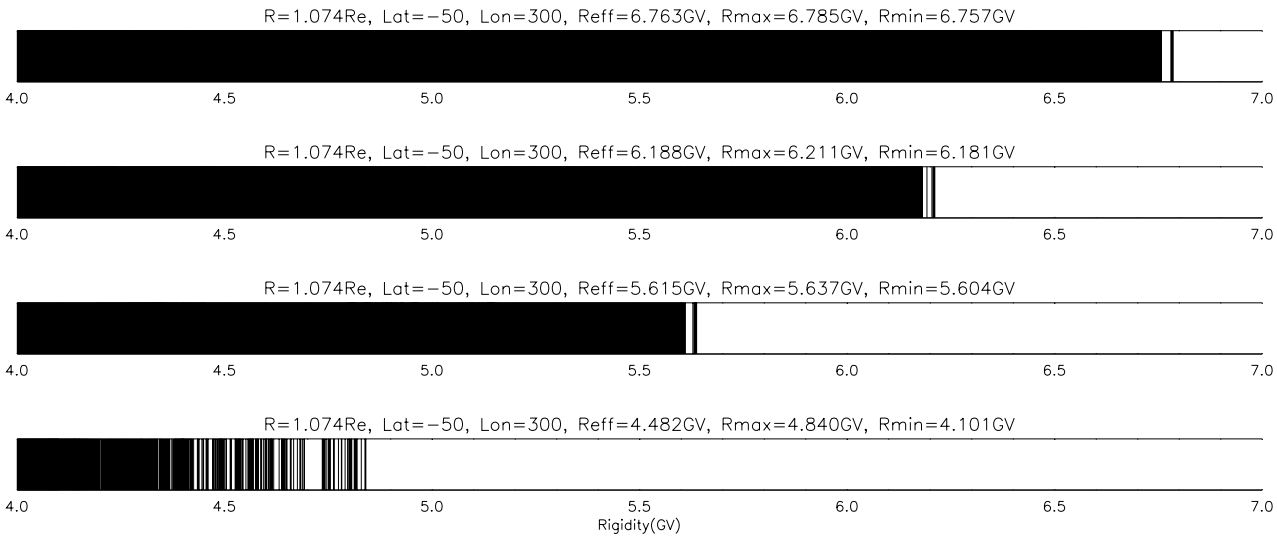


**FIGURE 4 |** Same as **Figure 3** but for different hemisphere.

## 3.2 Long-Term Variation of Cutoff Rigidities

The cutoff rigidities penumbra is an effective concept, which can reflect the motion of energetic particles at the observation position. The rigidity penumbra is shown in **Figures 3**, **4** for the north and south hemispheres for different years. These two figures show the maximum, minimum, and effective cutoff rigidity at intervals of 1 MeV for the calculation of the rigidity at an altitude of 450 km, determined by trajectory calculations. In this illustration, black indicates forbidden rigidities, and white indicates allowed rigidities. The transmission of energetic particles changes from fully allowed at rigidities above the maximum cutoff rigidity, $R_{max}$, to partly allowed in the cosmic ray penumbra, to totally forbidden at rigidities below the minimum cutoff rigidity, $R_{min}$. In addition, they are either allowed or forbidden to access with rigidities between $R_{max}$ and $R_{min}$, so it is named the penumbra area. The panels from top to bottom represent the changes of the penumbra of the cutoff rigidities at the same location in 1965, 1985, 2005, and 2025, respectively. Because the cutoff rigidities are not symmetrical about the magnetic equator or geographical equator and in order to compare the cutoff rigidities of the same order, we selected observation points with different longitude and latitude in the northern and southern hemispheres for comparative analysis. The geographical longitude and latitude of the observation point in the northern hemisphere are 30 and 300, while in the south hemisphere they are −50 and 300, respectively. By comparing different years, it can be found that from 1965 to 2025, the effective, maximum, and minimum cutoff rigidities of the same location in the northern hemisphere show an increasing trend. While, the trend in the southern hemisphere is the opposite, showing a decreasing trend. In the northern hemisphere, the effective cutoff rigidities changed from 4.234 GV in 1965 to 5.257 GV in 2025, which represents an increase of 24%. At the same time, the southern hemisphere changed from 6.763 to 4.482 GV, which represents a decrease of 34%.

Then, we expand the study scope to the global world. From **Figure 5**, which shows the variation of the global cutoff rigidities, it can be seen that there are mainly four regions of change in cutoff rigidities worldwide. Some regions of the northern hemisphere show that the cutoff rigidities decrease with the weakening of the magnetic field; however, there are also some regions where the cutoff rigidities increase while the magnetic field becomes weaker. **Figures 6**, **7** show the histogram of variation of background geomagnetic field and cutoff rigidities with the longitude and latitude between 1965 and 2025. The upper panel indicates that the relative change of the magnetic field changes with the longitude/latitude, and the lower panel indicates the relationship between the relative change of cutoff rigidities and longitude/latitude. The longitude and latitude distribution images corresponding to the changes of magnetic field and cutoff rigidities show that there is a deviation of about 60 degrees in longitude, and the dependence on the latitude is basically with expectations in the southern hemisphere. But, in the northern hemisphere, the relationship between the two is complex, which shows an anticorrelation relationship, which is puzzling. At the same time, although the second minimum intensity region of the magnetic field at the simulation altitude is not shown in the magnetic field distribution map, it can be found that the cutoff rigidities in this region have changed significantly (Longitude 0, about 30 south latitude). This finding is exciting because it shows that the magnetic field in the bottom region plays a decisive role in the motion of energetic particles. This also means that in the numerical simulation of energetic particles, especially in the process of single particles, it is necessary to reasonably and carefully set the inner boundary to prevent the deviation of particle motion caused by unreasonable boundary setting.

In order to illustrate the dependence of the change of cutoff rigidities caused by the change of the magnetic field, the

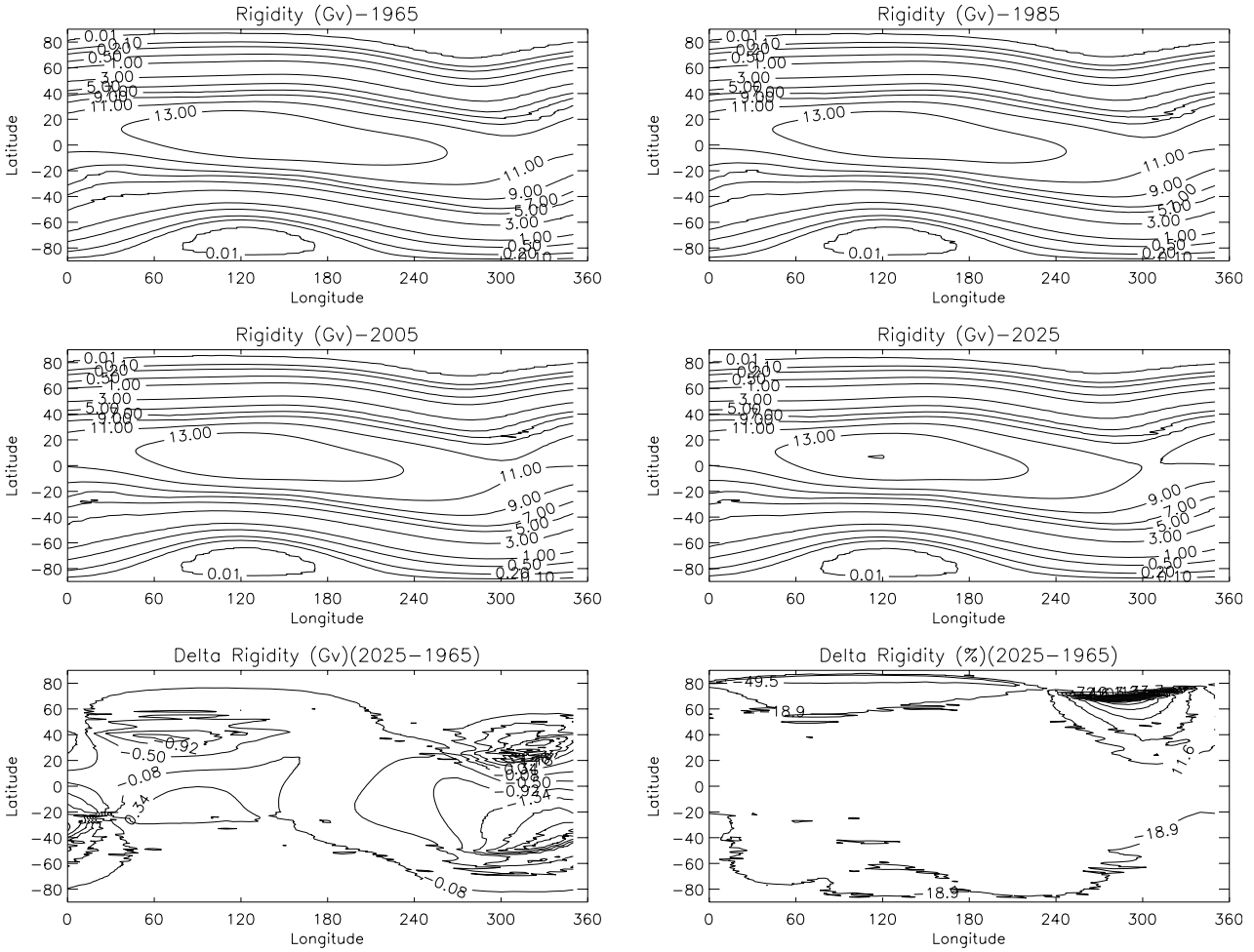


**FIGURE 5 |** Global contour of cutoff rigidities from 1965 to 2025 by every 20 years and their absolute and relative changes contour image.

relationship of the variation of the global rigidities and the global geomagnetic field is shown in **Figure 8**. It can be easily found that normally the decrease of the magnetic field cannot always lead to the decrease of the cutoff rigidities. For the global grids with the spatial resolution by 1 for latitude and 10 for longitude, nearly 40% of the changes of these two parameters are inconsistent. When the magnetic field becomes intense, 16.543 9% of the cutoff rigidities will become smaller, while 23.173 7% will become larger. Also, when the magnetic field becomes smaller, 11.694 3% of the cutoff rigidities will become smaller, while 48.572 7% will become larger.

**Figure 9** shows the cutoff latitude boundary with a cutoff rigidity of 200 MV in the northern and southern hemispheres (the cutoff latitude boundary is calculated by spline interpolation here). Different colors represent the simulation results of the background magnetic field in different years. The colors "black," "yellow," "red," "pink," "green," "sky blue," and "blue" represent 1965, 1975, 1985, 1995, 2005, 2015, and 2025, respectively. The left one is the boundary of the EPW in the northern hemisphere, and the right one is in the southern hemisphere. The cutoff latitude boundary image shown in the figure can be fitted with ellipses, and the eccentricity of ellipses in the northern and southern hemispheres is different. Obviously, the boundary curve in the southern hemisphere is similar to that of a circle, while in the northern hemisphere is more inclined to the shape of an ellipse, and the elliptical eccentricity in the northern hemisphere is greater than that in the southern hemisphere; this result is consistent with the result given by Dmitriev et al. (2010). The cutoff latitude boundary corresponding to the cutoff rigidities changes obviously with the magnetic field, especially in the northern hemisphere. However, this variable situation brings some difficulties to our study because it is difficult to determine how the global energetic particles radiation environment will change through the cutoff latitudes. Therefore, we introduced the concept of energetic particles' windows.

## 3.3 The Energetic Particles' Windows

As a concept corresponding to the cutoff rigidities, the cutoff latitude is expressed as the latitude boundary corresponding to the same cutoff rigidities. From the aforementioned global

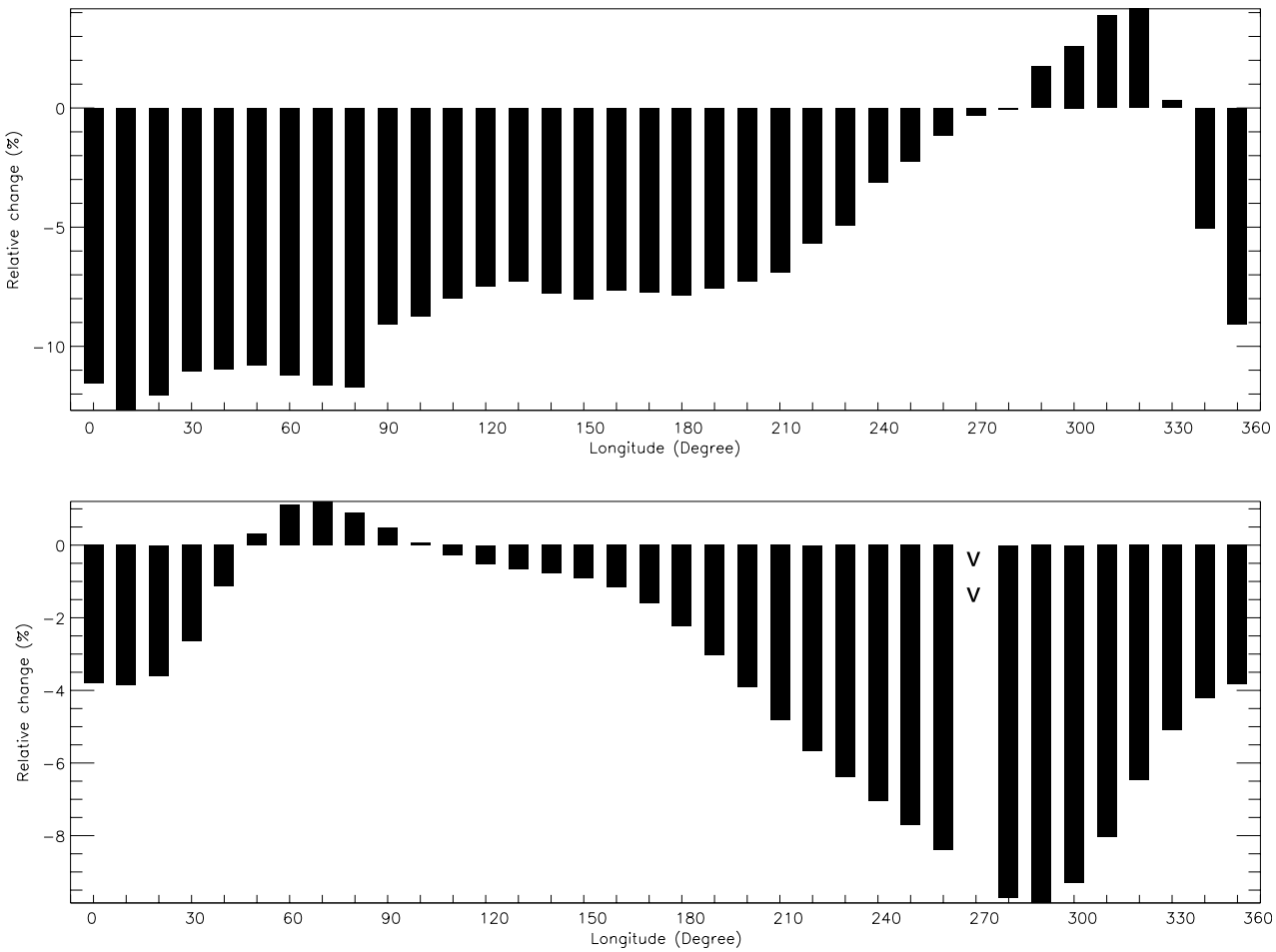


**FIGURE 6 |** Histogram of variation of background geomagnetic field and cutoff rigidities with the longitude between 1965 and 2025. The upper panel indicates that the relative change of the magnetic field changes with the longitude, and the lower panel indicates the relationship between the relative change of cutoff rigidities and longitude.

contour of cutoff rigidities, it can be found that when the cutoff rigidity is smaller than 11GV, the cutoff latitudes can form a closed curve. Different from the method of using the cutoff latitudes, we here define a region, energetic particles' windows (EPWs), where the vertical cutoff rigidities of energetic particles are less than or equal to a threshold value, $R_t$. A simple example is given in **Figure 10**; the shaded region indicates the EPWs with the threshold $R_t$ = 200 MV, and the big black dot indicates the center of the window. By calculating the area above the cutoff latitudes, the variation characteristics of the cutoff rigidities can be evaluated (Refer to Chu and Qin (2016) for detailed description).

## 3.4 Area Variation Characteristics Corresponding to Cutoff Latitudes

The areas and the centers of the EPWs can give us a better understanding of the coupling processing between the interplanetary and the magnetosphere. In this chapter, the area of the EPWs will be studied. **Figure 11** shows changes of the EPWs' area with time under different background magnetic fields for both the north and south hemispheres. The colors "black," "red," "orange," "pink," "green," "sky blue," "blue," "violet," "gray," and "purple" represent 0.1, 1, 2, 3, 4, 5, 6, 7, 8, and 9 GV, respectively. It is expected that when the intensity of the background magnetic field becomes weaker, the cutoff rigidities at the same location will become smaller, resulting in the shift of the cutoff latitude boundary to the equator. However, the change trends in the northern and southern hemispheres are obviously different. Next, we will give the time change rate of the area corresponding to EPWs. Although the change trend of EPWs' area in the northern and southern hemisphere is obviously different, when we select the standard, we take 1965 as the reference for both the northern and southern hemispheres. All of the information is given in **Figure 11**. Compared with the temporal change rate of EPWs' area in the northern and southern hemisphere, the temporal change rate in the southern hemisphere is greater than that in the northern hemisphere. **Figure 12** shows the area temporal

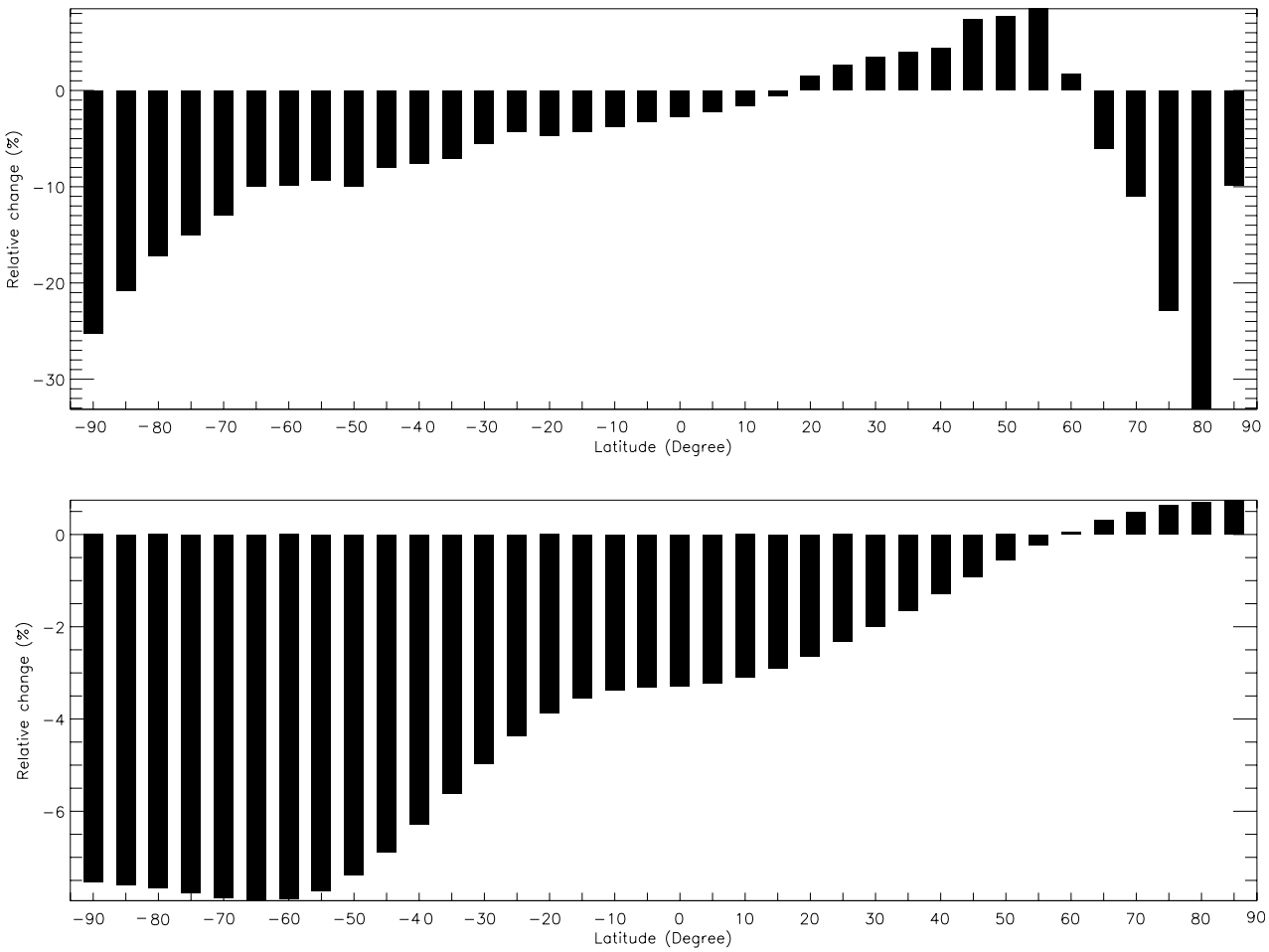


**FIGURE 7 |** Histogram of variation of background geomagnetic field and cutoff rigidities with the latitude between 1965 and 2025. The upper panel indicates that the relative change of magnetic field changes with the latitude, and the lower panel indicates the relationship between the relative change of cutoff rigidities and latitude.

change rate of EPWs corresponding to different rigidities obtained by polynomial fitting. The slope of the line obtained by first-order polynomial fitting in the northern hemisphere is less than 0, and the absolute value of the slope becomes smaller with the increase of the rigidities. The slope of the line varies between −0.03/yr and −0.004/yr. While in the southern hemisphere, they are large than 0, and the slope of the line becomes larger and larger when the rigidities increase. The maximal value is 0.12/yr, and the minimum is 0.056/yr. These parameters suggest that due to the change of the background magnetic field, the radiation flux of energetic particles in the southern hemisphere will increase by 5.6 to 12% in hundred years. In the northern hemisphere, the value will be around −3%. In combination with the change trend of the northern and southern hemispheres, from a global perspective, as shown in **Figure 13**, the radiation flux of energetic particles of different rigidities will increase by 1.1% to 5.6% in hundred years. Although its impact may be limited in the short term, when its time scale reaches a millennium or even longer, the radiation environment will change dramatically. Kudela and Bobik (2004) used the simulation method under the model geomagnetic field ($n = 2+$) and found that the maximum cutoff rigidity decreased from about 24 to 17 GV between 0 and 2000 years which means the time change rate is about 0.015%/yr. This value is obviously smaller than our simulation results which means that the variation maybe much more complex than what we expect. The linearity maybe impossible to claim with reliability accepted approach abnormal development of behavior of geomagnetic cutoff rigidity (Dorman et al., 2017); however, we can still use this method to evaluate the change of cutoff rigidities, as these values have the same order.

The pitch angle dependence of the cutoff rigidities that is carried out by our group (Chu et al., 2021) shows that the energetic particles corresponding to the cutoff rigidities tend to reach the observation points along the opposite direction of the magnetic field. This suggests that compared with the northern hemisphere, a large number of particles will tend to reach near-Earth space from the southern hemisphere. With the time goes, the flux of energetic particles in the southern hemisphere will be significantly higher than that in the northern hemisphere.

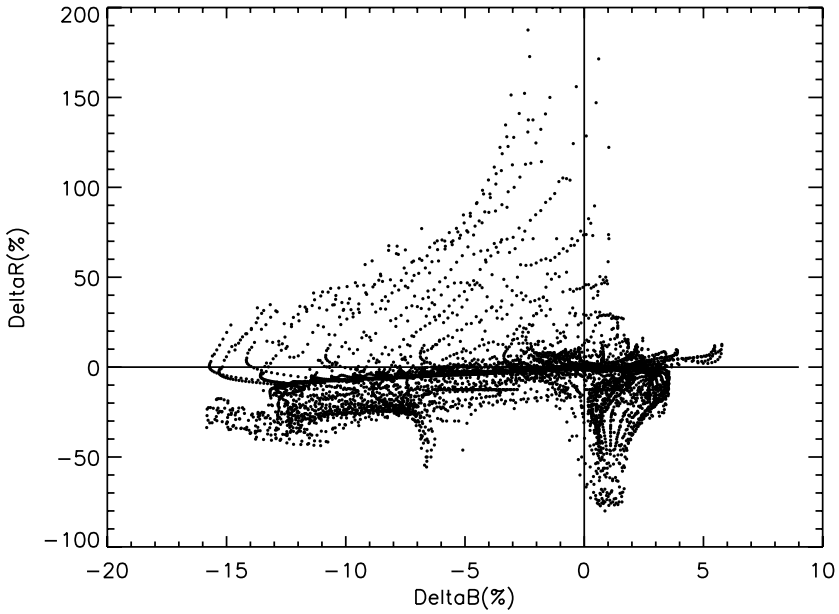


**FIGURE 8 |** Relationship of the variation of the global rigidities and the global geomagnetic field. For the global grids with the spatial resolution by 1 for latitude and 10 for longitude, nearly 40% of the changes of these two parameters are inconsistent. Also, when the magnetic field becomes intense, 16.5439% of the cutoff rigidities will become smaller, while 23.1737% will become larger. Also when the magnetic field becomes smaller, 11.6943% of the cutoff rigidities will become smaller, while 48.5727% will become larger.

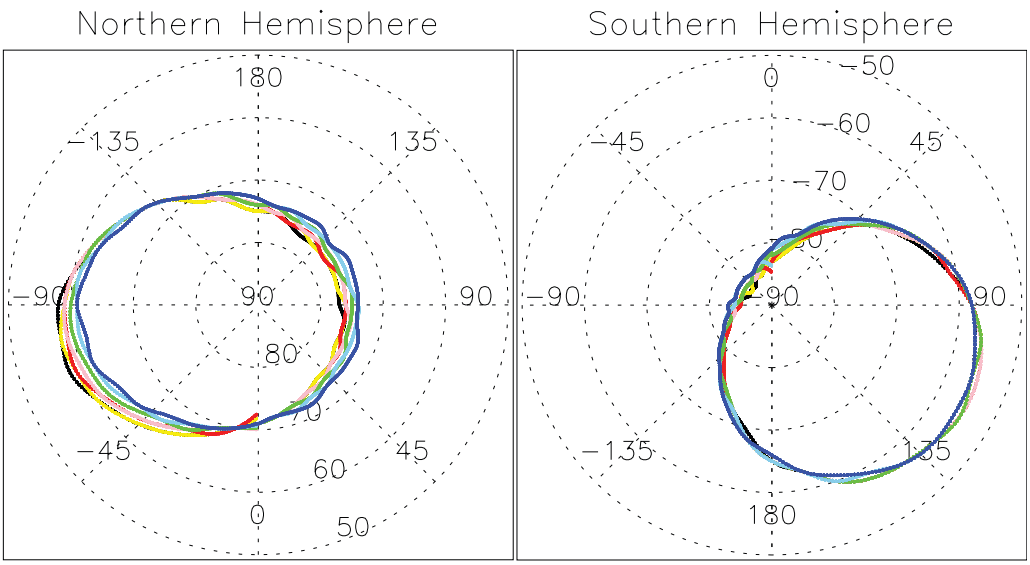


**FIGURE 9 |** Image of EPWs with 200 MV under different background magnetic fields for different years which are marked with different colors. The colors "black," "yellow," "red," "pink," "green," "sky blue," and "blue" represent 1965, 1975, 1985, 1995, 2005, 2015, and 2025, respectively. The left one is the boundary of the EPW in the northern hemisphere, and the right one is in the southern hemisphere.

## 3.5 Variation Characteristics of EPWs' Center Points

As one of the characteristics of geomagnetic field variation, by the end of 2019, the longitude of the magnetic dipolar pole in the north hemisphere has crossed the prime meridian (Alken et al., 2020) and also the geomagnetic poles are always in motion. Therefore, it will be very meaningful for us to study the corresponding relationship between the central point of the EPWs and the magnetic pole point. The center of the EPWs is the geometric center, and we do not perform any weighting

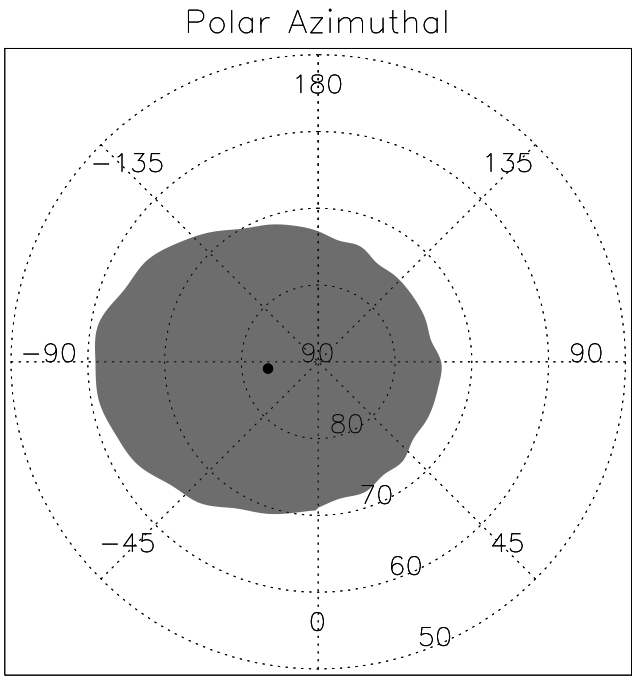


**FIGURE 10 |** Schematic diagram of EPWs defined in the article. Here, we use 200 *MV* as the cutoff rigidity, and the black dot represents the center of the EPW.

here. For the area surrounded by the above cutoff latitude, the longitude and latitude information of its geometric center can be calculated. As an important parameter, Dmitriev et al. (2010) used satellite observation results to fit the longitude and latitude coordinates of the center point of the cutoff latitude elliptic boundary. Here, we directly use the numerical simulation method to obtain the longitude and latitude information of the central points. Combined with the analysis of **Figures 2**, **14**, we can find that the central points of EPWs are closer to the magnetic pole point of geomagnetic rather than the magnetic pole point of the dipole magnetic field. This is easy to understand because IGRF gives the main geomagnetic field, not a simple dipole magnetic field. Although the dipole magnetic field plays a major role, the influence of other orders cannot be ignored. Combined with the paleomagnetic data, it can be obtained that the dipole moment of the geomagnetic field has decreased by nearly 1/4 in the past 1000 years. In sharp contrast to the decrease of the dipole moment, the non-dipole part of the geomagnetic field has increased rapidly. For 100 years, quadrupole and octupole are enhanced by 95% and 74%, respectively (Courtillot and Mouel, 1988; WEI and XU, 2001; Kudela and Bobik, 2004).

Meanwhile, compared with the position of the magnetic pole, the central points of EPWs are closer to the geographical north

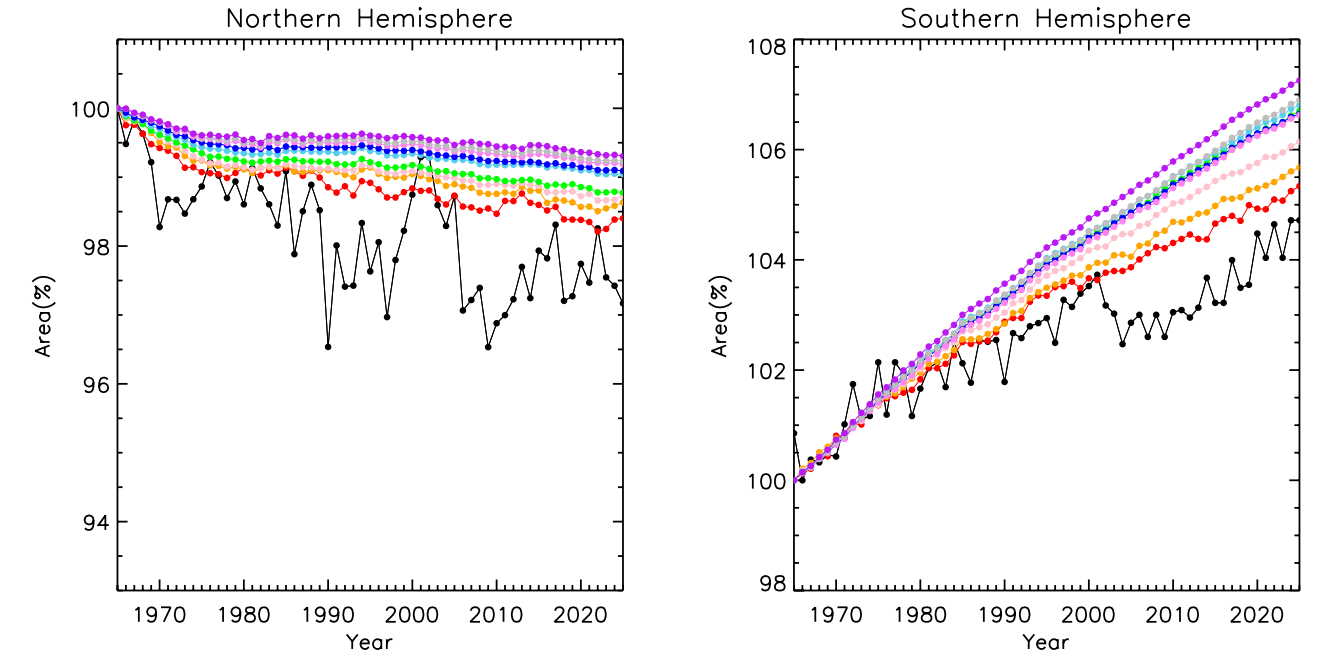


**FIGURE11 |** Changes of the EPWs' area with time under different background magnetic fields for both the north and south hemispheres. The colors "black," "red," "orange," "pink," "green," "sky blue," "blue," "violet," "gray," and "purple" represent 0.1, 1, 2, 3, 4, 5, 6, 7, 8, and 9 GV, respectively.

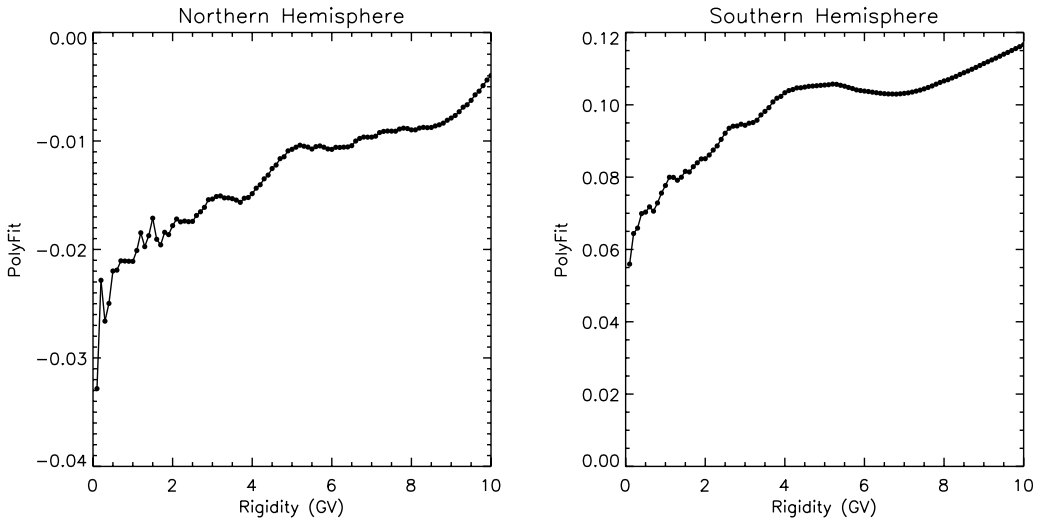


**FIGURE 12 |** Area time change rate of EPWs corresponding to different rigidities obtained by polynomial fitting.

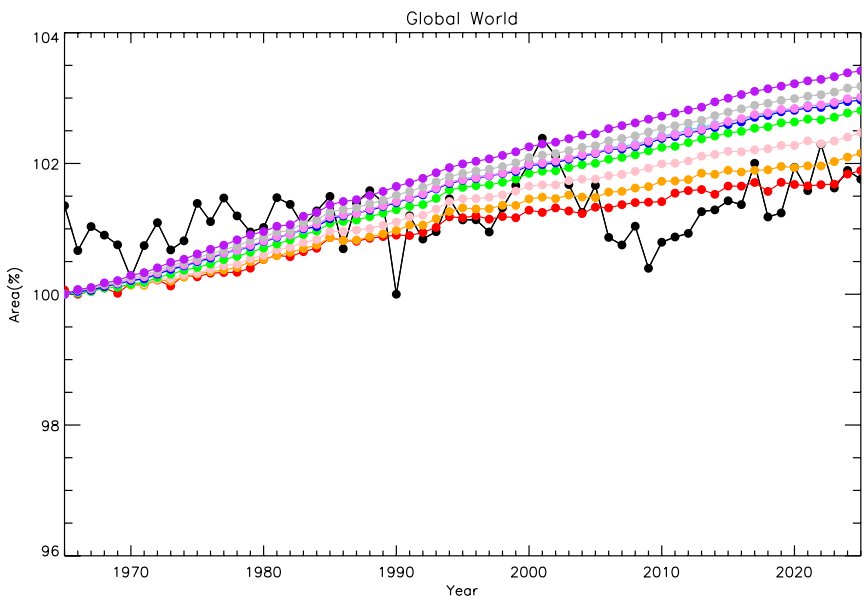


**FIGURE 13 |** Same as **Figure 11** but for the global world.

pole in the northern hemisphere, but in the southern hemisphere, the situation is just the opposite, and the central points of EPWs are closer to the low latitudes.

The central points of EPWs are usually close to the morning and dusk side, not on the day side or night side. This phenomenon may be due to the fact that the cusp region in the northern and southern hemispheres is usually on the dawn and dusk side, not on the day or night side. The cusp region is still the central region from where energetic particles enter the near-Earth space. Another interesting phenomenon is the relationship between the particle's rigidity and the longitude and latitude of the EPWs' center. **Figure 15** shows the center location of the EPW for different rigidities. It can be found that in the south hemisphere, the longitude of the center points changes obviously with the particle's rigidity; however, the situation in the northern hemisphere is somewhat different, and its change is not so strong. This may be because the Earth's magnetic field is not very effective in restraining or shielding the very high energy particles, especially when the energetic particles enter near-Earth space from the southern hemisphere. As this problem does not belong to the main content of this article, it will not be discussed in detail here and will be studied in the future works.

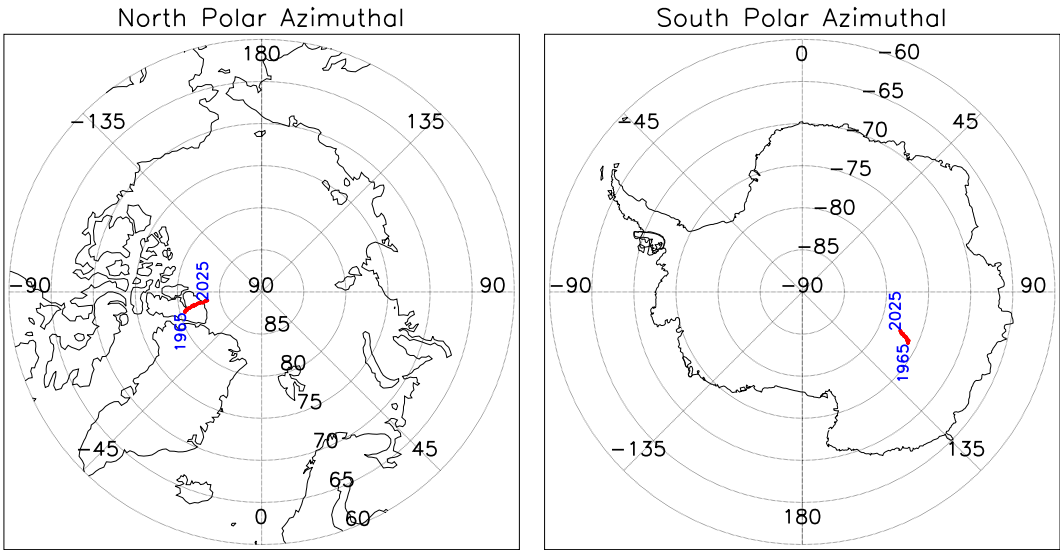


**FIGURE 14 |** Central location of the EPW for the rigidity of 1 GV for different years from 1965 to 2025 with the time resolution of 1 year.

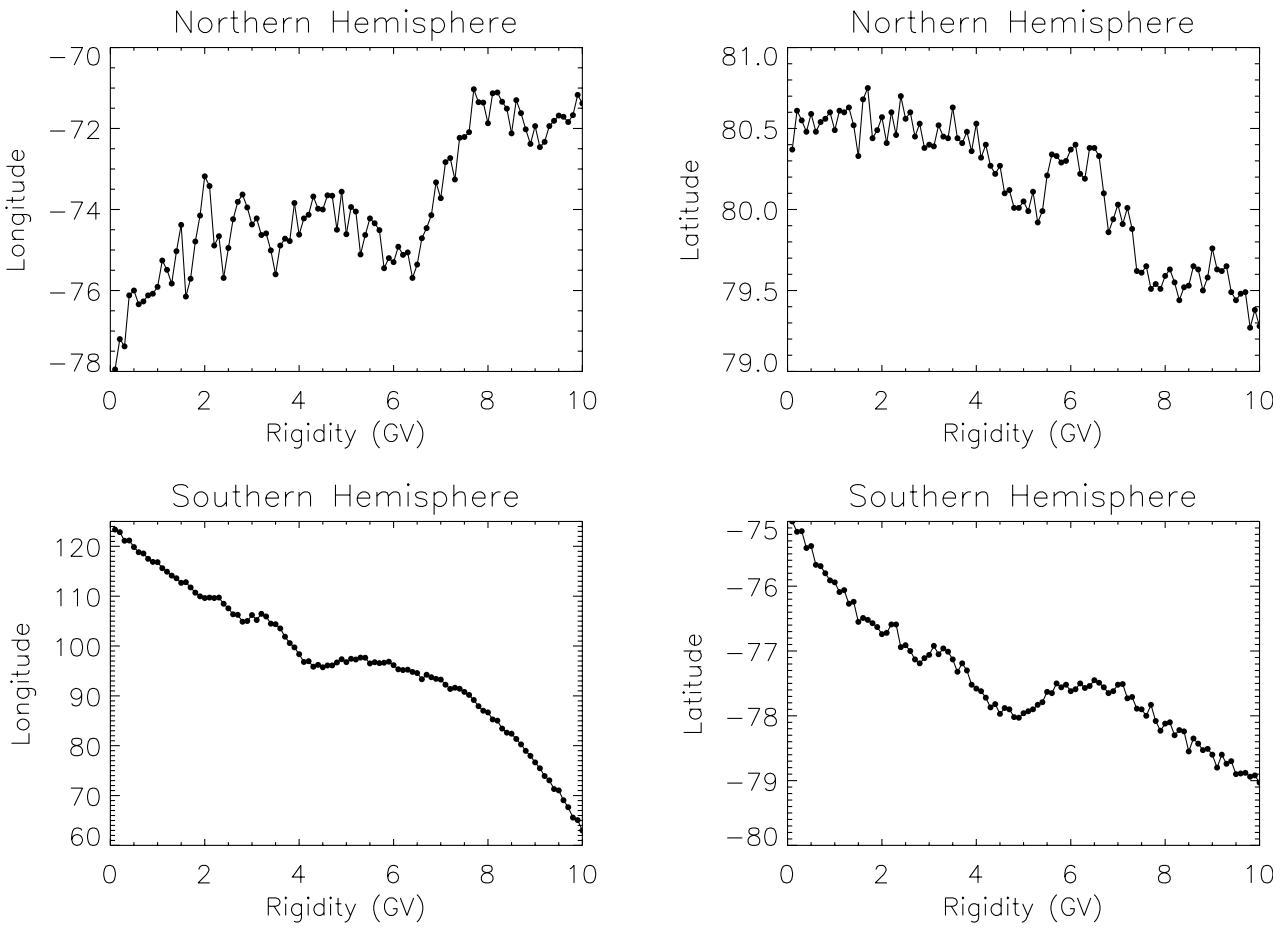


**FIGURE 15 |** Central location of the EPW for different rigidities.

## 4 CONCLUSION

A good description of energetic particle precipitation requires a good view that covers the temporal and spatial variation of the cutoff rigidities. The main purpose of this article was to present the variation of the cutoff rigidities caused by the background magnetic field for a long term. This investigation considers the fact that the geomagnetic field is not static but constantly changing in time and space. In this article, the vertical geomagnetic cutoff rigidities were calculated numerically by solving the trajectories of energetic particles in the geomagnetic field (IGRF-13 model) from 1965 to 2025 every year. Our numerical simulations show that there is a close relationship between the cutoff latitude corresponding to the cutoff rigidities and the background magnetic field intensity, but they are not in a simple relationship. The changes of the cutoff rigidities and geomagnetic field in the northern and southern hemispheres are asymmetric. For the grids of $1 \times 10$ in latitude and longitude, nearly 40% of the changes between the magnetic field intensity and the cutoff rigidities are inconsistent, which means when the magnetic field intensity becomes smaller/larger, 40% of the corresponding cutoff rigidities will become larger/smaller. From 1965 to 2025, the maximum cutoff rigidity decreased from 6.9 to 3.9 *GV* which occurred in the southern hemisphere of (330, −45), and the maximum cutoff rigidity increased from 7.2 to 10.0 *GV* in the northern hemisphere of (320, 21). On the other hand, by defining the energetic particles windows (EPWs), the areas and the centers of the EPWs were studied. The time change rate of the EPWs' areas is between −0.03/yr and −0.004/yr in the northern hemisphere, while in the southern hemisphere, it is 0.12/yr and the minimum is 0.056/yr, compared to the time change rate of about 0.015%/yr from 0 to 2000 years suggested by the article by Kudela and Bobik (2004). The long-term trajectory of the geomagnetic north poles does not correspond to the positions of the central point of EPWs. The weakening of the geomagnetic field will push the cutoff latitude toward the near equatorial region in the south hemisphere, but for the north hemisphere, the phenomenon is not always credible.

The energetic particles outside the magnetosphere tend to enter the near-Earth space in the direction antiparallel to the magnetic field other than in the direction along the magnetic field lines which combined the result that with the weakening of the magnetic field, in the southern hemisphere, the area of the EPWs will become larger and larger, and the radiation caused by the solar and cosmic energetic particles will be more intense. We have a reason to believe that the central position of the aurora may change with the movement of the central point of the energetic particles' windows (EPWs.)

In the future work, the non-vertical cutoff rigidities caused by the geomagnetic fields will be studied, to find out whether the dependence of the cutoff rigidities at different angles on the background magnetic field is the same, also to combine the *in situ* spacecraft observations such as NOAA and China Seismo-Electromagnetic Satellite (CSES), and to make out the differences between the simulation and observations.

Moreover, the knowledge acquired from cutoff rigidities in the near-Earth space and the sources of energetic particles' precipitation from the interplanetary should provide new insights for both the terrestrial and interplanetary researchers. Collaborations between scientists involved in these different fields are crucial for a better understanding of coupling between interplanetary and near-Earth space. It is hoped that our study can provide some useful suggestions of coupling mode and coupling efficiency, etc.

## DATA AVAILABILITY STATEMENT

The raw data supporting the conclusion of this article will be made available by the authors, without undue reservation.

## AUTHOR CONTRIBUTIONS

WC and YY put forward relevant ideas. WC performed the numerical simulation and carried out most of the analysis and wrote the manuscript. GQ provided part simulation codes, and others helped to review the manuscript and gave modification suggestions.

## FUNDING

Our work was partly supported by the National Key R and D Program of China (Grant No. 2018YFC1503502-05) and the APSCO Earthquake Research Project Phase II and ISSI-BJ (2019IT-33).

## ACKNOWLEDGMENTS

We acknowledge IAGA for the source code of the IGRF model (http://www.ngdc.noaa.gov/IAGA/vmod/igrf.html) and Dr. Nikolai Tsyganenko for the source code of the GEOPACK-2008 (http://geo.phys.spbu.ru/tsyganenko/Geopack-2008.html). We thank the useful discussion with Dr. Yang Wang from School of Science, Harbin Institute of Technology, Shenzhen. Additionally, the authors also wish to thank the reviewers for their constructive comments that helped to improve the scholarly quality of the article.

## REFERENCES

Alken, P., Thébault, E., Beggan, C. D., Amit, H., and Zhou, B. (2020). International Geomagnetic Reference Field: the Thirteenth Generation. *Earth Planets and Space* 73.

Baker, D. N. (2000). The Occurrence of Operational Anomalies in Spacecraft and Their Relationship to Space Weather. *IEEE Trans. Plasma Sci.* 28, 2007–2016. doi:10.1109/27.902228

Bhattacharyya, A., and Mitra, B. (1997). Changes in Cosmic ray Cut-Off Rigidities Due to Secular Variations of the Geomagnetic Field. *Ann. Geophys.* 15, 734–739. doi:10.1007/s00585-997-0734-6

Chu, W., Qin, G., ang Song Xu, J. H., Zeren, Z., and Shen, X. (2021). A Study on Non-vertical Geomagnetic Cutoff Rigidity of Magnetosphere Energetic Particles during Geomagnetic Quiet Period. *Chin. J. Geophys.* 64, 410–418.

Chu, W., and Qin, G. (2016). The Geomagnetic Cutoff Rigidities at High Latitudes for Different Solar Wind and Geomagnetic Conditions. *Ann. Geophys.* 34, 45–53. doi:10.5194/angeo-34-45-2016

Cordaro, E. G., Venegas, P., and Laroze, D. (2018). Latitudinal Variation Rate of Geomagnetic Cutoff Rigidity in the Active Chilean Convergent Margin. *Ann. Geophys.* 36, 275–285. doi:10.5194/angeo-36-275-2018

Cordaro, E. G., Venegas-Aravena, P., and Laroze, D. (2019). Variations of Geomagnetic Cutoff Rigidity in the Southern Hemisphere Close to 70°W (South-Atlantic Anomaly and Antarctic Zones) in the Period 1975-2010. *Adv. Space Res.* 63, 2290–2299. doi:10.1016/j.asr.2018.12.019

Courtillot, V., and Le Mouel, J. L. (1988). Time Variations of the Earth's Magnetic Field: From Daily to Secular. *Annu. Rev. Earth Planet. Sci.* 16, 389–476. doi:10.1146/annurev.ea.16.050188.002133

Dmitriev, A. V., Jayachandran, P. T., and Tsai, L.-C. (2010). Elliptical Model of Cutoff Boundaries for the Solar Energetic Particles Measured by Poes Satellites in December 2006. *J. Geophys. Res.* 115, a–n. doi:10.1029/2010JA015380

Dorman, L., Gvozdevsky, B., Belov, A., Gushchina, R., and Yanke, V. (2017). "The Secular Variations of Cosmic ray Cutoff Rigidities, Caused by century Variations in Geomagnetic Field, and Cosmic ray Variations," in *35th International Cosmic Ray Conference*. doi:10.22323/1.301.0067

Galand, M. (2001). Introduction to Special Section: Proton Precipitation into the Atmosphere. *J. Geophys. Res.* 106, 1–6. doi:10.1029/2000ja002015

Kirkby, J. (2007). Cosmic Rays and Climate. *Surv. Geophys.* 28, 333–375. doi:10.1007/s10712-008-9030-6

Koons, H., Mazur, J., Selesnick, R., Blake, J., Fennell, J., Roeder, J., et al. (1998). The Impact of the Space Environment on Space Systems. *paper presented 6th Spacecraft Charging Tech.* 1, 7–11.

Kress, B. T., Hudson, M., Perry, K., and Slocum, P. (2004). Dynamic Modeling of Geomagnetic Cutoff for the 23-24 November 2001 Solar Energetic Particle Event. *Geophys. Res. Lett.* 31. doi:10.1029/2003GL018599

Kress, B. T., Mertens, C. J., and Wiltberger, M. (2010). Solar Energetic Particle Cutoff Variations during the 29-31 October 2003 Geomagnetic Storm. *Space Weather* 8, a–n. doi:10.1029/2009SW000488

Kudela, K., and Bobik, P. (2004). Long-term Variations of Geomagnetic Rigidity Cutoffs. *Sol. Phys.* 224, 423–431. doi:10.1007/s11207-005-6498-9

Mavromichalaki, H., Souvatzoglou, G., Sarlanis, C., Mariatos, G., Plainaki, C., Gerontidou, M., et al. (2006). Space Weather Prediction by Cosmic Rays. *Adv. Space Res.* 37, 1141–1147. doi:10.1016/j.asr.2005.03.159

Nesse Tyssøy, H., Stadsnes, J., Søraas, F., and Sørbø, M. (2013). Variations in Cutoff Latitude during the January 2012 Solar Proton Event and Implication for the Distribution of Particle Energy Deposition. *Geophys. Res. Lett.* 40, 4149–4153.

Shea, M. A. (1971). "Changes in Neutron Monitor Response and Vertical Cutoff Rigidities Resulting from Secular Variations in the Geomagnetic Field," in 12th International Cosmic Ray Conference (ICRC12) (Hobart: University of Tasmania), Vol. 3, 859–864.

Shea, M. A., Smart, D. F., and Gentile, L. C. (1987). Estimating Cosmic ray Vertical Cutoff Rigidities as a Function of the McIlwain -parameter for Different Epochs of the Geomagnetic Field. *Phys. Earth Planet. Interiors* 48, 200–205. doi:10.1016/0031-9201(87)90145-2

Shea, M., and Smart, D. (2001). Vertical Cutoff Rigidities for Cosmic ray Stations since 1955. *Int. Cosmic Ray Conf. (Hamburg, Germany)* 10, 4063.

Smart, D. F., and Shea, M. A. (2005). A Review of Geomagnetic Cutoff Rigidities for Earth-Orbiting Spacecraft. *Adv. Space Res.* 36, 2012–2020. doi:10.1016/j.asr.2004.09.015

Smart, D. F., and Shea, M. A. (2009). Fifty Years of Progress in Geomagnetic Cutoff Rigidity Determinations. *Adv. Space Res.* 44, 1107–1123. doi:10.1016/j.asr.2009.07.005

Smart, D. F., Shea, M. A., and Flückiger, E. O. (2000). Magnetospheric Models and Trajectory Computations. *Space Sci. Rev.* 93, 305–333. doi:10.1007/978-94-017-1187-6_15

Smart, D. F., and Shea, M. A. (2003). The Space-Developed Dynamic Vertical Cutoff Rigidity Model and its Applicability to Aircraft Radiation Dose. *Adv. Space Res.* 32, 103–108. doi:10.1016/s0273-1177(03)90376-0

Störmer, C. (1955). *The Polar aurora*. Walton St. Oxford OX2 6DP United Kingdom: Clarendon Press. doi:10.1002/qj.49708235123

Terra-Nova, F., Amit, H., and Choblet, G. (2019). Preferred Locations of Weak Surface Field in Numerical Dynamos with Heterogeneous Core-Mantle Boundary Heat Flux: Consequences for the South Atlantic Anomaly. *Geophys. J. Int.* 217, 1179–1199. doi:10.1093/gji/ggy519

Tsyganenko, N. A. (1996). Effects of the Solar Wind Conditions in the Global Magnetospheric Configurations as Deduced from Data-Based Field Models. In International Conference on Substorms (France; Versailles) 389, 181.

Tsyganenko, N. A. (1995). Modeling the Earth's Magnetospheric Magnetic Field Confined within a Realistic Magnetopause. *J. Geophys. Res.* 100, 5599–5612. doi:10.1029/94ja03193

Tsyganenko, N. A., and Stern, D. P. (1996). Modeling the Global Magnetic Field of the Large-Scale Birkeland Current Systems. *J. Geophys. Res.* 101, 27187–27198. doi:10.1029/96ja02735

Wei, Z.-G., and Xu, W.-Y. (2001). Drifts and Intensity Variations of the Geomagnetic Field. *Chin. J. Geophys.* 44, 496–505. doi:10.1002/cjg2.167

**Conflict of Interest:** The authors declare that the research was conducted in the absence of any commercial or financial relationships that could be construed as a potential conflict of interest.

frontiers | Frontiers in Earth Science

ORIGINAL RESEARCH
published: 04 May 2022
doi: 10.3389/feart.2022.860234

# Correlation Between *Ne* and *Te* Around 14:00 LT in the Topside Ionosphere Observed by CSES, Swarm and CHAMP Satellites

*Rui Yan*[1,2]*, *Chao Xiong*[3,4]*, *Zeren Zhima*[1], *Xuhui Shen*[1], *Dapeng Liu*[1], *Chao Liu*[5], *Yibing Guan*[5], *Keying Zhu*[1], *Lin Zheng*[2] *and Fangxian Lv*[1]

[1]National Institute of Natural Hazards, Ministry of Emergency Management of China, Beijing, China, [2]Institute of Disaster Prevention, Langfang, China, [3]Department of Space Physics, Electronic Information School, Wuhan University, Wuhan, China, [4]Hubei Luojia Laboratory, Wuhan, China, [5]National Space Science Center, Chinese Academy of Science, Beijing, China

In this study, we have performed a detailed analysis for the correlation between electron density (*Ne*) and temperature (*Te*) at the topside ionosphere. *In situ* measurements from four satellites have been utilized, including the China Seismo-Electromagnetic Satellite (CSES), Swarm A and B, as well as the earlier Challenging Minisatellite Payload (CHAMP) satellite. To make a fair comparison, only simultaneous observations between CSES and Swarm A/B have been considered; while for CHAMP, as it doesn't have overlaps with CSES period, the observations during similar low solar activity years are considered. Our study has been confined to the dayside around 14:00 local time (LT), due to the fixed LT coverage of CSES. Observations from the four satellites show generally consistent relationship between the *Ne* and *Te* at the topside ionosphere. When *Ne* is low, the *Te* is negative correlated with *Ne*, while the slop of negative relation becomes shallower or even reverses to a positive relation after *Ne* exceeds a certain threshold. The slope of *Ne/Te* relation shows also dependence on season and magnetic latitude (MLat), as the ionospheric *Ne* and *Te* themselves are seasonal and MLat dependent. Interestingly, we find two abnormal features of the Swarm *Te* measurements: 1) when *Ne* is lower than $1\times10^{11}$ $m^{-3}$, *Te* sometimes becomes very scatter at low and middle latitudes; 2) when *Ne* is larger than $1\times10^{11}$ $m^{-3}$, *Te* is grouped into two branches at the equatorial and low latitudes. Further analysis reveals that the flags used in the Swarm Level-1 B plasma density product cannot well distinguish the two abnormal features of *Te*, implying further efforts are needed for the Swarm *Te* data calibration.

**Keywords: China seismo-electromagnetic satellite (CSES), electron density (Ne), electron temperature (Te), correlation of Ne and Te, abnormal features**

OPEN ACCESS

***Edited by:***
*Stelios M. Potirakis,*
*University of West Attica, Greece*

***Reviewed by:***
*Ivan Kutiev,*
*Bulgarian Academy of Sciences (BAS), Bulgaria*
*Sergey Alexander Pulinets,*
*Space Research Institute (RAS), Russia*

***Correspondence:**
*Rui Yan*
*ruiyan@ninhm.ac.cn*
*Chao Xiong*
*xiongchao@whu.edu.cn*

***Specialty section:***
*This article was submitted to Environmental Informatics and Remote Sensing, a section of the journal Frontiers in Earth Science*

***Received:*** *22 January 2022*
***Accepted:*** *04 April 2022*
***Published:*** *04 May 2022*

***Citation:***
*Yan R, Xiong C, Zhima Z, Shen X, Liu D, Liu C, Guan Y, Zhu K, Zheng L and Lv F (2022) Correlation Between Ne and Te Around 14:00 LT in the Topside Ionosphere Observed by CSES, Swarm and CHAMP Satellites. Front. Earth Sci. 10:860234. doi: 10.3389/feart.2022.860234*

## INTRODUCTION

The topside ionosphere is a highly dynamic region that varies significantly with latitude, longitude, altitude, local time, season, and solar cycle. These variations have been explored for decades using electron density (*Ne*) and temperature (*Te*) observed by different ground-based and satellite instruments (Hargreaves, 1992; Schunk and Nagy, 1978). Due to high thermal conductivity along the magnetic field lines, significant energy can be transferred by electrons from the

sources to the sinks (Rother et al., 2010). Therefore, investigation on the variation of ionospheric *Te* as well as its relation with *Ne* can greatly advance our understanding of the ionosphere-thermosphere dynamics and interaction (e.g., Bilitza, 1975).

It has been widely reported by earlier studies (Brace and Theis, 1978; Bailey et al., 2000; Schunk and Nagy, 1978) that at topside ionosphere the *Ne* is generally anti-correlated with *Te* during daytime. Above 200 km, the dominant electron cooling process is Coulomb collision between the electrons and the ambient ions and the cooling rate is proportional to $Ne^2$, while the heating rate by photoelectrons is proportional to Ne (Schunk and Nagy, 1978; Kakinami et al., 2011a; Su et al., 2015).

With the increment of data and research, positive correlation between the *Te* and *Ne* has also been identified (Zhang and Holt, 2004; Ren et al., 2008; Kakinami et al., 2011a; Zhang et al., 2014). By using over 30-years data from the incoherent scatter radar at Millstone Hill and Arecibo, Lei et al. (2007) found that the correlation between daytime *Te* and *Ne* at the F2 peak height sometimes can be positive, especially under high solar activity years. They explained that the *Ne* is usually sufficiently high under high solar activity condition, which leads to a rapid energy transfer from the electrons to the ions and from the ions to the neutrals. These processes result in small temperature differences between electrons, ions, and neutrals. Therefore, electron, ion, and neutral temperatures increase with higher solar flux because the neutral temperature increase as the solar flux increases, leading to a positive correlation between *Ne* and *Te* as *Ne* increases also with higher solar flux. However, such an explanation can't be applied to the findings of Kakinami et al. (2011a), as they found that positive correlation between *Ne* and *Te* occurs when *Ne* is larger than a threshold ($10^{12}$ $m^{-3}$) but regardless of solar flux. They suggested that additional heat should be involved for the positive correlation between *Ne* and *Te*, e.g., possible sources contributing to the integrated *Ne* along the magnetic field lines.

Similar positive relation between daytime *Ne* and *Te* has latter been confirmed from the Detection of Electro-Magnetic Emissions Transmitted from Earthquake Regions (DEMETER) observations, but such a feature was not seen from the nighttime data (Kakinami et al., 2013). Zhang et al. (2014) performed a comprehensive study focused on the relationship between *Ne* and *Te* detected by DEMETER from 2005 to 2010. They found that during daytime the *Ne* and *Te* showed strong negative correlation at equator and low latitudes, but during the solar minimum year (e.g., in March 2009) their correlation changed to be positive at 25°–30° magnetic latitudes. Su et al. (2015) investigated the relationship between *Ne* and *Te* from the perspective of seasonal and latitudinal dependences, and the negative correlation between daytime *Ne* and *Te* was found in most seasons except at high latitudes in the northern winter, where a positive correlation occurred. They further explained that the F region electron density is quite low at high latitude during northern winter, therefore, the collision between the electrons and the ions is low and thus leads to a weaker coupling between *Te* and *Ne*.

In addition, the relationship of *Ne* and *Te* in some specified areas, or under special conditions has also been investigated. For example, at the Weddle Sea Anomaly (WSA) region, Liu et al. (2015) found that the *Ne* is anti-correlated with the *Te* in both day and night times, by using concurrent measurements at 660–830 km altitude observed by Tatiana-2, DEMETER and Formosa Satellite 3/Constellation Observing System for Meteorology, Ionosphere and Climate (COSMIC). Shen et al. (2015) investigated the correlation of *Ne* and *Te* before and after large earthquakes, using DEMETER observations in nighttime. They found that over the seismic regions, the negative correlation between *Ne* and *Te* is increased at middle and low latitudes comparing with their normal background. Using 8 years of Challenging Minisatellite Payload (CHAMP) satellite observations, Stolle et al. (2011) found a significant negative correlation between *Ne* and *Te* during morning overshoot in equinoxes and June solstice ($R < -0.9$), while the correlation is much weaker during December solstice. The negative correlation between *Ne* and *Te* during morning overshoot hours has been further confirmed by the Swarm observations (Yang et al., 2020).

*The relationship between Ne and Te has been discussed and included in the International Reference Ionosphere (IRI)* model (Bilitza, 1975; Bilitza, 1985; Bilitza et al., 1993). Based on 4 years data from the radar at Millstone Hill, Bilitza (1975) constructed an empirical relation between *Ne* and *Te*. They further used the measurements from the radar at Arecibo to derive altitude-dependent correlation parameters (Bilitza, 1985; Bilizta et al., 1993). Considering the complex relation between *Ne* and *Te*, it was recommended in the IRI model to establish independent models for the *Ne* and *Te*, and then use the relation between the two parameters for adjusting relevant processes (Bilizta et al., 1993).

As discussed above, though many studies have been conducted on the relationship between *Ne* and *Te* at the topside ionosphere, there is no conclusion for explaining the positive correlation between them. A possible reason is that the variation of *F* region *Te* depends on several parameters, e.g., *Ne*, ion density (*Ni*), neutral density, neutral temperature and also neutral composition etc., while the solar activity, season, latitude, longitude and altitude affect the distributions of all these parameters. In addition, most of the above-mentioned studies used *Ne/Te* data from only one satellite, therefore, their results might be applied to a certain condition, for example, a relative fixed altitude range or local time, depending on the satellite orbits and mission period. To learn more about their physical mechanisms, it is necessary to perform further comprehensive investigation on the correlation of *Ne* and *Te* by including several satellites. Such a study is also helpful for inter-satellite measurements comparison, which is especially important for the recently-launched satellite, such as CSES.

In this study we performed a detailed analysis of *Ne* and *Te* probed by four different satellites, CSES, Swarm A and B, and CHAMP. Comparison between them will not only help us to reveal the controlling parameter of *Ne/Te* correlation, but can also be regarded as an inter-satellite validation for reflecting the data quality, especially for measurements from the most recently launched CSES. To simplify the comparison, for all three satellites we focus only on the dayside data around 14:00 LT. In *Satellite Missions and Data Source Selection* part, we provide

the descriptions of the satellites as well as their onboard Langmuir probe. Seasonal and latitudinal dependences of *Ne/Te* correlation are presented and compared in *Result* part. Discussions are provided in *Discussion* part. The final summary is drawn.

# SATELLITE MISSIONS AND DATA SOURCE SELECTION

## Plasma Data From CSES, Swarm and CHAMP Missions

CSES is the first satellite of Chinese space-based geophysical field observation system, which is aimed for the application prospects in earthquake and near-space science. It was launched into an altitude of about 507 km, with a nearly Sun-synchronous orbit of 98° inclination, and the ascending/descending node is at about 02:00/14:00 LT (*Shen* et al., 2018). The Langmuir probe (LAP) provides *in situ Ne* covering a range from $5\times10^2$–$1\times10^7$ $cm^{-3}$, and *Te* from 500 k to 10,000 K. Previous studies have confirmed the reliability of CSES measured *Ne* and *Te*, that show generally consistent global distributions with earlier satellites, e.g., DEMTER and Swarm (e.g., Liu et al., 2018; Yan et al., 2020; Yan et al., 2022).

The Swarm mission, consisting of three identical satellites (A, B, C), was launched on 22 November 2013 into nearly polar, circular orbits, in altitude of approximately 490 km. In the final constellation, the Swarm A and C are flying side-by-side (longitudinal separation of 1.4°) at about 460 km, while the Swarm B is flying by about 50 km higher (Lühr et al., 2015; Xiong et al., 2016a). One key instrument of Swarm satellites is the Electric Field Instrument (EFI) (Knudsen et al., 2017), consisting of a pair of Thermal Ion Imagers (TIIs), and a pair of LPs. The LPs provide the *Ne* and *Te* with a time resolution of 2 Hz. Quite good agreements have been found between Swarm measured *Ne/Te* and other techniques/model predictions, suggesting a good reliability of the Swarm plasma dataset (Lomidze et al., 2018; Palin et al., 2015; Pedatella et al., 2015). As the Swarm C is at the same altitude of Swarm A and their *Ne* measurements are very consistent with each other (Xiong et al., 2016b), the results from Swarm C are not shown in this study. In addition, only the data with good quality are selected, with the flags are satellite potential (*Vs.*), *Ne* and *Te* being set to 20, and flag of LPs being set to 1.

The CHAMP satellite was launched on 15 July 2000 into a nearly-polar (inclination = 87.3°), circular orbit with an initial altitude of about 450 km (Reigber et al., 2002). When the mission ended with the reentry into the atmosphere on 19 September 2010, its altitude decayed to about 150 km. The onboard Planar Langmuir Probe (PLP) provided the *in situ Ne* and *Te* measurements for every 15 s. In-flight calibration of the PLP instrument has been performed and CHAMP has been confirmed to provide reliable plasma data. The details of the calibration and the retrieval of electron density and temperature from the PLP observations are given by McNamara et al. (2007).

## Dataset Considered Between the Three Missions

**Figure 1A** shows the variation of altitude, local time from CSES and Swarm A/B satellites in 2019 and 2020. As there is no overlap between the CSES and CHAMP missions, we considered only the CHAMP data in 2008 and 2009 with low solar activity (**Figure 1B**), which is similar to the solar activity during CSES operation period. The solar flux in 2008–2009 and 2019–2020 are depicted in the first subpanel in **Figures 1A, B**. In order to reduce the influence of magnetic storm all data are selected under magnetically quiet conditions with $Kp < 3$.

For a fair comparison, we selected the simultaneous measurements from the CSES and Swarm satellites when they are close in both time and space. Three conjunction periods around 14:00 LT (marked with light-grey rectangles in the lower two panels of **Figure 1A**) are found between the two satellites, which are: Apr. 5–19, 2019, Aug. 22–31, 2019 and Jan. 10–23, 2020 for Swarm B and CSES, while Sep. 25- Oct. 10, 2019, May. 15- Jun. 4, 2019 and Feb. 5–22, 2020 for Swarm A and CSES, reflecting the periods at equinoxes, June solstice and December solstice (**Figure 1A**).

Considering CHAMP data gaps around 14:00 LT, data for the same season and local time in 2008 and 2009 were analyzed together so that sufficient data can be used for our comparison. To focus on 14:00 LT, the CHAMP data during Oct.5–21, 2008 are used for representing the situations of equinoxes; May. 28 - Jun. 18, 2008 and Jul. 1–11, 2009, as well as Feb. 25–28 & Nov. 11–14, 2009 are corresponding to June solstice and December solstice, respectively. These five conjunction periods between CSES and CHAMP have also been marked with light-grey rectangles (see **Figure 1B**) The CHAMP altitude in 2008 and 2009 is around 330 km (Stolle et al., 2011).

To sum up, we researched the correlation of *Ne* and *Te* at around LT 14:00 using satellites with different altitude (~330km, ~480 and ~500 km separately). And at around 500 km, we can get the data at closest time and distance from two satellites (CSES and Swarm B) for mutual authentication.

# RESULTS

## Distribution of *Ne/Te* Along Magnetic Latitude (MLat)

**Figure 2** presents the *Ne/Te* MLat profiles of CSES, Swarm B, Swarm A and CHAMP from top to bottom. Data have been separated into equinoxes, June solstice, and December solstice, as shown in three columns from left to right. For each satellite, the *Ne/Te* profiles during conjunction period are presented as black lines, and the red lines represent the average profile of each season. A common feature between all four satellites is the *Ne* peaks at the magnetic equator, corresponding to the well-known equatorial ionization anomaly (EIA), while the *Te* shows a clear valley above the magnetic equator, suggesting a negative relation between the *Ne* and *Te*.

Slight differences are also seen between the four satellites. For example, the double crests of EIA are more prominent from the *Ne* profiles of Swarm A and CHAMP, as they fly at a relative lower altitude; while for Swarm B and CSES, which fly at a similar altitude, the double crests are more evidenced from Swarm B. Such difference of *Ne* between CSES and Swarm B has been earlier reported by Yan et al. (2020), which might be caused by the lower

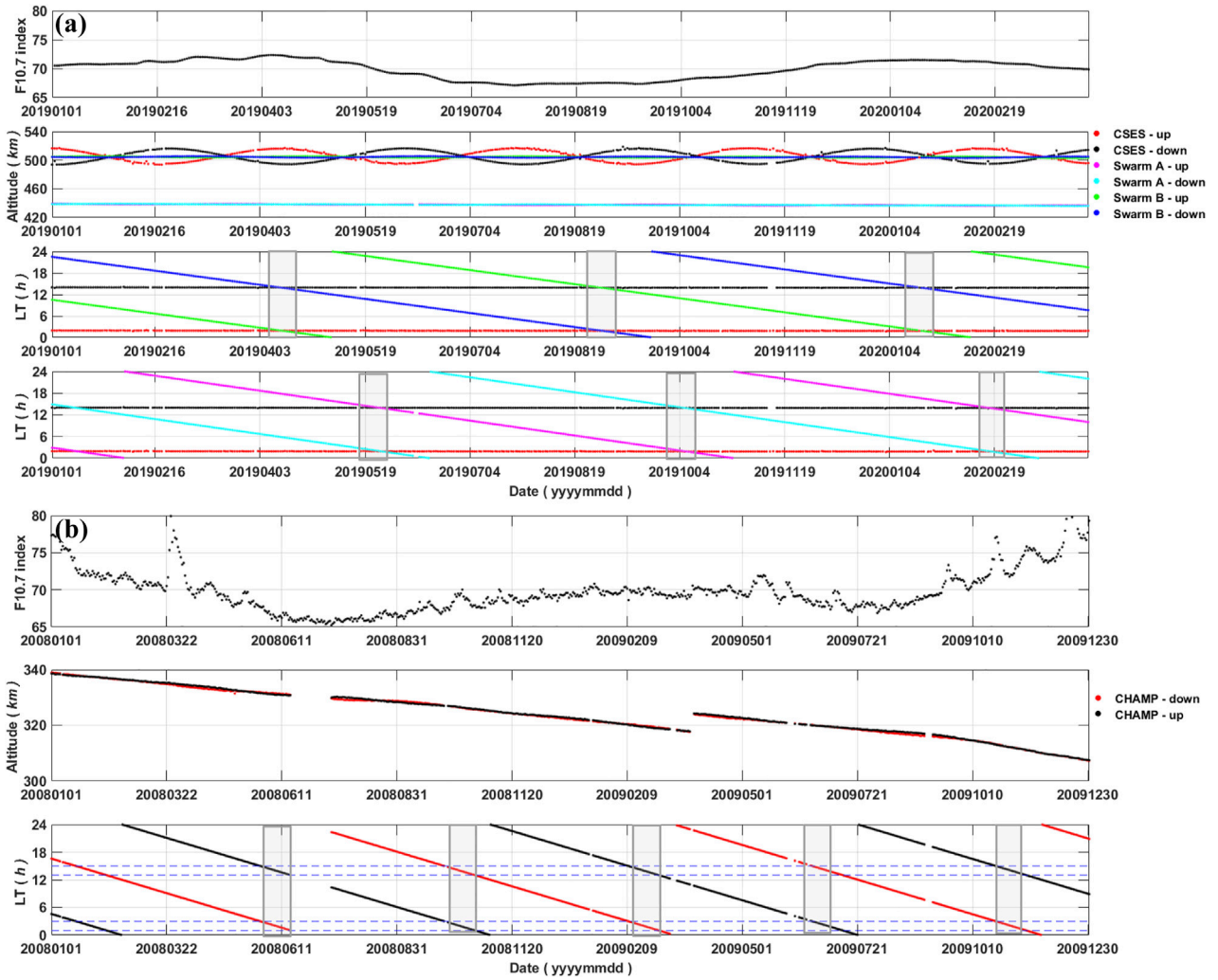


**FIGURE 1 |** The temporal variation of altitude, local time from four satellites and their corresponding solar flux. **(a)** for CSES, Swarm B, and Swarm A; **(b)** For CHAMP.

absolute *Ne* values measured by CSES and different data inversion method. The EIA crests show similar seasonal variations from Swarm B, Swarm A and CHAMP, with the same magnitude in the two hemispheres during equinoxes but with stronger crest in the local summer hemisphere during two solstices. Such a seasonal variation of the inter-hemispheric asymmetry of EIA crests is caused by the trans-equatorial plasma flue along magnetic fluxtube, which has been well discussed by Xiong et al. (2013). Another interesting feature seen in **Figure 2** is that the *Te* profiles from Swarm A and B seem to form two branches at the equatorial and low latitudes regardless of seasons, while such a feature cannot be seen from the CSES and CHAMP *Te* profiles.

**Figure 3** repeats the average profiles of *Ne/Te* from the four satellites by comparing variations along MLat between CSES with another satellite. To better show the comparison, the average profiles of CSES are repeated as black lines in each subpanels, while the profiles from the other three satellites are shown as blue lines. They are shown in dual coordinate axis so that we better compare their trend along MLat although the different absolute values of *Ne/Te*. Similar to **Figure 2**, the subpanels from left to right depict the results in three different seasons. Very similar variations of *Ne/Te* are seen between CSES and the other three satellites, except the single or double crests of EIA that being attributed to satellite probing altitude. In addition, a feature seen from CHAMP is that the *Te* exhibits two minima at latitudes corresponding well to the EIA crests.

## The General Correlation of *Ne* and *Te* Within ±50° MLat

**Figure 4** show the scatter distribution of *Ne* and *Te* around 14:00 LT from the four satellites (from top to bottom, CSES, Swarm B, Swarm A and CHAMP). The subpanels from left to right depict the results in equinoxes, June solstice, and December solstice. We have limited our analysis to the low and middle latitudes (±50° MLat) to avoid the much more complicate *Ne/Te* relation at

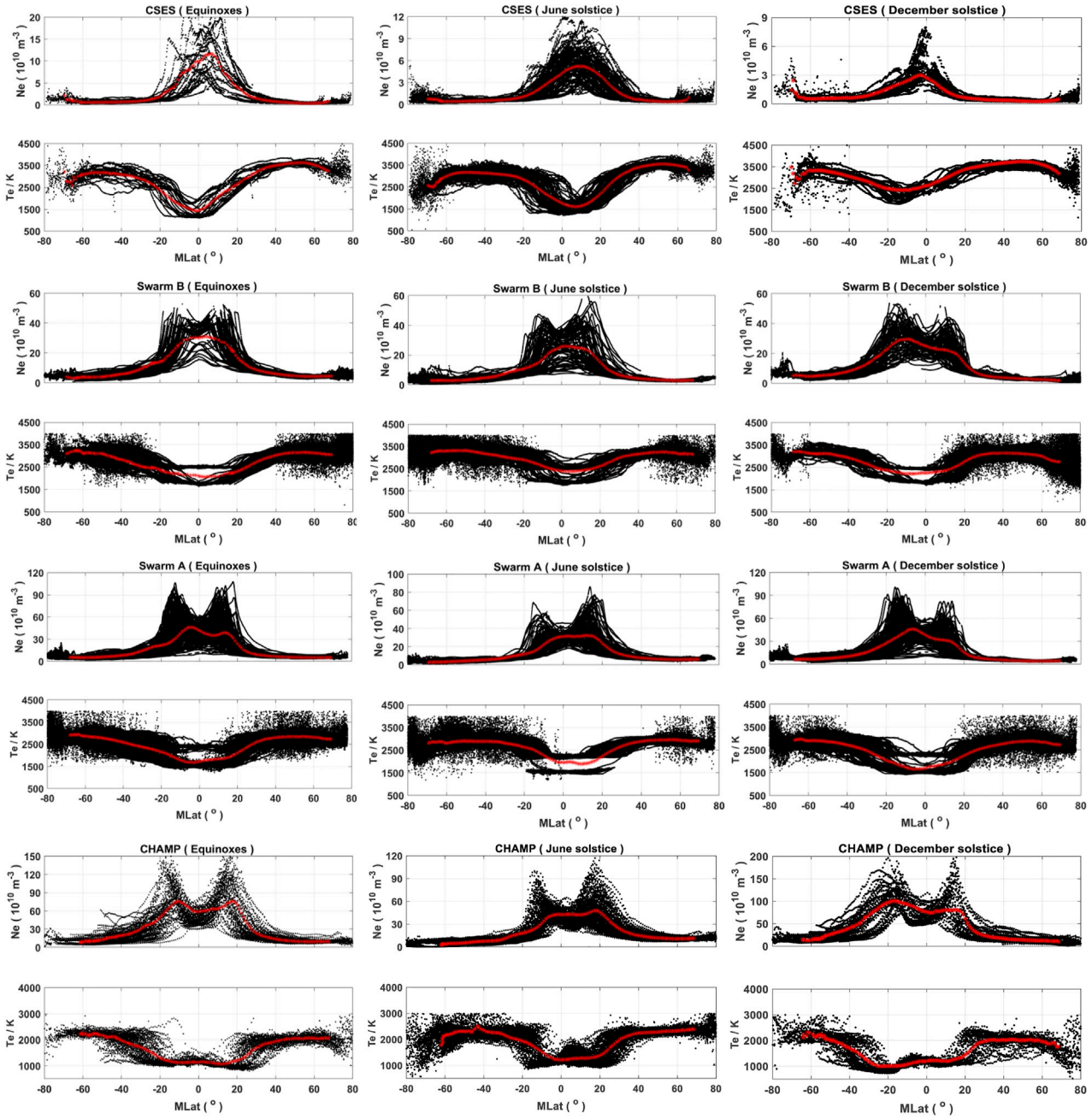


**FIGURE 2 |** The MLat distributions of *Ne/Te* profiles of CSES, Swarm B, Swarm A and CHAMP (from top to bottom). The equinoxes, June solstice, and December solstice are shown in columns from left to right. The red lines represent the average profile of each season.

auroral latitudes. The colors from blue to red represent the measurements at different MLat range. A general negative relation is found between the *Ne* and *Te* at 14:00 LT from all four satellites. However, the slope of the negative relation reduces and even becomes positive when the *Ne* becomes larger.

A feature for the two Swarm satellites is that the relation between *Ne* and *Te* is quite scatter when the *Ne* is low (less than $1\times10^{11}$ m$^{-3}$). For *Ne* at a fixed level, the *Te* can vary from 2000 K to over 4000 K. Similar wild variation of *Te* is also seen from the CSES observation, with less data points which are confined to equinoxes and June solstice seasons. However, such wild variation of *Te* can't be seen from the CHAMP observations. In addition, when the *Ne* is larger than $1\times10^{11}$ m$^{-3}$, the relation between *Ne* and *Te* forms two branches for Swarm A and B irrespective of seasons, which should be caused by the two groups of Swarm *Te* profiles at the equatorial and low latitudes as shown in **Figure 2**.

For CHAMP, we see similar *Ne/Te* relation as that observed by CSES. Slight difference is that instead of the positive relation

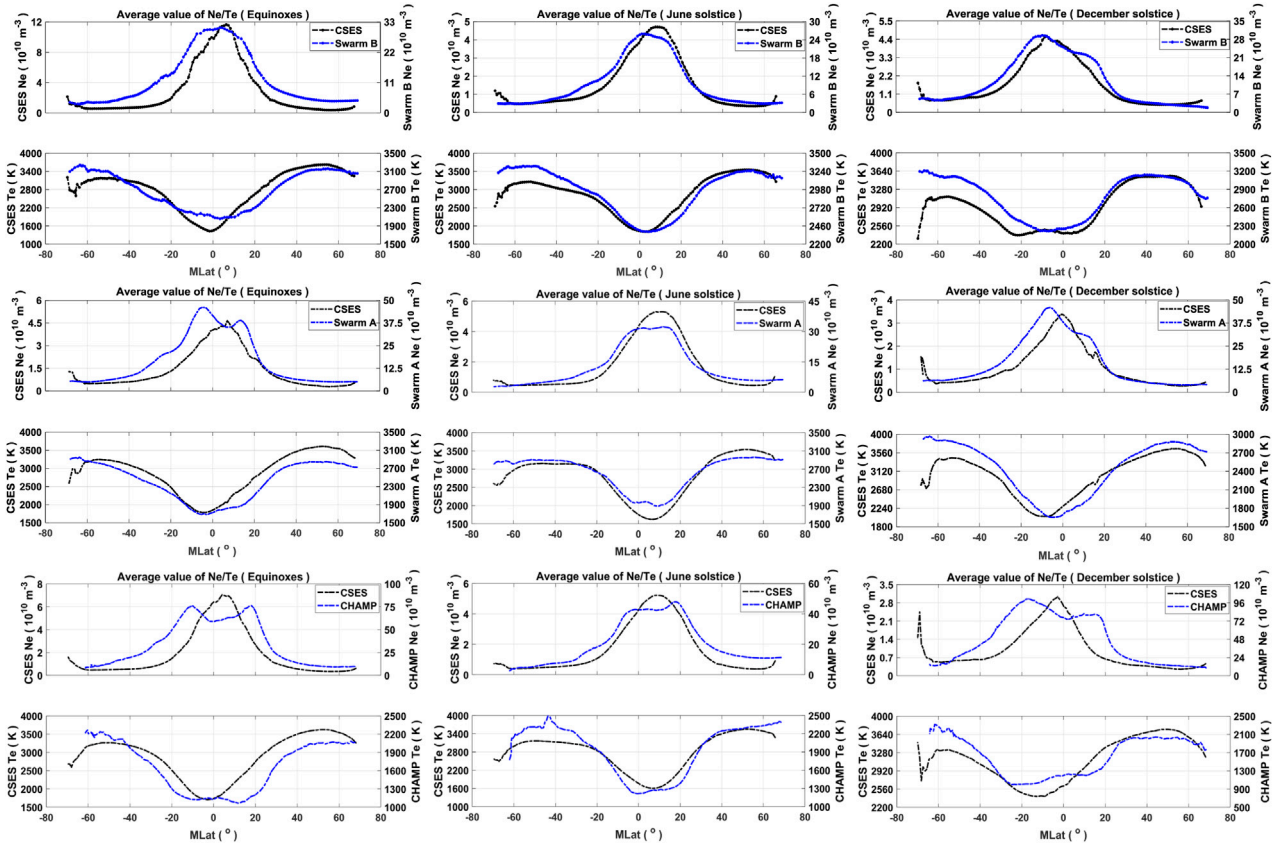


**FIGURE 3 |** The average profiles comparison of *Ne/Te* between CSES & Swarm B, CSES and Swarm A and CSES and CHAMP. The average profiles of CSES are shown as black lines, while the profiles from the other three satellites are shown as blue lines.

between *Ne* and *Te*, a saturation of *Te* is observed (or *Te* keeps at a same level) when *Ne* continues increases from $1\times10^{11.5}$ $m^{-3}$. Such a saturation of *Te* is also evidenced when *Ne* is very low, especially during June solstice.

## The Scatter Distribution of *Ne* and *Te* at Different MLat

To check if there is a latitudinal and seasonal dependence of the *Ne/Te* relation, the data in different MLat ranges are presented separately, and the results from the four satellites are presented in **Figures 5–8**. For each satellite, the observations are further divided into three seasons.

It is obvious that the correlation of *Ne* and *Te* at middle MLat (30°N -50°N and 30°S-50°S) are mainly negative, while at low and equatorial latitudes (from 30°S to 50°N), both negative and positive relation between *Ne* and *Te* are found. The reduced negative or even positive relation between *Ne* and *Te* is only found when *Ne* is larger. Around 14:00 LT, the *Ne* at middle latitudes is usually lower than the values at low and equatorial latitudes, especially when the EIA structure is well developed.

In addition, seasonal influence can also be seen. In equinoxes the correlation of *Ne* and *Te* are symmetric with respect to the geomagnetic equator. In solstice seasons, the correlation of *Ne* and *Te* vary with seasons and has similar characteristics when in same season hemisphere. For example, at MLat range 10°S-30°S, the *Ne* and *Te* measured from CSES show positive correlation only during December solstice hemisphere. This is because the southern hemisphere is in summer during December solstice, and the *Ne* is larger in southern hemisphere due to large solar illumination. Similar trend between *Ne* and *Te* is found in the northern hemisphere (10°N-30°N), though with no clear positive relation observed, the slope of the negative *Ne/Te* relation becomes spread during local summer (June solstice). From this perspective, whether the *Ne* is negatively and positively correlated with *Te*, depends largely on the absolute value of *Ne*.

The relation between *Ne* and *Te* from Swarm satellites (**Figures 6**, **7**) shows very similar latitudinal and seasonal dependences as that observed by CSES. However, additional two features need to be mentioned. First, the scatter of *Ne/Te* relation mainly happens at the low and middle latitudes (|MLat| >30°), as well as at MLat range 10°N-30°N in December solstice and 10°S-30°S in June solstice. Second, the two branches of *Ne/Te* relation happens mainly at equatorial and low latitudes (|MLat| <30°) when *Ne* is larger than $1\times10^{11}$ $m^{-3}$. From the latitudinal and seasonal distributions, we see the scatter of *Ne/Te* relation is dominated by MLat, while forming two branches of *Ne/Te* relation is dominated by the magnitude of *Te*.

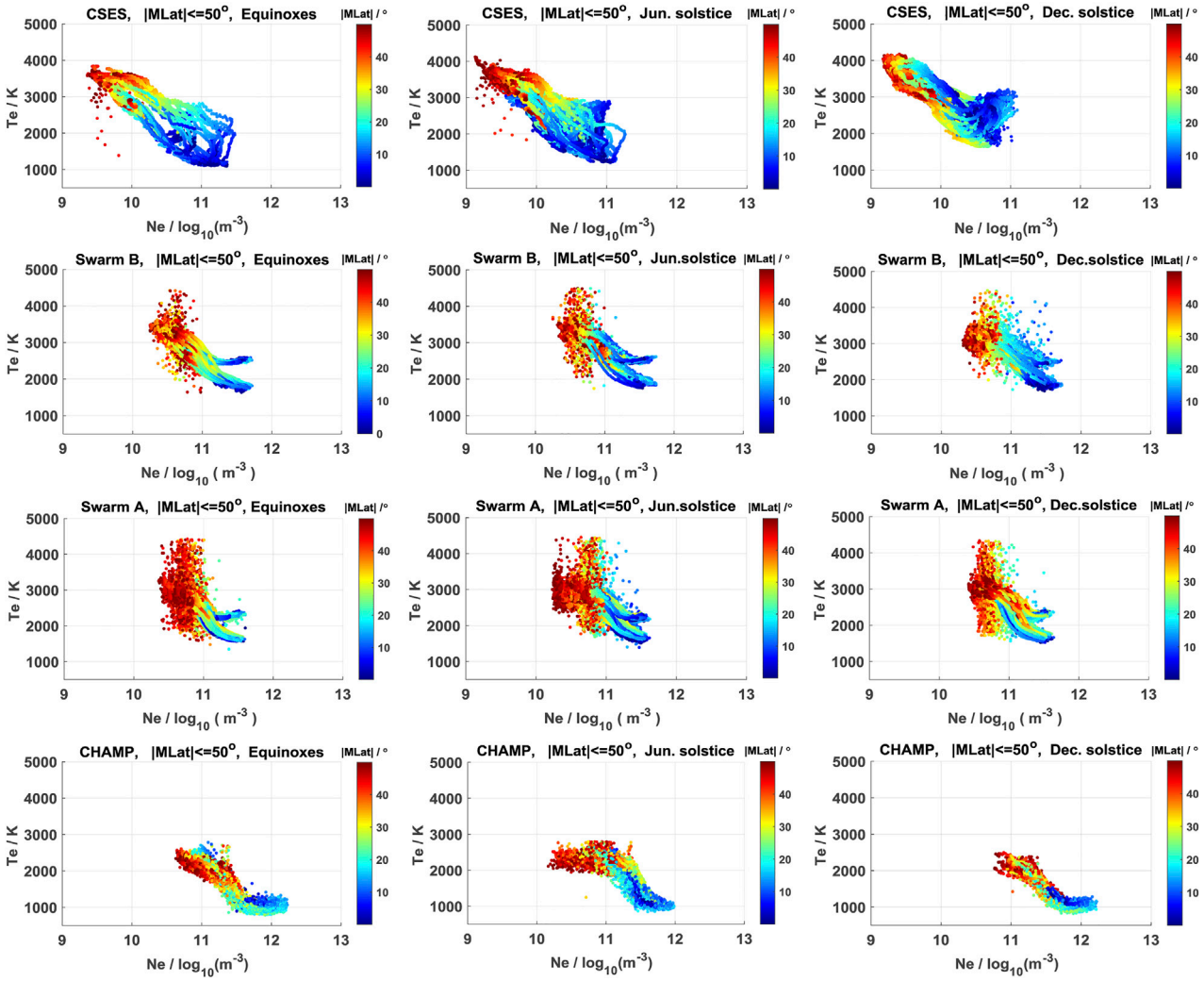


**FIGURE 4 |** The scatter distributions of *Ne* and *Te* around 14:00 LT from CSES, Swarm B, Swarm A and CHAMP are shown from top to bottom. The equinoxes, June solstice, and December solstice are shown in columns from left to right. The colors from blue to red represent the measurements at different MLat range (±50°).

For CHAMP (**Figure 8**), we see similar seasonal and MLat dependences of *Ne/Te* relation as that observed by CSES. In addition, a saturation of *Te* is observed (or *Te* keeps at a same level) at equatorial and low latitudes (|MLat|<30°), and also in the southern middle latitude (30°S -50°S) during June solstice.

# DISCUSSION

## Seasonal and MLat Dependence of the Correlation Between *Ne* and *Te*

The intensity of *Ne* and *Te* shows clear seasonal and magnetic latitudinal dependences from the measurements of all four satellites. For example, the *Ne* is symmetric about the magnetic equator in the equinoxes, while with larger values shifted towards the summer hemisphere in solstice seasons (seen **Figures 2**, **3**). Such seasonal and latitudinal variation of topside *Ne* is also consistent with pervious findings observed by other low earth orbiting satellites, e.g., the Gravity Recovery and Climate Experiment (GRACE) and DEMETER (Xiong et al., 2013; Zhang et al., 2014), as well as the total electron content (TEC) derived from the ground receivers of global navigation satellite system (GNSS) (e.g., Yeh et al., 2001). In addition, considering the altitude dependences, the *Ne* shows larger values and the two EIA crests are much more prominent from the satellites fly at lower altitude. This is well to be understood, as the EIA crests have stronger intensity at the F2 peak, and the four satellites fly above the F2 peak during almost all the time.

The *Te* in the low-latitude topside ionosphere is mainly controlled by the photoelectron heating and cooling through Coulomb collisions with ions that are both related to the integrated *Ne*. As shown in **Figures 5**–**8**, the *Te* in the same *Ne* range increases with increasing MLat. On the dayside around 14:00 LT, a clear negative correlation between *Te* and *Ne* is seen at low and middle latitudes; especially for the lower altitudes where Swarm A and CHAMP fly, two *Te* minima are observed right at

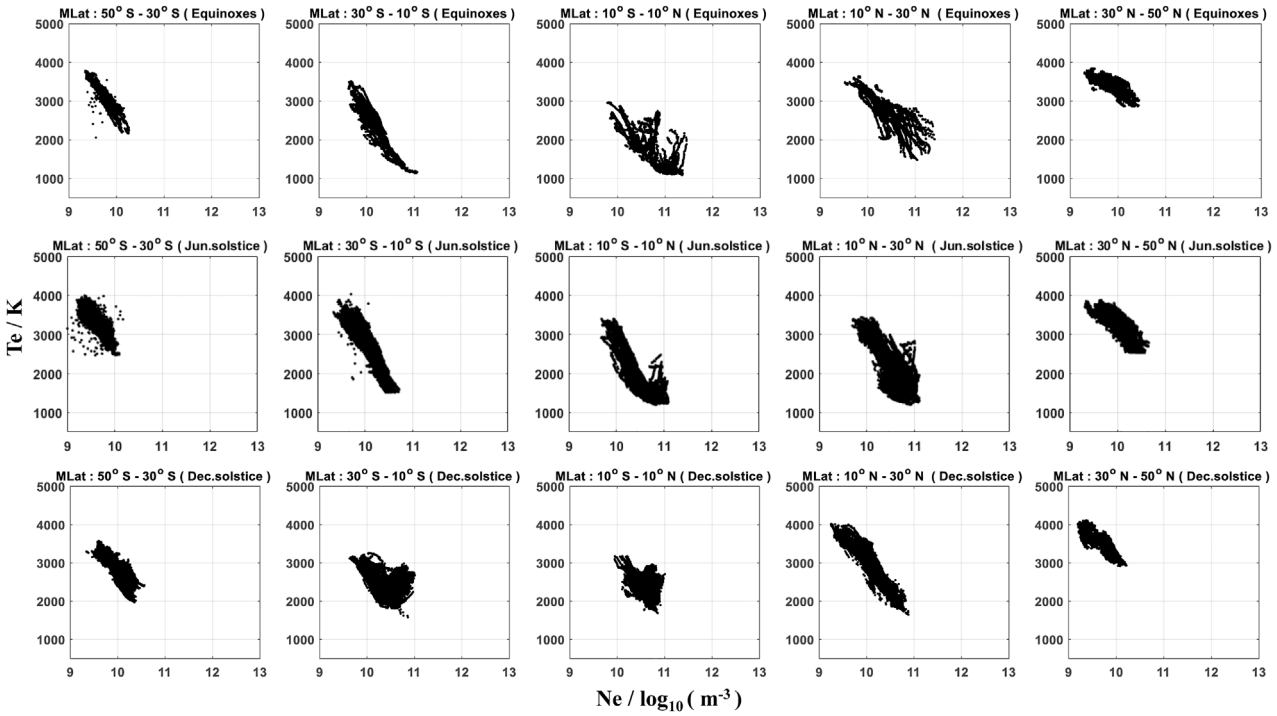


**FIGURE 5 |** Correlation of *Ne* and *Te* from CSES during different MLat ranges. From top to bottom, correspond to Equinoxes, June solstice, and December solstice. From left to right, the MLat range corresponds to 50° S - 30° S, 30° S - 10° S, 10° S - 10° N, 10° N - 30° N, 30° N- 50° N respectively.

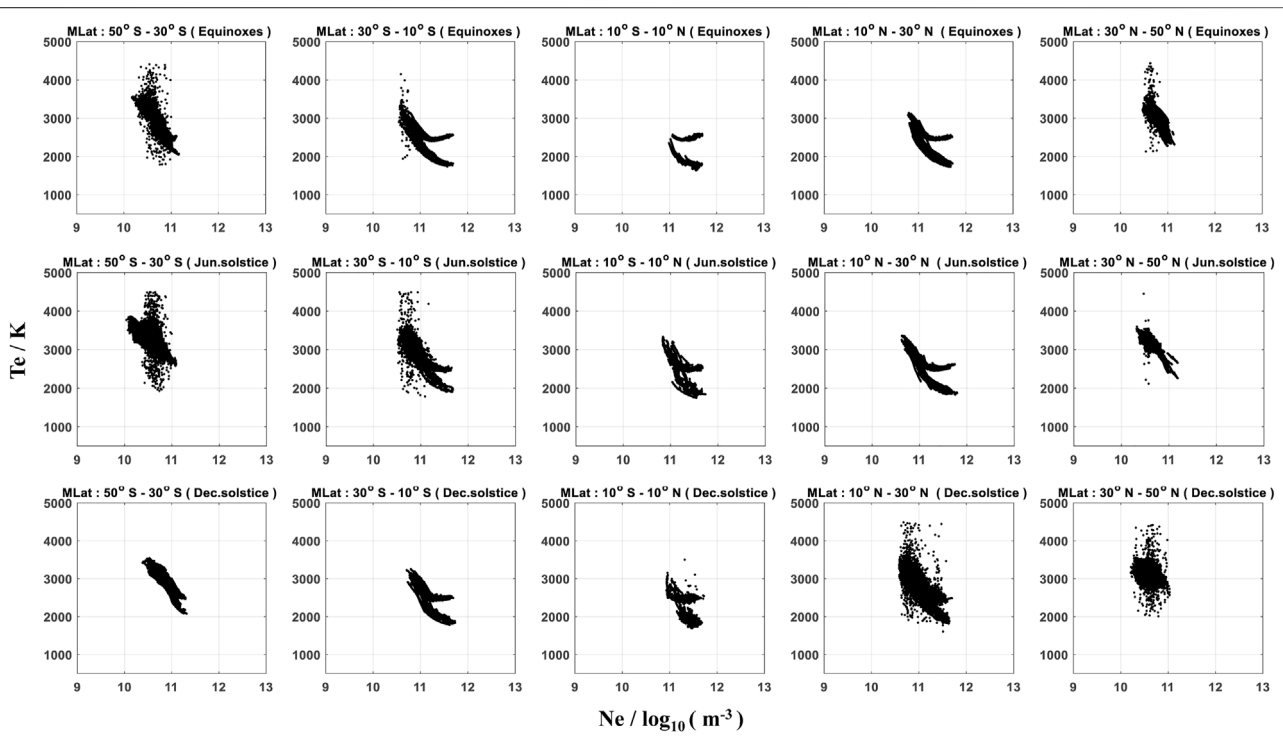


**FIGURE 6 |** As same as **Figure 5**, but for Swarm **B**

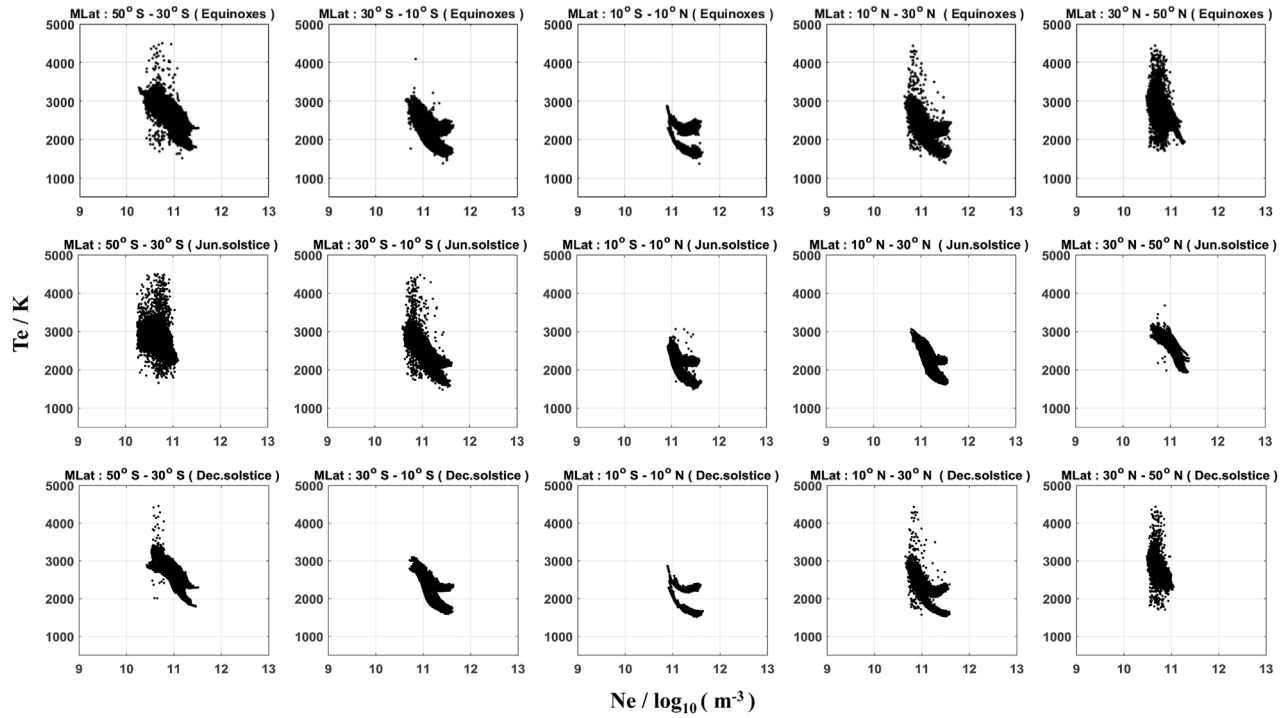


**FIGURE 7 |** As same as for **Figure 5**, but for Swarm A.

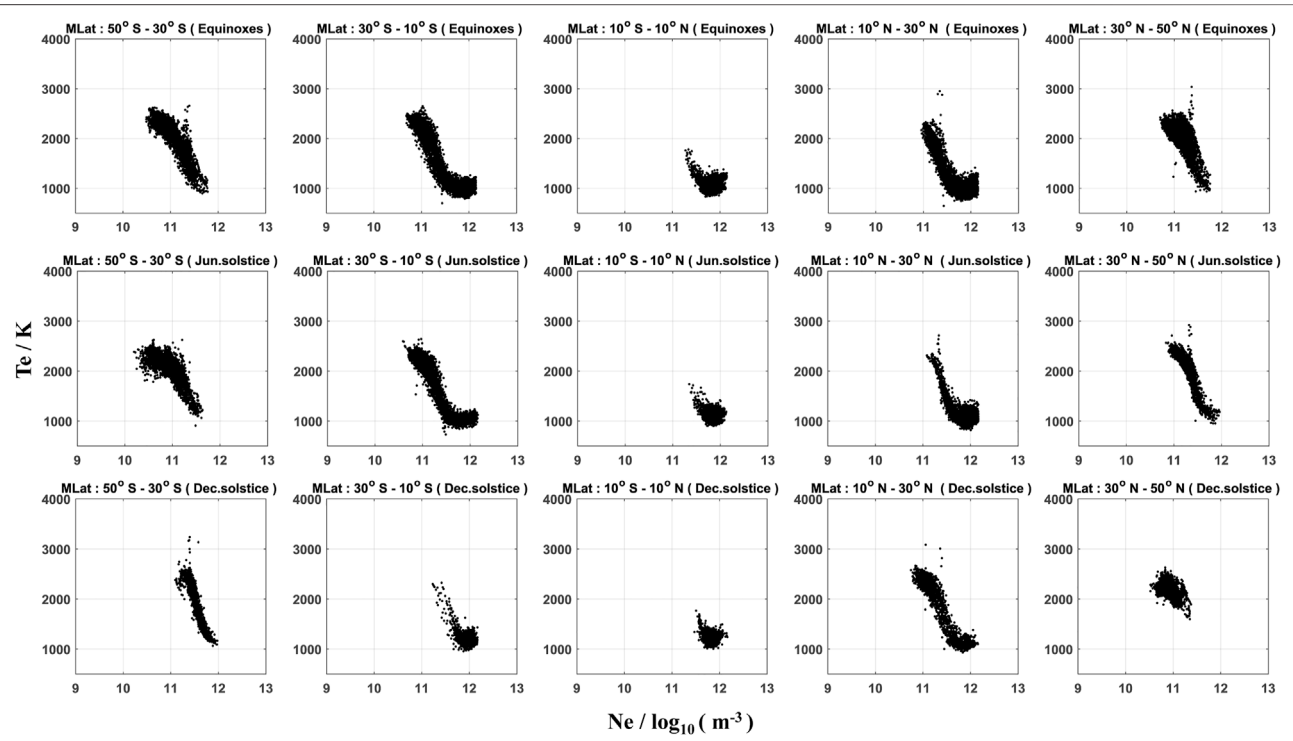


**FIGURE 8 |** As same as for **Figure 5**, but for CHAMP.

the latitudes of EIA crests (**Figure 2**). As shown in **Figure 4**, no scatter distribution between *Ne* and *Te* is observed from the CHAMP satellite. Even though, for a fixed *Ne* value, the *Te* can vary with a range over 500 K. One possible reason could be that the *Ne* considered here is the *in situ* measurement along the satellite track. As pointed out by Kakinami et al. (2011a), *Te* is more closely related to the integrated *Ne* along magnetic fluxtube, and the *in situ Ne* does not completely correlate with the integrated *Ne*, for example, the meridional wind can transport the plasma from one hemisphere to the other (Kelley, 2009).

In addition, due to influences from the lower atmospheric tidal and waves forcing, the topside ionospheric exhibit different longitudinal patterns in different seasons. The most prominent patterns are the longitudinal wave-4 and wave-3 structures during August and December solstice, which is considered to be dominated by the non-migrating tidal component of DE3 and DE2, respectively (e.g., Immel et al., 2006; Wan et al., 2010; Lühr et al., 2012). These results suggest that even at a fixed local time, the *Ne* can vary with quite a large range at different longitudes during different seasons, so it will further affect the seasonal dependence of *Ne* and *Te* relation as shown in **Figure 4**.

One interesting feature seen from CHAMP is that the *Te* keeps almost at a constant level when *Ne* is very low (in the southern middle latitude, 30°S -50°S, during June solstice). Kakinami et al. (2011a) reported an "inverted U shape" of the relation between *Ne* and *Te* during 06:00–08:00 LT from the Hinotori satellite observations The inverted U shape shown in their **Figure 1** arises from the positive correlation for lower *Ne* and a negative correlation for higher *Ne*, which looks very similar to the CHAMP results as shown in our **Figure 8**. And for both satellites, such low *Ne* values appear at middle latitudes.

## The Scatter and Two Branches of *Ne/Te* Correlation From Swarm

Two prominent features of the *Ne/Te* relation observed by Swarm satellites are: 1) when *Ne* is larger than $1\times10^{11}$ $m^{-3}$, *Te* are grouped into two branches at equatorial and low latitudes; 2) when *Ne* is lower than $1\times10^{11}$ $m^{-3}$, *Te* sometimes becomes very scatter at the low and middle latitudes.

For the first feature, we repeated the *Ne/Te* relation from Swarm B, shown in **Figure 9**. In **Figure 9A** the observations during equinoxes, June solstice and December solstice are marked with green, red and blue. *Te* has been grouped into two branches when *Ne* is larger than $1\times10^{11}$ $m^{-3}$, but no clear seasonal dependence of the two-branch feature of *Te* dependencies observed. For a fixed *Ne* level, the difference between the two *Te* branches is about 600 K. In addition, we checked further if the two branches of Swarm *Te* have geographical dependence, e.g. on longitude. As shown in **Figure 9B**, data have been divided into four geographic longitude bins: 180°– -90°, -90° 0°, 0° 90°, 90° 180° marked separately with red, green, blue and yellow. However, no clear longitude dependence is found of the two-branch feature.

From **Figures 4**, **9**, the *Ne* value of $1\times10^{11}$ $m^{-3}$ seems to be the threshold when the two branches of *Te* occur. However, as seen from **Figures 4**, **8**, the *Ne* observed by CHAMP are sometimes also greater than $1\times10^{11}$ $m^{-3}$, but the two branches of *Te* were not observed in the CHAMP data. So, it seems that the two branches of Swarm *Te* data are not directly related to the absolute value of *Ne*.

To have a further look at the two *Te* branches, we selected two orbits data both from Swarm B and CSES as examples, illustrated in **Figure 10**. **Figures 10A, C** show two latitudinal profile of *Ne* (first panel) and *Te* (second panel) from Swarm B marked as blue, while the *Ne* and *Te* measurements from CSES during this conjunction orbit are shown as black lines. The values of N*e*/*Te* from Swarm B and CSES are depicted by the left and right *y*-axis, respectively. The CSES orbits are quite close to Swarm, and the near-simultaneous footprints are presented also as black lines and blue lines (**Figures 10B, D**). Among them, in the first example (**Figures 10A, B**), *Ne* and *Te* profiles from CSES and Swarm B agree quite well with each other, except the difference of absolute value of *Ne*. The *Te* measurements from both satellites are basically at the same range, and the *Te* keeps at a lower value of about 2000 K at the low and equatorial latitudes, corresponding to the lower *Te* branch in **Figure 9**. From the second example (**Figures 10C, D**), we can see another characteristic, the *Te* from Swarm B keeps almost a constant value of about 2500 K at low and equatorial latitudes, representing the upper branch in **Figure 9**. For both examples, we see clearly that the *Te* from CSES keeps a value of about 1700 K at the low and equatorial latitudes. We checked also the quality flag of *Te* from Swarm B (third panel in **Figures 10A, C**), and the parameter "Flag-*Te*" is always marked as 20 for both orbits, suggesting no obvious disturbances during the two orbits. Such a direct comparison suggests that the upper branch of Swarm *Te* might be biased by a value of 600 K, though we don't know what causes the bias of the Swarm *Te*. The two-branch feature of *Te* seems exists in both hemispheres during all seasons, therefore, it might not be simply attributed to the illumination of the sunlight.

For the second feature, we see that the *Te* from Swarm B satellite shows clear fluctuations at the southern low and middle latitudes (15°S - 38°S), shown in **Figures 10A, C**. We also checked the flags of Swarm LP product, and the parameter "Flag-Te" is marked with a value of 20 during the *Te* fluctuations, indicating no abnormal behavior of *Te* data. However, we think such kind of *Te* fluctuations should not be related to natural geophysical structures, as the *Te* profile from CSES is quite smooth, especially considering their orbits are really close. **Figure 9B** shows also that there is no geophysical longitude dependence. In addition, we have further checked the Swarm orbits when such kind of *Te* fluctuations are observed and the parameter "Flag-Te" are also marked with a value of 20. When looking at the seasonal and latitudinal distributions of *Ne/Te* relation in **Figures 6**, **7**, for both Swarm B and A, the scatter of *Te* mainly happens at low and middle latitudes during equinoxes and local winter, while they are almost absent during local summer.

As the scatter of *Te* mainly happens at the upper-middle latitudes, where is close to the subauroral ionosphere. At this region, the *Te* varies often in a quite wide range, as it can be fed by the heat conduction from the outer plasmasphere (Fok et al., 1991). Though we only considered the data during geomagnetically quiet condition (Kp < 3), shorter time-scale processes or disturbances in the solar wind and

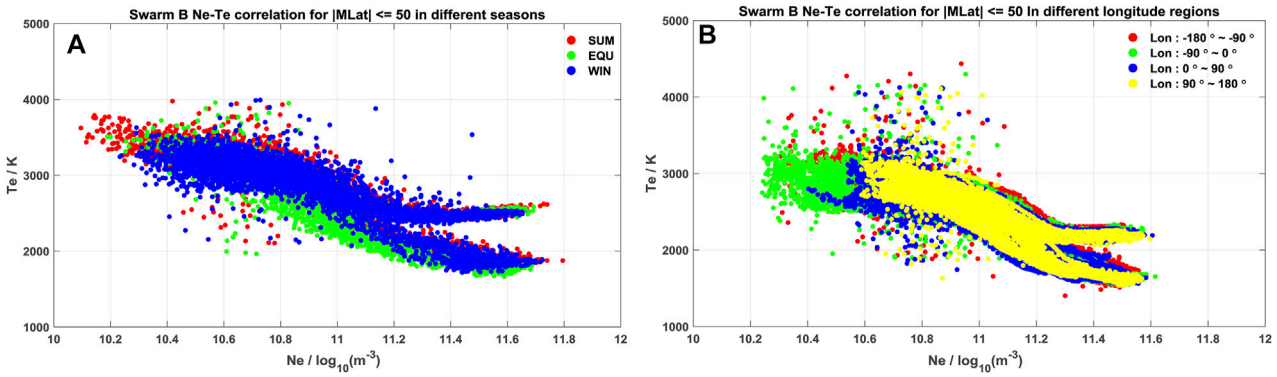


**FIGURE 9 |** Scatter plot of *Ne* and *Te* as measured by Swarm B. Each data point is confined into within the |MLAT|≤ 50° at around 14:00LT. **(A)** The observations during equinoxes, June solstice and December solstice are marked with green, red and blue. **(B)** The observations in different longitude regions including -180° ~ -90°, -90° ~ 0°, 0° ~ 90°, 90°~ 180° are marked with red, green, blue and yellow.

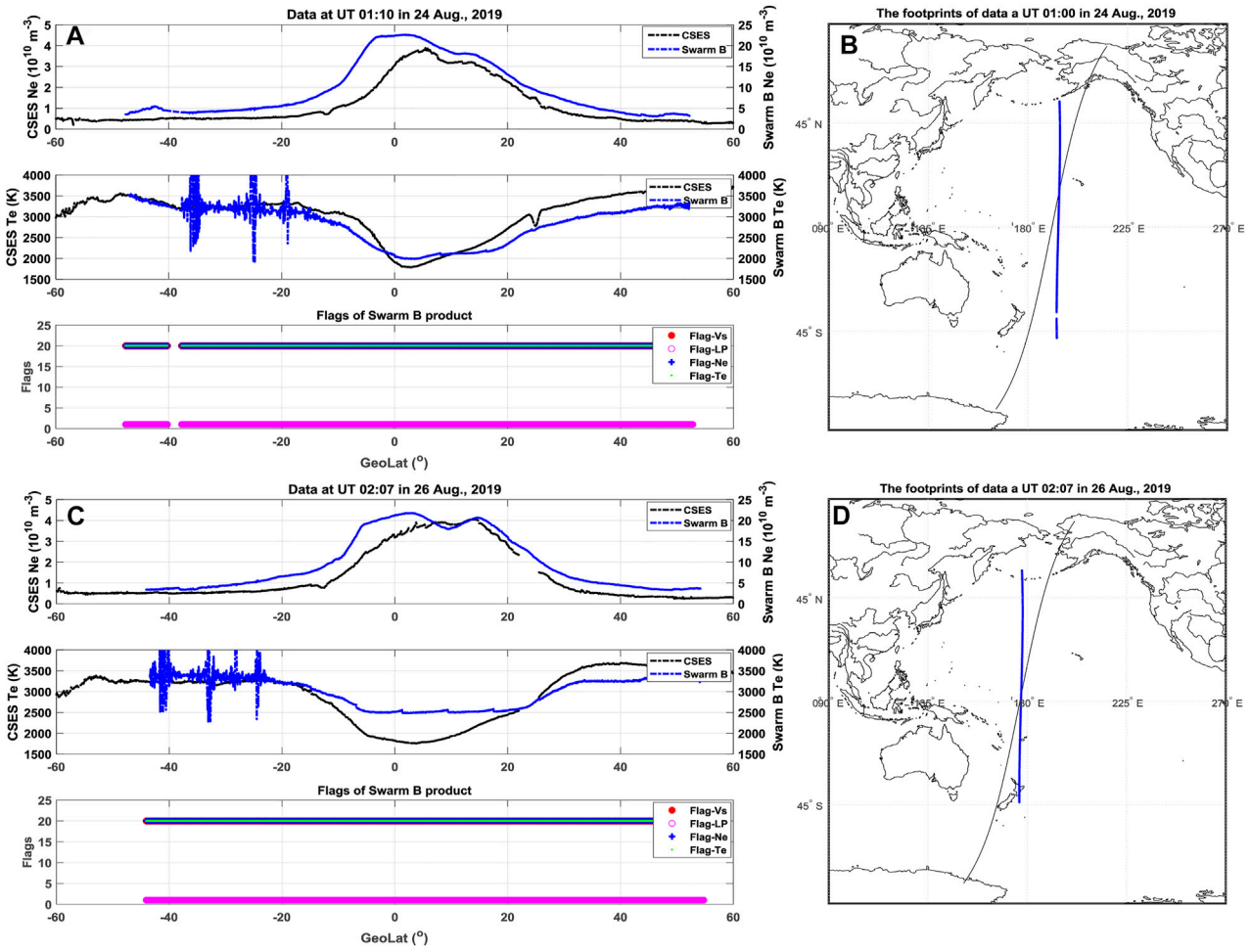


**FIGURE 10 | (A,C)** are the latitudinal profiles of Ne/Te from the CSES (black) and Swarm B (blue) when they are close in time and space. In addition, the flags of Swarm LP product are shown in the bottom panels of **(A,C)**. The two examples are taken on 24 and 26 August 2019, and their footprints of the two satellites are shown in Figure **(B,D)**.

magnetosphere can trigger heat flow to the ionosphere. Another possible reason to alter *Te* variations could be the Subauroral Ion Drifts (SAID) driven by large polarization electric fields from the auroral oval towards lower latitude (Moffett et al., 1998). Further dedicated study is encouraged for resolving this feature in details.

## Possible Mechanisms for Affecting the Correlation Between *Ne* and *Te*

*Ne* in the ionosphere is mainly produced by the solar EUV radiation, since the solar photons have significant energy to ionize the neutral atmosphere. Photoelectrons produce heat for the local electrons as well as remote electrons along the magnetic field line. *Te* is governed by the heating of photoelectron, cooling caused by collisions among ions and neutral species, and heat conduction in the ionosphere (e.g., Watanabe et al., 1995). In the topside ionosphere (above the F2 peak), the heat conduction becomes a dominant factor because of the reduced collision between charged particles and neutrals. Therefore, *Te* is not controlled by the local variation of *Ne* but rather by the integrated *Ne* along the magnetic field line below the F2 peak (Kakinami et al., 2011b). Above the magnetic equator, the plasma is transported upward by the E×B drift at the magnetic equator, so that the plasma for the EIA when diffusing poleward along the magnetic field line (e.g. Appleton, 1946). In addition, thermospheric winds also transport the plasma in the topside ionosphere upward/downward along the magnetic field line (Watanabe and Oyama, 1996; Kakinami et al., 2011b). Therefore, the positive dependence of *Ne/Te* at the EIA region is controlled mainly by the plasma dynamics. When the plasma is uplifted from below to the altitudes of interest, *Ne* increases, but *Te* is remains lower. When plasma is transported from higher altitudes, *Te* is higher while *Ne* is lower. In both cases the plasma transport results in negative *Te/Ne* dependence. The only case when we could expect a positive tendency is the uplifting of neutral gas along with the plasma. Then the photoionization will produce fresh photoelectrons which will heat the electron gas and increase *Te*.

## CONCLUSION

In this study, we investigated the characteristic of the correlation between *Ne* and *Te* around 14:00 LT using observations from four satellites, CSES, Swarm B, Swarm A and CHAMP during very low solar activity years. The Seasonal and MLat dependence of the correlation between *Ne* and *Te* are also discussed in this work. In addition, we also analyzed the two branches of *Ne/Te* correlation from Swarm. The main results can be summarized as follows:

(1) Observations from the four satellites show generally consistent relation between the *Ne* and *Te*. A general negative relation is found between the *Ne* and *Te* at 14:00 LT from all four satellites, while the slope of the negative relation reduces and even becomes positive when the *Ne* becomes larger.

(2) The correlation of *Ne a*nd *Te* shows dependences on season and magnetic latitude, as the *Ne* and *Te* themselves are seasonal and MLat dependent. By considering the *in situ* measurements from four satellites at different latitudes, the relation between ionospheric topside *Ne* and *Te* seems to be dominated by the absolute value of *Ne*.

(3) Two prominent features of the *Ne/Te* relation observed by Swarm satellites are: a) when *Ne* is lower than $1\times10^{11}$ $m^{-3}$, *Te* sometimes becomes very scatter at low and middle latitudes; b) when *Ne* is larger than $1\times10^{11}$ $m^{-3}$, *Te* are grouped into two branches at equatorial and low latitudes. Detailed analysis reveals that the flags used in the Swarm Level-1B plasma density product cannot well distinguish the two abnormal features of *Te*, implying further efforts are needed for the Swarm *Te* data calibration.

## DATA AVAILABILITY STATEMENT

The original contributions presented in the study are included in the article/Supplementary Materials, further inquiries can be directed to the corresponding authors.

## AUTHOR CONTRIBUTIONS

RY, CX, ZZ, and XS contributed to conception and design of the study. RY, CX, and DL organized the database. KZ, LZ, and FL performed the statistical analysis. RY wrote the first draft of the manuscript. RY, CX, CL, and YG wrote sections of the manuscript. All authors contributed to manuscript revision, read, and approved the submitted version.

## FUNDING

This work was supported by National Key R & D Program of China (Grant No. 2018YFC1503502-06), the Dragon five cooperation (Grant No. 59236), the Fundamental Research Funds for NINH (Grant No. ZDJ2019-22), the APSCO earthquake Project Phase II, the Stable-Support Scientific Project of CRIRP (Grant No. A132001W07) and ISSI-BJ project.

## ACKNOWLEDGMENTS

CX acknowledges the support from the Special Fund of Hubei Luojia Laboratory (220100011). This work used the data from the CSES mission (http://www.leos.ac.cn), a project funded by China National Space Administration (CNSA) and China Earthquake Administration (CEA). We acknowledge further the teams of Swarm and CHAMP, for providing the data at https://diss.eo.esa.int and https://isdc.gfz-potsdam.de/champ-isdc/access-to-the-champ-data/.

## REFERENCES


Appleton, E. V. (1946). Two Anomalies in the Ionosphere. *Nature* 157, 691. doi:10.1038/157691a0

Bailey, G. J., Su, Y. Z., and Oyama, K.-I. (2000). Yearly Variations in the Low-Latitude Topside Ionosphere. *Ann. Geophys.* 18, 789–798. doi:10.1007/s00585-000-0789-0

Bilitza, D. (1985). Implementation of the New Electron Temperature Model in IRI. *Adv. Space Res.* 5 (10), 117–121. doi:10.1016/0273-1177(85)90193-0

Bilitza, D. (1975). Models for the Relationship between Electron Density and Temperature in the Upper Ionosphere. *J. Atmos. Terrestrial Phys.* 37, 1219–1222. doi:10.1016/0021-9169(75)90193-2

Bilitza, D., Rawer, K., Bossy, L., and Gulyaeva, T. (1993). International Reference Ionosphere - Past, Present, and Future: II. Plasma Temperatures, Ion Composition and Ion Drift. *Adv. Space Res.* 13 (3), 15–23. doi:10.1016/0273-1177(93)90241-3

Brace, L. H., and Theis, R. F. (1978). An Empirical Model of the Interrelationship of Electron Temperature and Density in the Daytime Thermosphere at Solar Minimum. *Geophys. Res. Lett.* 5, 275–278. doi:10.1029/GL005i004p00275

Fok, M.-C., Kozyra, J. U., Warren, M. F., and Brace, L. H. (1991). Seasonal Variations in the Subauroral Electron Temperature Enhancement. *J. Geophys. Res.* 96 (A6), 9773–9780. doi:10.1029/91ja00791

Hargreaves, J. K. (1992). *The Solar-Terrestrial Environment an Introduction to Geospace-The Science of the Terrestrial Upper Atmosphere, Ionosphere, and Magnetosphere*. Cambridge, UK, and New York: Cambridge University Press.

Immel, T. J., Sagawa, E., England, S. L., Henderson, S. B., Hagan, M. E., Mende, S. B., et al. (2006). Control of Equatorial Ionospheric Morphology by Atmospheric Tides. *Geophys. Res. Lett.* 33, L15108. doi:10.1029/2006GL026161

Kakinami, Y., Kamogawa, M., Onishi, T., Mochizuki, K., Lebreton, J.-P., Watanabe, S., et al. (2013). Validation of Electron Density and Temperature Observed by DEMETER. *Adv. Space Res.* 52, 1267–1273. doi:10.1016/j.asr.2013.07.003

Kakinami, Y., Lin, C. H., Liu, J. Y., KamogawaWatanabe, M., Watanabe, S., and Parrot, M. (2011b). Daytime Longitudinal Structures of Electron Density and Temperature in the Topside Ionosphere Observed by the Hinotori and DEMETER Satellites. *J. Geophys. Res.* 116, A05316. doi:10.1029/2010JA015632

Kakinami, Y., Watanabe, S., Liu, J.-Y., and Balan, N. (2011a). Correlation between Electron Density and Temperature in the Topside Ionosphere. *J. Geophys. Res.* 116, a–n. doi:10.1029/2011JA016905

Kelley, M. C. (2009). *The Earth's Ionosphere, Plasma Physics and Electrodynamics*. 2nd Edn. San Diego Calif: Academic.

Knudsen, D. J., Burchill, J. K., Buchert, S. C., Eriksson, A. I., Gill, R., Wahlund, J. E., et al. (2017). Thermal Ion Imagers and Langmuir Probes in the Swarm Electric Field Instruments. *J. Geophys. Res. Space Phys.* 122, 2655–2673. doi:10.1002/2016JA022571

Lei, J., Roble, R. G., Wang, W., Emery, B. A., and Zhang, S.-R. (2007). Electron Temperature Climatology at Millstone Hill and Arecibo. *J. Geophys. Res.* 112, a–n. doi:10.1029/2006JA012041

Liu, C., Guan, Y., Zheng, X., Zhang, A., Piero, D., and Sun, Y. (2018). The Technology of Space Plasma *In-Situ* Measurement on the China Seismo-Electromagnetic Satellite. *Sci. China Technol. Sci.* 62, 829–838. doi:10.1007/s11431-018-9345-8

Liu, J. Y., Chang, F. Y., Oyama, K. I., Kakinami, Y., Yeh, H. C., Yeh, T. L., et al. (2015). Topside Ionospheric Electron Temperature and Density along the Weddell Sea Latitude. *J. Geophys. Res. Space Phys.* 120, 609–614. doi:10.1002/2014ja020227

Lomidze, L., Knudsen, D. J., Burchill, J., Kouznetsov, A., and Buchert, S. C. (2018). Calibration and Validation of Swarm Plasma Densities and Electron Temperatures Using Ground-Based Radars and Satellite Radio Occultation Measurements. *Radio Sci.* 53, 15–36. doi:10.1002/2017rs006415

Lühr, H., Park, J., Gjerloev, J. W., Rauberg, J., Michaelis, J. M. G., and Brauer, P. (2015). Field-Alignedcurrents' Scale Analysis Per-Formed With the Swarm Constellation. *Geophys. Res.* 42, 1–8. doi:10.1002/2014GL062453

Lühr, H., Rother, M., Häusler, K., Fejer, B., and Alken, P. (2012). Direct Comparison of Nonmigrating Tidal Signatures in the Electrojet, Vertical Plasma Drift and Equatorial Ionization Anomaly. *J. Atmos. Solar-Terrestrial Phys.* 75-76, 31–43. doi:10.1016/j.jastp.2011.07.009

McNamara, L. F., Cooke, D. L., Valladares, C. E., and Reinisch, B. W. (2007). Comparison of CHAMP and Digisonde Plasma Frequencies at Jicamarca, Peru. *Radio Sci.* 42, a–n. doi:10.1029/2006RS003491

Moffett, R. J., Ennis, A. E., Bailey, G. J., Heelis, R. A., and Brace, L. H. (1998). Electron Temperatures during Rapid Subauroral Ion Drift Events. *Ann. Geophys.* 16 (4), 450–459. doi:10.1007/s00585-998-0450-x

Palin, L., Opgenoorth, H., Buchert, S., Knudsen, D., Archer, W., Erickson, P., et al. (2015). *Comparison of Plasma Density and Temperature by* In-Situ *Langmuir Probes and by Incoherent Scatter Radars, 26th IUGG General Assembly*. Prague, Czech Republic.

Pedatella, N. M., Yue, X., and Schreiner, W. S. (2015). Comparison between GPS Radio Occultation Electron Densities and *In Situ* Satellite Observations. *Radio Sci.* 50, 518–525. doi:10.1002/2015rs005677

Reigber, C., Lühr, H., and Schwintzer, P. (2002). CHAMP mission Status. *Adv. Space Res.* 30, 129–134. doi:10.1016/s0273-1177(02)00276-4

Ren, Z., Wan, W., Liu, L., Zhao, B., Wei, Y., Yue, X., et al. (2008). Longitudinal Variations of Eletron Temperature and Total Ion Density in the sunset Equatorail Topside Ionosphere. *Geophys. Res. Lett.* 35, L15108. doi:10.1029/2007gl032998

Rother, M., Schlegel, K., Lühr, H., and Cooke, D. (2010). Validation of CHAMP Electron Temperature Measurements by Incoherent Scatter Radar Data. *Radio Sci.* 45, a–n. doi:10.1029/2010RS004445

Schunk, R. W., and Nagy, A. F. (1978). Electron Temperatures in theFregion of the Ionosphere: Theory and Observations. *Rev. Geophys.* 16, 355–399. doi:10.1029/RG016i003p00355

Shen, X. H., Zhang, X., Liu, J., Zhao, S. F., and Yuan, G. P. (2015). Analysis of the Enhanced Negative Correlation between Electron Density and Electron Temperature Related to Earthquakes. *Ann. Geophys.* 33, 471–479. doi:10.5194/angeo-33-471-2015

Shen, X. H., Zhang, X. M., Yuan, S. G., Wang, L. W., Cao, J. B., Huang, J. P., et al. (2018). The State-Of-The-Art of the China Seismo-Electromagnetic Satellite mission. *Sci. China, Technol. Sci.* 61, 634. doi:10.1007/s11431-018-9242-02018

Stolle, C., Liu, H., Truhlik, V., Luhr, H., and Richards, P. G. (2011). Solar Flux Variation of the Electron Temperature Morning Overshoot in the Equatorial F Region. *J. Geophys. Res.* 116, A04308. doi:10.1029/2020JA01623510.1029/2010ja016235

Su, F., Wang, W., Burns, A. G., Yue, X., and Zhu, F. (2015). The Correlation between Electron Temperature and Density in the Topside Ionosphere during 2006-2009. *J. Geophys. Res. Space Phys.* 120 (10), 724739–724810. doi:10.1002/2015JA021303

Wan, W., Xiong, J., Ren, Z., Liu, L., Zhang, M.-L., Ding, F., et al. (2010). Correlation between the Ionospheric WN4 Signature and the Upper Atmospheric DE3 Tide. *J. Geophys. Res.* 115, a–n. doi:10.1029/2010JA015527

Watanabe, S., Oyama, K.-I., and Abdu, M. A. (1995). Computer Simulation of Electron and Ion Densities and Temperatures in the equatorialFregion and Comparison with Hinotori Results. *J. Geophys. Res.* 100 (14), 14581–14590. doi:10.1029/95JA01356

Watanabe, S., and Oyama, K.-I. (1996). Effects of Neutral Wind on the Electron Temperature at a Height of 600 Km in the Low Latitude Region. *Ann. Geophys.* 14, 290–296. doi:10.1007/s00585-996-0290-5

Xiong, C., Lühr, H., and Ma, S. Y. (2013). The Magnitude and Inter-hemispheric Asymmetry of Equatorial Ionization Anomaly-Based on CHAMP and GRACE Observations. *J. Atmos. Solar-Terrestrial Phys.* 105-106, 160–169. doi:10.1016/j.jastp.2013.09.010

Xiong, C., Stolle, C., Lühr, H., Park, J., Fejer, B. G., and Kervalishvili, G. N. (2016a). Scale Analysis of Equatorial Plasma Irregularities Derived from Swarm Constellation. *Earth, Planets and Space* 68 (1). doi:10.1186/s40623-016-0502-5

Xiong, C., Zhou, Y. L., Lühr, H., and Ma, S. Y. (2016b). Diurnal Evolution of the F Region Electron Density Local Time Gradient at Low and Middle Latitudes Resolved by the Swarm Constellation. *J. Geophys. Res. Space Phys.* 121, 9075–9089. doi:10.1002/2016JA023034

Yan, R., Guan, Y., Miao, Y., Zhima, Z., Xiong, C., Zhu, X., et al. (2022). The Regular Features Recorded by the Langmuir Probe Onboard the Low Earth Polar Orbit Satellite CSES. *J. Geophys. Res. Space Phys.* 127, e2021JA029289. doi:10.1029/2021ja029289

Yan, R., Zhima, Z., Xiong, C., Shen, X., Huang, J., Guan, Y., et al. (2020). Comparison of Electron Density and Temperature from the CSES Satellite with Other Space-Borne and Ground-Based Observations. *J. Geophys. Res. Space Phys.* 125, e2019JA027747. doi:10.1029/2019JA027747

Yang, T. Y., Park, J., Kwak, Y. S., Oyama, K. I., Minow, J. I., and Lee, J. (2020). Morning Overshoot of Electron Temperature as Observed by the Swarm Constellation and the International Space Station. *J. Geophys. Res. Space Phys.* 125, e2019JA027299. doi:10.1029/2019JA027299

Yeh, K. C., Franke, S. J., Andreeva, E. S., and Kunitsyn, V. E. (2001). An Investigation of Motions of the Equatorial Anomaly Crest. *Geophys. Res. Lett.* 28 (24), 4517–4520. doi:10.1029/2001gl013897

Zhang, S.-R., and Holt, J. M. (2004). Ionospheric Plasma Temperatures during 1976-2001 over Millstone Hill. *Adv. Space Res.* 33, 963–969. doi:10.1016/j.asr.2003.07.012

Zhang, X., Shen, X., Liu, J., Zeren, Z., Yao, L., Ouyang, X., et al. (2014). The Solar Cycle Variation of Plasma Parameters in Equatorial and Mid Latitudinal Areas during 2005-2010. *Adv. Space Res.* 54, 306–319. doi:10.1016/j.asr.2013.09.012

**Conflict of Interest:** The authors declare that the research was conducted in the absence of any commercial or financial relationships that could be construed as a potential conflict of interest.

frontiers | Frontiers in Environmental Science

ORIGINAL RESEARCH
published: 05 May 2022
doi: 10.3389/fenvs.2022.902508

# Uncommon Electromagnetic Radiations Related to Extra-High Voltage/Ultra-High Voltage Power Projects in China

*Jing Wu*[1]*, *Jingwen Zhang*[1] and *Li Xie*[2]

[1]School of Automation Science and Electrical Engineering, Beihang University, Beijing, China, [2]China Electric Power Research Institute, Beijing, China

Based on the high-resolution electromagnetic field intensity observed by the DEMETER satellite, the harmonic electromagnetic radiations in the ionosphere closely above the extra-high voltage and ultra-high voltage power projects in the Chinese power grid have been detected. In the time-frequency spectrograms, these radiations are characterized by parallel spectral lines with spacings of 50, 100, 150, or 600 Hz. The highest frequency can reach approximately 8,850 Hz. The radiations are probably attributed to the nonlinear devices such as converters or geomagnetic disturbance. The harmonic radiations over alternating current-to-direct current (AC-to-DC) substations of power system are generally more diverse and stronger than those over AC-to-AC substations. The measurements on the ground demonstrate that the weak magnetic radiations at several kilohertz with an intensity in the order of nT do exist around substations. A simple physical model is established to understand the characteristics of harmonic radiations propagating from the Earth's surface to the ionosphere.

**Keywords: near-Earth electromagnetic environment, artificial ELF/VLF waves, satellite-based observation, interference in the top ionosphere, EHV/UHV power lines**

OPEN ACCESS

***Edited by:***
*Zeren Zhima,*
*Ministry of Emergency Management, China*

***Reviewed by:***
*Michel Parrot,*
*UMR7328 Laboratoire de physique et chimie de l'environnement et de l'Espace (LPC2E), France*
*Vyacheslav Pilipenko,*
*Institute of Physics of the Earth, Russia*

***Correspondence:**
*Jing Wu*
*wujing06@buaa.edu.cn*

***Specialty section:***
*This article was submitted to Environmental Informatics and Remote Sensing, a section of the journal Frontiers in Environmental Science*

***Received:*** *23 March 2022*
***Accepted:*** *21 April 2022*
***Published:*** *05 May 2022*

***Citation:***
*Wu J, Zhang J and Xie L (2022) Uncommon Electromagnetic Radiations Related to Extra-High Voltage/Ultra-High Voltage Power Projects in China. Front. Environ. Sci. 10:902508. doi: 10.3389/fenvs.2022.902508*

## 1 INTRODUCTION

It is usually believed that the electromagnetic radiations from the power grid are confined to the Earth's surface, and they could interfere with the measurement of the geomagnetic field, the safe operation of oil or gas pipelines, the navigation of ships, and geophysical explorations. However, in the 1960s, observations at two pairs of geomagnetic conjugate stations—Siple in Antarctica and Roberval in Quebec, Canada, and Halley Bay in Antarctica and St. Anthony in Newfoundland, Canada—showed that power line harmonic radiation (PLHR) can propagate between the geomagnetic conjugate points in a whistler mode (Helliwell et al., 1975; Park and Chang, 1978; Park and Helliwell, 1978; Park et al., 1983). In the time-frequency spectrogram of the electromagnetic field intensity, PLHR is characterized by a cluster of parallel spectral lines spaced by almost exactly 50/100 Hz or 60/120 Hz and without any drift over time, and their intensity is (5–40) dB stronger than the natural background noise.

The existence of PLHR and its associated triggered nonlinear emissions have been demonstrated by multiple satellites, such as Ariel III (the in-orbit duration is 1967–1978 and with an altitude of 497 km), Ariel IV (1971–1978, 497–590 km), OGO-4 (1967–1970, 409–895 km), ISEE-1 (1977–1987, 280–140,162 km), AUREOL-3 (1981–1986, 408–2000 km), OHZORA (1984–1989, 350–850 km),

DEMETER (2004–2010, 660 km), and Chibis-M (2012–2014, 484–504 km) (Bullough et al., 1976; Luette et al., 1979; Bell et al., 1982; Tomizawa and Yoshino, 1985; Parrot, 1994; Němec et al., 2007). The occurrence rate of PLHR is high between local times of 06:00 A. M and 03:00 P. M, and its intensity is weaker on Sundays, consistent with the local power consumption (Park and Miller, 1979); thus, they have been thought to be related closely with the power grid. The suggested sources include the Čerenkov-like radiation generated by an electron beam traversing a dielectric interface when coronal discharge occurs along high-voltage transmission lines, but their frequency is generally more than MHz (Kikuchi, 1983); the unbalanced harmonic currents flow through three-phase long transmission lines, but their radiation power was measured to be far lower than the threshold power of PLHR propagating into the near-Earth space obtained from the experiments at geomagnetically conjugated stations (Park and Chang, 1978; Yearby et al., 1983); the harmonic radiations are generated by nonlinear 12-pulse converters, but the measurements on the ground indicate that these radiations mainly contain linear and left-handed polarization components, which does not support that PLHR is right-handed polarization and propagates along the geomagnetic field in a whistler mode (Yearby and Smith, 1994; Manninen, 2005). To date, a consensus has been reached that PLHR in the near-Earth space is related to the local power grid on the ground, however, its exact source is still uncertain. It is noteworthy that the power line emission (PLE) at 50/60 Hz still exists in the near-Earth space (Park and Helliwell, 1981; Rodger et al., 1995; Dudkin et al., 2015; Wu et al., 2019). The frequency of PLE depends on the local power system and could be largely recorded at night (Pilipenko et al., 2021). PLHR usually occurs with PLE, but PLE does not necessarily occur with PLHR.

The electromagnetic radiations from the power grid including PLHR and PLE have been recognized as a kind of pollutant to the near-Earth space (Parrot and Zaslavski, 1996). They undoubtedly interfere with ionospheric and magnetospheric studies based on ground and satellite experiments. They can even affect the lifetime of energetic electrons in the radiation belt through wave-particle cyclotron resonance and may lead to frequent thunderstorms (Bullough et al., 1976; Yearby and Smith, 1994). With the increase of global power consumption, PLHR will become more serious (Parrot and Zaslavski, 1996). The large changes in the Chinese power grid during the in-orbit operation of the DEMETER satellite create an opportunity to further understand the mechanism of PLHR. In this study, some uncommon power harmonic radiations observed by DEMETER related to the large-capacity ±500 kV DC, and 500 and 1,000 kV AC power projects in the Chinese power grid are illustrated, and a simple physical model was established to analyse some characteristics of these radiation waves.

## 2 MATERIALS AND METHODS

### 2.1 The DEMETER Satellite

The DEMETER satellite adopted a near sun-synchronous orbit and operated at an altitude of 660 km from 29 June 2004, to 9 December 2010. Its daytime orbit (from the Northern Hemisphere to the Southern Hemisphere) passed over a specific zone at 10:30 LT, while its night-time orbit (from the Southern Hemisphere to the Northern Hemisphere) passed over the same zone at 22:30 LT. DEMETER has two operating modes: survey and burst. The burst mode was turned on for several minutes or tens of minutes when the satellite flew over some specific zones and provided observation data with a higher sampling frequency.

DEMETER measured the data in the burst mode of electric field $E$ and magnetic field density $B$ in the band of 0–20 kHz using an electric field detector (ICE) and an inductive magnetic field detector (IMSC) with a sampling frequency of 40 kHz. Rather than $B$ which was easily interfered by natural noise, $E$ was analyzed using a short-time Fourier transform with a Hanning window to obtain spectrograms with frequency resolution of 1 Hz and time resolution of 0.8192s, sufficient to detect PLHR. Plasma electron density $N_e$ measured by the Langmuir probe (ISL) with a time resolution of 1s was used to check the variation of the ionospheric state when PLHR occurred.

### 2.2 The Magnetic Field Measurement

In order to detect the weak magnetic field, a three-axis orthogonal coil with an electric field shielding layer is designed (Li et al., 2021) which is shown in **Figure 1**. The size of the coil can make its thermal noise level much lower than the natural background noise in the atmosphere (ITU-R P. 372-10). The signal conditioning module uses a two-stage amplification. The signal of the coil induction voltage is acquired by a 16-bit data acquisition card NI-9222, and the maximum sampling frequency is 500 kHz. The sensor can measure a weak magnetic field of 0.15 pT. In the frequency band of 10 Hz–20 kHz, the noise level is lower than $10\text{pT}/\sqrt{\text{Hz}}$.

## 3 RADIATIONS RELATED TO EXTRA-HIGH VOLTAGE/ULTRA-HIGH VOLTAGE AC AND DC SUBSTATIONS

**Figure 2** shows the geographical projections of four daytime orbits with PLHR on the Earth's surface, where thin black lines represent the satellite orbits and the blue and orange segments are respectively the locations of common PLHR events containing at least three parallel spectral lines spaced by 50 Hz/100 Hz in the band of 1–5 kHz, and uncommon PLHR events newly detected. Lines in green show geomagnetic field lines across PLHR segments which obtained from the geomagnetic dipole model (Walt, 1994). Assume that PLHR propagates along the geomagnetic field in whistler mode, and the northern footprints of green geomagnetic field lines across the centres of orange PLHR segments are respectively close to the ±500 kV Yimin AC-to-DC substation in which the low AC voltage is converted to the high DC voltage before realizing high voltage DC transmission and the 500 kV AC-to-AC Shunyi substation in which the low AC voltage is converted to the high AC voltage

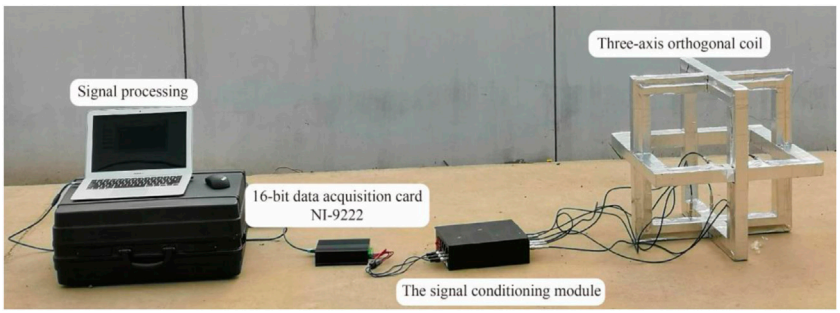


**FIGURE 1 |** The magnetic field measurement device.

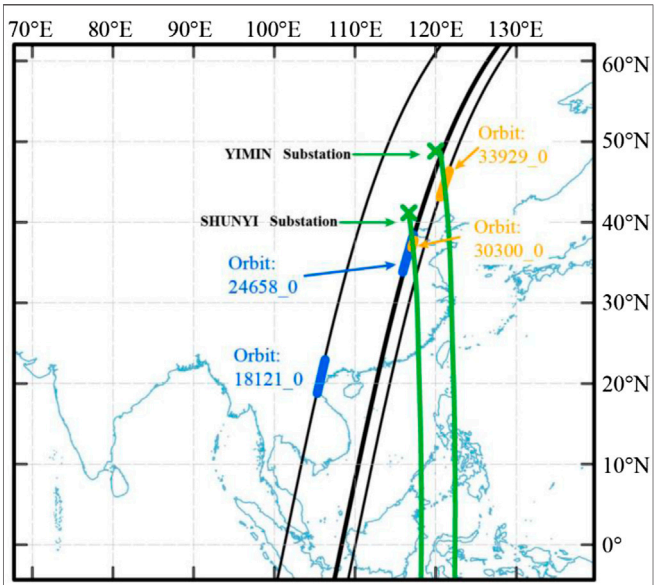


**FIGURE 2 |** Geographical projections of the satellite orbits with typical PLHR events.

before realizing high voltage AC transmission. The location of substation is marked by green cross.

## 3.1 Common PLHR Events

Until now, all reported PLHR events are in the band of 1–5 kHz and with the frequency spacings of 50/100 Hz or 60/120 Hz, which are called as common events. From the spectrogram along orbit 18,121_0 on 23 November 2007 in **Figure 3A**, there are some obvious spectral lines at 1,448/1548/1,648/1748/1848/1948/2048/2147/2,248/2347/2,447/2547/2,847/2,947 Hz with the peak intensity of 0.183 μV/m. Similarly, from the spectrogram along orbit 24,658_0 on 10 February 2009 in **Figure 3B**, some obvious spectral lines occur at 4,150/4250/4,350/4450/4,750/4,850/4,950 Hz with the peak intensity of 0.252 μV/m. The similar common PLHR events were often detected when DEMETER flew over China. Their dependence on the power consumption, season, and geomagnetic activity has been systematically studied in Wu et al. (2017).

## 3.2 Uncommon PLHR Events

### 3.2.1 Events Related to the 500 kV AC-To-AC Substation

**Figure 4A** shows the spectrogram of the electric field intensity along orbit 30,300_0 on 1 March 2010. Some obvious lines at 2,350/2,450 Hz, 4,151/4251/4,351/4,451 Hz, and 8,351/8452/8,551/8651/8,751/8,851 Hz are detected, which have far exceeded the frequency band of common PLHR events. Particularly, the harmonic spectral lines in the bands of (2,350–2,450) Hz, (4,150–4,450) Hz and (8,350–8,850) Hz are not simultaneously observed. The distances between their centres are approximately 9.97 km (0.08°) and 18.7 km (0.15°) at the satellite altitude. From **Figure 2**, these PLHRs seem to be related to the 500 kV Shunyi substation at (40.24°N, 116.74°E) with a capacity of (2 × 750 + 2 × 1,250) MVA. It is the load-centre substation in 500 kV Fengzhen-Wanquan-Shunyi power project. From **Figure 4B**, the smallest and greatest intensities of PLHR lines are 0.087 μV/m at 8,651 Hz and 0.228 μV/m at 4,251 Hz, which are 3.88 and 11.81 dB higher than the average background noise, respectively. Three days before PLHR occur, the maximum SYM-H index is only 18 nT and during its occurrence the SML and SMU index shown in **Figure 4C** have a very small disturbance. Cross-covariance analysis of PLHR between (4–4.5) kHz and (8–9) kHz was performed, and the correlation coefficient is less than 0.2, which indicate that the radiations in the two bands are more likely to be independent, and there are no wave-wave coupling between them (Němec et al., 2017).

The magnetic field around the Shunyi substation was measured in April 2020. **Figures 5A,B** shows the harmonic ratio at 50 m away from the substation and along the transmission line (280 m away from the substation). The greatest intensities of the harmonic radiations are respectively 0.68 nT in the band of (1,500–2,200) Hz, 0.93 nT in the band of (3,900–4,000) Hz and 0.23 nT in the band of (7,600–8,000) Hz. It is noted that the harmonic radiation frequencies in **Figures 4B**, **5A** are not exactly same. Their difference may be due to the big change of the substation structure from 2010 to 2020, the doppler frequency shift, or the nonlinear effect of ionosphere. Particularly, the radiations at several kHz are gradually attenuated according to **Figure 5C** and it is difficult to detect them at distances beyond 500 m from the substation. Therefore, the source of PLHR is inferred to be in the substation.

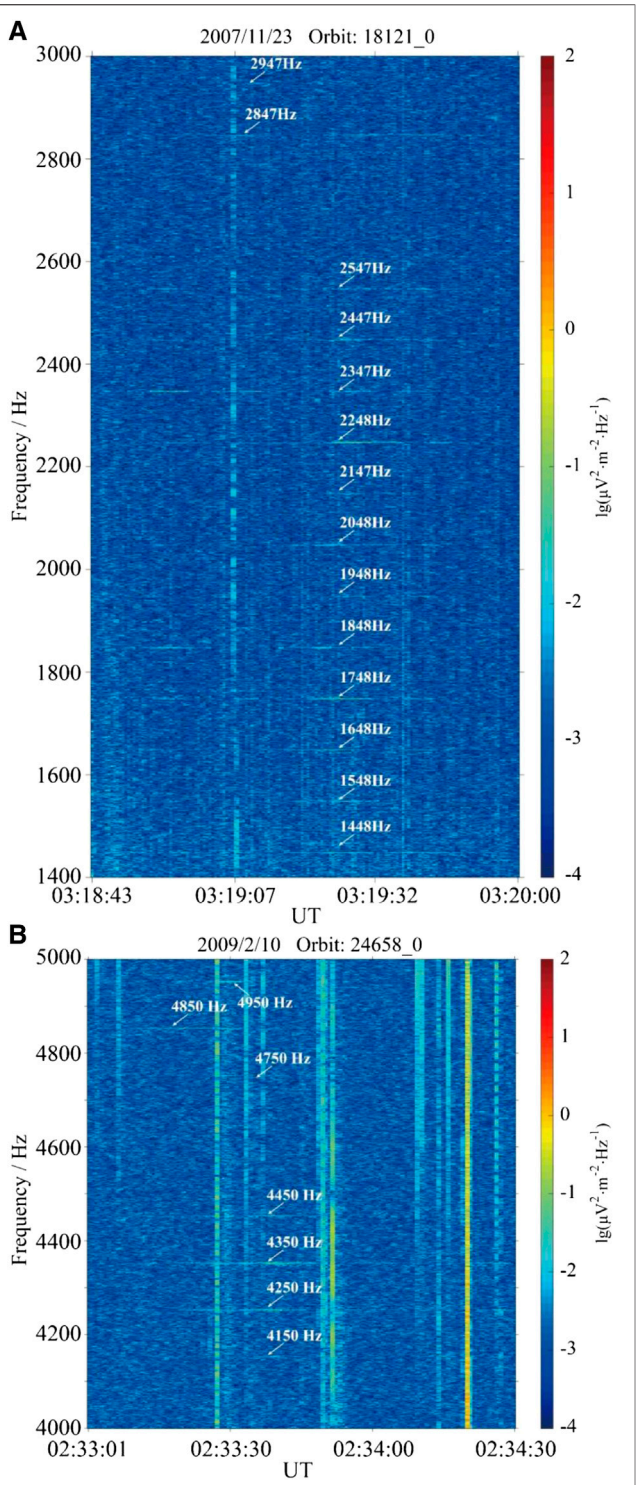


**FIGURE 3 |** Typical PLHR occurrences over an AC-to-AC substation **(A)** and an AC-to-DC substation **(B)**.

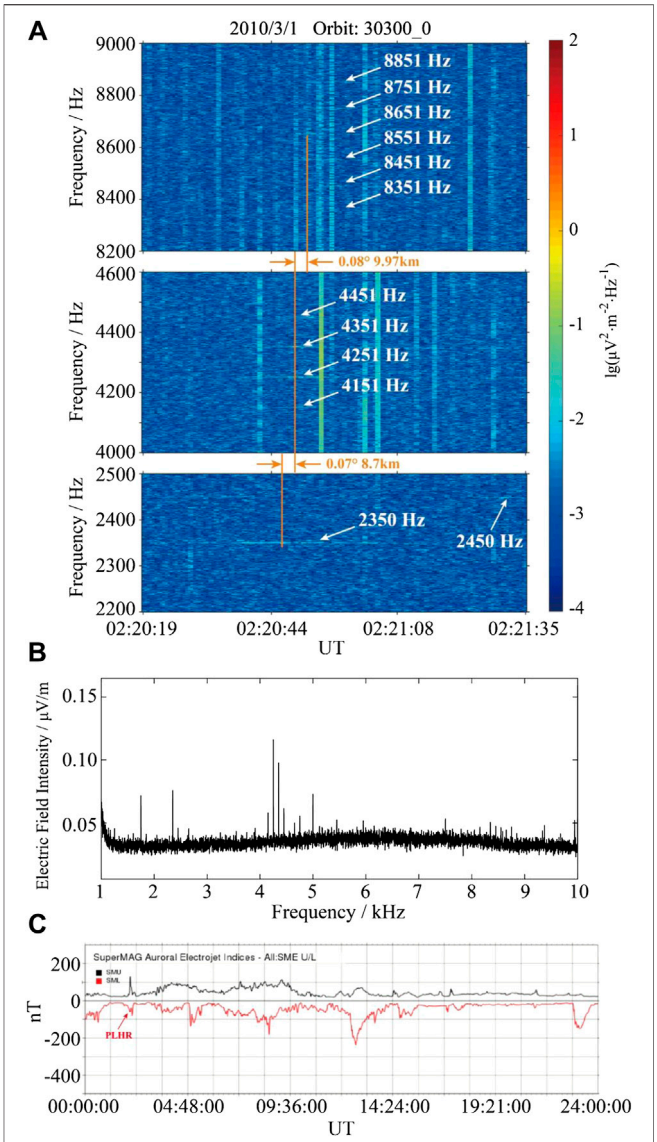


**FIGURE 4 |** Uncommon PLHR occurrences over the 500 kV Shunyi AC-to-AC substation. **(A)** Time-frequency spectrogram of the electric field intensity along orbit 30,300_0. **(B)** Amplitude-frequency characteristics of the electric field intensity. **(C)** Fluctuation of the geomagnetic indices SMU/SML.

### 3.2.1 Events Related to the ±500 kV AC-To-DC Substation

The ±500 kV Hulunbeier-Liaoning power project was the first EHV DC interregional interconnection project in the northeast power grid of China. The ±500 kV Yimin substation with the capacity of (1,000 + 2×600) MVA located at (48.65°N, 119.79°E) is the starting point of the project and is approximately 5 km away from the Yimin power plant. There has been no PLHR detected until this substation was put into operation on 28 September 2010. **Figure 6A** shows the time-frequency spectrogram of the electric field intensity along orbit 33,929_0 on 3 November 2010. During 02:03:02–02:04:00 universal time (UT), in the band of (2.3–4.5) kHz, besides those common radiations at frequencies 2,350 Hz, 2,401 Hz, 2,449 Hz and 2,551 Hz with the interval of ≈50 Hz and frequencies 2,851 Hz and 2,949 Hz with the interval of ≈100 Hz, there are some particular radiations at frequencies

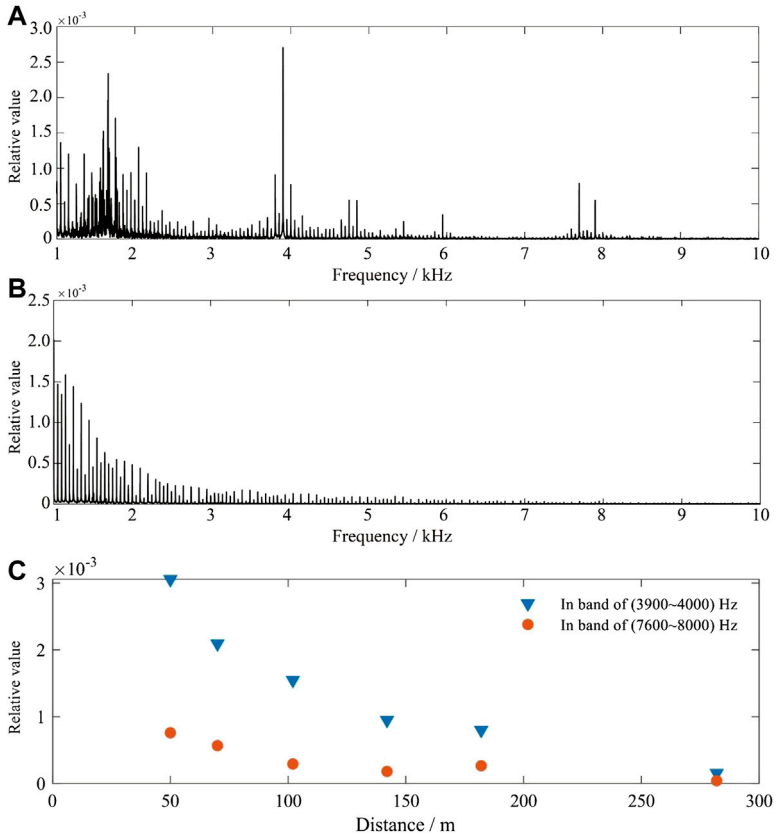


**FIGURE 5 |** Measurement results of the magnetic field near the Shunyi AC-to-AC substation. Normalized values of the magnetic field density at 50 m **(A)** and 280 m **(B)** away from the substation. Panel **(C)** show variations of the maximum magnetic field density in bands of 3,900–4,000 Hz and 7,600–8,000 Hz with distance away from the substation.

2,551 Hz, 2,701 Hz and 2,851 Hz with the interval of ≈150 Hz and at frequencies 3,549/3,649 Hz and 4,149/4,249 Hz with the interval of ≈600 Hz. From the amplitude-frequency characteristic in **Figure 6B**, the smallest and greatest intensities of PLHR are 0.62 μV/m at 2,851 Hz and 1.39 μV/m at 3,549 Hz, and they are 11.42 and 27.30 dB higher than the average background noise, respectively.

Three days before PLHR occur, the maximum SYM-H index is only 16 nT, but in **Figure 6C** during its occurrence the SML index decreases rapidly by more than 100 nT and the SMU index is larger than 30 nT. The geomagnetic disturbance became a little stronger than that in **Figure 4C**, which can promote the generation of the geomagnetic-induced currents (GICs). GICs can make the converting transformers DC-biased and result in harmonic voltage at frequencies $f = 3f_N$ where $f_N$ is the nominal frequency, so it is speculated that GICs may be the origin of radiations spaced by 150 Hz. Additionally, due to the characteristic harmonic frequencies of the 12-pulse AC/DC converter are $f = f_N \times (12n \pm 1)$Hz, it is natural to associate the origin of the radiations at 3,549/3,649 Hz and 4,149/4,249 Hz with the harmonics of the converter at $n = 6$ and $n = 7$.

The event shown in **Figure 6** is a good example to illustrate the dependence of PLHR on the harmonic source in the power grid and its propagation characteristics in the ionosphere can be studied by a quasi-linear model. Compared with results in (Yearby and Smith, 1994; Manninen, 2005), this event shows that the radiations of converters do not have to be left-handed polarised, or their polarization direction will be changed during the propagation into the near-Earth space.

## 4 PROPAGATION CHARACTERISTICS OF PLHR

The ionosphere is a coupling system between the atmosphere and magnetosphere, so DEMETER can capture the energetic particles precipitated from the radiation belt. During the propagation of PLHR wave along the geomagnetic field line, it can interact resonantly with the charged particles in cyclotron motion along the geomagnetic field line in which the wave intensity will be amplified by energy exchange between PLHR waves and energetic electrons (Bruce and Gurbax, 1997). Due to the complexity of the space environment and the limitation of satellite-based observation technology, now it is quite difficult to solve rigorously and scientifically the propagation mechanism of PLHR and their effects. This section attempts to explain some characteristics of PLHR through a simple linear model.

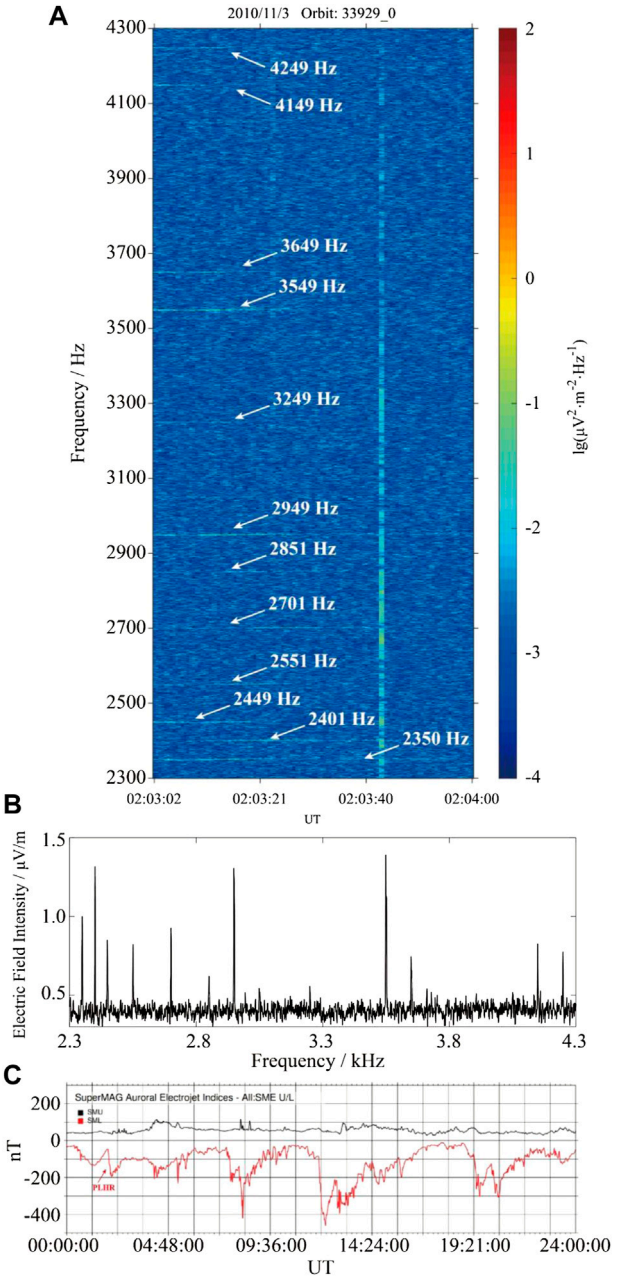


**FIGURE 6 |** Uncommon PLHR occurrences over the ±500 kV Yimin AC-to-DC substation. **(A)** Time-frequency spectrogram of the electric field intensity along orbit 33,929_0. **(B)** Amplitude-frequency characteristics of the electric field intensity. **(C)** Fluctuation of the geomagnetic indices SMU/SML.

Considering that the dimensions of the substation on the Earth's surface are far less than the Earth's radius, a horizontal stratified model is established in **Figure 7** to study the propagation characteristics of PLHR. The first layer ($z \le z_1$) is the Earth with conductivity $\sigma_1$ and relative permittivity $\varepsilon_{r1}$, and the second and third layers are in the neutral atmosphere ($z_1 < z \le z_3$) with conductivity $\sigma_2 = \sigma_3 = 0$ and relative permittivity $\varepsilon_{r2} = \varepsilon_{r3} = 1$. The ionosphere ($z > z_3$) is assumed to be a uniformly stratified, anisotropic, lossless and collisionless plasma for simplicity, and the relative permittivity tensor $\boldsymbol{K}_n$ of the $n$th layer ($3 < n \le N$) can be expressed as (Fedorov et al., 2016):

$$\boldsymbol{K}_n = \begin{bmatrix} 1 - \sum_j \frac{\omega_{n\_pj}^2}{\omega^2 - \omega_{n\_cj}^2} & -\mathrm{j}\sum_j \frac{\omega_{n\_cj}\omega_{n\_pj}^2}{\omega(\omega^2 - \omega_{n\_cj}^2)} & 0 \\ \mathrm{j}\sum_j \frac{\omega_{n\_cj}\omega_{n\_pj}^2}{\omega(\omega^2 - \omega_{n\_cj}^2)} & 1 - \sum_j \frac{\omega_{n\_pj}^2}{\omega^2 - \omega_{n\_cj}^2} & 0 \\ 0 & 0 & 1 - \sum_j \frac{\omega_{n\_pj}^2}{\omega^2} \end{bmatrix}$$

where $j$ is the imaginary unit; $\omega$ is the angular frequency; the subscript $n$ represents the $nth$ layer; $\omega_{n\_pj}$ and $\omega_{n\_cj}$ are the plasma frequency and the cyclotron frequency of the $j$-type particle whose density can be extracted from IRI2016 and NRLMSISE-00 models; $\boldsymbol{B}_0$ is the local geomagnetic induction intensity and has an angle of $\theta_0$ with respect to the $z$-axis which can be extracted from the IGRF model,. The harmonic radiation source located at the interface $z = z_2$ in the neutral atmosphere is equivalent to a horizontal dipole $\boldsymbol{P} = I_f l e^{\mathrm{j}2\pi f t}\boldsymbol{e}_x$ in the $x$-direction where $l$ is the current loop length and $I_f$ is the current magnitude derived from the magnetic field density $B_f$ at harmonic frequency $f$ measured on the ground (Ward and Hohmann, 1987):

$$I_f = \frac{5c^3 \times B_f}{240\pi^2 l f^2 \left(z_2 + \frac{1}{\sqrt{2\pi f \mu_0 \sigma_1}}\right)} \quad (1)$$

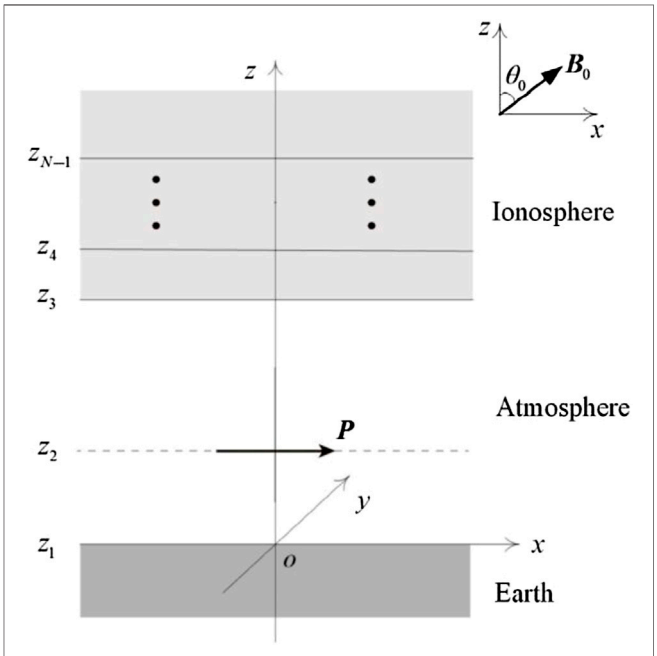


**FIGURE 7 |** Propagation model of waves radiated from a dipole above the ground.

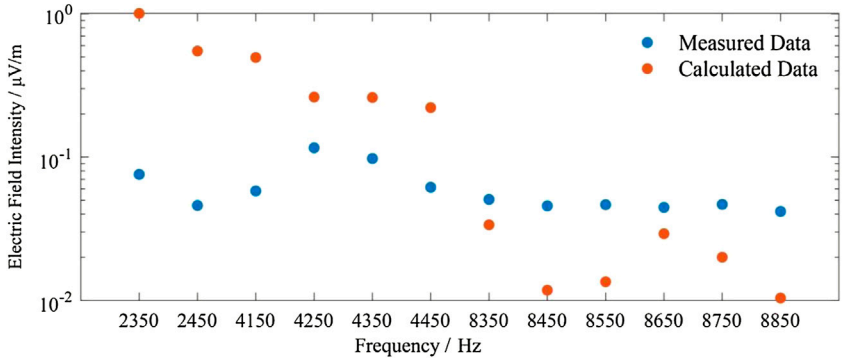


**FIGURE 8 |** Comparison of the electric field intensity observed by DEMETER and calculated by FWM.

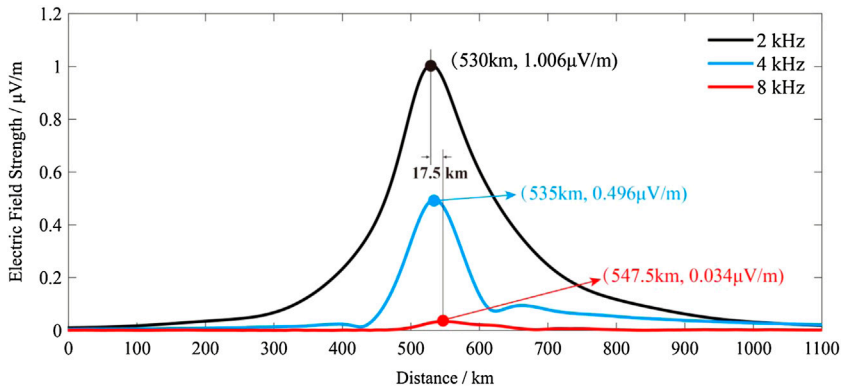


**FIGURE 9 |** Variation in the electric field intensity at the satellite altitude calculated by the FWM.

where $c$ is the light speed in the vacuum and $\mu_0$ is the vacuum permeability.

Assuming $\sigma_1 = 5 \times 10^{-3}$S/m, $\varepsilon_{r1} = 9$, $z_2 = 5$m, $z_3 = 60$km, $l = 3$km and $N = 52$, $B_0 = 5 \times 10^{-5}$T, $\theta_0 = 40^\circ$ and $B_f$ takes the values in **Figures 5C**, **8**, compares the peak values of electric field intensity at the height of 660 km observed by DEMETER and calculated by the full-wave theory method (FWM). It seems that the observed values do not attenuate much with increasing frequency, while the calculated values have a decreasing tendency. The calculated values are larger than the observed values at 2,350/2450/4,150/4250/4,350/4450 Hz but smaller than the observed values at the band of 8,350–8,850 Hz. The difference between them may result from the complicated gyro-resonance effects between the harmonic radiation wave and the energetic electron which cannot be described by FWM. **Figure 9** shows the variation of the electric field intensity along the $x$-direction at the satellite altitude calculated by the FWM in which the peak intensities at lower frequencies occur earlier and the distance between the peak intensities at 2 and 8 kHz is 17.5 km. From the observation result in **Figure 4A**, the distances between the strongest harmonic spectral lines in the bands of (2,350–2,450) Hz, (4,150–4,450) Hz and (8,350–8,850) Hz are approximately 8.7 and 9.97 km, totally 18.67 km, in agreement with the calculated distance 17.5 km.

In addition, if the electromagnetic wave in the range of (2–9) kHz generated by the Shunyi substation at 40.24°N is supposed to be guided by the geomagnetic field and propagate into the space plasma, then the wave is located at approximately 35.9°N when it reaches the altitude 660 km. The horizontal distance between Shunyi substation and PLHR segment is 515 km and their latitude derivation is 4.2° in **Figure 2**, which is in agreement with the horizontal distance 530–547.5 km and the latitude derivation 4.3°–4.5° between the dipole source and the peak electric field intensity in **Figure 9**.

## 5 DISCUSSION AND CONCLUSION

This paper discussed the electromagnetic environment issue due to power projects from the perspective of near-Earth space. Based on the observation data of DEMETER, many uncommon PLHR events have been detected after some EHV/UHV substations put into the Chinese power grid. Compared with those common events in the band of 1–5 kHz and spaced by 50/100 Hz, the frequency band of newly identified events is extended to approximately 8,850 Hz and spaced by 50/100/150/600 Hz, which further demonstrated PLHR is closely related to the local power grid.

Since PLHR was identified (Helliwell et al., 1975), its source has been focused on the power lines. However, the measurements on the ground show the harmonic radiation around the EHV/UHV substation is stronger than that around the power line, and it contains more abundant harmonic components. Although the frequencies of the harmonic radiation components observed by satellite in 2010 and measured around the substations in 2020 are not exactly identical, they are similar. As an important part of power grid, the substation contains not only high-voltage systems composed of buses, transformers, breakers, inductors, and grounding electrodes to implement power collection, distribution, and transformation but also weak electronic systems to implement the functions of protection, control, and communication. They are easier to generate steady-state radiations due to three-phase unbalanced current, GIC and corona current and transient radiations due to lightning strikes, faults, and switch operations. Under the excitation of specific source, the substation is more likely to act as an artificial transmitter than the power line, generate high-order harmonic radiation and transmit them to the near-Earth space. Compared with the AC-to-AC substations, the AC-to-DC substations have an extra 12-pulse converter, and their harmonic radiation is more diverse and stronger, which have been verified by our satellite-based PLHR events. However, the harmonic current along the long-distance power line will be affected by the distribution parameters and has an attenuation tendency, and their radiation can also be weakened by the demagnetization of overhead ground wire. The EHV/UHV substation is more likely to be a source of PLHR.

To date, a common consensus is that PLHR will become more and more severe, and its triggered emissions increase the background VLF noise level in the near-Earth space. These additional noise makes the experiment design for magnetospheric study more complicated, degrades VLF communication links, and interferes with ground-based experiments. With the development of modern power grid, its effects on the ionospheric state which is closely related to human activities, such as radio communication, broadcasting, radio navigation, radar positioning and so on, should arouse attention and be evaluated seriously. Our work has only promoted the solution of the corresponding source of PLHR on the ground. How the radiation in the substation is generated still needs to be systematically demonstrated in future. Moreover, the propagation characteristics of PLHR between the hemispheres, and its impacts on the dynamics of energetic electrons in the Earth's radiation belt also need the support of a large amount of satellite-based observation events and thoroughly theoretical analysis.

## DATA AVAILABILITY STATEMENT

The raw data supporting the conclusions of this article will be made available by the authors, without undue reservation.

## AUTHOR CONTRIBUTIONS

JW led the study, supervised the project development and contributed significantly to explain the results. JZ contributed to the satellite-based and ground-based data analysis. JW, JZ and LX contributed to the measurements on the ground and the original draft. All authors approved the final manuscript.

## FUNDING

The study was supported by the National Natural Science Foundation of China under Grant 51,777,006. Beijing Natural Science Foundation under Grant 8222063.

## REFERENCES

Bell, T. F., Luette, J. P., and Inan, U. S. (1982). ISEE 1 Observations of VLF Line Radiation in the Earth's Magnetosphere. *J. Geophys. Res.* 87 (A5), 3530–3536. doi:10.1029/JA087iA05p03530

Bullough, K., Tatnall, A. R. L., and Denby, M. (1976). Man-made e.l.f./v.l.f. emissions and the radiation belts. *Nature* 260 (5550), 401–403. doi:10.1038/260401a0

Dudkin, F., Korepanov, V., Dudkin, D., Pilipenko, V., Pronenko, V., and Klimov, S. (2015). Electric Field of the Power Terrestrial Sources Observed by Microsatellite Chibis-M in the Earth's Ionosphere in Frequency Range 1-60 Hz. *Geophys. Res. Lett.* 42 (14), 5686–5693. doi:10.1002/2015GL064595

Fedorov, E., Mazur, N., Pilipenko, V., and Baddeley, L. (2016). Modeling the High-Latitude Ground Response to the Excitation of the Ionospheric MHD Modes by Atmospheric Electric Discharge. *J. Geophys. Res. Space Phys.* 121 (11), 11282–11301. doi:10.1002/2016JA023354

Helliwell, R. A., Katsufrakis, J. P., Bell, T. F., and Raghuram, R. (1975). VLF Line Radiation in the Earth's Magnetosphere and its Association with Power System Radiation. *J. Geophys. Res.* 80 (31), 4249–4258. doi:10.1029/JA080i031p04249

Kikuchi, H. (1983). Power Line Transmission and Radiation. *Space Sci. Rev.* 35 (1), 59–80. doi:10.1007/bf00173693

Li, X. L., Wu, J., Jin, H. B., and Li, Y. M. (2021). Development of Low-Frequency Three-Dimensional Magnetic Field Measurement System. *J. Astronaut. Metrol. Meas.* 41 (1), 33–39. doi:10.1109/TMI.2008.2007361

Luette, J. P., Park, C. G., and Helliwell, R. A. (1979). The Control of the Magnetosphere by Power Line Radiation. *J. Geophys. Res.* 84 (A6), 2657–2660. doi:10.1029/JA084iA06p02657

Manninen, J. (2005). Some Aspects of ELF-VLF Emissions in Geophysical Research. Oulu: University of Oulu. [dissertation].

Němec, F., Čížek, K., Parrot, M., Santolík, O., and Záhlava, J. (2017). Line Radiation Events Induced by Very Low Frequency Transmitters Observed by the DEMETER Spacecraft. *J. Geophys. Res. Space Phys.* 122, 7226–7239. doi:10.1002/2017JA024007

Němec, F., Santolík, O., Parrot, M., and Berthelier, J. J. (2007). Power Line Harmonic Radiation: A Systematic Study Using DEMETER Spacecraft. *Adv. Space Res.* 40 (3), 398–403. doi:10.1016/j.asr.2007.01.074

Park, C. G., and Chang, D. C. D. (1978). Transmitter Simulation of Power Line Radiation Effects in the Magnetosphere. *Geophys. Res. Lett.* 5 (10), 861–864. doi:10.1029/gl005i010p00861

Park, C. G., Helliwell, R. A., and Lefeuvre, F. (1983). Ground Observations of Power Line Radiation Coupled to the Ionosphere and Magnetosphere. *Space Sci. Rev.* 35 (2), 131–137. doi:10.1007/978-94-009-7063-2_11

Park, C. G., and Helliwell, R. A. (1978). Magnetospheric Effects of Power Line Radiation. *Science* 200 (4343), 727–730. doi:10.1126/science.200.4343.727

Park, C. G., and Helliwell, R. A. (1981). Power Line Radiation in the Magnetosphere. *Adv. Space Res.* 1 (2), 423–437. doi:10.1016/0273-1177(81)90317-3

Park, C. G., and Miller, T. R. (1979). Sunday Decreases in Magnetospheric VLF Wave Activity. *J. Geophys. Res.* 84 (A3), 943–950. doi:10.1029/JA084iA03p00943

Parrot, M. (1994). Observations of Power Line Harmonic Radiation by the Low-Altitude AUREOL 3 Satellite. *J. Geophys. Res.* 99 (A3), 3961–3969. doi:10.1029/93JA02544

Parrot, M., and Zaslavski, Y. (1996). Physical Mechanisms of Man-Made Influences on the Magnetosphere. *Surv. Geophys.* 17 (1), 67–100. doi:10.1007/BF01904475

Pilipenko, V., Fedorov, E., Mazur, N., and Klimov, S. (2021). Electromagnetic Pollution of Near-Earth Space by Power Line Emission. *Solar-Terrestrial Phys.* 7 (3), 105–113. doi:10.12737/stp-73202107

Rodger, C. J., Thomson, N. R., and Dowden, R. L. (1995). VLF Line Radiation Observed by Satellite. *J. Geophys. Res.* 100 (A4), 5681–5689. doi:10.1029/94JA02865

Tomizawa, I., and Yoshino, T. (1985). Power Line Radiation Observed by the Satellite "OHZORA". *J. Geomagn. geoelec* 37 (3), 309–327. doi:10.5636/jgg.37.309

Tsurutani, B. T., and Lakhina, G. S. (1997). Some Basic Concepts of Wave-Particle Interactions in Collisionless Plasmas. *Rev. Geophys.* 35 (4), 491–501. doi:10.1029/97RG02200

Walt, M. (1994). *Introduction to Geomagnetically Trapped Radiation*. Cambridge: Cambridge University Press.

Ward, S. H., and Hohmann, G. W. (1987). *Electromagnetic Methods in Applied Geophysics*. Tulsa: Society of Exploration Geophysicists.

Wu, J., Guo, Q., Yue, C., Xie, L., and Zhang, C. (2020). Special Electromagnetic Interference in the Ionosphere Directly Correlated with Power System. *IEEE Trans. Electromagn. Compat.* 62 (3), 947–954. doi:10.1109/TEMC.2019.2918280

Wu, J., Zhang, C., Zeng, L., and Ma, Q. (2017). Systematic Investigation of Power Line Harmonic Radiation in near-Earth Space above China Based on Observed Satellite Data. *J. Geophys. Res. Space Phys.* 122 (3), 3448–3458. doi:10.1002/2016JA023131

Yearby, K. H., Smith, A. J., Kaiser, T. R., and Bullough, K. (1983). Power Line Harmonic Radiation in Newfoundland. *J. Atmos. Terr. Phys.* 45 (6), 409–419. doi:10.1016/S0021-9169(83)81100-3

Yearby, K. H., and Smith, A. J. (1994). The Polarisation of Whistlers Received on the Ground Near L = 4. *J. Atmos. Terr. Phys.* 56 (11), 1499–1512. doi:10.1016/0021-9169(94)90117-1

**Conflict of Interest:** The authors declare that the research was conducted in the absence of any commercial or financial relationships that could be construed as a potential conflict of interest.

**Publisher's Note:** All claims expressed in this article are solely those of the authors and do not necessarily represent those of their affiliated organizations, or those of the publisher, the editors and the reviewers. Any product that may be evaluated in this article, or claim that may be made by its manufacturer, is not guaranteed or endorsed by the publisher.

frontiers | Frontiers in Earth Science

ORIGINAL RESEARCH
published: 23 May 2022
doi: 10.3389/feart.2022.850078

# The Conjugated Ionospheric Anomalies Preceding the 2011 Tohoku-Oki Earthquake

*Liming He*[1]*, *Lixin Wu*[2], *Kosuke Heki*[3] and *Cong Guo*[1]

[1]Department of Geodesy and Geomatics, School of Resources and Civil Engineering, Northeastern University, Shenyang, China, [2]School of Geosciences and Info-Physics, Central South University, Changsha, China, [3]Department of Earth and Planetary Sciences, Hokkaido University, Sapporo, Japan

We present the conjugated ionospheric total electron content (TEC) anomalies prior to the 2011 $M_w$9.0 Tohoku-oki earthquake, Japan, observed by the Global Navigation Satellite System (GNSS) stations in northern Australia. The onset time of the anomaly, determined by the Akaike's information criterion, is 41.5 min before the earthquake in Australia, which is very close to the time observed in Japan. The positive TEC anomalies in Australia emerged on the same longitude as the land area of NE Japan. This supports the model that electric fields within the ionosphere redistributed the electrons immediately before large earthquakes. However, the observed anomaly is shifted equatorward by ~500 km reflecting the difference in physical mechanisms between the two hemispheres. We also found that the geomagnetic declination near the conjugate point simultaneously started to change ~40 min before the earthquake, but its physical implication is yet to be explored.

**Keywords: large earthquake, ionospheric anomaly, total electron content, GNSS, conjugate observation**

OPEN ACCESS

***Edited by:***
*Chao Xiong,*
*Wuhan University, China*

***Reviewed by:***
*Zeren Zhima,*
*Ministry of Emergency Management (China), China*
*Fuqing Huang,*
*University of Science and Technology of China, China*

***Correspondence:**
*Liming He*
*heliming@mail.neu.edu.cn*

***Specialty section:***
*This article was submitted to Geohazards and Georisks, a section of the journal Frontiers in Earth Science*

***Received:*** *07 January 2022*
***Accepted:*** *27 April 2022*
***Published:*** *23 May 2022*

***Citation:***
*He L, Wu L, Heki K and Guo C (2022) The Conjugated Ionospheric Anomalies Preceding the 2011 Tohoku-Oki Earthquake. Front. Earth Sci. 10:850078. doi: 10.3389/feart.2022.850078*

## INTRODUCTION

On 11 March 2011, the Tohoku-oki earthquake with a moment magnitude ($M_w$) 9.0 occurred at the Japan Trench off Northeastern (NE) Japan at 05:46:23 UT. Heki (2011) reported anomalies in ionospheric total electron content (TEC) started ~40 min before the earthquake above NE Japan, using the dense Japanese network of ground Global Navigation Satellite System (GNSS) receivers, GEONET (GNSS Earth Observation Network). Subsequent studies confirmed that similar ionospheric changes were observed immediately before most earthquakes with $M_w \geq 8.2$ where a reasonable number of GNSS stations are available (Heki and Enomoto, 2015). He and Heki (2017) further studied 32 earthquakes with $M_w$7.0–8.0 in this century and found that the 1/4 earthquakes showed possible preseismic changes starting 20–10 min before earthquakes. Statistical analyses of the 18 earthquakes ($M_w$7.3–9.2) indicated that leading times, areal extents, and intensities of ionospheric anomalies (relative to background TEC) have a positive correlation with the earthquake magnitude ($M_w$). A detailed summary of the debates between opponents (Kamogawa and Kakinami, 2013; Utada and Shimizu, 2014; Masci et al., 2015) and our rebuttals (Heki and Enomoto, 2013; 2014; 2015) can be found in the introduction of He and Heki (2017).

He and Heki (2016), He and Heki (2018), and Muafiry and Heki (2020) discussed the three-dimensional (3D) distribution of the positive and negative electron density anomalies responsible for the observed TEC changes. They found that the positive and negative anomalies roughly align along the local geomagnetic field, which suggests that the electric field within the ionosphere may be responsible for the redistribution of the ionospheric electrons (Kuo et al., 2014; Kelley et al., 2017).

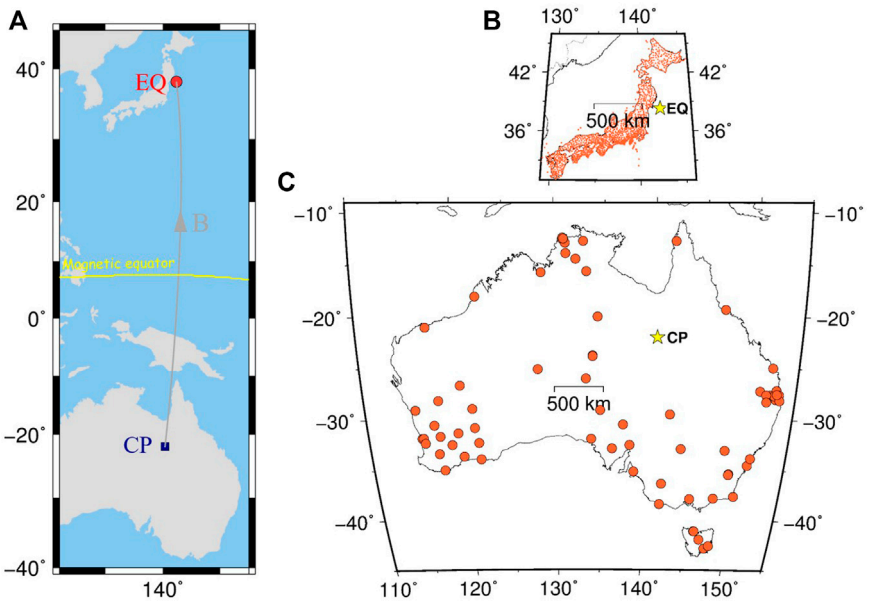


**FIGURE 1 | (A)** The magnetic conjugate point (CP, blue square) of the epicenter (EQ, red circle) of the 2011 Tohoku-oki earthquake, Japan, lies in northern Australia (the gray curve indicates the ground projection of the geomagnetic field connecting the two points). The yellow curve denotes the magnetic equator. GNSS stations in Japan **(B)** and in Australia **(C)** were drawn using the Hammer equal-area projection. In **(B)** and **(C)**, the red circles represent GNSS stations and the yellow stars show the epicenter **(B)** and its CP **(C)**.

Ionospheric phenomena associated with electric fields within the ionosphere are known to appear simultaneously at two points connected by geomagnetic fields (i.e., conjugated points, CP). Otsuka *et al.* (2004) and Shiokawa *et al.* (2005) showed simultaneous emergence of Medium-Scale Traveling Ionospheric Disturbances (MSTID) in Japan and Australia. They also showed that high geomagnetic activities enhance Large-Scale Traveling Ionospheric Disturbances (LSTID) in both hemispheres. However, an individual LSTID within one hemisphere didn't show the synchronously conjugated phenomenon. This supports our understanding that electric fields play important roles in generating MSTIDs, but LSTIDs are excited mechanically as internal gravity waves.

If preseismic ionospheric electron redistributions are due to electric fields, similar ionospheric TEC anomalies would emerge concurrently in the other hemispheres around the CP of the epicenter. We track the location of CP at an altitude of 85 km right over the epicenter of the 2011 Tohoku-oki earthquake using the IGRF-11 model. Here we investigate the behaviors of VTEC around the conjugate region of the epicenter before and after the earthquake occurrence using GNSS stations in Australia.

## GNSS DATA AND METHODS

### TEC Changes in Australia on 11 March 2011

To investigate the ionospheric TEC variations in Australia associated with the 2011 Tohoku-Oki earthquake, we used raw data from 76 continuously operating GNSS stations in Australia (**Figure 1**). We first converted slant TEC (STEC) to vertical TEC (VTEC) following He and Heki (2016), by removing the inter-frequency biases of the satellite and receiver, and by multiplying with the cosine of the incident angle of the ray path into a thin shell at 300 km above the ground.

VTEC time series are modeled using polynomial excluding a specific time window possibly influenced by disturbances due to the earthquake. This exclusion window and the polynomial degree should be selected objectively and carefully to isolate the earthquake-related signals. To determine the start of the exclusion window, we followed Heki and Enomoto (2015) to identify the significant bends in VTEC time series before the earthquake using the Akaike's information criterion (AIC). This will be discussed further in *Definition of Reference Curves and Onset Times of the Preseismic Anomaly*. Because we do not have to consider postseismic TEC drops caused by acoustic disturbances associated with coseismic vertical crustal movements (Shinagawa et al., 2013), we fixed the ending time of the excluding window to 20 min after the earthquake.

We utilized the L-curve method to select the optimal polynomial degrees of the reference curves for individual GNSS satellites, following He and Heki (2017). This will be explained in detail in the next section. We define the positive and negative departures from the models as VTEC anomalies. **Figure 2** presents VTEC time series observed using Global Positioning System (GPS) PRN05, 09, and 25 in the southern hemisphere and PRN15 in the northern hemisphere over a 3.5-h interval including the 2011 Tohoku-oki earthquake. Positive anomalies of VTEC (**Figures 2A–1**) start ~40 min before the mainshock around the region to the north of CP in the same way as those observed in Japan (**Figures 2B–1**).

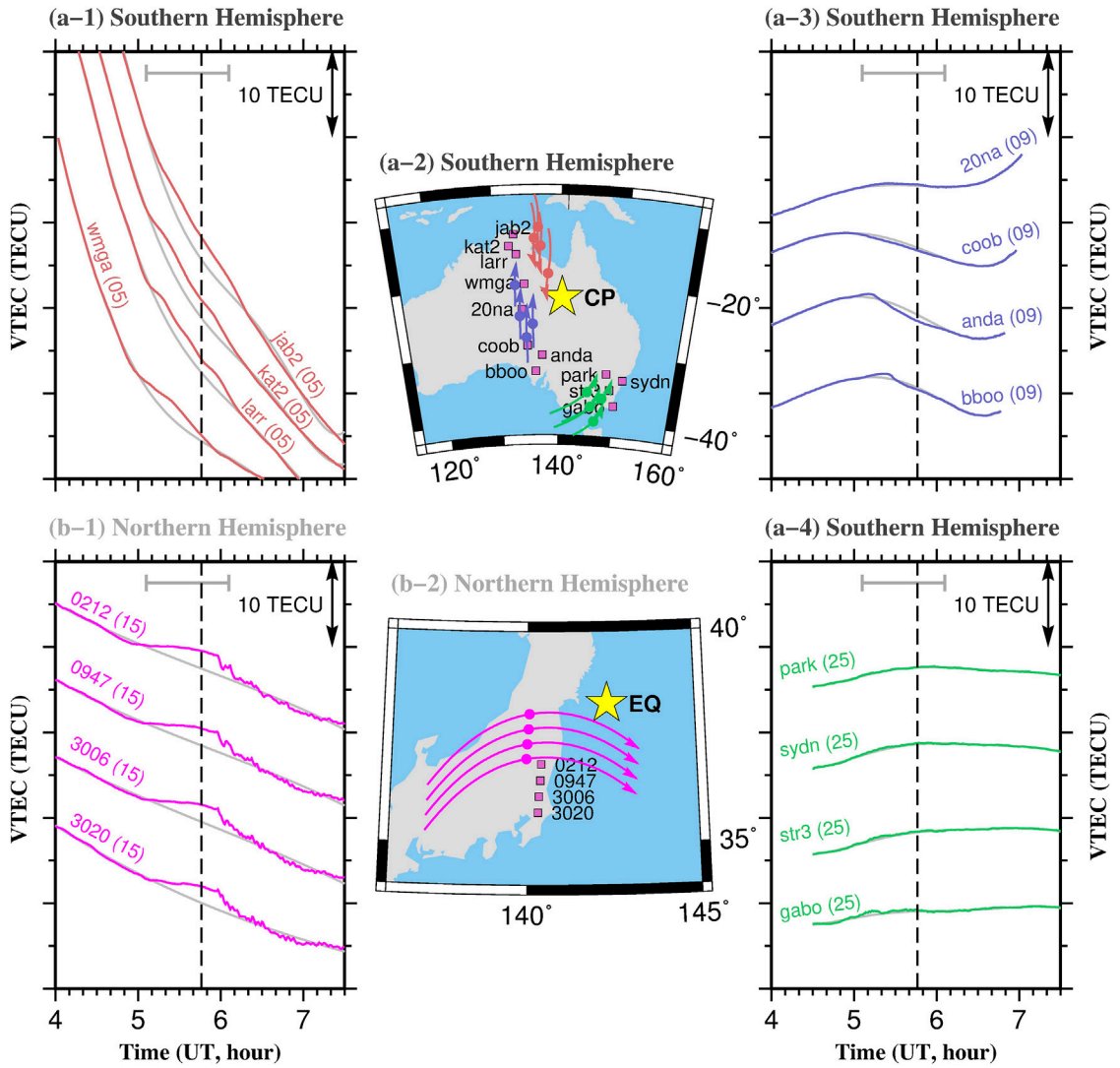


**FIGURE 2 |** VTEC time series observed using four satellite-station pairs on 11 March 2011 in Australia showing preseismic ionospheric enhancements **(A-1)** around CP, and no significant changes **(A-3, A-4)**. We also show four VTEC time series (b-1) observed in Japan showing preseismic enhancements, which is the VTEC version of **Figure 2** in Heki (2011). The vertical dashed lines show the occurrence of the 2011 Tohoku-oki earthquake. The gray horizontal bars represent the exclusion windows in defining the reference curves. The two maps in the middle panel show the locations of GNSS stations (pink squares) and sub-ionospheric point (SIP) trajectories in Australia **(A-2)** and in Japan **(B-2)**. The circles on the tracks indicate the SIP positions at the earthquake occurrence time. The yellow stars show the epicenter **(B-2)** and it is CP **(A-2)**. We assume the ionospheric height at 350 km to draw the SIP trajectories.

The Japanese data show coseismic ionospheric disturbances ~8 min after the mainshock caused by the acoustic waves excited by the vertical crustal movements (e.g. Astafyeva et al., 2011). Such disturbances are absent in the Australian data. To demonstrate the localized emergence of the anomalies, we show four VTEC time series observed at stations in central Australia (**Figures 2A–3**), and in southeast Australia far from CP (**Figures 2A–4**). Although we set up the same excluding window in defining the reference curves, these TEC time series smoothly connect before and after the earthquake without significant anomalies. Two curves in **Figures 2A–3** (anda, bboo) show an insignificant TEC decrease just before the earthquake, but its relevance to the earthquake is unclear.

## Definition of reference curves and onset times of the preseismic anomaly

As He and Heki (2017) discussed, optimal and objective selection of the exclusion window and the polynomial degree is vital to isolate VTEC changes related to earthquakes. VTEC changes with PRN05 have large negative slopes coming from a steep north-south gradient of VTEC (**Figures 2A–1**). We removed constant trends from the curves to make it easier to see the starts of the positive TEC anomalies (**Figure 3**). We show results of the L-curve tests for two of the time series to select the most appropriate degree of polynomials (5 in this case). More examples are shown in **Supplementary Figure S1**.

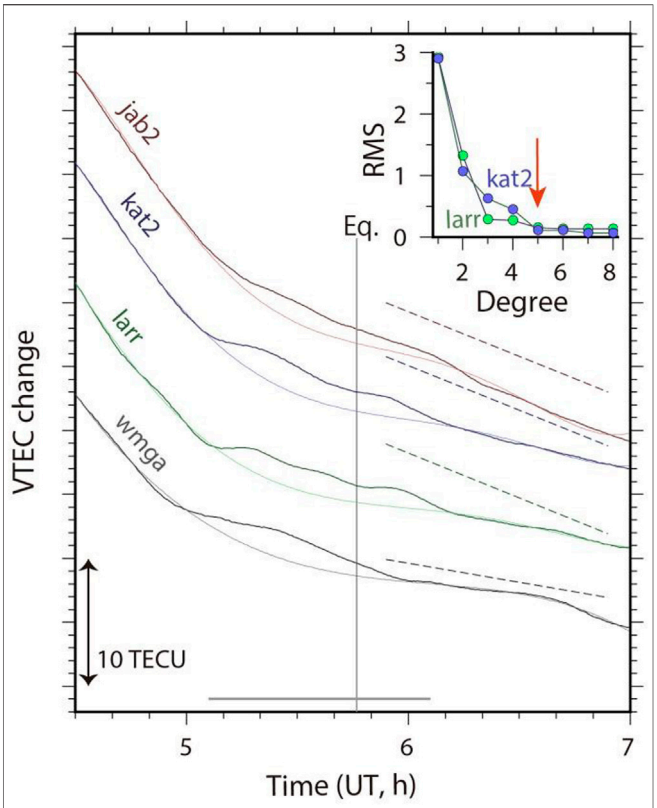


**FIGURE 3 |** The same VTEC time series as **Figures 2A–1**, but constant trends (attached to each curve as a dashed line) are removed from individual time series for visual clarity of the positive anomalies. The exclusion window is given at the bottom as a horizontal gray line. From the inset showing the behavior of RMS of post-fit residuals (calculated outside the exclusion window) for different polynomial degrees, we considered degree five the most appropriate.

To precisely compare the onset times of ionospheric anomalies in the two hemispheres, we pinpoint the occurrences of the positive breaks in three TEC time series using AIC following Heki and Enomoto (2015). We found significant breaks occurred 42.0 min before the earthquake time in Japan (**Figure 4A**) and 41.5 min before the earthquake time in Australia (**Figure 4B**), respectively. The coincidence suggests that the anomalies started in both hemispheres without significant delays. On the other hand, the amounts of the VTEC rate changes in the two hemispheres were different, i.e. more significant in Australia (**Figure 4C**). We think the difference partly reflects the more considerable background VTEC (~45 TECU) in Australia than in Japan (~30 TECU) (**Figure 4D**).

## TEC ANOMALIES AND LSTID

LSTIDs are often observed with GNSS-TEC under active geomagnetic conditions (Tsugawa et al., 2004), making significant bending in TEC time series similar to preseismic anomalies (Heki and Enomoto, 2013). Geomagnetic activity on the day of the 2011 Tohoku-oki earthquake was relatively high, as shown in the time series of various indices given in **Figure 6A** of Heki and Enomoto (2013). Indeed, Heki and Enomoto (2015) recognized a small amplitude LSTID propagating southward through NE Japan about 1 hour before the earthquake.

We also observed a significant LSTID using GPS PRN05 in southwestern Australia (**Figure 5**). The LSTID emerged above Southwestern Australia around 5.5 UT, ~15 min before the 2011 Tohoku-oki earthquake. It propagated northward with a speed of ~0.6 km/s and reached the north coast of Australia around 6.0 UT. From the difference in time and space, this LSTID is not related to the observations of possible preseismic positive bending in the TEC time series at ~5 UT shown in **Figures 2A–1, A–3**. If these positive TEC anomalies are due to LSTID, we would see signatures like **Figure 5** in **Figures 2A–3** in earlier times. We think this is not the case, and it is unlikely that positive TEC anomalies shown in **Figure 3** are of LSTID origin.

## DISCUSSION

### Conjugate Effects of Other Large Earthquakes

Seventeen earthquakes of $M_w$7.3–9.2 with possible preseismic ionospheric TEC anomalies have been reported in addition to the 2011 Tohoku-oki earthquake (Heki and Enomoto, 2015; He and Heki, 2017). To see whether preseismic changes commonly occur around the epicenters of these earthquakes and their CPs, we examined the availability of GNSS data around the CPs of the 17 cases. Unfortunately, we did not find a meaningful amount of GNSS observations (**Figure 6**) near the CPs for 16 earthquakes (they were either within ocean or on land with few GNSS stations). The only exception is Colombia, around the CP of the 2015 Illapel earthquake ($M_w$8.3). There we observed weak positive TEC enhancements as we reported in He and Heki (2018). However, we considered these results inconclusive because the anomalies were faint.

The TEC anomalies that started together ~40 min before the 2011 Tohoku-oki earthquake in both hemispheres are more significant possibly owing to the larger magnitude ($M_w$) and higher background VTEC. We also found geomagnetic declination change in Australia (**Supplementary Figure S2**) similar to the change in Japan (Heki and Enomoto, 2013). However, we do not know the physical mechanisms underlying the preseismic geomagnetic field changes. Hence, we do not discuss them in detail in this article.

### Spatial Distribution of Conjugate Anomalies

**Figure 7** shows the spatial distribution of ionospheric anomalies 1 minute before the earthquake over Australia observed using GPS satellites, PRN02, 05, 09, 12, 25, and 29. Positive anomalies emerged to the north of the CP of the epicenter with a certain westward shift (**Figure 7B**). This also shows that such anomalies do not appear in regions far from the CP despite the same exclusion window used for the analysis. The LSTID shown in **Figure 5** in southwestern Australia around 06:00 UT is outside this map.

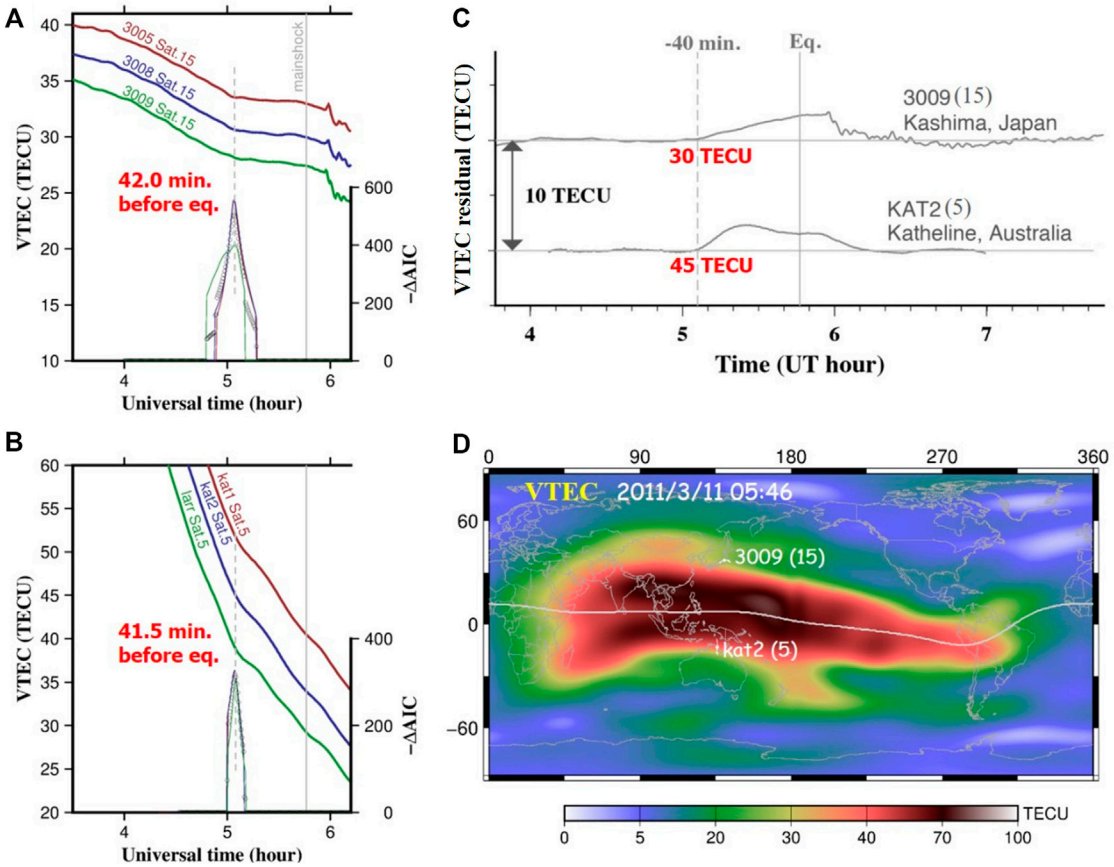


**FIGURE 4 |** The onset times of the preseismic VTEC enhancements were observed **(A)** near the epicenter of the 2011 $M_w$9.0 Tohoku-oki earthquake and **(B)** near its CP in Australia, inferred using AIC following Heki and Enomoto (2015). The colored thick curves in **(A)** and **(B)** show the selected VTEC time series before and after the earthquake in Japan and in Australia, respectively (kat1 is very close to kat2). The vertical gray lines represent the earthquake occurrence time. In calculating the–ΔAIC (decrease of AIC by assuming a break at the middle of the moving window), we used the moving time windows of ±30 min, and the absolute and relative thresholds of three TECU/h and 50%, respectively. The time window was shortened to ±20 min for the Australian data. The colored thin curves show the–ΔAIC time series (same colors for same station-satellite pairs). We calculated the averages of the–ΔAIC changes of the three GNSS stations and found significant positive breaks ~40 min before the earthquake both in Japan and Australia. To compare the VTEC rate change, we plot the VTEC residuals from reference curves together with instantaneous VTEC values at the onset time of the anomalies in **(C)** (~30 and ~45 TECU for Japan and Australia, respectively). The global ionospheric map (from ftp.aiub.unibe.ch) in **(D)** shows the VTEC distribution at the earthquake occurrence time. The SIP trajectories same as in **Figure 2** are plotted in **(D)** in white.

For comparison, we also show the spatial distribution of ionospheric anomalies observed using GPS PRN15 in Japan (**Figure 7A**). Due to the limited and sparsely distributed GNSS stations around the CP (**Figure 1C**), it is impossible to reconstruct the 3D structure of the anomalies as He and Heki (2018) did for the 2015 Illapel earthquake. It is also difficult to determine the height of the anomalies by minimizing the scatters of the positive anomalies (He and Heki, 2016) because only one satellite (PRN05) clearly recorded the TEC enhancements.

## Implications for Physical Models of Preseismic Ionospheric Anomalies

Two hypotheses have been proposed to explain the observed preseismic ionospheric anomalies. Kuo *et al.* (2014) showed that the anomaly could be generated by an upward electric current from stressed rock immediately before a large earthquake. This leads to the westward Hall electric field and the oblique-downward magnetic field drives the downward ***E*×*B*** drift of the ionospheric plasma, and subsequently a pair of positive and negative electron density anomalies. This model, however, needs large electric fields near the ground to let electric current flow overcoming the high atmospheric resistivity there. Kelley *et al.* (2017) suggested that the ***E*×*B*** drift could be driven directly by surface electric charges. Such charges could produce electric fields in the ionosphere and redistribute ionospheric electrons. A significant difference in this hypothesis is that we require surface electric fields only ~1/500 of the fair-weather field.

We basically support the model by Kelley *et al.* (2017) but emphasize the importance of induced charges within the ionosphere (**Figure 8**). Electric fields made by surface charges would first penetrate the ionosphere and let electrons redistribute along with geomagnetic fields. If surface charges are positive, the electron will descend and make an electric field opposite to those

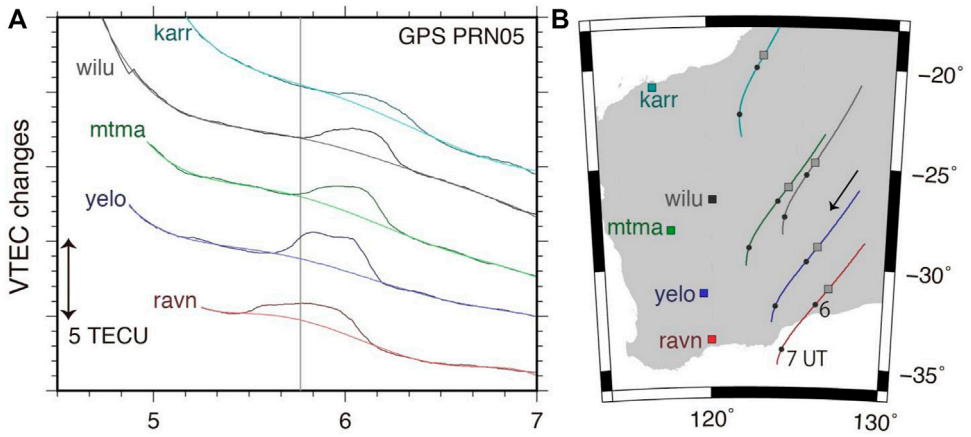


**FIGURE 5 |** An LSTID was observed using GPS PRN05 in Western Australia propagating northward with a speed of ~0.6 km/s. In **(A)**, we plot the VTEC time series at five stations, shown with squares in **(B)**. The colors of the curves in **(A)** correspond to stations and SIP tracks in **(B)**. Circles on the SIP tracks indicate hourly time marks and grey squares show SIP positions at the time of the earthquake. Reference curves in **(A)** are estimated as polynomials of degree five excluding the time periods influenced by LSTID.

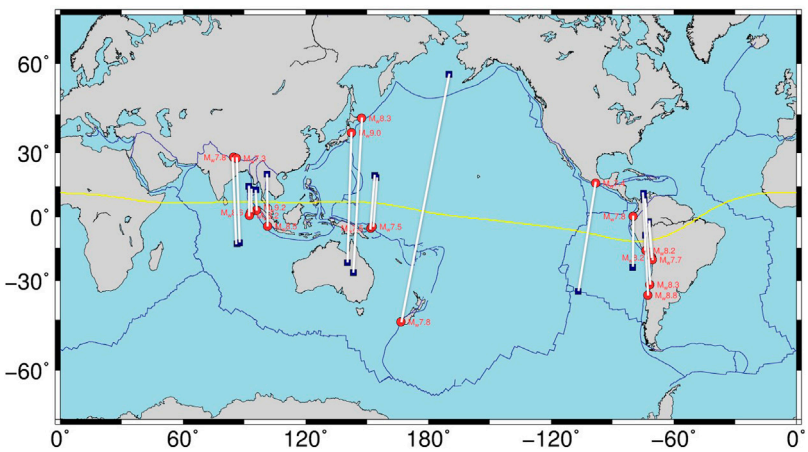


**FIGURE 6 |** The epicenters (red circles) of eighteen earthquakes ranging from $M_w$7.3 to $M_w$9.2 with possible preseismic ionospheric TEC anomalies and their corresponding conjugate points (blue squares). The white curves show geomagnetic field lines. The yellow curve shows the magnetic equator. The numbers of available GNSS stations are not sufficient when these earthquakes occurred except for the 2011 Tohoku-oki (present study) and the 2015 Illapel (He and Heki, 2018) earthquakes.

made by surface charges. This process would continue until induced electric fields offset the surface-origin electric fields, realizing uniform electric potential within magnetic field lines. The induced charges would result in positive and negative electron density anomalies at the lower and higher ends of magnetic field lines within the ionosphere. This would be the main process that caused positive TEC anomalies just above the surface charges, i.e. above the future epicenter (He and Heki, 2018). This electron redistribution will make an upward electric current, which may be responsible for the eastward temporary magnetic field as observed in NE Japan (Heki and Enomoto, 2013).

Above CP (Australia in **Figure 8**), such induced charges would not develop because of the long distance from the epicenter. Nevertheless, geomagnetic field lines extending from NE Japan would have electric potential higher than the surrounding field lines, generating electric fields radiating perpendicularly from the magnetic field line. This would make downward/upward $\boldsymbol{E}\times\boldsymbol{B}$ drift at the western/eastern side of the magnetic field line (**Figure 8**), and positive/negative electron density anomalies in the lower ionosphere (see **Figure 3** of Kuo *et al.* (2011)).

Although the longitudes of the anomalies in both hemispheres are similar, the peak of the positive anomalies in Australia appeared hundreds of kilometers to the north of the epicenter's CP. Downward $\boldsymbol{E}\times\boldsymbol{B}$ drift would occur at the west side of the geomagnetic field over a large distance along the magnetic field line. This makes a clear contrast to the TEC anomalies in NE Japan where a positive electron density

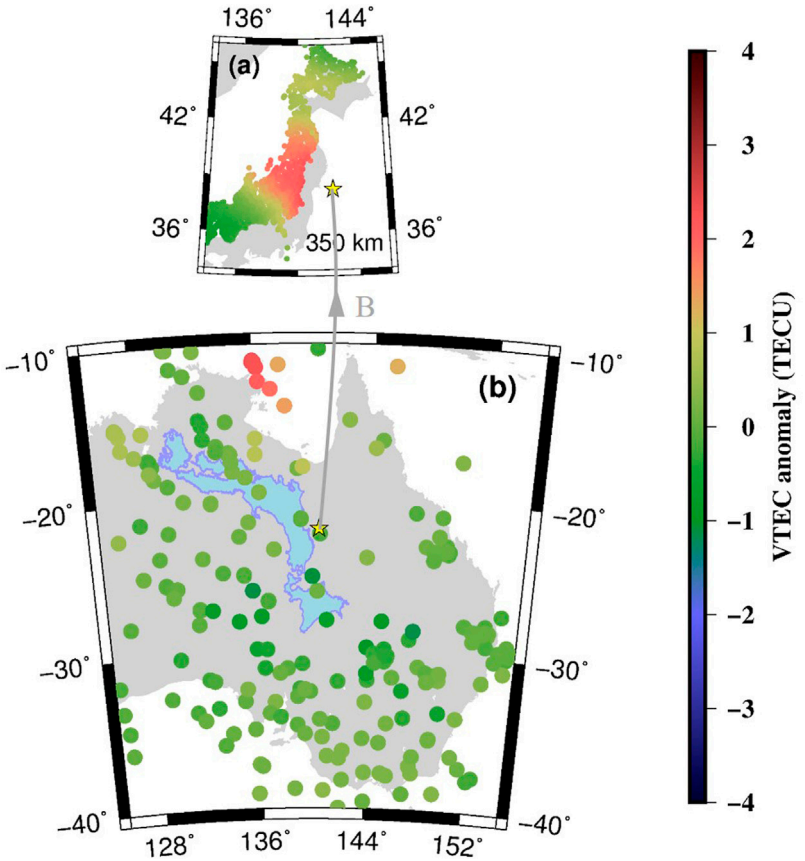


**FIGURE 7 |** Distribution of VTEC anomalies at 05:45 UT (1 min before the Tohoku-oki earthquake) on 11 March 2011 drawn using GPS PRN02, 05, 09, 12, 25, and 29 in Australia **(B)**, and using PRN15 in Japan **(A)**. The light blue map in **(B)** shows the geomagnetic conjugate image of the Japanese Islands. The yellow stars represent the epicenter of the earthquake in **(A)** and the corresponding CP in **(B)**. The gray curve indicates the ground projection of the geomagnetic field connecting the epicenter and the corresponding CP. We calculated the SIP positions assuming the ionospheric height of 350 km in **(A)** and **(B)**.

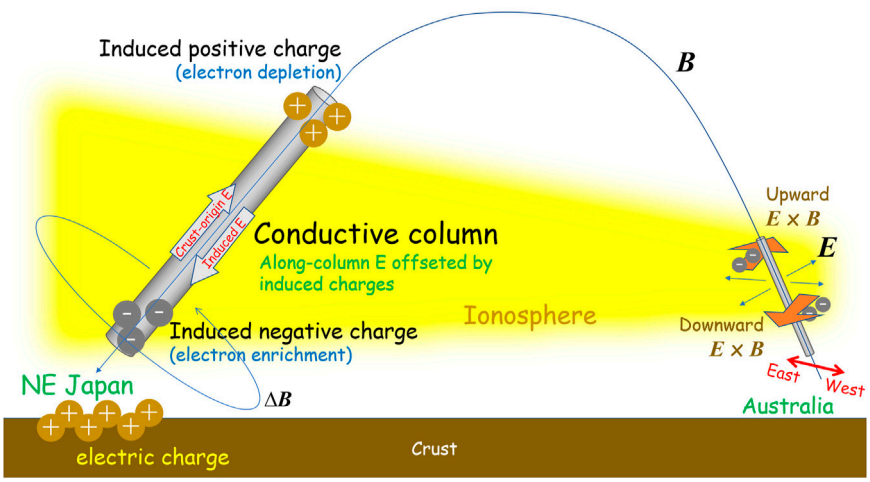


**FIGURE 8 |** Image of the electron redistribution above the epicenter and its CP.

anomaly occurs near the lower end of the geomagnetic field within the ionosphere. Such difference of mechanisms would make different electron density anomalies in the two hemispheres, i.e. they are not exact mirror images as illustrated in Kuo *et al.* (2011; 2014). This might explain the equatorward shift of the observed positive electron density anomaly above CP.

## SUMMARY

In this paper, we observed the geomagnetic conjugate ionospheric TEC anomalies immediately before the 2011 Mw9.0 Tohoku-oki earthquake using the GNSS stations located at Australia in the southern hemisphere. The onset time and magnitude of the ionospheric TEC enhancements in the conjugate region are consistent with the results observed in Japan in the northern hemisphere reported by Heki (2011). For the spatial distribution of the anomalies, the longitudes of the observed TEC enhancements in Australia and in Japan are similar. However, the positive anomalies in Australia appeared ~500 km to the north of the epicenter's CP. The most probable cause for this spatial shift of anomalies is the difference in physical mechanisms between the two hemispheres, i.e., a balanced process between the surface-origin electric fields and the induced electric fields above the future epicenter, which is different from the process in the conjugate region.

A striking feature seen in both hemispheres is that the observed TEC enhancements are stationary, which would be useful to discriminate from other TEC changes, e.g., large-scale traveling ionospheric disturbance, in practical purpose for detection of earthquake-related ionospheric anomalies in the future.

## DATA AVAILABILITY STATEMENT

The original contributions presented in the study are included in the article/**Supplementary Material,** further inquiries can be directed to the corresponding author.

## AUTHOR CONTRIBUTIONS

Conceptualization, methodology and original draft preparation, LH; review and editing, LW and KH; visualization, CG.

## FUNDING

This work was supported by the National Natural Science Foundation of China (41974028) and the Fundamental Research Funds for the Central Universities (N2201013).

## ACKNOWLEDGMENTS

We downloaded the GNSS data from GEONET (www.terras.gsi.go.jp) in Japan and from AuScope (www.auscope.org.au) and ARGN (www.ga.gov.au) in Australia. We downloaded the geomagnetic data from the INTERMAGNET (www.intermagnet.org).

## SUPPLEMENTARY MATERIAL

The Supplementary Material for this article can be found online at: https://www.frontiersin.org/articles/10.3389/feart.2022.850078/full#supplementary-material

## REFERENCES

Astafyeva, E., Lognonné, P., and Rolland, L. (2011). First Ionospheric Images of the Seismic Fault Slip on the Example of the Tohoku-Oki Earthquake. *Geophys. Res. Lett.* 38, a–n. doi:10.1029/2011GL049623

Cahyadi, M. N., and Heki, K. (2015). Coseismic Ionospheric Disturbance of the Large Strike-Slip Earthquakes in North Sumatra in 2012: Mw Dependence of the Disturbance Amplitudes. *Geophys. J. Int.* 200, 116–129. doi:10.1093/gji/ggu343

He, L., and Heki, K. (2017). Ionospheric Anomalies Immediately before M W 7.0-8.0 Earthquakes. *J. Geophys. Res. Space Phys.* 122 (8), 8659–8678. doi:10.1002/2017ja024012

He, L., and Heki, K. (2016). Three-dimensional Distribution of Ionospheric Anomalies Prior to Three Large Earthquakes in Chile. *Geophys. Res. Lett.* 43 (14), 7287–7293. doi:10.1002/2016gl069863

He, L., and Heki, K. (2018). Three-Dimensional Tomography of Ionospheric Anomalies Immediately before the 2015 Illapel Earthquake, Central Chile. *J. Geophys. Res. Space Phys.* 123 (5), 4015–4025. doi:10.1029/2017JA024871

Heki, K., and Enomoto, Y. (2015). M W Dependence of the Preseismic Ionospheric Electron Enhancements. *J. Geophys. Res. Space Phys.* 120, 7006–7020. doi:10.1002/2015ja021353

Heki, K., and Enomoto, Y. (2013). Preseismic Ionospheric Electron Enhancements Revisited. *J. Geophys. Res. Space Phys.* 118 (10), 6618–6626. doi:10.1002/jgra.50578

Heki, K., and Enomoto, Y. (2014). Reply to Comment by K. Heki and Y. Enomoto on "Preseismic Ionospheric Electron Enhancements Revisited". *J. Geophys. Res. Space Phys.* 119 (7), 6016–6018. doi:10.1002/2014ja020223

Heki, K. (2011). Ionospheric Electron Enhancement Preceding the 2011 Tohoku-Oki Earthquake. *Geophys. Res. Lett.* 38 (17), L17312. doi:10.1029/2011gl047908

Kamogawa, M., and Kakinami, Y. (2013). Is an Ionospheric Electron Enhancement Preceding the 2011 Tohoku-Oki Earthquake a Precursor? *J. Geophys. Res. Space Phys.* 118 (4), 1751–1754. doi:10.1002/jgra.50118

Kelley, M. C., Swartz, W. E., and Heki, K. (2017). Apparent Ionospheric Total Electron Content Variations Prior to Major Earthquakes Due to Electric Fields Created by Tectonic Stresses. *J. Geophys. Res. Space Phys.* 122 (6), 6689–6695. doi:10.1002/2016ja023601

Kuo, C. L., Huba, J. D., Joyce, G., and Lee, L. C. (2011). Ionosphere Plasma Bubbles and Density Variations Induced by Pre-earthquake Rock Currents and Associated Surface Charges. *J. Geophys. Res.* 116, a–n. doi:10.1029/2011JA016628

Kuo, C. L., Lee, L. C., and Huba, J. D. (2014). An Improved Coupling Model for the Lithosphere-Atmosphere-Ionosphere System. *J. Geophys. Res. Space Phys.* 119, 3189–3205. 2013JA019392. doi:10.1002/2013ja019392

Masci, F., Thomas, J. N., Villani, F., Secan, J. A., and Rivera, N. (2015). On the Onset of Ionospheric Precursors 40 Min before Strong Earthquakes. *J. Geophys. Res. Space Phys.* 120 (2), 1383–1393. doi:10.1002/2014ja020822

Muafiry, I. N., and Heki, K. (2020). 3-D Tomography of the Ionospheric Anomalies Immediately before and after the 2011 Tohoku-Oki (M W 9.0) Earthquake. *J. Geophys. Res. Space Phys.* 125 (10). e2020JA027993. doi:10.1029/2020JA027993

Otsuka, Y., Shiokawa, K., Ogawa, T., and Wilkinson, P. (2004). Geomagnetic Conjugate Observations of Medium-Scale Traveling Ionospheric Disturbances

at Midlatitude Using All-Sky Airglow Imagers. *Geophys. Res. Lett.* 31, L15803. doi:10.1029/2004GL020262

Shinagawa, H., Tsugawa, T., Matsumura, M., Iyemori, T., Saito, A., Maruyama, T., et al. (2013). Two-dimensional Simulation of Ionospheric Variations in the Vicinity of the Epicenter of the Tohoku-oki Earthquake on 11 March 2011. *Geophys. Res. Lett.* 40, 5009–5013. doi:10.1002/2013GL057627

Shiokawa, K., Shiokawa, K., Otsuka, Y., Tsugawa, T., Ogawa, T., and Wilkinson, P. (2005). Geomagnetic Conjugate Observation of Nighttime Medium-Scale and Large-Scale Traveling Ionospheric Disturbances: FRONT3 Campaign. *J. Geophys. Res.* 110, A05303. doi:10.1029/2004JA010845

Tsugawa, T., Saito, A., and Otsuka, Y. (2004). A Statistical Study of Large-Scale Traveling Ionospheric Disturbances Using the GPS Network in Japan. *J. Geophys. Res.* 109, A06302. doi:10.1029/2003JA010302

Utada, H., and Shimizu, H. (2014). Comment on "Preseismic Ionospheric Electron Enhancements Revisited" by K. Heki and Y. Enomoto. *J. Geophys. Res. Space Phys.* 119 (7), 6011–6015. doi:10.1002/2014ja020044

**Conflict of Interest:** The authors declare that the research was conducted in the absence of any commercial or financial relationships that could be construed as a potential conflict of interest.

frontiers | Frontiers in Earth Science

ORIGINAL RESEARCH
published: 06 June 2022
doi: 10.3389/feart.2022.883836

# Study of the Statistical Characteristics of Artificial Source Signals Based on the CSES

*Jianping Huang*[1,2], *Juan Jia*[2], *Huichao Yin*[3], *Zhong Li*[2]*, *Jinwen Li*[2], *Xuhui Shen*[1] and *Zeren Zhima*[1]

[1]National Institute of Natural Hazards, Ministry of Emergency Management of China, Beijing, China, [2]Institute of Intelligent Emergency Information Processing, Institute of Disaster Prevention, Langfang, China, [3]School of Information Engeering, Institute of Disaster Prevention, Langfang, China

The ground-based artificial source electromagnetic signal transmitted to space will form a pair of intensity regions over the station and its conjugate point. In order to study the position and intensity of the strongest points in the two regions, the power-spectrum density (PSD) of the electric field on board the Zhangheng-1 satellite (CSES) was selected when it passed over the NWC artificial source transmitting station. The selected frequency is centered at 19.8 kHz with a bandwidth of 200 Hz. The strongest point is defined as the location with the maximum power spectral density of ±10° around the NWC station within 5 days, which is the revisiting period of the CSES. The results show that statistical characteristics of strongest points vary as day/night, local/conjugate point, longitude/latitude, and different components of electric field vectors. In terms of longitude deviation, it is mostly westward offset at night and on both sides in the day over the NWC but opposite at the conjugate point. In terms of latitude deviations, it is equator-ward at night and the same during the day with a smaller deviation. While over the conjugate point, it is northward offset in the day and both at night with a bigger offset. In terms of intensity, it is stable without obvious seasonal changes over the NWC and its conjugate point. The intensity of PSD is higher at night than during the day. For the PSD intensity of the three components, the descending order over the NWC is Ead, Eab, and Ecd at night and Ecd, Ead, and Eab in the day, and the opposite is true for over the conjugate point.

**Keywords: CSES, NWC station, conjugate point, electric power spectrum, statistical characteristics**

OPEN ACCESS

***Edited by:***
*Chao Xiong,*
*Wuhan University, China*

***Reviewed by:***
*Angelo De Santis,*
*Istituto Nazionale di Geofisica e Vulcanologia (INGV), Italy*
*Essam Ghamry,*
*National Research Institute of Astronomy and Geophysics, Egypt*

***Correspondence:**
*Zhong Li*
*lizhong@cidp.edu.cn*

***Specialty section:***
*This article was submitted to Environmental Informatics and Remote Sensing, a section of the journal Frontiers in Earth Science*

***Received:*** *25 February 2022*
***Accepted:*** *19 April 2022*
***Published:*** *06 June 2022*

***Citation:***
*Huang J, Jia J, Yin H, Li Z, Li J, Shen X and Zhima Z (2022) Study of the Statistical Characteristics of Artificial Source Signals Based on the CSES. Front. Earth Sci. 10:883836. doi: 10.3389/feart.2022.883836*

## INTRODUCTION

When super large magnitude and shallow earthquakes occur, the energy of VLF electromagnetic waves will become stronger, resulting in space ionospheric disturbance, which is possibly useful for short-term strong earthquake prediction (Ni et al., 2013). One method to monitor ionospheric disturbances is to observe the propagation of artificially generated VLF (very low frequency, 3000–30000 Hz) electromagnetic signals in the lower ionosphere (Ni et al., 2019). Thus, scientists have deployed a number of ground-based artificial source transmitting stations around the world to continuously transmit VLF electromagnetic waves to space according to different frequencies. These signals can penetrate the ionosphere, propagate upward, and be reflected back to the ground and are synchronously received by satellites and ground receiving stations (Zhang et al., 2020). Although the energy of VLF electromagnetic waves emitted by artificial sources will decay

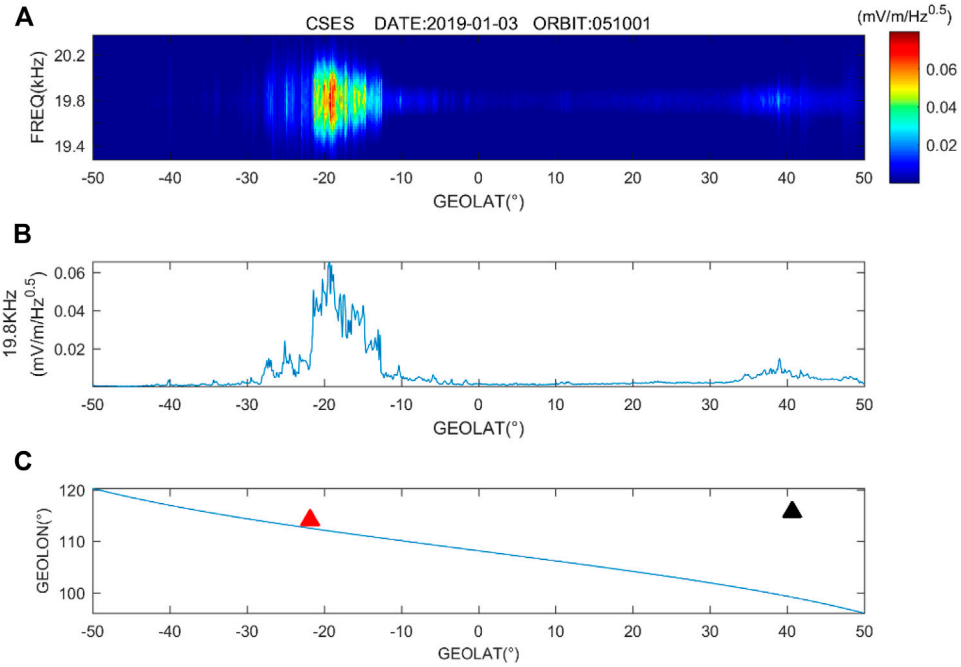


**FIGURE 1 |** Electric field PSD of the Eab component of the 051001 orbit.

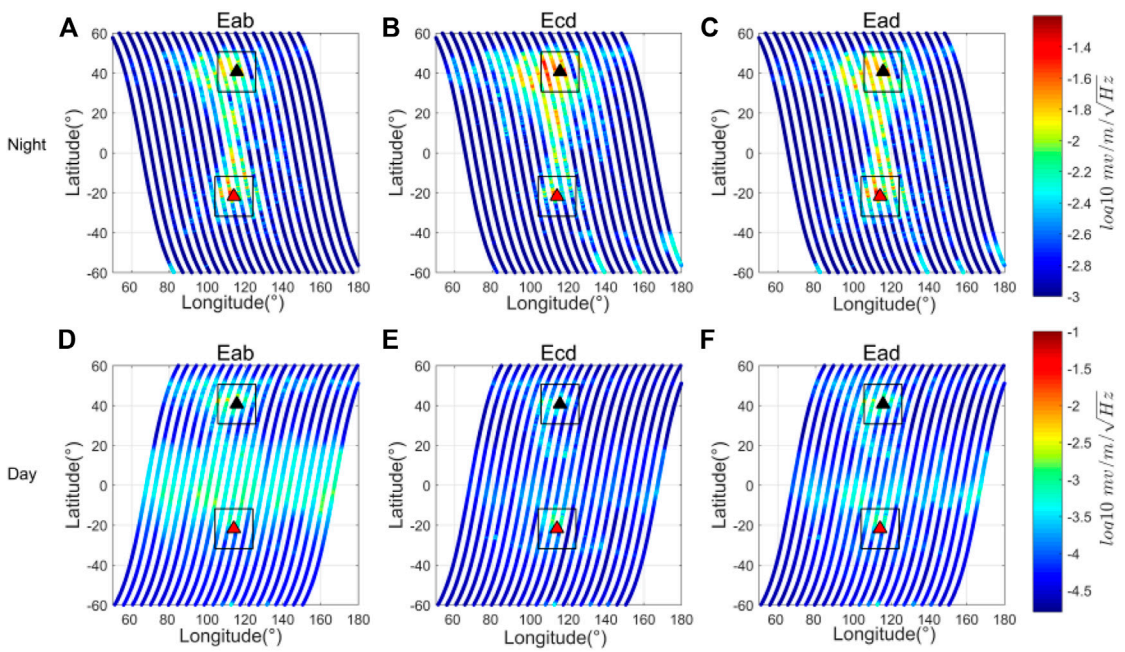


**FIGURE 2 |** Spatial distribution of the NWC signal in one cycle observed by the CSES (The abscissa is the geographic longitude, the ordinate is the geographic latitude, the color code is the PSD, and the red triangle and black triangle represent the projection position of the NWC station and its conjugate point on the ground, respectively. The first row **(A–C)** and the second row **(D–F)** represent the PSD distribution of the three components of the electric field on the nightside and the dayside, respectively.

while passing through the ionosphere (Lehtinen and Inan, 2009; Greninger and Colman, 2021), they generally show the characteristics of low energy loss and long transmission distance and can realize long-distance propagation in the earth ionospheric waveguide system. Moreover, it has obvious particle effects (Potirakis et al., 2018; Singh and Obara, 2020). When the

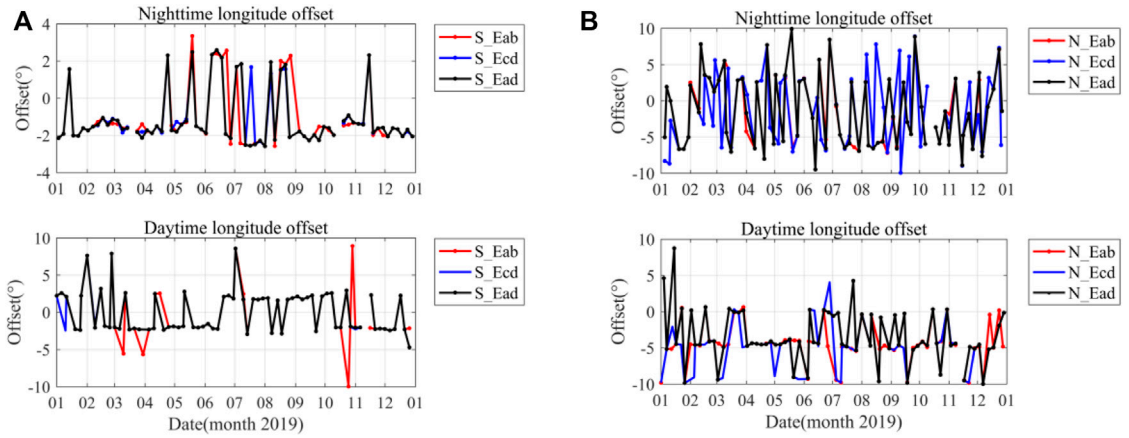


**FIGURE 3 |** Longitude shift of the strongest point of PSD of the electric field's three components.

satellite flies over the launch station, it can receive a stable artificial source signal in a specific frequency range. Due to the change in the velocity and phase of an electromagnetic wave when it propagates in the ionosphere, refraction, reflection, scattering, and other effects will also occur. Therefore, the electromagnetic response excited by the artificial source VLF signal in the ionosphere has temporal and spatial variation background characteristics of its own. The Australian NWC launching station (location: 21.82 S, 114.17 E, transmission frequency: 19.8 kHz, and transmission power: 1000 kW) is the only artificial source still in operation in the southern hemisphere (Li et al., 2014; Zhao et al., 2015). The transmitted VLF signal can produce a strong radiation effect on the ionosphere (Xu, 2016; Ivarsen et al., 2021).

On 2 February 2018, the China Seismo-Electromagnetic Satellite (CSES) dedicated to earthquake monitoring was launched; it is named "Zhangheng-1" and referred to as ZH-1. Its purpose is to establish a space test platform for monitoring the global space electromagnetic field, electromagnetic wave, ionospheric plasma, high-energy particle sedimentation, and other physical quantities and carry out electromagnetic monitoring of earthquakes above a magnitude of 7 in the world and above magnitude 6 in China (Shen et al., 2018). The CSES adopts a near-circular Sun-synchronous orbit divided into an ascending half orbit and a descending half orbit. The ascending one is the orbit of the satellite flying from south to north, and the descending one refers to the satellite flying from the north latitude to the southern latitude. The orbit is at an altitude of about 507 km, the inclination of about 97.4°, descending node at 14:00 LT, and the designed lifetime is 5 years. The revisit period is 5 days, and there will be 76 orbits in one revisit period (Yuan et al., 2018). The orbital distance in one period is between 4.7° and 4.8°. The CSES has two working modes: survey mode and burst mode. The CSES enters the burst mode when passing over China and the 1000 km area surrounding China or the global seismic belts, and in other areas, it is in the survey mode. The eight scientific payloads carried by the CSES are as follows: search coil magnetometer (SCM), high-precision magnetometer (HPM), electric field detector (EFD), GNSS occultation receiver, plasma analyzer package, high-energy particle detector, Langmuir probe, and tri-band beacon transmitter (Wang et al., 2016; Lu et al., 2017). Among them, the EFD adopts a dual-probe mode and calculates the electric field by obtaining the electric potential difference between two points in space. On the CSES, there are four 4.5-m-long extension rods. The end has a 60 mm diameter coating ball (respectively called a, b, c, and d), forming a tetrahedral structure.

The space vector electric field strength is obtained based on the electric potential difference in three directions and the corresponding distance between two balls. The detection frequency band is divided into ULF (0–16 Hz), ELF (6 Hz–2.2 kHz), and VLF (1.85 kHz-20 kHz) 、HF (18 kHz-3.5 MHz) (Ma et al., 2018). Among them, the sampling rate of VLF is 50 kHz, and its sampling period is 40.96 ms; thus, there are 2048 sampling points in each period. Because of the storage and downlink onboard the CSES, the duty ratio is 50% (Huang et al., 2018).

This study uses the electric field power spectrum density data detected by the EFD to study the characteristics of the maximum power spectrum density (MPSD) over the NWC station and the conjugate point and compares the statistic characteristics in the longitude offset, latitude offset, intensity of regional MPSD over NWC, and its conjugate point.

## Data Selection

Using the single-component PSD of the electric field VLF band recorded by the French DEMETER satellite, several earthquake researchers have conducted in-depth research on the phenomenon of ionospheric disturbance before the earthquake and obtained some understandings, such as the similarity of power-spectrum morphology in different periods, the enhancement of electric field intensity on the nightside, and so on (Zhu, 2010; Yao et al., 2011; Shufan et al., 2016; Yang et al., 2018; Meredith et al., 2019). In addition, the change in high-energy electrons in the ionosphere caused by NWC is found by PROBAV and the nightside is stronger than the dayside (Cunningham et al., 2020). Based on DEMETER's findings, the distribution range of the strongest electric field

**TABLE 1 |** Comparison of the longitude offset of the three-component strongest point over the NWC and its conjugate point.

| | *Δlon* | *count* | *\|min\|* | *\|max\|* | *\|mean\|* | *std* |
|---|---|---|---|---|---|---|
| S_Eab_night | >0 | 13 | 1.56 | 3.34 | 2.21 | 0.45 |
| | <0 | 59 | 1.06 | 3.84 | 1.82 | 0.46 |
| S_Ecd_night | >0 | 13 | 1.33 | 2.59 | 1.95 | 0.43 |
| | <0 | 59 | 0.92 | 6.4 | 1.83 | 0.71 |
| S_Ead_night | >0 | 12 | 1.52 | 2.59 | 2.05 | 0.37 |
| | <0 | 60 | 0.92 | 3.84 | 1.81 | 0.46 |
| S_Eab_day | >0 | 32 | 1.58 | 8.9 | 2.95 | 2.07 |
| | <0 | 39 | 1.56 | 9.97 | 2.56 | 1.46 |
| S_Ecd_day | >0 | 31 | 1.58 | 8.56 | 2.73 | 1.81 |
| | <0 | 40 | 1.56 | 4.72 | 2.26 | 0.49 |
| S_Ead_day | >0 | 32 | 1.58 | 8.56 | 2.73 | 1.78 |
| | <0 | 39 | 1.56 | 4.72 | 2.26 | 0.49 |
| N_Eab_night | >0 | 28 | 1.25 | 8.89 | 4.09 | 2.27 |
| | <0 | 44 | 0.02 | 9.49 | 4.98 | 2.36 |
| N_Ecd_night | >0 | 31 | 0.41 | 8.89 | 4.13 | 2.4 |
| | <0 | 41 | 0.5 | 9.94 | 5.21 | 2.28 |
| N_Ead_night | >0 | 29 | 1.25 | 9.92 | 4.27 | 2.48 |
| | <0 | 43 | 0.02 | 9.49 | 4.86 | 2.41 |
| N_Eab_day | >0 | 7 | 0.03 | 0.62 | 0.36 | 0.23 |
| | <0 | 64 | 0.14 | 9.98 | 4.91 | 2.34 |
| N_Ecd_day | >0 | 7 | 0.16 | 4.04 | 0.81 | 1.43 |
| | <0 | 64 | 0.13 | 9.98 | 5.44 | 2.67 |
| N_Ead_day | >0 | 12 | 0.17 | 8.75 | 1.71 | 2.73 |
| | <0 | 59 | 0.06 | 9.98 | 4.49 | 2.71 |

radiation area over the NWC showed that the area with strong day–night and day-side radiation of the NWC is located on the equator side, and the conjugate area also has an enhanced electric field radiation area (Cohen et al., 2012; Cohen and Inan, 2012; Němec et al., 2020), and the effect of thermionic temperature enhancement was found over NWC and conjugated regions (Bell et al., 2011).

In summary, the areas of electric field disturbances over the NWC and its conjugate point are studied based on DEMETER's findings, and there is a lack of research on the temporal and spatial distribution characteristics of the maximum electric field power spectrum over the NWC and conjugate point. Since the DEMETER satellite had fallen in 2010, this study uses the electric field PSD recorded by the CSES to explore the deviation of the latitude and longitude of the strongest point in each cycle and the variation of the strongest point. The PSD of the electric field VLF band comprises three components, Eab, Ecd, and Ead, which are collected by three pairs of probes ab, cd, and ad, respectively (Gao et al., 2021). While studying the electric field ULF band waveform data, it is found that the performance characteristics of the three components of the electric field are inconsistent (Li et al., 2022), which provides a reference for this study. Since the frequency of the NWC transmitting station is 19.8kHz, with a bandwidth of 200 Hz, the VLF PSD with 19.8 kHz ± 200 Hz of EFD onboard the CSES is extracted for statistical analysis.

## The Spatial Distribution Characteristics of PSD

When the electromagnetic satellite passes over the NWC station and its conjugate point, the electric field PSD peaks due to signal resonance. By observing the PSD curve of the three components of the electric field, it is found that the position and intensity of the wave crest change with time, and the variation characteristics of each component are also different. Taking the Eab component as an example, the PSD of an orbit passing directly over the NWC station from south to north is shown in **Figure 1**. An obvious spectral line in **Figure 1A** is the signal of the NWC transmitting station (frequency is 19.8 KHz), **Figure 1B** shows the variation diagram of the PSD value corresponding to the NWC station with latitude. **Figure 1C** shows the orbital position passing over the NWC, the red triangle represents the position of the NWC station, and the black triangle represents the position of the conjugate point. As can be seen from **Figure 1**, wave peaks appear within 10° of latitude near the NWC station and its conjugate point. The peak value and the corresponding spatial position are regarded as the information of the strongest point of the electric field power spectrum. Due to different satellite orbit intervals and different distances to the NWC station in a cycle, the search for the MPSD will produce large errors. Therefore, taking the operation cycle as a single unit, the distribution characteristics of the strongest points of the PSD at the NWC station and its conjugate points are studied.

The VLF band electric field three-component PSD of the NWC station from 6 January 2019 to 10 January 2019 is selected to obtain the PSD of the spatial orbit distribution diagram of electric field power spectrum intensity of 19.8 khz VLF band on the nightside and dayside in a cycle, as shown in **Figure 2**.

As can be seen from **Figure 2**, between 50°S ~ 50°N in latitude and 110°E ~ 130°E in longitude, there are two local strongest regions at Ecd and Ead components during the day and all three components in the night, while the Eab component on the dayside is the local strongest area. From the perspective of distribution, the local strongest area and MPSD intensity of the three components on the nightside are larger than those on the dayside. On the nightside, the PSD of the three components over the NWC station is greater than that over the conjugate area, while the Ecd component is the opposite; On the dayside, the PSD of the three components near the equator is significantly enhanced, and there is also a significant effect over its conjugate point; the strongest areas on the nightside and the dayside are concentrated within 10° above the NWC station and the conjugate point, and the strongest points of the NWC are concentrated near the equator, and the strongest points at the conjugate point are concentrated to its northwest.

In order to further analyze the variation trend of the local strongest point over time and in the three components, it is necessary to continue extracting the information of the strongest point of each cycle in 2019 for spatiotemporal analysis.

## The Position and Amplitude Variation Characteristics of the Strongest Point of PSD

Using the VLF signal PSD in the 10° range near the NWC (southern hemisphere) station and its conjugate point (northern

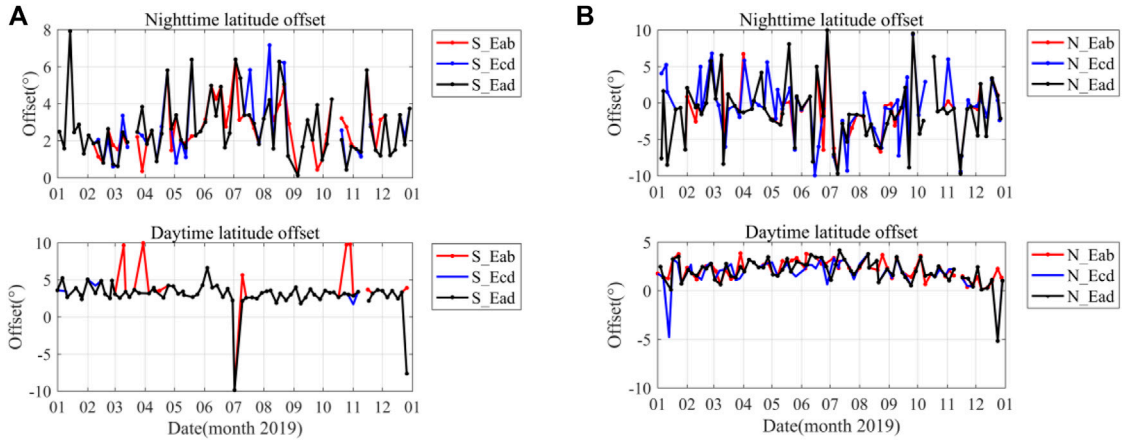


**FIGURE 4 |** Latitude offset of the strongest point of the three components of the electric field.

**TABLE 2 |** Comparison of the latitude offset of the three-component strongest point over the NWC and its conjugate point.

| | *Δlat* | *count* | *\|min\|* | *\|max\|* | *\|mean\|* | *std* |
|---|---|---|---|---|---|---|
| S_Eab_night | >0 | 71 | 0.13 | 7.91 | 2.67 | 1.44 |
| | <0 | 1 | 9.36 | 9.36 | 9.36 | 0.00 |
| S_Ecd_night | >0 | 72 | 0.13 | 7.91 | 2.75 | 1.75 |
| | <0 | 0 | Null | Null | Null | Null |
| S_Ead_night | >0 | 71 | 0.13 | 7.91 | 2.71 | 1.6 |
| | <0 | 1 | 9.36 | 9.36 | 9.36 | 0 |
| S_Eab_day | >0 | 70 | 1.81 | 9.96 | 3.74 | 1.72 |
| | <0 | 1 | 9.87 | 9.87 | 9.87 | 0 |
| S_Ecd_day | >0 | 69 | 1.69 | 6.60 | 3.23 | 0.83 |
| | <0 | 2 | 7.65 | 9.87 | 8.76 | 1.57 |
| S_Ead_day | >0 | 69 | 1.81 | 6.60 | 3.26 | 0.84 |
| | <0 | 2 | 7.65 | 9.87 | 8.76 | 1.57 |
| N_Eab_night | >0 | 23 | 0.10 | 10.00 | 3.06 | 3.07 |
| | <0 | 49 | 0.03 | 9.70 | 3.38 | 2.92 |
| N_Ecd_night | >0 | 28 | 0.28 | 10.00 | 3.31 | 2.85 |
| | <0 | 44 | 0.30 | 9.95 | 3.20 | 3.15 |
| N_Ead_night | >0 | 20 | 0.28 | 10.00 | 3.62 | 3.14 |
| | <0 | 52 | 0.03 | 9.70 | 3.29 | 2.87 |
| N_Eab_day | >0 | 71 | 0.10 | 3.86 | 2.18 | 0.96 |
| | <0 | 0 | Null | Null | Null | Null |
| N_Ecd_day | >0 | 69 | 0.10 | 3.79 | 2.04 | 0.89 |
| | <0 | 2 | 4.77 | 5.17 | 4.97 | 0.28 |
| N_Ead_day | >0 | 70 | 0.09 | 4.16 | 2.09 | 0.97 |
| | <0 | 1 | 5.17 | 5.17 | 5.17 | 0.00 |

hemisphere), that is, (11.82 S–31.82 S; 104.17 E ~ 124.17 E) and (30.647–50.647 N; 105.692 E ~ 125.692 E), the position of the strongest point of the PSD value and the characteristics of PSD changing with time in each cycle on the nightside and dayside of the three components are studied. The calculation formulas of the longitude offset and latitude offset are as follows:

$$\Delta lon = lon\_obs - lon\_sta. \quad (1)$$

$$\Delta lat = lat\_obs - lat\_sta. \quad (2)$$

Among them, lon_obs represents the longitude of the strongest point, lon_sta represents the longitude of the NWC station or its conjugate point, Δlon represents the longitude offset, lat_obs represents the latitude of the strongest point sought, lat_sta represents the latitude of the NWC station or its conjugate point, and Δlat represents the latitude offset quantity.

## Longitude Variation Characteristics of the Strongest Point of PSD

The variation characteristics of the longitude of the strongest point of the electric field PSD in each cycle are calculated by **formula (1)**, as shown in **Figure 3**. The longitude offset of the strongest point of the NWC station is shown in **Figure 3A**, in which the longitude offset of the three components on the nightside is within [−2°,2°], and most of the data are offset to the west of the NWC station by about 2°. From April to August and November, three components began to offset to the east of the NWC station, and the offset exceeded 2°. The longitude offset of most of the data on the three components on the dayside is within [−2°,2°], and the longitude offset to the east of the NWC station is more than 5° in February, July, and November. The offset of the Eab component is significantly different from that of the other two components in March and October, and its offset to the NWC station exceeds 5°.

The longitude offset of the strongest point of the conjugate point is shown in **Figure 3B**, in which the longitude offset of the three components on the nightside is within [0°,10°], and most of the data of the three components are relatively evenly offset to the east and west sides of the conjugate point, with a range of [− 5°,5°]; the longitude offset of the three components on the dayside is within [−10°,10°], and most of the data are offset to about 5° to the west of the conjugate point.

It can be seen that the longitude offset of the three strongest points of the NWC station is generally distributed on the west side on the nightside and relatively evenly distributed on the east and west sides on the dayside; The longitude offset at the conjugate point is mainly concentrated in the range of 5° on east and west sides on the nightside and near 5° on the west side on the dayside.

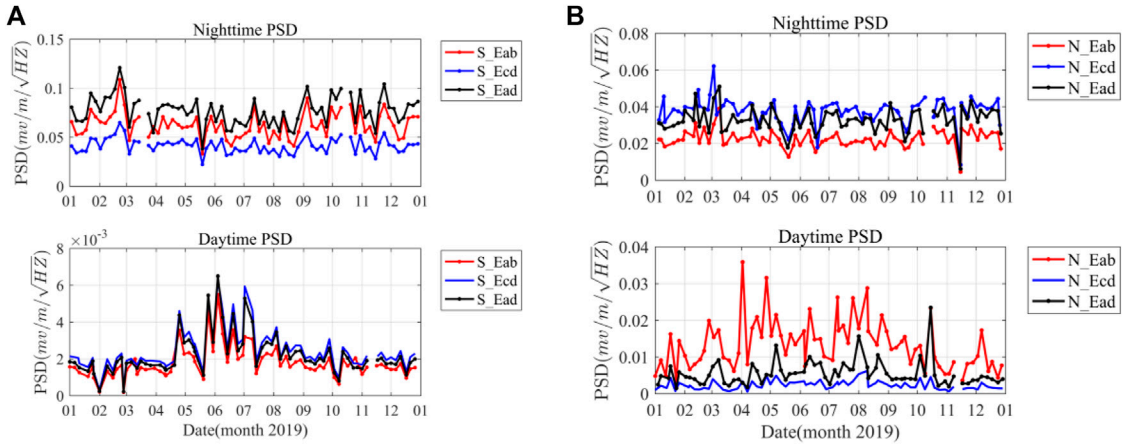


**FIGURE 5 |** Variation characteristics of MPSD.

**TABLE 3 |** Comparison of the annual average power spectrum values of the three-component strongest point over the NWC and its conjugate point.

| | | Night (mv/m/HZ ^ 0.5) | | | Day (mv/m/HZ ^ 0.5) | | |
|---|---|---|---|---|---|---|---|
| | | Ecd | Ead | Eab | Ecd | Ead | Eab |
| NWC | *\|mean\|* | 0.0626 | 0.0414 | 0.0769 | 0.0018 | 0.0024 | 0.0022 |
| | *std* | 0.0132 | 0.0075 | 0.0149 | 0.0009 | 0.0011 | 0.0011 |
| Conjugate point | *\|mean\|* | 0.0225 | 0.0377 | 0.0327 | 0.0134 | 0.0023 | 0.0054 |
| | *std* | 0.0048 | 0.0072 | 0.0068 | 0.0068 | 0.0012 | 0.0034 |

The comparison results of the longitude offsets of the strongest point of the three-component PSD of the electric field over the NWC station and its conjugate points in 2019 on the dayside and nightside are shown in **Table 1**, where $|min|$ represents the absolute value of the minimum offset, $|max|$ represents the absolute value of the maximum offset, $|mean|$ represents the absolute value of the average offset, std is the mean square deviation of the offset, the count represents the number of points in this range, *S* represents the NWC station, *N* represents its conjugate point, and S_Eab_night represents the nightside Eab component value of the NWC station, and other variables are analogized meanings.

The Eab component is taken as an example from **Table 1**:

1) Considering the longitude shift of the strongest point of the PSD, it is biased to the west over the NWC station, and the nightside (accounting for more than 80%) is more obvious than the dayside (accounting for slightly more than 55%); over the conjugate point, it is also biased to the west, and the dayside (accounting for more than 88%) is stronger than the nightside (accounting for more than 56%), which is contrary to the diurnal characteristics over the NWC station. The other two components have similar characteristics.
2) Considering the offset range of the strongest point of the PSD, the offset range of the east and west sides over the NWC station is within [1°, −4°]; the average value of the east offset is greater than that of the west, and the offset range and average value of the dayside are greater than those of the nightside. Over the conjugate point, the offset range of the east and west sides is between [0°, 10°] and the east offset range and the average value of the dayside are much smaller than those of the nightside, while the west offset range and the average value of the dayside and nightside have minor differences; the average value of eastward migration is less than that of westward migration, which is contrary to the situation over the NWC station, with its migration range being larger. The performance characteristics of the other two components are similar to those of this component.
3) Analyzing the stability of longitude migration data, the stability of nightside data over the NWC station is greater than that of the dayside and the stability of the dayside and nightside data over the conjugate point is similar. In general, the stability of the data over the NWC station is greater than that of its conjugate point, and the stability of the other two components is similar.

## Latitude Variation Characteristics of the Strongest Point of PSD

The time-varying characteristics of the latitude of the strongest point of the electric field PSD in each cycle are shown in **Figure 4** in which **Figures 4A,B**, respectively, represent the latitude offset over the NWC station and its conjugate point. As can be seen from **Figure 4A**, the offset to the equator side of the three components on the nightside is between 0° and 6°,

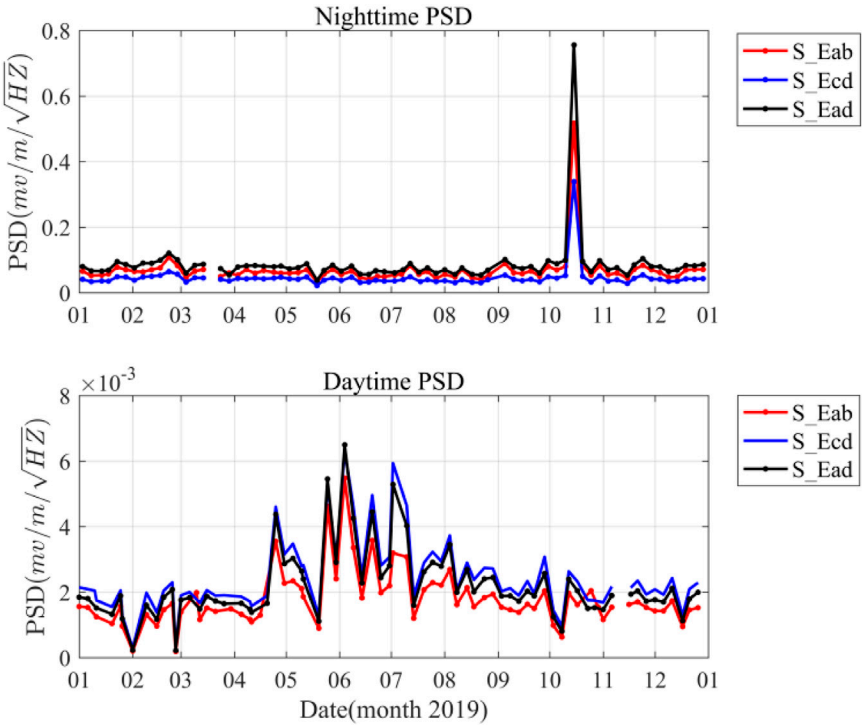


**FIGURE 6 |** Abnormal change characteristics of the PSD of the strongest points on the night and daysides of the magnetic conjugate point.

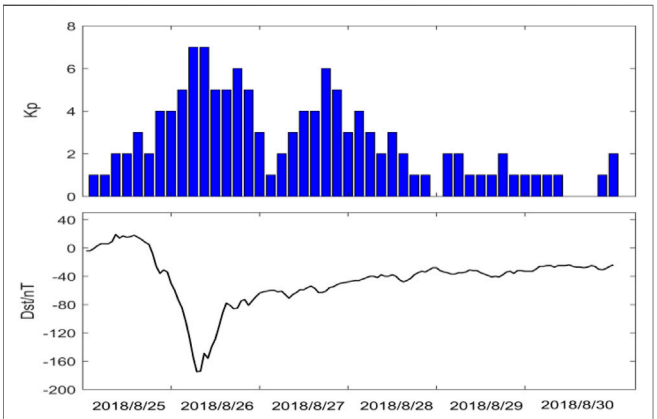


**FIGURE 7 |** Variation of geomagnetic indexes Kp and Dst.

showing an increasing trend from June to August, and the offset of the Ecd component exceeds 6°. The three components on the dayside are mainly offset to the equatorial side, with an amplitude of 2°–5°. The offset of the Eab component to the equatorial side is more than 5° in March, April, and October, and the three components are offset to the south of the NWC station in July and December and all for more than 5°.

As can be seen from **Figure 4B**, most of the data of the three components on the nightside are evenly shifted to the north and south sides of the conjugate point, with an amplitude of [– 5°, 5°]. From June to September, the data are mainly shifted to the south of the conjugate point. Most of the data of the three components on the dayside are offset to the north of the conjugate point, with an amplitude of [0°, 5°]. The Ecd and Ead components are offset to the south of the conjugate point by nearly 5° in January and December, respectively.

It can be seen that the latitude offset of the three components of the NWC station is mainly distributed in the north, and only very few points on the dayside are distributed in the south. The latitude offset of the three components of the conjugate point is distributed on the north and south sides on the nightside and mainly on the north side on the dayside. The latitude offset on the three components of the NWC station and conjugate point is compared and analyzed. The offset direction on the nightside is inconsistent, and the offset on the dayside is mostly on the north side.

The latitude shift results of the strongest points of the electric field PSD in 2019 are listed in **Table 2**, and the meaning of each parameter is shown in **Table 1**.

Still, taking the Eab component as an example to discuss

1) Considering the latitude offset of the strongest point of the PSD, when it is over the NWC station, its latitude is mainly biased to the north (more than 95%); over the conjugate point, the daytime latitude is biased to the north (more than 98%) and the nighttime latitude is mainly biased to the south (more than 60%). The offset direction of the other two components is similar to the day and night characteristics of the Eab component.
2) To analyze the latitude offset range, while over the NWC station, the offset range and average value on the north side of the dayside are greater than those of the nightside. Over the

conjugate point, the offset range and average value on the north side of the nightside conjugate point are greater than those on the dayside. and the other two components are similar to this component.

3) To analyze the stability of latitude migration, the migration stability over the NWC station is better, the stability of nightside is greater than that of the dayside, and the opposite is found over the conjugate point. The stability of the other two components also has similar characteristics.

## Variation Characteristics of Electric Field MPSD Amplitude

The statistics of the intensity of electric field MPSD in each operation cycle in 2019 are shown in **Figure 5**, in which **Figures 5A,B** represent the variation diagram of the intensity of MPSD at the NWC station and its conjugate point, respectively.

As can be seen from **Figure 5A**, over the NWC station, the MPSD of the three components on the nightside is between 0.04 and 0.12 mv/m/Hz ^0.5 and meets the relation Ead > Eab > Ecd; the MPSD of the three components on the dayside is between 0 and 0.007 mv/m/Hz ^0.5, showing an increasing trend from May to July and meets the relation: Ecd > Ead > Eab.

As can be seen from **Figure 5B**, the MPSD of the three components on the nightside is mainly distributed between 0.02 and 0.05 mv/m/Hz ^0.5 above the conjugate point and meets the relation: Ecd > Ead > Eab. The MPSD of the three components on the dayside is mainly distributed between 0 and 0.025 mv/m/Hz^ 0.5 and meets the relation: Eab > Ead > Ecd.

The changes in the MPSD of the three components with time in each cycle are similar such that they increase or decrease at the same time. The change range of the nightside is small and that of the dayside is large.

The comparison of annual average values of three component MPSD of the NWC station and its conjugate points is shown in **Table 3**.

It can be seen from **Table 3** that the mean value of the MPSD of the NWC station and its conjugate point on the three components on the nightside is greater than that on the dayside and that of the NWC station is much greater than that of its conjugate point. On the diurnal side, that of the conjugate point is larger than that of the NWC station, and only the Ecd component has the opposite effect. To analyze the data stability, the stability over the conjugate point on the nightside is greater than that of the NWC station, while on the dayside, it is the opposite.

# CONCLUSION AND DISCUSSION

Based on the VLF band PSD of the electric field recorded by the CSES from January to December 2019, taking the NWC artificial source transmitting station and the 10° range near its conjugate point as the research area, this study includes a statistical analysis of the temporal and spatial variation of the strongest point in each cycle and obtains some understanding of the variation law of spatial electric field intensity with time.

# DISCUSSION

The MPSD of the three components in each cycle over the NWC station and its conjugate points is different, which may be related to the direction of the satellite or the type of orbit. There is an abnormal sudden change value in the nightside MPSD in October 2019, as shown in **Figure 6**. However, Dst ≤ -100 and Kp > 5 occurred on August 26 and 27, 2018. It is estimated that a large magnetic storm occurred during this period (Liao et al., 2018; Zhu et al., 2021), as shown in **Figure 7**, and the MPSD in these 2 days has reached 0.05 mv/m/Hz ^0.5, which is far less than the abnormal abrupt mutation value. It is speculated that the abnormal value abrupt value change in October 2019 has no obvious relationship with the magnetic storm. It is necessary to analyze whether the MPSD value variation is related to the earthquake in subsequent work.

# CONCLUSION

## There Are Four Main Conclusions

1) In terms of longitude, most of the three components of the nightside of the NWC station are mainly offset to the west, and those on the dayside is offset on its east and west sides; on the nightside of the conjugate point, the strongest points of the three-component PSD are offset to the east and west and those on the dayside is mainly offset to the west, and the offset of the conjugate point is greater than that of the NWC station.

2) In terms of latitude, the strongest points of the PSD of the three components in the NWC station are all biased to the north, the offset amplitude of the nightside increases with time, and the offset amplitude of the dayside tends to be stable, but the Eab component has an abnormal offset in March and October, and the amplitude reaches 10°. The strongest points of the nightside at the conjugate point are offset on the south and north sides, the diurnal side is offset to the north, and the offset amplitude of the nightside is larger than that of the dayside.

3) On the nightside of the NWC station, the variation range of the MPSD of the three components is stable, and there are no obvious seasonal characteristics. and it meets the order: Ead > Eab > Ecd; The variation of MPSD on the dayside has an obvious increase from May to July, and it meets the order: Ecd > Ead > Eab; The variation range of MPSD on the nightside of the conjugate point is stable, there are no obvious seasonal characteristics, and it meets the order: Ecd > Ead > Eab; The MPSD variation amplitude of the Eab component on the dayside is greater than that of the other two components, and it meets the order: Eab > Ead > Ecd; The MPSD of different components on the nightside and the dayside is obviously different, and the nightside is all greater than that on the dayside.

4) Over the NWC station and its conjugate point, the longitude offset, latitude offset, and MPSD value of the strongest point in PSD in each cycle have similar variation shapes with time, and

these three parameters change more obviously every month at the NWC station than at its conjugate point.

## DATA AVAILABILITY STATEMENT

The datasets presented in this study can be found in online repositories. The names of the repository/repositories and accession numbers can be found below: www.leos.ac.cn.

## AUTHOR CONTRIBUTIONS

JH contributed to the conception and design of the study, JJ contributed to model construction, ZL contributed to the methodology, HY contributed to the editing and typesetting, and JL contributed to data analysis, XS and ZR contributed to writing. All authors approved the final manuscript.

## FUNDING

This research was funded by Dragon 5 cooperation Proposal(#58892, #59308) the National Key R&D Program(2018YFC1503501),APSCO Earthquake Project:Phase II,ISSI-BJ2019.

## ACKNOWLEDGMENTS

In this study, the observed electric field power spectrum data of the CSES supported by the China National Space Administration and China Seismological Bureau are used. We thank all members of the CSES team of the National Institute for Natural Disaster Prevention and Control of the Ministry of Emergency Management for the data provided for this research, especially Dr. Zhang Xuemin of the Prediction Institute of China Earthquake Administration for her valuable opinions.

## REFERENCES

Bell, T., Graf, K., Inan, U., Piddyachiy, D., and Parrot, M. (2011). DEMETER Observations of Ionospheric Heating by Powerful VLF Transmitters. *Geophys. Res. Lett.* 38 (11), 47503. doi:10.1029/2011gl047503

Cohen, M. B., and Inan, U. (2012). Terrestrial VLF Transmitter Injection into the Magnetosphere. *J. Geophys. Res. space Phys.* 117 (A8). doi:10.1029/2012ja017992

Cohen, M. B., Lehtinen, N. G., and Inan, U. S. (2012). Models of Ionospheric VLF Absorption of Powerful Ground Based Transmitters. *Geophys. Res. Lett.* 39 (24). doi:10.1029/2012gl054437

Cunningham, G. S., Botek, E., Pierrard, V., Cully, C., and Ripoll, J. F. (2020). Observation of High-energy Electrons Precipitated by NWC Transmitter from PROBA-V low-Earth Orbit Satellite. *Geophys. Res. Lett.* 47 (16), e2020GL089077. doi:10.1029/2020gl089077

Gao, P., Wang, X., Yang, D., Li, W., and Gu, F. (2021). Electric Field Data Storage Experiment of the ZH-1 Satellite. *Prog. Geophys.* 36 (04), 1386. doi:10.6038/pg2021EE0250

Greninger, P. T., and Colman, J. J. (2021). The Seasonality of VLF Attenuation through the Ionosphere Verified by DEMETER Satellite. *JGR Space Phys.* 126 (8), e2020JA028383. doi:10.1029/2020JA028383

Huang, J., Lei, J., Li, S., Zeren, Z., Li, C., Zhu, X., et al. (2018). The Electric Field Detector(EFD) Onboard the ZH-1 Satellite and First Observational Results. *Earth Planet. Phys.* 2 (06), 469–478. doi:10.26464/epp2018045

Ivarsen, M. F., Park, J., Jin, Y., and Clausen, L. B. (2021). Ionospheric Plasma Fluctuations Induced by the NWC Very Low Frequency Signal Transmitter. *J. Geophys. Res. Space Phys.* 126 (5), e2021JA029213. doi:10.1029/2021ja029213

Lehtinen, N. G., and Inan, U. S. (2009). Full-wave Modeling of Transionospheric Propagation of VLF Waves. *Geophys. Res. Lett.* 36 (3), a–n. doi:10.1029/2008GL036535

Li, J. D., Spasojevic, M., Harid, V., Cohen, M. B., Gołkowski, M., and Inan, U. (2014). Analysis of Magnetospheric ELF/VLF Wave Amplification from the Siple Transmitter Experiment. *J. Geophys. Res. Space Phys.* 119 (3), 1837–1850. doi:10.1002/2013ja019513

Li, Z., Li, J., Huang, J., Yin, H., and Jia, J. (2022). Research on Pre-seismic Feature Recognition of Spatial Electric Field Data Recorded by CSES. *Atmosphere* 13 (2), 179. doi:10.3390/atmos13020179

Liao, Z., Wu, B., Shen, X., and Min, M. (2018). Analysis of Ionospheric VTEC Temporal-Spatial Characteristics in Guangxi and Surrounding. *Sci. Surv. Mapp.* 43 (09), 40–45+62. doi:10.16251/j.cnki.1009-2307.2018.09.008

Lu, H., Liu, D., Zhao, S., Ou, M., Huang, J., and Wang, L. (2017). Three-frequency Beacon Data Processing and Product Introduction of Electromagnetic Monitoring Test Satellites." in 2017 China Earth Sciences Joint Academic Annual Conference Proceedings (38)-Special Topics 71: Dynamics of the Inner Magnetosphere, Topic 72: Computational Geophysical Methods and Techniques, Topic 73: Geothermal: "Study" to "Use", Topic 74: Electromagnetic Satellite Observations and Applications, Beijing, 2017.

Ma, M., Lei, J., Li, C., Li, S., Zong, C., Liu, Z., et al. (2018). Design Optimization of Zhangheng-1 Space Electric Field Detector. *Chin. J. Vac. Sci. Technol.* 38 (07), 582–589. doi:10.13922/j.cnki.cjovst.2018.07.06

Meredith, N. P., Horne, R. B., Clilverd, M. A., and Ross, J. P. J. (2019). An Investigation of VLF Transmitter Wave Power in the Inner Radiation Belt and Slot Region. *J. Geophys. Res. Space Phys.* 124 (7), 5246–5259. doi:10.1029/2019ja026715

Němec, F., Pekař, J., and Parrot, M. (2020). NWC Transmitter Effects on the Nightside Upper Ionosphere Observed by a Low-Altitude Satellite. *J. Geophys. Res. Space Phys.* 125 (12), e2020JA028660. doi:10.1029/2020JA028660

Ni, B., Bortnik, J., Thorne, R. M., Ma, Q., and Chen, L. (2013). Resonant Scattering and Resultant Pitch Angle Evolution of Relativistic Electrons by Plasmaspheric Hiss. *J. Geophys. Res. Space Phys.* 118 (12), 7740–7751. doi:10.1002/2013ja019260

Ni, B., Huang, H., Zhang, W., Gu, X., Zhao, H., Li, X., et al. (2019). Parametric Sensitivity of the Formation of Reversed Electron Energy Spectrum Caused by Plasmaspheric Hiss. *Geophys. Res. Lett.* 46 (8), 4134–4143. doi:10.1029/2019gl082032

Potirakis, S., Asano, T., and Hayakawa, M. (2018). Criticality Analysis of the Lower Ionosphere Perturbations Prior to the 2016 Kumamoto (Japan) Earthquakes as Based on VLF Electromagnetic Wave Propagation Data Observed at Multiple Stations. *Entropy* 20 (3), 199. doi:10.3390/e20030199

Shen, X., Yuan, S., Zhang, X., Huang, J., and Zhu, X. (2018). "General Progress of Zhang Heng-1 Satellite Plan," in *2018 Academic Seminar and Seminar on New Technology Advances and Applications of Seismic Electromagnetic Detection by the Seismoelectromagnetics* (Dandong: Professional Committee of China Seismological Society), 62.

Shufan, Z., Li, L., Xuemin, Z., and Xuhui, S. (2016). Full Wave Calculation of Ground-Based VLF Radiation Penetrating into the Ionosphere. *Chin. J. Radio Sci.* 31 (5), 825. doi:10.13443/j.cjors.2016021701

Singh, V., and Obara, Y. (2020). Simultaneous Study of VLF/ULF Anomalies Associated with Earthquakes in Japan. *Open J. Earthq. Res.* 9 (2), 15. doi:10.4236/ojer.2020.92012

Wang, L., Shen, X., Zhang, Y., Zhang, X., Hu, Z., Yan, R., et al. (2016). Developing Progress of China Seismo-Electromagnetic Satellite Project. *Acta Seismol. Sin.* 38 (03), 376. doi:10.11939/jass.2016.03.005

Xu, W. (2016). Signal Processing of Artificial VLF Wave and Study on Electromagnetic Disturbance Characteristics in Space. Dissertation/Master's thesis. Langfang: Institute of Disaster Prevention.

Yang, M., Huang, J., Zhang, X., Shen, X., Wang, L., Zhima, Z., et al. (2018). Analysis on Dynamic Background Field of Ionosphere ELF/VLF Electric Field in Northeast Asia. *Prog. Geophys.* 33 (06), 2285. doi:10.6038/pg2018BB0492

Yao, L., Chen, H., Liu, X., and He, Y. (2011). The Global Characteristics of VLF Electric Field Frequency Spectrumin Ionosphere. *Seismol. Geomagnetic Observation Res.* 32 (04), 27. doi:10.3969/j.issn.1003-3246.2011.04.006

Yuan, S., Zhu, X., and Huang, J. (2018). System Design and Key Technology of China Seismo-Electromagnetic Satellite. *Natl. Remote Sens. Bull.* 22 (S1), 32. doi:10.11834/jrs.20188177

Zhang, X., Qian, J., Shen, X., Liu, J., Wang, Y., and Huang, J. (2020). The Seismic Application Progress in Electromagnetic Satellite and Future Development. *Earthquake* 40 (02), 18. doi:10.12196/j.issn.1000-3274.2020.02.002

Zhao, S., Zhang, X., Zhao, Z., Shen, X., and Zhou, C. (2015). Temporal Variations of Electromagnetic Responses in the Ionosphere Excited by the NWC Communication Station. *Chin. J. Geophys.* 58 (07), 2263. doi:10.6038/cjg20150705

Zhu, J., Liu, Y., Dai, C., and Lin, Z. (2021). *Analysis of the Ionospheric TEC Temporal-Spatial Characteristics in Sichuan and Surrounding Area*. Guilin: Journal of Guilin University of Technology, 1

Zhu, T. (2010). A Preliminary Study on Characteristics of Average Power Spectrum Density of LF/MF Electric Field Observed by DEMETER Satellite. *Acta Seismol. Sin.* 32 (04), 476. doi:10.3969/j.issn.0253-3782.2010.04.010

**Conflict of Interest:** The authors declare that the research was conducted in the absence of any commercial or financial relationships that could be construed as a potential conflict of interest.

**Publisher's Note:** All claims expressed in this article are solely those of the authors and do not necessarily represent those of their affiliated organizations, or those of the publisher, the editors, and the reviewers. Any product that may be evaluated in this article, or claim that may be made by its manufacturer, is not guaranteed or endorsed by the publisher.

frontiers | Frontiers in Earth Science

ORIGINAL RESEARCH
published: 27 June 2022
doi: 10.3389/feart.2022.895561

# Effects of Solar Proton Events Associated With X-Ray Flares on Near-Earth Electron and Proton Fluxes Based on ZH-1 Satellite Observations

*Lu Wang[1,2], Zhenxia Zhang[2]*, Xunhui Shen[2], Xinqiao Li[3], Xiaohua Liang[3], Zeren Zhima[2], Wei Chu[2], Feng Guo[2], Na Zhou[2], Huaran Chen[4] and Daihui Wei[5]*

[1]School of Emergency Management Science and Engineering, UCAS, Beijing, China, [2]National Institute of Natural Hazards, MEMC, Beijing, China, [3]Institute of High Energy Physics, CAS, Beijing, China, [4]Institute of Geophysics, CEA, Beijing, China, [5]Guangxi Normal University, Guilin, China

Solar eruptions can cause violent effects on the space environment. Electromagnetic radiation from solar flares will be the first to arrive on the Earth at the speed of light, followed by solar energetic charged particles. The last to appear will be coronal mass ejections and geomagnetic storms. Based on observations of ZH-1 satellite, we report three strong disturbed space environment events, all of them with solar proton events (SPEs), and analyze the driving mechanisms: 1) On 29 November 2020, an M4.4 flare accompanied with a full halo CME caused a gradual SPE, which was mainly driven by CME shocks. 2) On 28 May 2021, a C9.4 flare brought an impulsive SPE, which was accelerated by the flare. The heliolongitude of this small flare was 63°W, near the footpoint of the magnetic field line leading from the Sun to the Earth. 3) On 28 October 2021, a full-halo CME accompanied with an X1.1 flare brought a gradual SPE. On 2 November 2021, another fast full halo CME accompanied with flare was ejected. The faster CME of November 2 caught up and swept up the slower CME of November 1, and subsequently caused a severe geomagnetic storm (minimum Dst = -101) and a high-energy electron storm on November 4. The observations of the above three space environmental events confirm that the data quality of the high-energy particle package (HEPP) from ZH-1 is highly reliable and accurate and is highly advantageous to monitoring the variation of energetic particles and X-rays in the radiation belt of the Earth during solar activities.

**Keywords: solar x-ray flares, solar proton event, CSES satellite, geomagnetic storm, coronal mass ejections, ZH-1 satellite**

OPEN ACCESS

***Edited by:***
*Juergen Pilz,*
*University of Klagenfurt, Austria*

***Reviewed by:***
*Maria Alexandra Pais,*
*University of Coimbra, Portugal*
*Eino Valtonen,*
*University of Turku, Finland*

****Correspondence:***
*Zhenxia Zhang*
*zxzhang2018@163.com*

***Specialty section:***
*This article was submitted to Environmental Informatics and Remote Sensing, a section of the journal Frontiers in Earth Science*

***Received:*** *14 March 2022*
***Accepted:*** *18 May 2022*
***Published:*** *27 June 2022*

***Citation:***
*Wang L, Zhang Z, Shen X, Li X, Liang X, Zhima Z, Chu W, Guo F, Zhou N, Chen H and Wei D (2022) Effects of Solar Proton Events Associated With X-Ray Flares on Near-Earth Electron and Proton Fluxes Based on ZH-1 Satellite Observations. Front. Earth Sci. 10:895561. doi: 10.3389/feart.2022.895561*

## 1 INTRODUCTION

Usually, the space environment is not always stable. Space weather events, such as flares, coronal mass ejections (CMEs), and solar proton events (SPEs) can lead to the damage of satellite systems, communication systems, navigation systems, and power systems, which causes enormous economic losses (Feynman and Gabriel, 2000). Therefore, it is important to monitor the space environment to defend and alleviate space environmental hazards. SPE is a phenomenon that is mostly associated with strong flares and fast halo coronal mass ejections (CMEs) (Reames, 1999). NOAA Space Weather Prediction Center (SWPC) defines the SPE to have a flux level of 10 $cm^{-2}s^{-1}sr^{-1}$ for 15 min at $>10MeV$ energy in geosynchronous orbit.

There are two different types of solar proton events: gradual events and impulsive events. Impulsive SPEs last about a few hours and often carry many electrons in 1–100 keV. The component ratios of Fe/O, 3He/4He for events accelerated by flares are significantly higher than those accelerated by CMEs (Kallenrode et al., 1992; Cane et al., 2003). A common explanation is that 3He is preferentially heated by certain waves, such as ion cyclotron waves, due to gyroresonance, because it is the only isotope whose cyclotron frequency lies between $He^{++}$ and $H^{+}$ (Fisk, 1978). Another interesting thing is that the heliolongitude corresponding to the flare-driven SPE is concentrated at around 60°W, which is the solar longitude that is magnetically connected to the Earth by the Parker spiral (Park et al., 2010). However, the heliolongitude distribution also has a wide dispersion, which is mainly due to the variation of the solar wind. Also, the random walk of the interplanetary magnetic field plays a partial role (Reames, 1999).

Usually, gradual SPEs last several days and are rich in protons. It is widely believed that the particles of gradual SPEs are accelerated by CME shocks. The heliolongitude distribution of these events on the visible disk of the Sun is roughly uniform. Some CMEs occurring even on the back side of the Sun can also cause gradual SPEs observed near Earth. The full halo CMEs with $V \geq 1{,}500$ km/s have the highest probability of triggering SPE (Park et al., 2012). Generally, the flux of the proton event corresponding to the CMEs in the western hemisphere quickly peaks at the beginning, while the flux of the event corresponding to the eastern hemisphere rises slowly (Cane et al., 1988; Reames, 1999).

CMEs are often associated with flares, and the correlation is related to the duration of flares. A small part of CMEs is associated with prominence bursts. It is not easy to distinguish the sources of SPEs, and many SPE events are blended events driven by both CMEs and flares. It means these SPEs involve two different acceleration mechanisms. Cane and Kallenrode pointed out that the acceleration information of energetic particles can be found in the abundance of heavy ions (Kallenrode et al., 1992; Cane et al., 2003).

As coronal mass ejections (CMEs) occur, huge clumps of material from the solar atmosphere are ejected into interplanetary space, and these clumps take on the structure of interplanetary magnetic ropes or magnetic clouds. The CMEs can cause magnetic storms when they cause a continuous increase in the southward component of the interplanetary magnetic field (Gonzalez et al., 1999; Burlaga et al., 2002). In SPEs, the protons are mainly injected into the outer radiation belt ($L \geq 4$). But for the SPEs accompanied with strong magnetic storms, the protons can be injected into the lower L layers, resulting in a trapped protons belt. Hudson et al. reported a long-term trapped protons belt with 10.7 MeV energy in the region of $L = 3.5 \sim 4$, which was caused by SPEs accompanied with large magnetic storms. This result was observed in 1990–1991 by CRRES, and it is a geostationary transfer orbit satellite. Hudson also gave an explanation for the formation of the new trapped proton band that the induction electric field accompanying storm sudden commencement (SSC) transports particles radially inward, and injects energetic protons deeply into the inner magnetosphere. Due to the high magnetic field strength in the inner magnetosphere, the energetic protons are easily trapped. (Hudson et al., 1997; Hudson et al., 1998). The protons in the inner radiation belt are considerably stable for a lengthy period of time and usually vary with the 11-year solar activity cycle (Li et al., 2001; Domingos et al., 2017). However, the outer boundary of the inner radiation belt also has some fluctuations when strong geomagnetic storms occur. Zhang et al. reported the proton loss of the inner radiation belt during the geomagnetic storm of 2018 based on ZH-1 satellite observation. The non-adiabatic magnetic field line curvature scattering plays a significant role in the proton loss mechanism within the energy level of 30–100 MeV(Zhang Z.-X. et al., 2021).

ZH-1 is the first space-based platform in China for both earthquake observation and geophysical field measurement. A space platform is established for monitoring global space electromagnetic waves/fields, ionospheric plasma, high-energy particles, and space weather. On 2 February 2018, ZH-1 was launched into solar synchronous orbits with an altitude of 507 km, 97° inclination. The orbit cycle is 94.6 min, and the ascending node is 14:00 p.m. with a revisiting period of 5 days (Shen et al., 2018).

In previous work, ZH-1 has got many results in the study of perturbations in the ionosphere and radiation belts during the geomagnetic storms (Yang et al., 2019; Zhang et al., 2020; Palma et al., 2021; Zhang Z. et al., 2021; Zhima et al., 2021). The SPEs may cause battery damage and the single-particle effect on MEO and GEO satellites in orbit (Tylka et al., 1996; Jackman et al., 2008). Therefore, the study of SPE not only has scientific significance but also has practical meaning to astronaut safety and space mission execution. In this article, we report three events during the on-orbit period of ZH-1: the first event is a gradual SPE in November 2020, the second event is an impulsive SPE in May 2021, and the third event is a geomagnetic storm in November 2021 following the occurrence of SPEs. We take full advantage of the characteristics of the sun-synchronous orbit, and the ability to observe X-rays, high-energy protons, and electrons with high-energy resolution simultaneously. Combining data from NOAA-19, GOES, and SOHO satellites, we analyze the driving mechanisms of the two typical lower energy (mainly $\leq 10MeV$) SPEs and one geomagnetic storm event as mentioned above.

## 2 DATA INTRODUCTION

ZH-1 satellite carries eight scientific payloads, of which the high-energy particle package (HEPP) consists of a high-energy band probe (HEPP-H), a low-energy band probe (HEPP-L), and a solar X-ray monitor (HEPP-X) (Li et al., 2019). Besides the HEPP, the ZH-1 satellite also carries another independent particle detector which was developed by the Italian Space Agency named High Energy Particle Detector (HEPD) (Picozza et al., 2019).

HEPP-L is installed on the side of the ZH-1 satellite facing the Earth (YOZ) and has an angle of 20° with the Sun–Earth line. HEPP-L can measure the electron fluxes with energy ranging from 0.1 to 3 MeV and the proton fluxes with an energy of

2–20 MeV. The energy ranges are divided into 256 energy channels with energy resolution $\leq 8.9\%$ at 1 MeV for electron and $\leq 7\%$ at 2–20 MeV. The maximum field of view of HEPP-L is $100^{\circ} \times 30^{\circ}$, it is composed of nine silicon slice detector units and the nine units are divided into two groups according to their field of view: five units with a narrow half angle of 6.5° and four units with a wide half angle of 15° (Li et al., 2019). No significant changes in higher energy protons were observed by the detector HEPP-H during the SPEs in 2020 November and 2021 May.

HEPP-X is an SDD detector with Si installed in the skyward direction. The half angle of the field of view of HEPP-X is $30^{\circ} \times 50^{\circ}$. The angle between the main axis of HEPP-X and the $+Y$ direction to the Sun is 70°. It can detect photon counts in the energy range of 0.9–35 keV with a time resolution of 1s, the energy resolution of HEPP-X is 170 eV@5.9 keV. When the satellite operates on the night side, the shading of the Earth

interferes with the X-ray observation, so HEPP-X can achieve 11.5 h of solar observation each day (Li et al., 2019).

In addition, in this work, we also use NOAA-19 satellite proton data and GOES satellite X-ray data for comparison with ZH-1. Also, we analyze the CME images from the SOHO satellite to identify the source of the SPEs. The NOAA-19 satellite has a sun-synchronous orbit launched by NOAA (American National Oceanic and Atmospheric Administration), with an orbit altitude of 804 km, inclination of 98.6°, and orbit cycle of 101.1 min (Evans and Greer, 2004). The satellite carries MEPED detector which can detect protons and electrons, consisting of MEPED-0 and MEPED-90. A 0° telescope is mounted on the three-axis stabilized NOAA spacecraft such that the center of the field of view of each detector is directed approximately outward along the local zenith, whereas the 90° telescope is mounted perpendicular to the 0° telescope (Rodger et al., 2010). GOES series satellites are geosynchronous orbit satellites developed by NOAA and NASA (American National Aeronautics and Space Administration) operating at an altitude of 36,000 km. It carries a space environment detector to monitor high-energy particles and solar X-rays and is widely used in space weather monitoring and early warning. SOHO, the Solar and Heliospheric Observatory, is a project of international cooperation between ESA and NASA to study the Sun, from its deep core to the outer corona, and the solar wind. The LASCO instrument is one of 12 instruments included in SOHO. The LASCO instrument is a set of three coronagraphs that image the solar corona from 1.1 to 32 solar radii (Brueckner et al., 1995). The data of GOES and NOAA-19 are downloaded from the NOAA National Geophysical Data Center at https://satdat.ngdc.noaa.gov/. The data of SOHO can be downloaded at http://cdaw.gsfc.nasa.gov/CME_list/.

# 3 OBSERVATION OF FLARES AND SPES

## 3.1 Flare Observation From HEPP-X

A solar flare is an intense brightening of partial regions of the solar atmosphere (mainly in the chromosphere and the corona), accompanied by strong electromagnetic radiation and a stream of energetic particles of a wide energy range. When a solar flare erupts, the protons travel through the corona by diffusion, reach the root region of the interplanetary magnetic fields (IMF) located in the corona, and then propagate along with the open magnetic field lines and through the interplanetary to near-Earth space (Cane et al., 1988). It is found that the probability of SPE occurrence strongly depends on the heliolongitude of the flare. Flares occurring between 30°W and 90°W have the greatest probability of inducing SPEs (Park et al., 2010).

HEPP-X can detect photons with energy of 0.9–35 keV, divided into 1,024 energy channels. Each energy channel has a photon count rating in unit (counts/s). To compare with other satellite data, we convert the photon counts to X-ray flux in units ($W/m^2$) with the formula:

$$Flux_{X-ray} = \frac{E_{photon} \times Counts_{photon} \times 1.6 \times 10^{-16}}{S \times Effi}$$

where $E_{photon}$ is the energy of one photon and $Counts_{photon}$ denotes the detected count rating of photons. $1.6 \times 10^{-16}$ is the energy conversion constant with the unit J/keV; $S$ is the sensor area of HEPP-X with the value of $3.14 \times 10^{-6} m^2$; and $Effi$ denotes the detection efficiency of 95%@10 keV, which is obtained from the ground calibration experiment.

The X-ray flux enhancement is observed before both SPE events. **Figure 1A** shows the energy and flux distributions of the M4.4 class X-ray flare observed on 29 November 2020. And **Figure 1B** shows the C9.4 class flare observed on 28 May 2021. The energy range of both the two flares covers 2.3–5 keV and the X-ray flux shows a significant increase compared to the quiet time. By comparing the observations of ZH-1 and GOES satellites, we find that the occurrence time of X-ray peaks is basically consistent, as shown in **Table 1**. The time difference of several minutes is due to the shading of the Earth which affects the observation of X-rays when ZH-1 is operating on the night side. It is reasonable as long as the difference is less than half of the ZH-1 orbital period (47.3 min).

We integrated the X-ray fluxes on all energy channels to obtain the total flux value. **Figures 1C** and **1D** show the orbit paths of the two flare observations. and **Figures 1E and 1F** are a more direct display of the X-ray fluxes in the peak flux orbits. It should be noted that HEPP-X also responds to electrons, so HEPP-X has a higher measurement value in the South Atlantic Anomaly (SAA) region. For the M4.4 flare on 29 November 2020, ZH-1 is operating in the SAA region. The peak of X-ray fluxes is $1.0 \times 10^{-6}$ $W/m^2$, which is much higher than the quiet time ($10^{-8}$ to $10^{-7}$ $W/m^2$). For the C9.4 flare on 28 May 2021 observed in the non-SAA region, the peak of X-ray fluxes is $3.1 \times 10^{-7}$ $W/m^2$, also much higher than in the quiet period ($10^{-9}$ to $10^{-8}$ $W/m^2$).

## 3.2 HEPP-L Observation of Two SPEs

### 3.2.1 A Gradual SPE in November 2020

**Figure 2** shows the space environment before the gradual SPE in November 2020 (**Figure 2A**), the impulsive SPE in May 2021 (**Figure 2B**), and the geomagnetic storm in November 2021 (**Figure 2C**). From the top to the bottom are the solar wind dynamic pressure (nPa), geomagnetic index Kp, equatorial ring current index Dst (nT), interplanetary magnetic field component Bz (nT), F10.7 index, sunspot number, and solar wind speed (km/s).

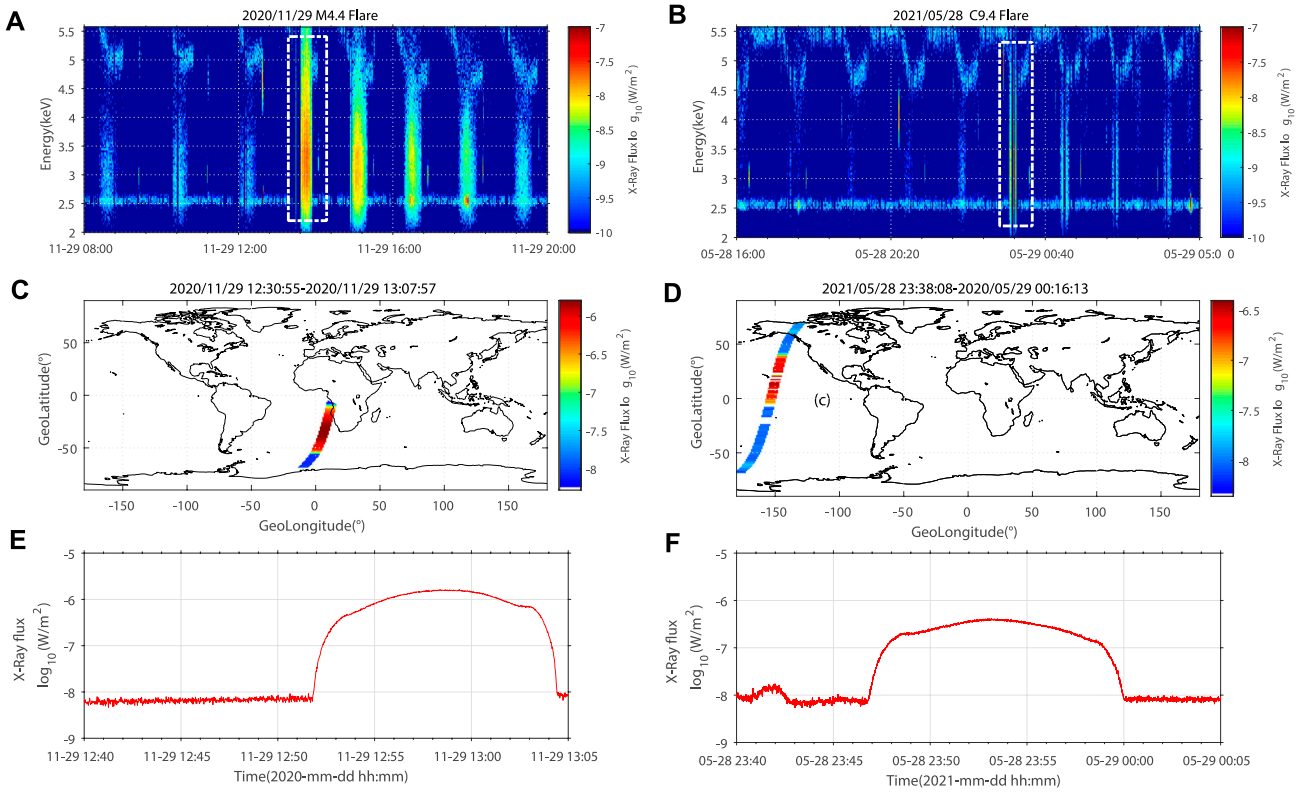


**FIGURE 1 |** X-ray fluxes before the two SPEs measured by HEPP-X. **(A,C,E)** The M4.4 flare flux distribution before 2020 gradual SPE. **(B,D,F)** The C9.4 flare flux distribution before 2021 impulsive SPE.

**TABLE 1 |** The time difference of X-ray flux peak of flare observations between ZH-1 and GOES satellite.

| Date | Time of Flux Peak on ZH-1 | Time of Flux Peak on GOES | Time Difference |
|---|---|---|---|
| 2020/11/29 | 12:59 UTC | 13:11 UTC | -12 min |
| 2020/12/07 | 16:45 UTC | 16:32 UTC | +13 min |
| 2021/05/28 | 23:52 UTC | 23:13 UTC | +39 min |

**Figures 3** and **4** show the observations and evolutions of X-ray fluxes from HEPP-X, electron fluxes (0.1–3 MeV), and proton fluxes (2.5–6.9 MeV, 6.9–20 MeV) from HEPP-L, and proton fluxes (2.5–6.9 MeV) from NOAA with L-shell value. For X-rays, we only take into account data on dayside with a time resolution of 1 minute. Proton and electron measurements are color coded in logarithm scale and sorted in L-shell (L bin width: 0.1) with a time resolution of 3 h.

According to the observations in **Figure 2A**, the space environment before the 2020 SPE is considerably calm. The F10.7 and sunspot number reached a maximum on November 29 with sunspot number 84. The solar wind speed had a small increase on November 29, from 400 km/s to 500 km/s.

On 29 November 2020 at 12:59 UTC, a significant X-ray flux enhancement was observed with a peak X-ray flux at 1.0, ×, $10^{-6}$ ($W/m^2$), shown in **Figure 3A**. The geosynchronous satellite GOES observed an M4.4 flare at 13:11 UTC from sunspot AR2786. According to SOHO satellite observations, this flare was accompanied with a full and fast CME, but the CME was not facing toward the Earth at the beginning. One day later, on November 30 at 10:00 UTC, proton fluxes started to increase, shown in **Figures 3B** and **3C**. The increased protons are mainly located in the outer radiation belt with L values from 5 to 9. The maximum flux of 2.5–6.9 MeV protons reaches 4,982 $cm^{-2}s^{-1}sr^{-1}$, and the maximum flux of 6.9–20 MeV protons reaches 550 $cm^{-2}s^{-1}sr^{-1}$. On December 7, a C7 flare erupted with a small CME from sunspot AR2790. This event caused a slight increase in proton flux again on December 8 and lasted for 1 day. 0.1–0.3 MeV electron flux does not show a significant increase (see **Figure 3E**).

To compare the proton fluxes observed by ZH-1 and NOAA-19 in the same time period, we investigate the evolution of proton data at 2.5–6.9 MeV with 2s time resolution from the NOAA P5-90 probe (see **Figure 3D**). It is obvious that the NOAA observations are approximately consistent with the ZH-1 observations, and the proton fluxes are in the same order of magnitude. The flux value of ZH-1 is slightly higher than NOAA because the ZH-1 collects data from a wider pitch angle range. In addition, the two satellites have different operating heights, energy ranges, and installation directions. It is hard to accurately compare the flux values. Compared to other similar satellite, the observation advantages of ZH-1 brings much more significance to this report.

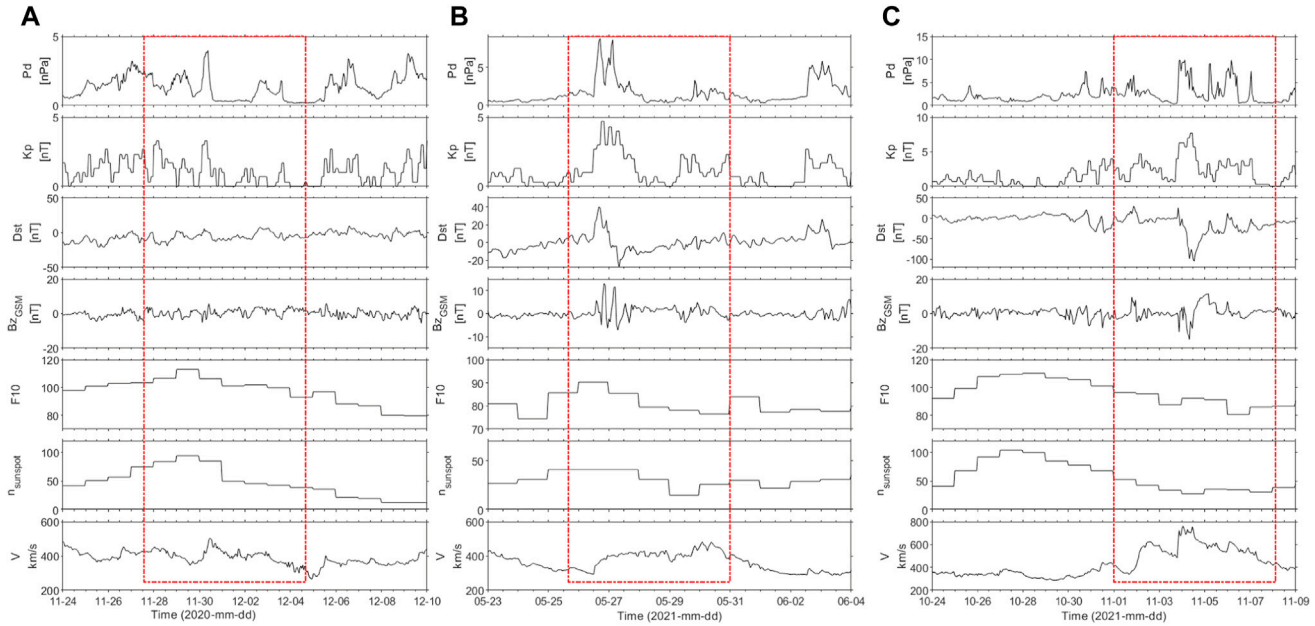


**FIGURE 2 |** The space weather index for these three typical events **(A)** for SPE in November 2020, **(B)** for SPE in May 2021, and **(C)** for geomagnetic storm in November 2021.

It is clear that this event belongs to a gradual SPE, and the proton flux does not show a significant increase immediately after the M4.4 flare occurred on November 29 at 13:00 UTC. We can conclude that the increase of proton fluxes on November 30 is mainly driven by the CME and ICME shocks because the flare-accelerated particles will reach the Earth within a few minutes to a few hours. After that, the shocks driven by the CME and ICME are likely the only source to accelerate particles.

### 3.2.2 An Impulsive SPE in May 2021

**Figure 2B** shows the activity index of space environment before the 2021 SPE. On May 26 and 27, a small geomagnetic storm (Kp = 5) occurred, while the solar wind speed increased from 300 km/s up to about 450 km/s, and the sunspot number was around 50. **Figure 4A** shows a significant enhancement in X-ray fluxes at 23:52 UTC on 28 May 2021, with peak X-ray fluxes of $3.1 \times 10^{-7}$°(W/m$^2$). The GOES observed a C9.4 flare at 23:18 with the position at N21°W63° (sunspot AR2824). Following the flare occurrence, the proton flux increased significantly at a rapid speed, shown in **Figures 4B** and **4C**. The maximum flux of 2.5–6.9 MeV protons reached 4,274.1°cm$^{-2}$s$^{-1}$sr$^{-1}$ and lasted for about 1 day. The 6.9–20 MeV proton maximum flux reached 1,000.6 cm$^{-2}$s$^{-1}$sr$^{-1}$ and lasted for only several hours. The 0.1–0.3 MeV electron fluxes did not show significant changes, as shown in **Figure 4E**. **Figure 4D** gives the results of the NOAA P5-90 probe showing that the 2.5–6.9 MeV proton flux enhancement is also demonstrated during the same period, which is consistent with the ZH-1 results.

By investigating the CME observations from the SOHO satellite, this C9.4 flare is not accompanied with a fast full halo CME. The source longitude of the flare is near 63°W, which is near the solar longitude that is magnetically connected to the Earth by the Parker spiral. The flares occurring in this region can rapidly reach the Earth along the magnetic field lines. The occurrence probability of flare-driven SPE is strongly correlated with the heliolongitude of the flare source as aforementioned, even though this flare was only C9.4 class. Therefore, we can infer that this SPE is mainly driven by the solar flare. By the way, conversely, X-class flares occurring in the eastern hemisphere are hardly likely to induce SPE (Park et al., 2010). Based on the profile of the proton flux evolution, this event is thought to be an impulsive SPE.

### 3.2.3 Global Distribution of Protons

**Figure 5** shows the global distribution of the proton fluxes observed by the HEPP-L during the quiet and SPE periods, with energy divided into 2–10 MeV and 10–20 MeV in 1 ° × 1 ° pixel. Protons are mainly concentrated in the SAA during quiet time, shown in **Figures 5C** and **5D**. This is a region full of captured particles due to the deviation of the geomagnetic dipole center relative to the Earth's center and the tilt of the magnetic axis relative to the Earth's rotation axis (Heirtzler, 2002). The latitude and longitude values of the SAA flux peak in the SAA region have ever been estimated based on ZH-1 satellite data (Zhang Z.-X. et al., 2021).

**Figures 5A** and **5B** show the global distribution of proton fluxes during the November 2020 SPE. Energetic protons injected during the SPE are mainly distributed at high latitudes ≥±55°, and the latitude that solar energy particles can reach is related to the cutoff rigidity. During large geomagnetic storms, the geomagnetic field is warped which induces solar energy particles to reach lower latitudes. This compression can reach at most up to about 15° toward

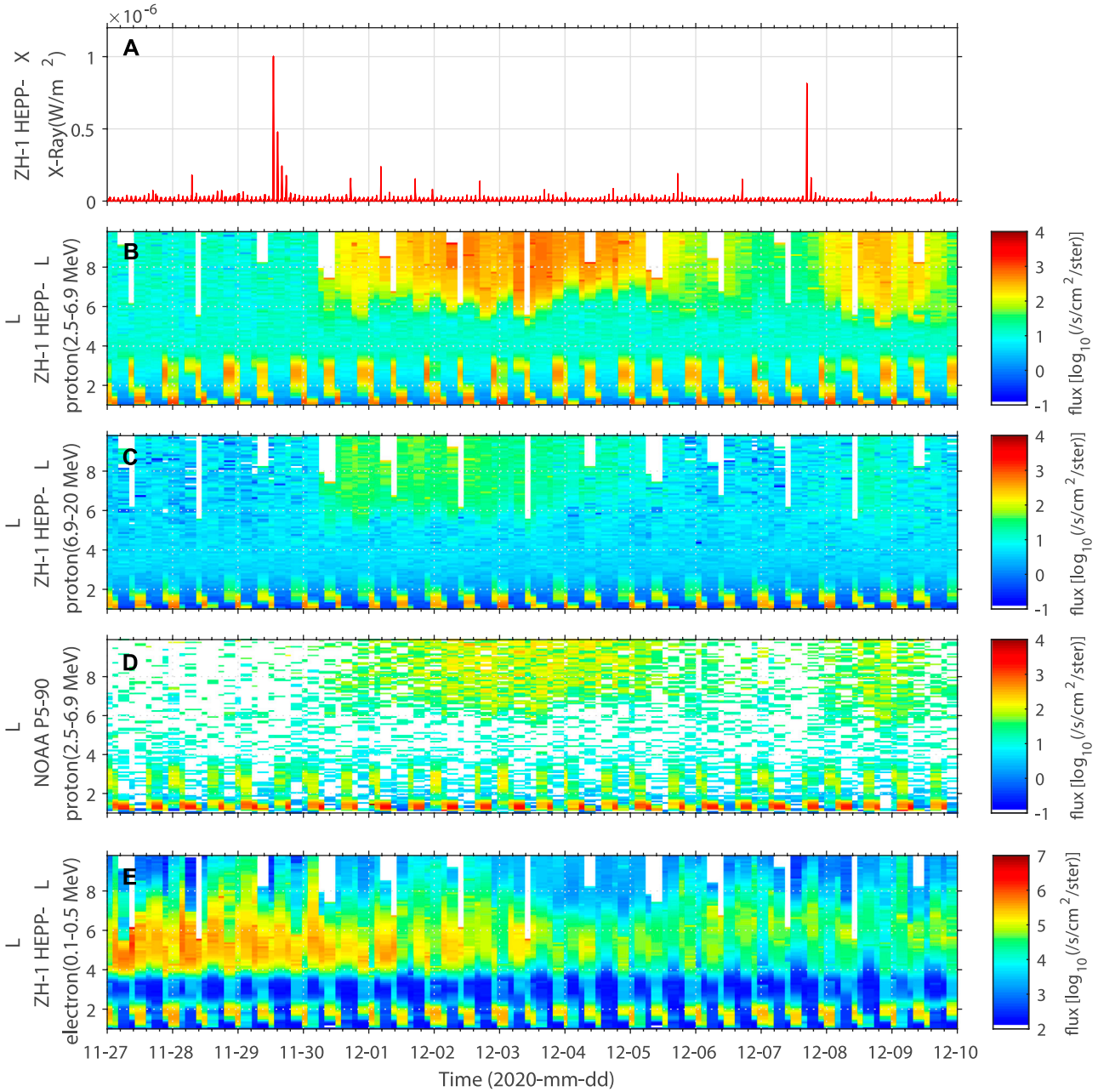


**FIGURE 3 |** The evolution of X-rays, protons, and electrons during the gradual SPE from 27 November 2020 to 10 December 2020. **(A)** X-ray fluxes observed by HEPP-X. **(B,C)** The proton fluxes observed by ZH-1 with energies of 2.5–6.9 MeV and 6.9–20 MeV. **(D)** The proton fluxes from the NOAA-19 satellite. **(E)** 0.1–0.5 MeV electron flux distribution from ZH-1.

the equator, exposing lower latitudes to the harmful radiation environment (Smart and Shea, 2003). **Figure 6** shows more directly the daily variation of proton fluxes in three regions during the SPE occurrence, namely, the SAA region (longitude −100° ~ 40°, latitude −40° ~ 0°), the high-latitude region (latitude 50° ~ 70°, -70° ~ – 50°), and other low-latitude regions (latitude 0° ~ 50°). We can find the proton fluxes in high-latitude regions increase significantly during SPEs, but not in lower latitude regions.

### 3.2.4 Flux Evolution of SPEs in Different Energies

HEPP-L has a high-energy resolution, it divides the 2–20 MeV protons into 256 energy channels. **Figure 7** shows the evolution of the 2–16 MeV proton fluxes with energy intervals in 2 MeV corresponding to $L$ = 5 ~ 9. We can see that the higher energy protons arrive at the satellite faster than the lower energy protons and the latter last for a longer time. For the impulsive SPE driven by flares, the protons travel along the magnetic lines, arrive at the

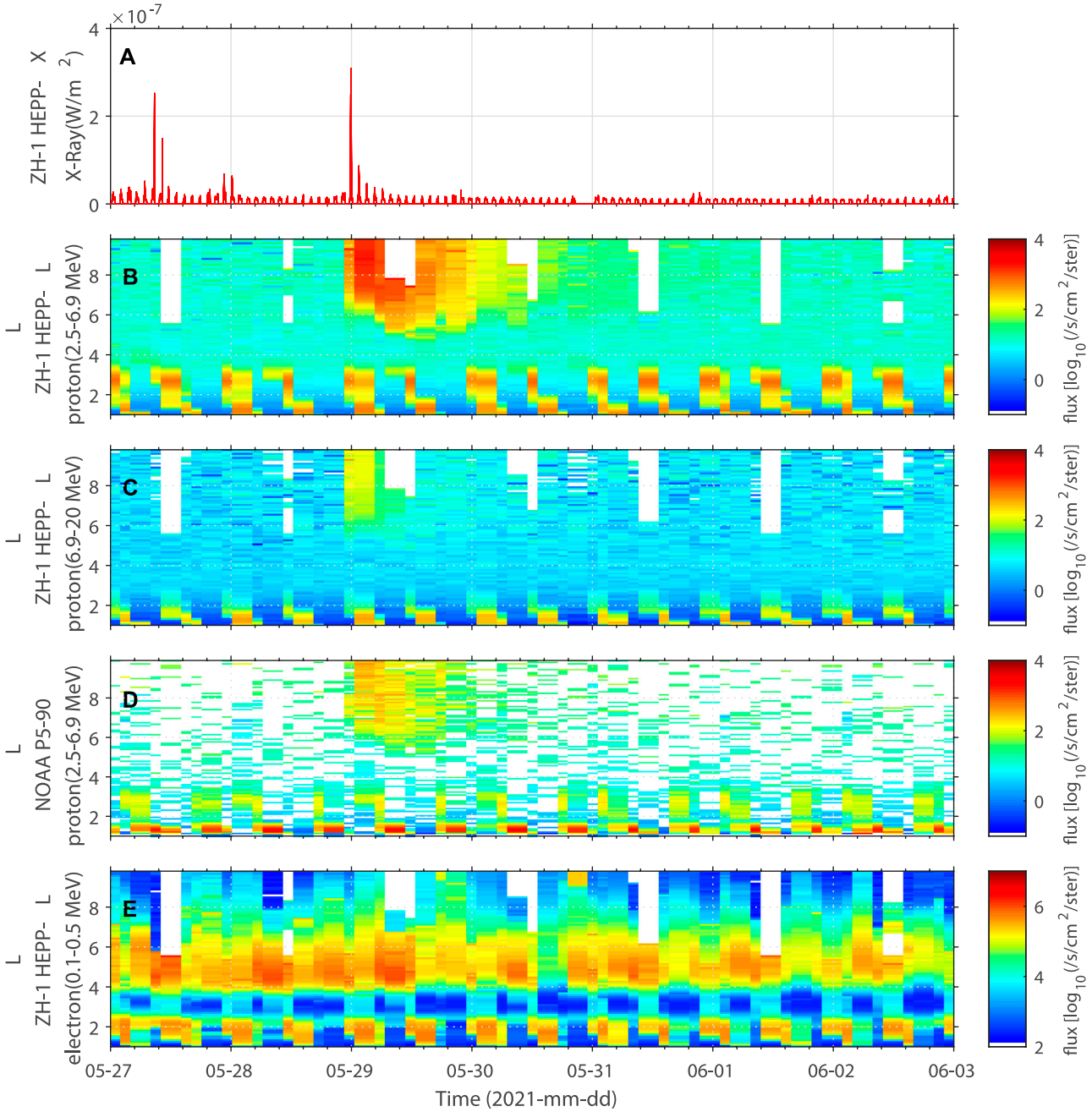


**FIGURE 4 |** The evolution of X-rays, protons, and electrons during the impulsive SPE from 27 May 2021 to 3 June 2021. **(A)** X-ray fluxes observed by HEPP-X. **(B)**, **(C)** The proton fluxes observed by ZH-1 with energies of 2.5–6.9 MeV and 6.9–20 MeV. **(D)** The proton fluxes from the NOAA-19 satellite. **(E)** 0.1–0.5 MeV electron flux distribution from ZH-1.

Earth after a few hours, and then drop rapidly. For the gradual SPE, shown in **Figure 7A**, it has a smoother time-intensity profile and longer duration than impulsive SPE. The flux evolution of SPEs also depends on the source longitude of the flare, the angular width of the CME, the solar wind speed, and so on. It is believed that flares can accelerate particles at higher energies more often than the interplanetary shocks from CMEs (Gloeckler, 1984).

### 3.2.5 Pitch Angle Distribution of Trapped Protons Related to SPE

The pitch angle distribution of particles is an important indicator of the particle dynamics in the radiation belt, which provides an important reference for studying the source, acceleration, and loss of particles. In this article, we refer to D. G Sibeck's classification of pitch angle to classify the distribution of pitch angle into three

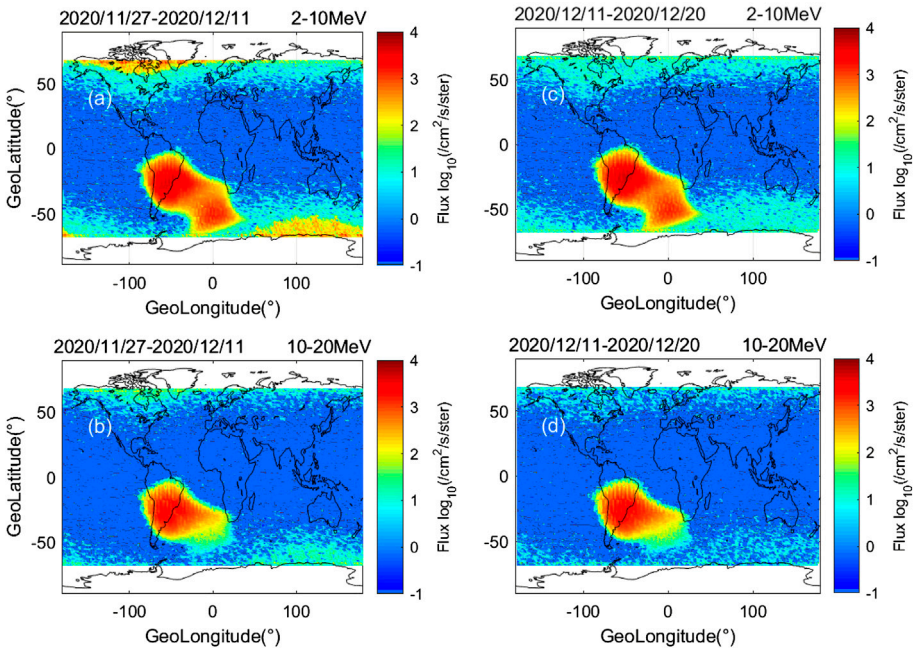


**FIGURE 5 |** Global distribution of proton fluxes during SPE occurrence and quiet time observed by ZH-1 **(A,B)** for the SPE period and **(C,D)** for the quiet time. The energy range of **(A)** and **(C)** is 2–10 MeV and **(B)** and **(D)** is 10–20 MeV.

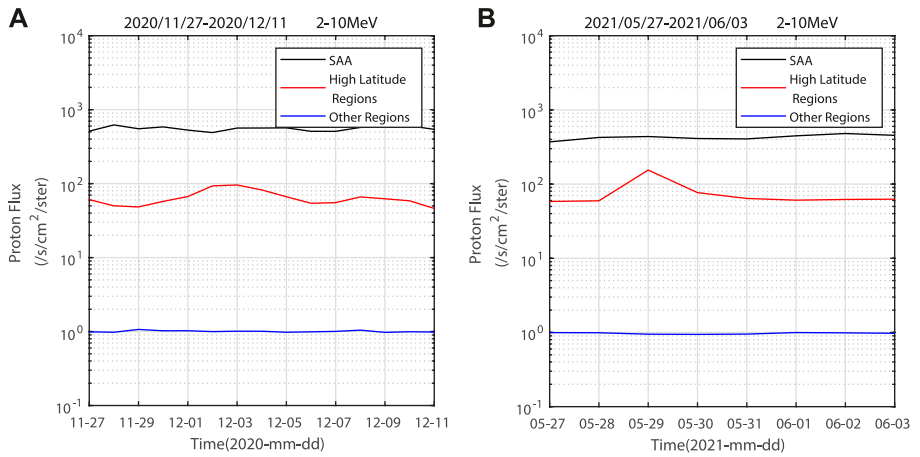


**FIGURE 6 |** Daily variation of proton fluxes in different regions during the SPEs. The black line refers to the SAA region, the red line refers to the high latitude region, and the blue line refers to the other regions.

types: pancake, butterfly, and flattop (Sibeck et al., 1987). The pancake distribution features a peak near 90° and a smooth decline toward a small pitch angle. The observed values in the range less than 60° and more than 120° are almost 0. The butterfly-type distribution is characterized as valley flux at the 90°. Flattop-type distributions have approximately equal fluxes around the 90° pitch angles. ZH-1 covers a very narrow range of local time, so we do not consider the variation of the pitch angle with local time (**Figures 8C,F**), but only distinguish the difference between the dayside and the nightside.

We choose 5 days of data for both the SPE period and the background period, showing the pitch angle distributions of 2–6.9 MeV and 6.9–20 MeV protons at dayside and nightside, respectively, with the L value range $L = 8 \sim 10$ (see **Figure 8**). The protons of 6.9–20 MeV show a significant butterfly-type pitch angle distribution, and the protons of 2–6.9 MeV look approximately between flattop and butterfly type. The possible reasons for butterfly distribution may come from the drift shell splitting and the magnetopause shadowing (Sibeck et al., 1987; Hudson et al., 2014). It may also be developed from the butterfly

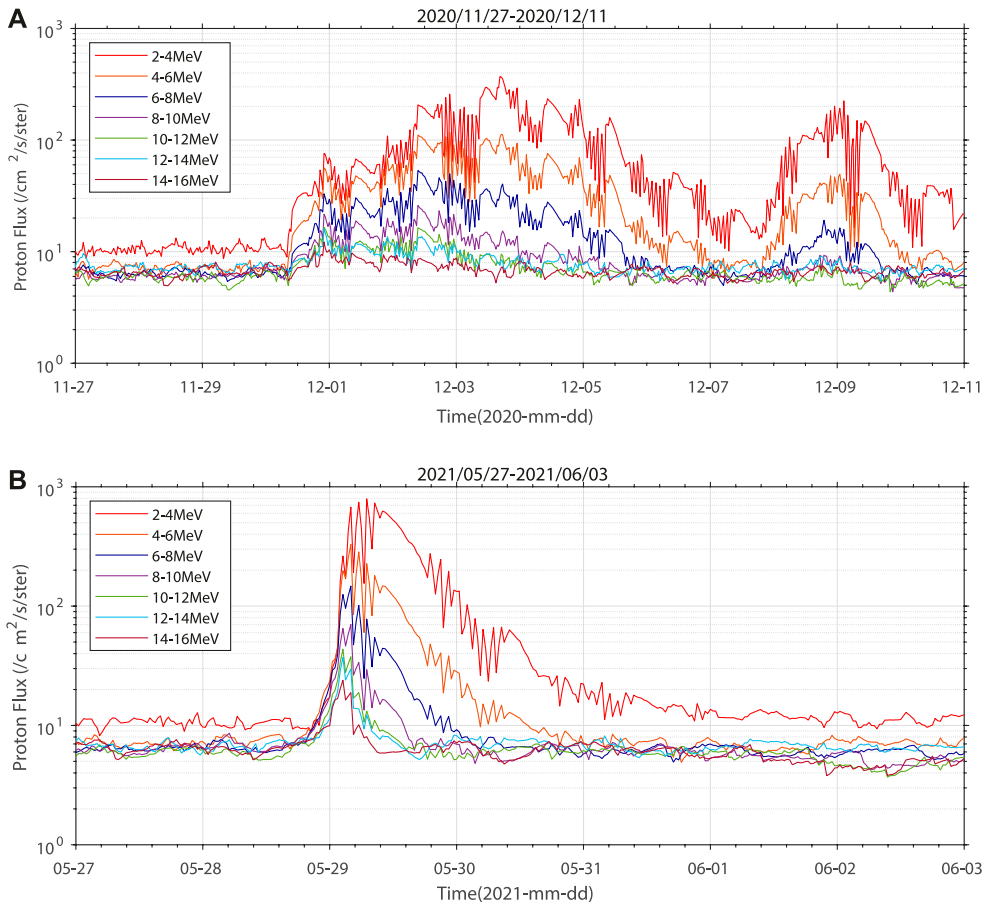


**FIGURE 7 |** The evolution of the proton fluxes at different energies corresponding to $L = 5 \sim 9$ **(A)** for the gradual SPE of 2020 and **(B)** for the impulsive SPE of 2021.

distribution in the high L value through an inward radial diffusion acceleration mechanism, or from the pancake distribution in the low L value region through a pitch angle diffusion mechanism (Yang et al., 2014). The accurate mechanism of pitch angle formation needs further study in the future.

## 3.3 Another Typical Event of Geomagnetic Storm Following the SPE and Solar Flare

Besides the aforementioned SPEs, here we report another typical space weather event, that is, an occurrence of one geomagnetic storm following the SPE and solar flare.

As we enter the 25th solar cycle, solar activity begins to be more active. At 15:35 UTC, on 28 October 2021, an X1.1 flare with a full halo CME erupted from Earth-facing sunspot AR2887. This event caused SPE as shown in **Figures 9C–G**. Three days later, on November 1, sunspot AR2887 erupted again, producing an M1 flare and a CME. On November 2, another fast full halo CME accompanied with an M1.7 flare was ejected from sunspot AR2891. The faster CME of November 2 caught up and swept up the slower CME of November 1 and caused tangled magnetic fields and compressed plasma which can spark geomagnetic storms well. The CME occurred on November 1 and 2 resulting in an enhancement of proton flux on November 4, and the geomagnetic index Dst dropped to −101, as shown in **Figures 2C** and **9A**. In other words, complex structure CMEs are the source of SPE and geomagnetic storm on November 4. This explanation is also consistent with the space environment alert website (https://spaceweather.com/). From **Figures 9E–G**, before the onset of the geomagnetic storms, the 0.5–1.0 MeV high-energy electrons are mainly distributed in the outer radiation belt at $L = 4 \sim 6$. During the main phase of the November 4 magnetic storm, there was a significant increase in electron flux in all three energy bands as the solar wind dynamic pressure increased. When the Dst index reached its minimum (-101), the boundary of the outer radiation electron moves downward, and the electrons ($\leq 1MeV$) are injected and filled the slot region ($L = 2 \sim 3$).

The interplanetary driving sources of geomagnetic storms are mainly CMEs and CIRs. The primary causes of geomagnetic storms on the Earth are strong dawn-to-dusk electric fields associated with the passage of southward directed IMF, which affect the Earth for sufficiently long intervals of time. The solar wind energy transfer mechanism is the magnetic reconnection between the IMF and the Earth's magnetic field (Gonzalez et al.,

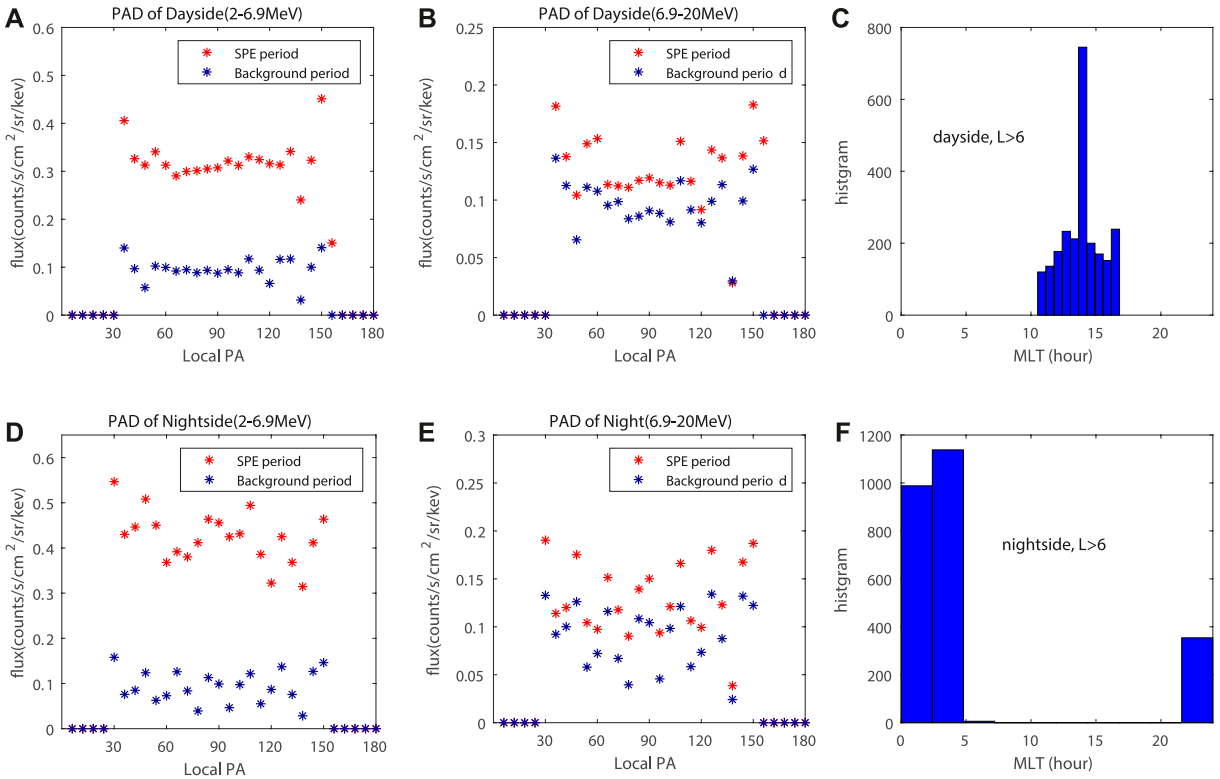


**FIGURE 8 |** Pitch angle distribution of protons in the outer radiation belt during SPE, **(A)** and **(B)** at dayside, **(D)** and **(E)** at nightside. Red dots indicate flux distribution during the SPE period. Blue dots indicate quiet time. **(C)** and **(F)** are the local time covered by ZH-1.

1994; Gonzalez et al., 1999). For magnetic storms caused by CMEs, the southward magnetic field (Bs) in shock sheaths and ICMEs or magnetic clouds contribute to the generation of the geomagnetic storms (Burlaga et al., 2001). Such magnetic storms typically occur 3–5 days after the CME, or even less. By statistics of CME-related geomagnetic storm events for 1996–1999, it is found that the halo CMEs occurring within 50° from the center meridian of the heliopause are more likely to cause geomagnetic storms (Cane et al., 2000). The principle of CIR-driven magnetic storms is similar to CMEs, also due to magnetic reconnection. The southward component of the IMF is provided by the Alfvén perturbation in the high-speed solar wind from the coronal hole. CIR-driven magnetic storms mainly occur during the declining period of the solar cycle, when there is less solar eruption activity but more solar wind high-speed flow (Feynman and Gu, 1986). Usually, CIR-driven magnetic storms are smaller than CME-driven storms and have a cycle of 27-day recurrence (Tsurutani et al., 1995).

Sometimes, the source of a magnetic storm may not come from a single CME but from the interaction of multiple CMEs. CMEs will generate some interplanetary composite structures after catching up and colliding during propagation (Burlaga et al., 2002). By statistics of the interplanetary sources of 37 long-lived strong magnetic storms during 1998–2002, they concluded that 64.9% (24 of 37) of magnetic storms are caused by multiple CMEs, 21.6% (7 of 37) are caused by single CME, and 13.5% are caused by CIR (5 of 37) (Xie et al., 2006). The intensity of geomagnetic storms is well correlated with the number of CMEs, more CMEs result in stronger and longer-lasting geomagnetic storms. The geomagnetic storm in November 2021 was a typical event since it was generated by the collision of multiple CMEs and had a large impact on the space weather environment worthy of our attention.

## 4 SUMMARY AND DISCUSSION

This article aims to present the solar flare X-ray and solar proton events based on ZH-1 data, which is highly advantageous to exhibit the observation characteristics of these space weather, such as wide energy ranges, high-energy resolution, and good particle identification, compared to NOAA data. What's more, ZH-1 is a sun-synchronous orbit satellite and can observe all the solar proton events in wide L-shells (covering $L = 1 \sim 10$), compared to the synchronous orbit of GOES. So based on the advantage of the ZH-1 satellite, we analyze the recently occurred solar proton event and also provide more confidence to scientists to use ZH-1 data for study of space weather. The following results are obtained:

- Before the two SPEs occurred on 29 November 2020 and on 28 May 2021, significant X-ray flux enhancements are

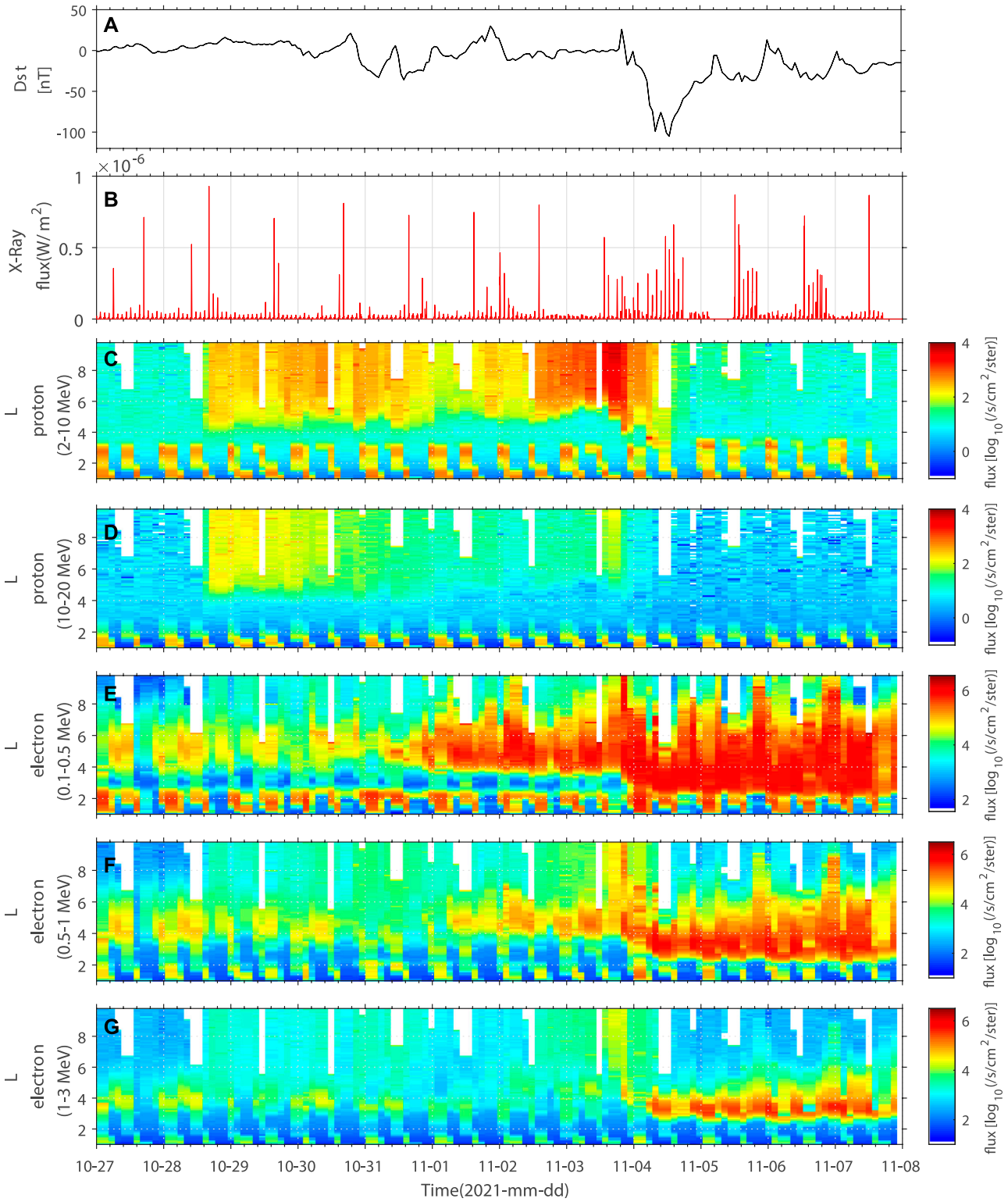


**FIGURE 9 |** The evolution of the Dst index, X-rays, protons, and electrons during the SPE and induced geomagnetic storm from 27 October 2021 to 8 November 2021. **(A)** Evolution of the Dst index. **(B)** X-ray fluxes observed by HEPP-X. **(C)** and **(D)** are the proton fluxes observed by ZH-1 with energies of 2–10 MeV and 10–20 MeV. **(E)**, **(F)**, and **(G)** are the electron flux distribution at 0.1–0.5 MeV, 0.5–1 MeV, and 1–3 MeV energies, respectively.

observed by the ZH-1 satellite, and the flare time is consistent with the GOES satellite observations.

- When strong disturbances such as CMEs and flares occur, the energetic proton from the Sun will sink into the high-latitude region along the open magnetic field lines. The injection latitude can reach ±55°, corresponding to L-shell values around L = 5, and the observations are consistent with NOAA satellites.
- The gradual SPE that occurred in November 2020 was mainly driven by CME and ICME shocks, with protons reaching Earth about a day later. The impulsive SPE occurred in May 2021 SPE was mainly driven by flares, with protons reaching Earth rapidly after a few minutes.
- In addition to SPEs, CMEs causing geomagnetic storms are also reported in this work. On 28 October 2021, a full-halo CME accompanied with an X1.1 flare brought a gradual SPE. On November 2, another fast full halo CME accompanied with flare was ejected, the faster CME of November 2 caught up and swept up the slower CME of November 1 and brought a large magnetic storm on November 4.

With the advent of the space age, various space missions are in progress. It is meaningful to forecast and attempt to avoid the SPEs, flares, and CMEs in advance. Forecasting SPEs include long-term forecasting models such as King, JPL, and ESP(King, 1974; Feynman et al., 1991; Xapsos et al., 2000), and short-term forecasting models mostly utilized real-time observations of X-rays (Núñez, 2011). During solar eruptions, solar X-rays are the first to reach Earth at the speed of light, while energetic particles follow in a few hours to a few days later. Taking advantage of X-ray supervision in advance, we can try to forecast SPEs and reduce their hazards to satellites in orbit, space stations, and astronauts, which is the next work objective in the future.

## DATA AVAILABILITY STATEMENT

Publicly available datasets were analyzed in this study. This data can be found here: https://www.leos.ac.cn.

## AUTHOR CONTRIBUTIONS

LW performed the data process and wrote the original manuscript version. ZZ put forward the main idea and guide the whole analysis process of this work. XL is in charge of the reconstruction method of the ZH-1 raw data and data application method. XL designed and developed X-ray detector (HEPP-X). XS, ZZ, WC, FG, NZ, HC, and DW provided consultation on the idea and manuscript writing of the work.

## FUNDING

This study was supported by grants from the National Natural Science Foundation of China (NNSFC) (41904149 and 12173038), the Asia-Pacific Space Cooperation Organization Project (APSCO-SP/PM-EARTHQUAKE), the research grants from the National Institute of Natural Hazards, Ministry of Emergency Management of China (Grant Number: 2021-JBKY-11), and the Stable-Support Scientific Project of China Research Institute of Radiowave Propagation (A132001W07).

## ACKNOWLEDGMENTS

We are grateful for the satellite data download.

## REFERENCES

Brueckner, G. E., Howard, R. A., Koomen, M. J., Korendyke, C. M., Michels, D. J., Moses, J. D., et al. (1995). The Large Angle Spectroscopic Coronagraph (Lasco). *Sol. Phys.* 161, 357–402. doi:10.1007/bf00733434

Burlaga, L. F., Plunkett, S. P., and Cyr, O. C. S. (2002). Successive Cmes and Complex Ejecta. *J. Geophys. Res.* 107, 1266. doi:10.1029/2001JA000255

Burlaga, L. F., Skoug, R. M., Smith, C. W., Webb, D. F., Zurbuchen, T. H., and Reinard, A. (2001). Fast Ejecta during the Ascending Phase of Solar Cycle 23: ACE Observations, 1998-1999. *J. Geophys. Res.* 106, 20957–20977. doi:10.1029/2000ja000214

Cane, H. V., Reames, D. V., and von Rosenvinge, T. T. (1988). The Role of Interplanetary Shocks in the Longitude Distribution of Solar Energetic Particles. *J. Geophys. Res.* 93, 9555–9567. doi:10.1029/ja093ia09p09555

Cane, H. V., Richardson, I. G., and Cyr, O. C. S. (2000). Coronal Mass Ejections, Interplanetary Ejecta and Geomagnetic Storms. *Geophys. Res. Lett.* 27, 3591–3594. doi:10.1029/2000GL000111

Cane, H. V., von Rosenvinge, T. T., Cohen, C. M. S., and Mewaldt, R. A. (2003). Two Components in Major Solar Particle Events. *Geophys. Res. Lett.* 30, 8017. doi:10.1029/2002GL016580

Domingos, J., Jault, D., Pais, M. A., and Mandea, M. (2017). The South Atlantic Anomaly throughout the Solar Cycle. *Earth Planet. Sci. Lett.* 473, 154–163. doi:10.1016/j.epsl.2017.06.004

Evans, D. S., and Greer, M. S. (2004). *Polar Orbiting Environmental Satellite Space Environment Monitor-2 Instrument Descriptions and Archive Data Documentation*, 1.4. Boulder, Colorado: NOAA Tech. Mem.

Feynman, J., and Gabriel, S. B. (2000). On Space Weather Consequences and Predictions. *J. Geophys. Res.* 105, 10543–10564. doi:10.1029/1999JA000141

Feynman, J., and Gu, X. Y. (1986). Prediction of Geomagnetic Activity on Time Scales of One to Ten Years. *Rev. Geophys.* 24, 650–666. doi:10.1029/RG024i003p00650

Feynman, J., Spitale, G., Wang, J., and Gabriel, S. (1991). Interplanetary Proton Fluence Model: Jpl 1991. *J. Geophys. Res.* 98, 13281–13294. doi:10.1029/92ja02670

Fisk, L. A. (1978). $^3$He-Rich Flares: A Possible Explanation. *Astrophysical J.* 224, 1048–1055. doi:10.1086/156456

Gloeckler, G. (1984). Characteristics of Solar and Heliospheric Ion Populations Observed Near Earth. *Adv. Space Res.* 4, 127–137. doi:10.1016/0273-1177(84)90302-8

Gonzalez, W. D., Joselyn, J. A., Kamide, Y., Kroehl, H. W., Rostoker, G., Tsurutani, B. T., et al. (1994). What is a Geomagnetic Storm? *J. Geophys. Res.* 99, 5771–5792. doi:10.1029/93JA02867

Gonzalez, W. D., Tsurutani, B. T., and Clúa de Gonzalez, A. L. (1999). Interplanetary Origin of Geomagnetic Storms. *Space Sci. Rev.* 88, 529–562. doi:10.1023/A:1005160129098

Heirtzler, J. R. (2002). The Future of the South Atlantic Anomaly and Implications for Radiation Damage in Space. *J. Atmos. Sol.-Terr. Phys.* 64, 1701–1708. doi:10.1016/s1364-6826(02)00120-7

Hudson, M. K., Baker, D. N., Goldstein, J., Kress, B. T., Paral, J., Toffoletto, F. R., et al. (2014). Simulated Magnetopause Losses and Van Allen Probe Flux Dropouts. *Geophys. Res. Lett.* 41, 1113–1118. doi:10.1002/2014GL059222

Hudson, M. K., Elkington, S. R., Lyon, J. G., Marchenko, V. A., Roth, I., Temerin, M., et al. (1997). Simulations of Radiation Belt Formation during Storm Sudden Commencements. *J. Geophys. Res.* 102, 14087–14102. doi:10.1029/97JA03995

Hudson, M. K., Marchenko, V. A., Roth, I., Temerin, M., Blake, J. B., and Gussenhoven, M. S. (1998). Radiation Belt Formation during Storm Sudden Commencements and Loss during Main Phase. *Adv. Space Res.* 21, 597–607. doi:10.1016/s0273-1177(97)00969-1

Jackman, C. H., Marsh, D. R., Vitt, F. M., Garcia, R. R., Fleming, E. L., Labow, G. J., et al. (2008). Short- and Medium-Term Atmospheric Constituent Effects of Very Large Solar Proton Events. *Atmos. Chem. Phys.* 8, 765–785. doi:10.5194/acp-8-765-2008

Kallenrode, M.-B., Cliver, E. W., and Wibberenz, G. (1992). Composition and Azimuthal Spread of Solar Energetic Particles from Impulsive and Gradual Flares. *Astrophysical J.* 391, 370–379. doi:10.1086/171352

King, J. H. (1974). Solar Proton Fluences for 1977-1983 Space Missions. *J. Spacecr. Rockets* 11, 401–408. doi:10.2514/3.62088

Li, X., Baker, D. N., Kanekal, S. G., Looper, M., and Temerin, M. (2001). Long Term Measurements of Radiation Belts by Sampex and Their Variations. *Geophys. Res. Lett.* 28, 3827–3830. doi:10.1029/2001gl013586

Li, X. Q., Xu, Y. B., Liang, X. H., Wang, P., Zhao, X. Y., Wang, H. Y., et al. (2019). The High-Energy Particle Package Onboard Cses. *Radiat. Detect. Technol. Methods* 3, 22. doi:10.1007/s41605-019-0101-7

Núñez, M. (2011). Predicting Solar Energetic Proton Events (e > 10 mev). *Space Weather* 9, S07003. doi:10.1029/2010SW000640

Palma, F., Sotgiu, A., Parmentier, A., Martucci, M., Piersanti, M., Bartocci, S., et al. (2021). The August 2018 Geomagnetic Storm Observed by the High-Energy Particle Detector on Board the Cses-01 Satellite. *Appl. Sci.* 11, 5680. doi:10.3390/app11125680

Park, J., Moon, Y.-J., and Gopalswamy, N. (2012). Dependence of Solar Proton Events on Their Associated Activities: Coronal Mass Ejection Parameters. *J. Geophys. Res.* 117, A08108. doi:10.1029/2011JA017477

Park, J., Moon, Y.-J., Lee, D. H., and Youn, S. (2010). Dependence of Solar Proton Events on Their Associated Activities: Flare Parameters. *J. Geophys. Res.* 115, A10105. doi:10.1029/2010JA015330

Picozza, P., Battiston, R., Ambrosi, G., Bartocci, S., Basara, L., Burger, W. J., et al. (2019). Scientific Goals and In-Orbit Performance of the High-Energy Particle Detector on Board the Cses. *Astrophysical J. Suppl. Ser.* 243, 16. doi:10.3847/1538-4365/ab276c

Reames, D. V. (1999). Particle Acceleration at the Sun and in the Heliosphere. *Space Sci. Rev.* 90, 413–491. doi:10.1023/A:1005105831781

Rodger, C. J., Clilverd, M. A., Green, J. C., and Lam, M. M. (2010). Use of POES SEM-2 Observations to Examine Radiation Belt Dynamics and Energetic Electron Precipitation into the Atmosphere. *J. Geophys. Res.* 115, A040202. doi:10.1029/2008JA014023

Shen, X., Zhang, X., Yuan, S., Wang, L., Cao, J., Huang, J., et al. (2018). The State-Of-The-Art of the china Seismo-Electromagnetic Satellite Mission. *Sci. China Technol. Sci.* 61, 634–642. doi:10.1007/s11431-018-9242-0

Sibeck, D. G., Mcentire, R. W., Lui, A. T. Y., Lopez, R. E., and Krimigis, S. M. (1987). Magnetic Field Drift Shell Splitting: Cause of Unusual Dayside Particle Pitch Angle Distributions during Storms and Substorms. *J. Geophys. Res.* 92, 13485–13497. doi:10.1029/JA092iA12p13485

Smart, D. F., and Shea, M. A. (2003). The Space-Developed Dynamic Vertical Cutoff Rigidity Model and its Applicability to Aircraft Radiation Dose. *Adv. Space Res.* 32, 103–108. doi:10.1016/s0273-1177(03)90376-0

Tsurutani, B. T., Gonzalez, W. D., Gonzalez, A. L. C., Tang, F., Arballo, J. K., and Okada, M. (1995). Interplanetary Origin of Geomagnetic Activity in the Declining Phase of the Solar Cycle. *J. Geophys. Res.* 100, 21717–21733. doi:10.1029/95JA01476

Tylka, A. J., Dietrich, W. F., Boberg, P. R., Smith, E. C., and Adams, J. H. (1996). Single Event Upsets Caused by Solar Energetic Heavy Ions. *IEEE Trans. Nucl. Sci.* 43, 2758–2766. doi:10.1109/23.556863

Xapsos, M. A., Summers, G. P., Barth, J. L., Stassinopoulos, E. G., and Burke, E. A. (2000). Probability Model for Cumulative Solar Proton Event Fluences. *IEEE Trans. Nucl. Sci.* 47, 486–490. doi:10.1109/23.856469

Xie, H., Gopalswamy, N., Manoharan, P. K., Lara, A., Yashiro, S., and Lepri, S. (2006). Long-Lived Geomagnetic Storms and Coronal Mass Ejections. *J. Geophys. Res.* 111, A01103. doi:10.1029/2005JA011287

Yang, S. C., Zhang, X. G., Wang, Y., Wang, C. Q., Chang, Z., Qin, M. R., et al. (2014). Pitch Angle Distribution Research of Radiation Belt Protons Based on the Noaa Data (In Chinese). *Chin. J. Space Sci.* 34, 390–397. doi:10.11728/cjss2014.03.390

Yang, Y. Y., Zhima, Z. R., Shen, X. H., Chu, W., Huang, J. P., Wang, Q., et al. (2019). The First Intense Geomagnetic Storm Event Recorded by the China Seismo-Electromagnetic Satellite. *Space Weather* 18, 1. doi:10.1029/2019sw002243

Zhang, Z.-X., Shen, X.-H., Li, X.-Q., and Wang, Y.-F. (2021a). Proton Loss of Inner Radiation Belt during Geomagnetic Storm of 2018 Based on zh-1 Satellite Observation. *Chin. Phys. B* 30, 129401. doi:10.1088/1674-1056/ac1f00

Zhang, Z., Chen, L., Liu, S., Xiong, Y., Li, X., Wang, Y., et al. (2020). Chorus Acceleration of Relativistic Electrons in Extremely Low L-Shell during Geomagnetic Storm of August 2018. *Geophys. Res. Lett.* 47, e2019GL086226. doi:10.1029/2019GL086226

Zhang, Z., Xiang, Z., Wang, Y., Ni, B., and Li, X. (2021b). Electron Acceleration by Magnetosonic Waves in the Deep Inner Belt (L=1.5-2) Region during Geomagnetic Storm of August 2018. *JGR Space Phys.* 126, e2021JA029797. doi:10.1029/2021JA029797

Zhima, Z., Hu, Y., Shen, X., Chu, W., Piersanti, M., Parmentier, A., et al. (2021). Storm-Time Features of the Ionospheric Elf/vlf Waves and Energetic Electron Fluxes Revealed by the china Seismo-Electromagnetic Satellite. *Appl. Sci.* 11, 2617. doi:10.3390/app11062617

**Conflict of Interest:** The authors declare that the research was conducted in the absence of any commercial or financial relationships that could be construed as a potential conflict of interest.

**Publisher's Note:** All claims expressed in this article are solely those of the authors and do not necessarily represent those of their affiliated organizations, or those of the publisher, the editors, and the reviewers. Any product that may be evaluated in this article, or claim that may be made by its manufacturer, is not guaranteed or endorsed by the publisher.

frontiers | Frontiers in Earth Science

ORIGINAL RESEARCH
published: 12 July 2022
doi: 10.3389/feart.2022.866438

# Comparison of Scalar Magnetic Field Data of China Seismo-Electromagnetic Satellite and Swarm Bravo Satellite

*Zhang Jianing[1,2], Cheng Bingjun[1]*, Tong Yuqi[1,2], Miao Yuanqing[2,3], Zhou Bin[1], Pollinger Andreas[4], Zhu Xinghong[3], Yang Yanyan[5], Gou Xiaochen[1], Zhang Yiteng[1], Wang Jindong[1], Li Lei[1], Magnes Werner[4], Lammegger Roland[6], Zeren Zhima[5] and Shen Xuhui[5]*

[1]National Space Science Center, Chinese Academy of Sciences, Beijing, China, [2]University of Chinese Academy of Sciences, Beijing, China, [3]DFH Satellite Co. Ltd., Beijing, China, [4]Space Research Institute, Austrian Academy of Sciences, Graz, Austria, [5]National Institute of Natural Hazards, Ministry of Emergency Management of China, Beijing, China, [6]Institute of Experimental Physics, Graz University of Technology, Graz, Austria

OPEN ACCESS

**Edited by:**
Mirko Piersanti,
University of L'Aquila, Italy

**Reviewed by:**
Pierdavide Coïsson,
UMR7154 Institut de Physique du Globe de Paris (IPGP), France
Fan Yin,
Wuhan University, China

***Correspondence:**
Cheng Bingjun
chengbj@nssc.ac.cn

**Specialty section:**
This article was submitted to Environmental Informatics and Remote Sensing, a section of the journal Frontiers in Earth Science

**Received:** 31 January 2022
**Accepted:** 23 May 2022
**Published:** 12 July 2022

**Citation:**
Jianing Z, Bingjun C, Yuqi T, Yuanqing M, Bin Z, Andreas P, Xinghong Z, Yanyan Y, Xiaochen G, Yiteng Z, Jindong W, Lei L, Werner M, Roland L, Zhima Z and Xuhui S (2022) Comparison of Scalar Magnetic Field Data of China Seismo-Electromagnetic Satellite and Swarm Bravo Satellite. Front. Earth Sci. 10:866438. doi: 10.3389/feart.2022.866438

Based on the in-orbit magnetic field data of the China Seismo-Electromagnetic Satellite (CSES) and Swarm satellites, some research studies on the data consistency cross comparison were carried out. The condition applied is that two satellites pass by in a relatively short period of time and through the spatial location at a relatively close range, and different spatial-temporal scale standards were set, combined with the Kp index to screen for geomagnetic quiet periods. Then, with the help of the CHAOS model, indirect analysis was realized. Furthermore, the difference between the in-orbit data and model value was visualized, and the phenomenon and possible reason for data variation with time and geomagnetic latitude variation were analyzed. These analysis results are displayed in this study, which may evaluate the reliability of the satellite magnetic field detection data and the consistency of multiple satellite detection results and provide a methodological reference for carrying out similar evaluation and analysis subsequently.

**Keywords: China Seismo-Electromagnetic Satellite, Swarm Satellites, magnetometer, scalar magnetic field, cross comparison analysis**

## 1 INTRODUCTION

The China Seismo-Electromagnetic Satellite (CSES), also called ZHANGHENG-1, was successfully launched from Jiuquan Satellite Launch Center on 2 February 2018 and started in-orbit operation on 5 February 2018. CSES is the first satellite in China to provide space-based data for earthquake observation and geomagnetic field measurement (Shen et al., 2018). The High Precision Magnetometer (HPM) onboard CSES comprises two fluxgate magnetometers (FGMs) and the Coupled Dark State Magnetometer (CDSM), which is developed by the National Space Science Center, Chinese Academy of Sciences in cooperation with the Space Research Institute, Austrian Academy of Sciences and the Institute of Experimental Physics, Graz University of Technology (Cheng et al., 2015). The CDSM measures the magnitude of the field with higher accuracy and stability, thus being used to ensure the accuracy of the vector magnetic field measurement in orbit (Cheng et al., 2018). The satellite is in a sun-synchronous orbit with an altitude of approximately 507 km and an inclination angle of 97.4°. The descending node of the CSES is at around 14:00 in local

time, and the revisiting period is 5 days. The distance between adjacent orbits is about 2,650 km in 1 day and 530 km in the 5-day revisiting (Shen et al., 2018).

The Swarm satellites were successfully launched into orbit on 22 November 2013. The mission consists of three identical satellites Alpha, Bravo, and Charlie. On 17 April 2014, they formed a constellation to observe and study the Earth's magnetic field. Each satellite carries an Absolute Scalar Magnetometer (ASM) measuring scalar magnetic field intensity and a Vector Fluxgate Magnetometer (VFM) measuring vector components. The ASM was designed by Laboratoire d'électronique des technologies de l'information, Commissariat à l'énergie atomique et aux énergies alternatives (CEA-Leti) in Grenoble and developed in close partnership with Centre National d'Etudes Spatiales (CNES), with scientific support from Institut de physique du globe de Paris (IPGP). It has the characteristic of being capable of continuously measuring both scalar and vector data at the same time, benefiting from its innovative design (Fratter et al., 2016). Alpha and Charlie satellites started their missions at an altitude of about 462 km, flying almost side by side in a near-polar orbit with an inclination of 87.35°. Bravo has an altitude of about 511 km and an inclination angle of about 87.75°. According to the mission design, the orbital planes of the three satellites drift slowly in local time, with a drifting rate of 2.74 h per month for Alpha and Charlie and a drifting rate of 2.61 h for Bravo (Olsen and Floberghagen, 2018).

The cross comparison and validation between satellites is an effective means of space exploration, which is of great significance to the data processing algorithm and data product quality in space exploration. At present, CSES and Swarm satellites are operating well in orbit and have obtained high-quality space magnetic field data in accordance with their own specifications for a long period of time. The two satellite missions are in orbit at the same time and have similar altitudes, and they have the same type of observation payloads (scalar magnetometer), which can be selected to carry out cross-study of magnetic field data. According to the satellite orbit characteristics, CSES and Swarm satellites have different orbital heights and inclination angles, so they cannot achieve long-term orbital overlapping flight and do not have the conditions to carry out direct data cross comparison. So, the data screening method and cross comparison method were applied to realize an indirect comparison analysis between the CSES and Swarm scalar magnetic field data.

The CHAOS-7 model describes the near-Earth geomagnetic field based on observations collected by satellites including Swarm, CryoSat-2, CHAMP, SAC-C, and Ørsted (Finlay et al., 2020). Only the data from dark regions (Sun elevation angle 10° below the horizon) were used to reduce the influence of ionospheric currents, and more detailed information about the CHAOS model can be obtained from the study by Olsen et al. (2006). As a reference field model, CHAOS can relate the magnetic vector, at the location and time of measurement, to the geographic directions (Finlay et al., 2020). So, the model can be taken advantage of to assist the cross comparison research.

# 2 CROSS COMPARISON METHODS

On the basis of the research objective, several steps are required during the data processing and analysis, including data screening methods with different criteria, cross comparison by virtue of the CHAOS-7.8 model, and methods of analysis.

## 2.1 Data Screening Methods

The CDSM data of CSES were derived from the scalar magnetic field level 2 data of HPM from the official website of the Center of Satellite Application in Earthquake Science, with a sampling frequency of 1 Hz and a time range from 2019 to 2020. The ASM data of Swarm Bravo were acquired from the 1 Hz sampling frequency L1b data product published on the official website of the European Space Agency, with a file version of 0505 and 0506, covering a period of time from 2019 to 2020. The Kp index was obtained from the page of GeoForschungsZentrum (GFZ) Potsdam (Matzka et al., 2021).

Some comparison conditions were set up in previous studies. The comparison between scalar measurements from the different satellites of Swarm was carried out for the data on 21 December 2013 which was magnetically quiet, and for each position of Alpha, the nearest Bravo and Charlie positions were selected for spatial co-localization (Fratter et al., 2016). The CSES and Swarm data for the period from August 30 to 3 September 2018 when the geomagnetic field was relatively quiet were chosen to perform a comparison (Zhou et al., 2019). Data for the time interval from November 15 to 30, 2018 were selected for comparison as the local time ranges overlapped for the CSES and Swarm Bravo night-side orbits (Pollinger et al., 2020). In this study, the condition was applied that two satellites pass by in a relatively short period of time and through the spatial location at a relatively close range, which means that the differences in UTC time and geographic longitude and latitude are small. As it was considered that the time and spatial difference may have an influence on the comparison results, it is necessary to choose an appropriate spatial–temporal scale standard. So, the term "time interval" was defined as the UTC time difference between the CDSM and ASM, and the term "spatial distance" as geographic longitude and latitude differences between the CDSM and ASM. The difference of altitude was taken into account by the application of the CHAOS model and precise calculation. To figure out whether the standards had an influence on the final results, several spatial–temporal scales were set up.

Applying the same analysis process, the influence of different scales would be further evaluated. A time interval of 30 min and spatial distance ranging from 1° × 1° to 20° x 20° in longitude and latitude can be compared to assess the influence of spatial scale. Meanwhile, spatial distance of 10°×10° and different time intervals can be compared to assess the influence of the time scale. Also, the dataset size on different spatial–temporal scales would be focused on and elaborated.

It is thought to be proper to apply a certain constraint that the time interval was set to be 180 min, and the spatial distance was set to be 5° × 5°. The results of other scales and periods will be discussed together later. Moreover, in consideration of geomagnetic field activities, the time periods when the Kp

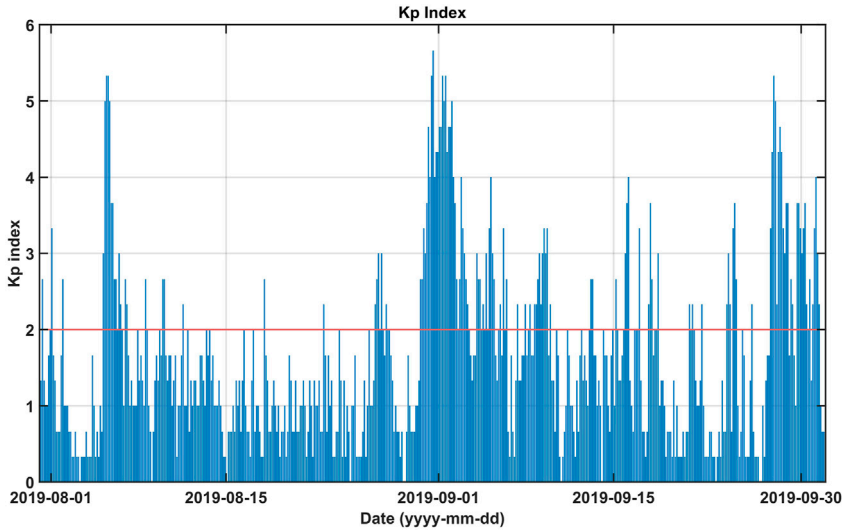


**FIGURE 1 |** Kp index variation for the period from 31 July 2019 to 30 September 2019.

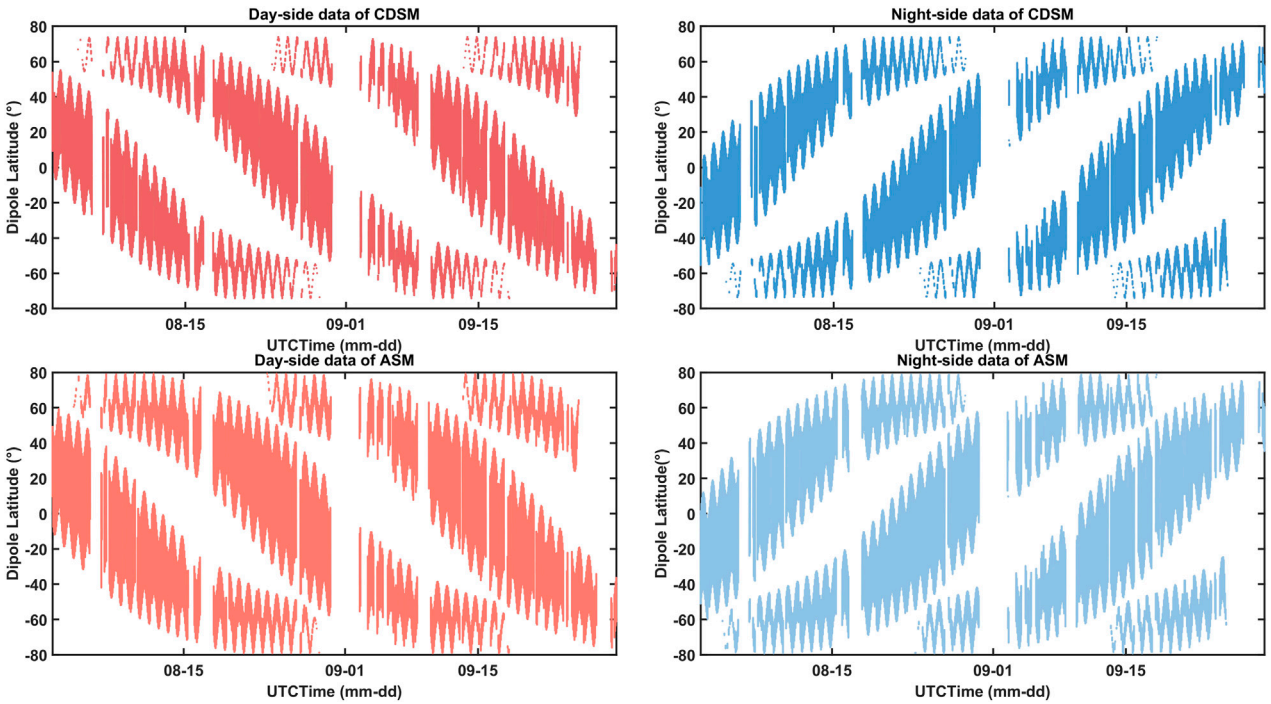


**FIGURE 2 |** Data distribution of the CDSM and ASM for the period from 31 July 2019 to 30 September 2019 after the data screening.

index is lower than 2+ were selected to screen for geomagnetic activity quiet periods (Yang et al., 2021). Other restrictions included Flags_F of ASM is 0 or 1, FLAG_MT of CDSM is 0, and parameter A211 should not be −9999.0. Flags_F of ASM characterizes the magnetic field intensity measurement. When its value is 0, the ASM works in scalar mode, and value 1 means the ASM running in vector mode. Both the values can ensure that ASM data is available for normal measurement, while other values represent some abnormal situations (National Space Institute Technical University of Denmark, 2019). For more details about the data product definition, product data handbooks are available released by the European Space Agency (see https://earth.esa.int/eogateway/missions/swarm/product-data-handbook). FLAG_MT of CDSM characterizes the disturbance of magnetic torque. When the magnetic torque is working, usually in high-latitude regions or near the

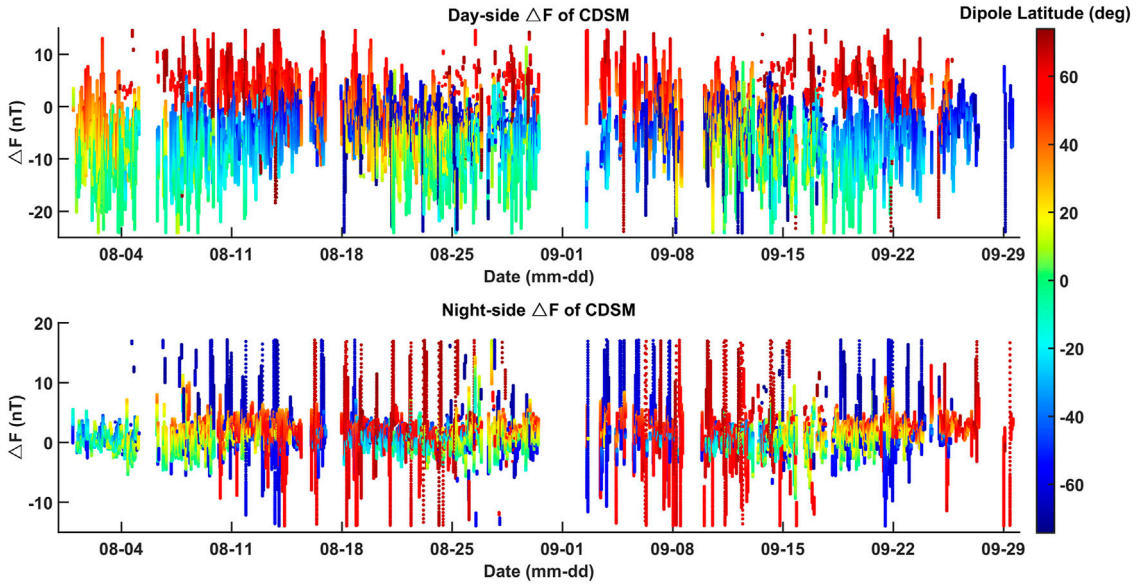


**FIGURE 3 |** $\Delta F$ of the CDSM from 31 July 2019 to 30 September 2019 (different colors represent the dipole latitudes of data points).

equator, there is interference and the value is 1; otherwise, the value is 0. A211 is the scalar magnetic field intensity, and the value −9999.0 means invalid data (National Institute of Natural Hazards Ministry of Emergency Management of China, 2020).

To begin with, data from August to September 2019 was selected to perform a preliminary analysis, and the detailed process and results will be elaborated on. After this data screening process, suitable data were selected and distributed on some of the orbits of dates from 31 July 2019 to 30 September 2019. The dataset size is 550604 of CDSM day-side data, 546082 of CDSM night-side data, 713315 of ASM day-side data, and 658684 of ASM night-side data.

**Figure 1** shows all the Kp indexes during this period, and the data corresponding to the index smaller than or equal to 2, which are below the red line shown in the figure, were selected.

According to these requirements, finally, the data needed to perform subsequent analysis were acquired. **Figure 2** shows the data distribution of the CDSM and ASM for this period. Day side and night side are distinguished based on the local time of the data points. The data between 6:00 and 18:00 in local time belong to the day-side datasets; otherwise, the data belong to the night-side datasets (Yang et al., 2021).

In the figure, the selected data are distributed at most of the geomagnetic dipole latitude ranges. The datasets are abundant, and the statistical analysis can be statistically representative.

## 2.2 Cross Comparison

As was assumed before, the data of the two payloads are not exactly identical to each other in time and location. So, the CHAOS-7.8 model was used to calculate the magnetic field intensity of the corresponding model value using the same parameters such as UTC time, altitude, longitude, and latitude. A core field of spherical harmonic degree 20 and a crustal field of degree 110 were adopted.

For every data point, there are scalar magnetic field values measured by satellites in orbit and calculated by models in correspondence with each other. The difference between the measured value and the model value can indicate the deviation of the satellite in-orbit magnetic field measured data from the model. The calculation is applied in the equation:

$$\Delta F = F_0 - \left|B_{total}\left(\text{mjd2000, colatitude, longitude, altitude}\right)\right|,$$

where $\Delta F$ is the difference between the measured data and the CHAOS model value, $F_0$ is the in-orbit measured data, and $|B_{total}|$ is the scalar intensity value of the field calculated by the CHAOS model (Finlay et al., 2020). The ionospheric field may be responsible for some discrepancies between the satellite data, such as the influence of the Sq current system, the equatorial and auroral electrojets, and the field-aligned currents. So some statistical method was used to reduce these effects on data analysis. Since the available data set is large enough, the 3 sigma criterion can be used to remove data that are more than three standard deviations away from the mean value so as to eliminate the outliers of data fluctuation which may be caused by large magnetic field disturbance and retain data that can be used for further analysis. The data may still contain small short-term magnetic field fluctuations, but in the long-term data analysis, they have little impact on the overall results. The data span used to define the mean value and standard deviation in the 3 sigma criterion is the period from 31 July 2019 to 30 September 2019. **Figure 3** shows the variation of $\Delta F$ overtime for CDSM selected data, with a color bar indicating the dipole latitudes of data points, and **Figure 4** shows that of the ASM.

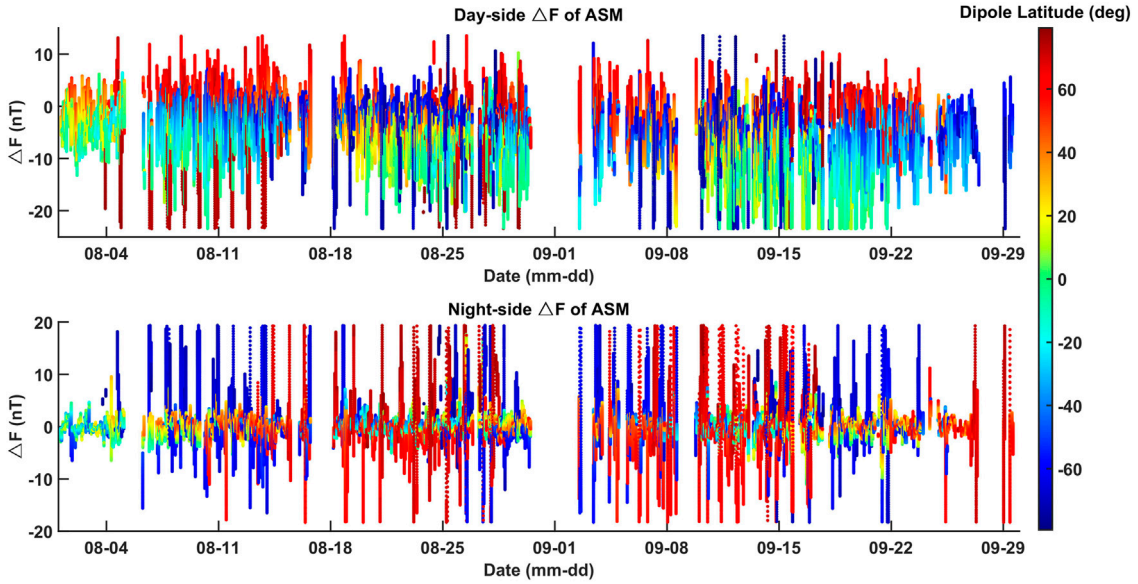


**FIGURE 4 |** $\Delta F$ of the ASM from 31 July 2019 to 30 September 2019 (different colors represent the dipole latitudes of data points).

As shown in the figures, $\Delta F$ does not have obvious variation over time, but with some weak fluctuation occasionally, and most data vary near the value of 0. The results indicate that most in-orbit data are in good agreement with the CHAOS model, and the fluctuation of $\Delta F$ in night side is weaker than day side, which may be related to the CHAOS model's optimization for the night side and the influence of solar wind or the disturbance of solar illumination and temperature on the day-side orbit data. Also, it appears that many outliers occur at high dipole latitudes or near the equator, and the coherency between the CSES and Swarm patterns can be observed, suggesting that they may be related to some dynamic ionospheric current systems and magnetospheric activities. Therefore, the data and the $\Delta F$ of night-side orbits are paid attention to in the following analysis.

## 2.3 Methods of Analysis

By virtue of the CHAOS model, the indirect comparison analysis was realized. The $\Delta F$ can be visualized in some statistical approaches. Global distribution of $\Delta F$ plotted with geomagnetic dipole latitudes may reflect the spatial distribution regularities of $\Delta F$ during the day-side orbit and night-side orbit. The $\Delta F$ distribution along the dipole latitude may reveal latitudinal regularities.

The mean value and standard deviation analysis can intuitively show the characteristics of $\Delta F$. The mean of the difference between the magnetic measured value and the model value and the population standard deviation are calculated and displayed in the form of error bars. The mean value reflects the central tendency of $\Delta F$ and represents the magnitude of $\Delta F$ in an average level. The standard deviation reflects the deviation of data relative to the mean value and measures the dispersion degree of data.

The mean values and standard deviations of the differences were calculated with a 10° resolution of the dipole latitude (Pollinger et al., 2020). On this basis, the differences of $\Delta F$ between the CDSM and ASM were further calculated, and the line graph drawn reflected the statistical results of the difference between the CDSM and ASM.

# 3 ANALYSIS RESULTS AND DISCUSSION

According to the scheme and methods, some visualized results are obtained, which are displayed as follows, including the distribution of the difference between in-orbit data and the CHAOS model on the global scale and along dipole latitude and the mean value and standard deviation analysis.

## 3.1 Difference Between In-Orbit Data and Model Value

Focusing on the data selected which were distributed on some orbits from the dates of 31 July 2019 to 30 September 2019, the corresponding location in the geomagnetic coordinate of the Swarm Bravo data was calculated using IGRF-13 (Alken et al., 2021). **Figure 5** shows the distribution of $\Delta F$ in the geographic reference frame plotted with the magnetic dipole latitudes and longitudes of data points for the CDSM and ASM in day-side orbits and night-side orbits, respectively.

It can be seen from the figure that the $\Delta F$ of the night-side data is small and has little variation. Also, it is obvious that the distribution along dipole latitude has some characteristics, and data at the middle geomagnetic dipole latitude are more consistent with the CHAOS model. The cause might be the interference of field-aligned current in the high-latitude region

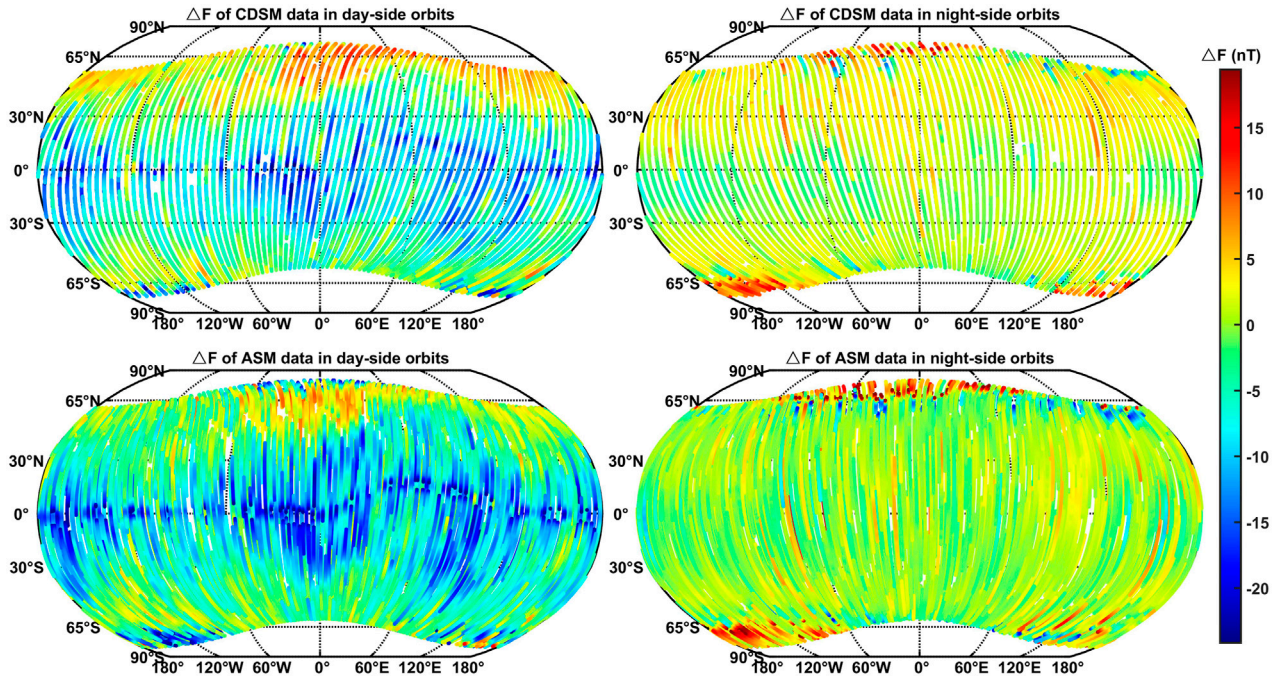


**FIGURE 5 |** Distribution of *ΔF* from 31 July 2019 to 30 September 2019 in geographic reference frame for CDSM and ASM selected data.

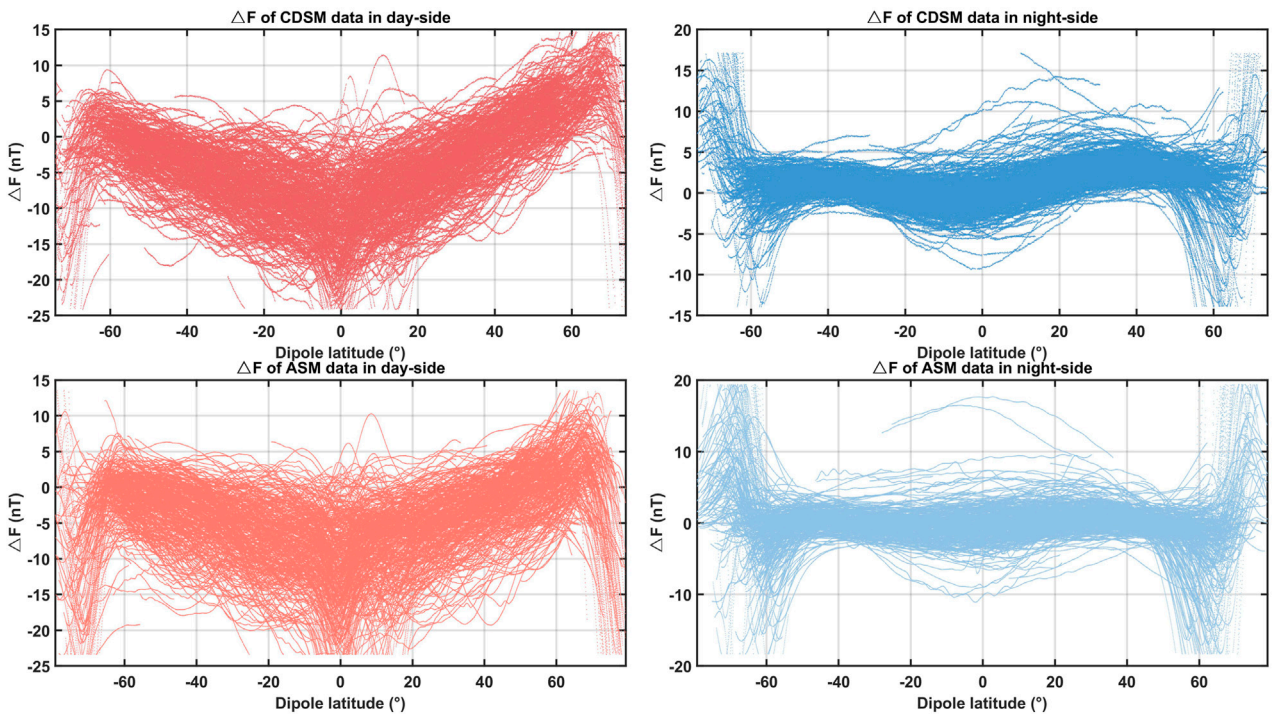


**FIGURE 6 |** *ΔF* distribution along the dipole latitude from 31 July 2019 to 30 September 2019 (red dots represent the *ΔF* of the day-side data, and blue dots represent the *ΔF* of the night-side data).

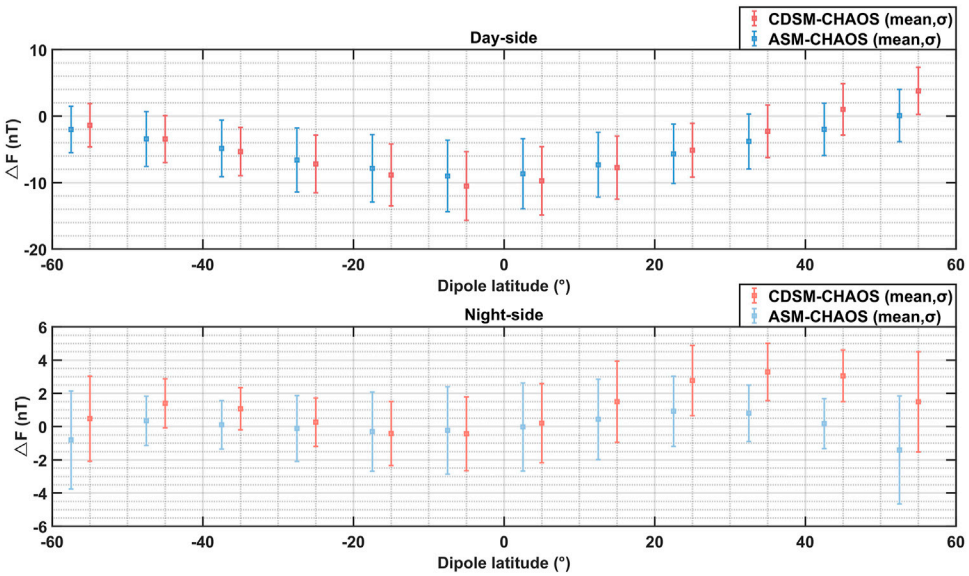


**FIGURE 7 |** Error bars of $\Delta F$ of the CDSM and ASM using selected data from July 31 to 30 September 2019 are similar (the error bars of Swarm Bravo have been shifted 2.5° horizontally to the left in order to allow a visual comparison).

and equatorial electrojet current in the low-latitude region. Therefore, the data and $\Delta F$ at the middle geomagnetic dipole latitude are focused on in the following analysis. For the same datasets and period, the regularities of the $\Delta F$ distribution along the dipole latitude can be observed more clearly in **Figure 6**.

Overall, the CDSM data and ASM data showed a good agreement in the figure. The data in the middle-latitude region are close to the model value, $\Delta F$ is close to 0, and the fluctuation range is small. Most of the night-side orbit data are consistent with the model, with a small fluctuation range and being stable near 0.

## 3.2 The Mean Value and Standard Deviation Analysis

The scalar residuals between CHAOS and Swarm magnetic field data are much larger in the auroral region because of the presence of field-aligned currents. It is to be noted that the Swarm data have been used to generate the CHAOS model; therefore, it is expected that scalar residuals should be small but dependent on the current systems not included in the CHAOS model (Finlay et al., 2015). After considering the purpose of the study comprehensively, the suitable data from 31 July 2019 to 30 September 2019 of dipole latitude within the range of -60° to 60° were concentrated on. The mean value and standard deviation of $\Delta F$ are calculated with a 10° resolution of the dipole latitude, and the results are shown in the form of error bars in **Figure 7**. The error bars in each dipole latitude interval correspond with each other and are plotted separately in the figure so that they can be distinguished clearly.

The mean values of $\Delta F$ for most latitudes are small and stable, indicating that the consistency of the night-side data with the CHAOS model is good. In the geomagnetic dipole latitude range of −30° to 10°, the mean values of $\Delta F$ in the night side of both magnetometers are small, which are −0.17 nT for the ASM and −0.094nT for the CDSM. In the geomagnetic dipole latitude range of −50 to −20°, the deviations of $\Delta F$ in the night side of both magnetometers are small, which are 1.64 nT for the ASM and 1.40 nT for the CDSM.

It can be seen that the error bars start to separate at dipole latitudes greater than 20° (Pollinger et al., 2020). These error bars of the CDSM are very similar to those of the ASM in other dipole latitude regions, so subtraction using both the mean value and standard deviation was performed in **Figure 8**. Also, it indicates that the data of both instruments are relatively consistent and stable.

It reflects that the deviation of the in-orbit scalar magnetic field measurement value is small compared with the value of the CHAOS model. The mean value and standard deviation distribution of the CDSM and ASM show a similar variation trend, and the dispersion is weak, reflecting a good consistency. Especially in middle- and low-latitude areas such as −30 to 10°, where the mean values fluctuate around 0, the standard deviation is smaller and the consistency is better.

## 3.3 Analysis Applying Other Scales

The equivalent analysis process was carried out with other spatial–temporal scales using the datasets from 31 July 2019 to 30 August 2019. The time interval between satellite data points was set to be 30 min, while the spatial distances were analyzed from 1° × 1° to 20° × 20°, considering non-overlapping range selections in order to understand the effect of data selected in specific ranges. Statistical analysis in terms of mean values and standard deviations was carried out. The results are shown in **Figure 9**.

These aforementioned curves have very similar variation trends and cross each other, and these mean values remain

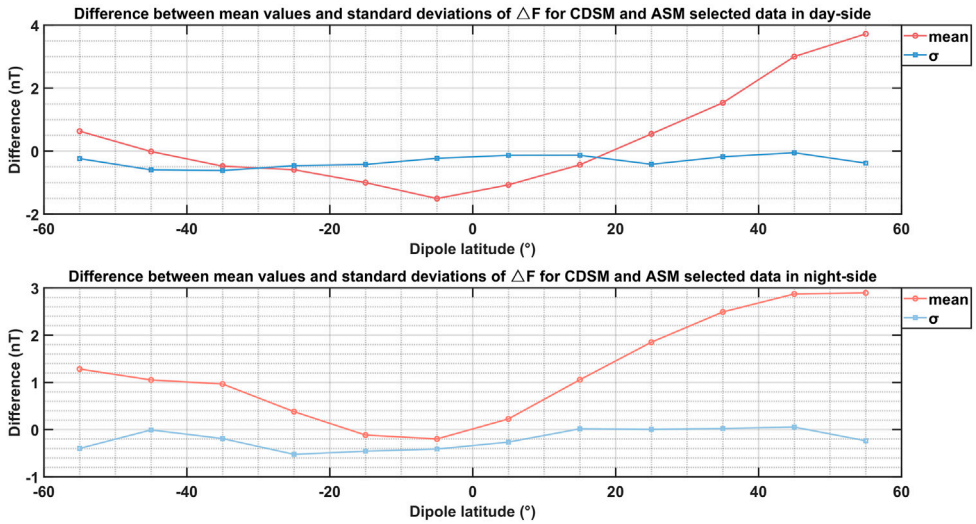


**FIGURE 8 |** Difference between mean values and standard deviations of ΔF for the CDSM and for ASM selected data from July 31 to 30 September 2019.

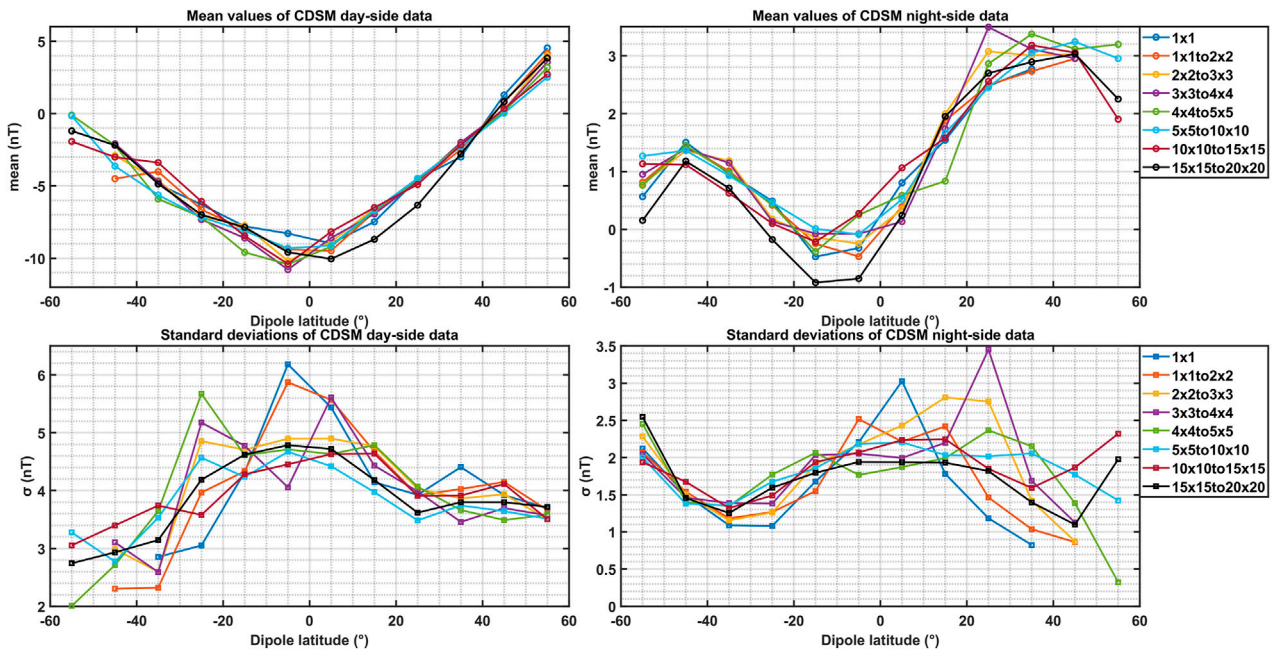


**FIGURE 9 |** Statistical results of mean values and standard deviations of *ΔF* from 31 July 2019 to 30 August 2019 with a time interval of 30 min and at increasing, non-overlapping distance ranges from 1°×1° to 20°×20°.

close to each other. On the night side, the difference of mean values between different curves is within 0.65 nT in the dipole latitude range of −40° to −30° and 30° to 40°, where the CHAOS model is thought to be the most accurate (Finlay et al., 2015). As the different datasets used for the figure are non-overlapping, the dataset amounts of different scales were examined and are shown in **Table 1**. It can be inferred that the influence on the results with different spatial scales is slight.

The selection of spatial distance being 10°×10° and time intervals being 60, 120, and 180 min with the Kp index lower than 2 + using data of September 2019 was carried out. Also, the non-overlapping time window is used and additional data are focused on. **Figure 10** shows the statistical results of mean values and standard deviations of *ΔF*. The dataset size of 60 min is 74826 on the day side and 74452 on the night side, the dataset size of 60–120 min is 320661 on the day side and 321810 on the night

**TABLE 1 |** Amounts of data on different spatial scales with the time interval being 30 min (For each category Day side/Night side, there are two lines: the first contains all data between 0 and the corresponding distance, the second only data between successive ranges.).

| Spatial distance (°) | 1 × 1 | 2 × 2 | 3 × 3 | 4 × 4 | 5 × 5 | 10 × 10 | 15 × 15 | 20 × 20 |
|---|---|---|---|---|---|---|---|---|
| | | 1 × 1 to 2 × 2 | 2 × 2 to 3 × 3 | 3 × 3 to 4 × 4 | 4 × 4 to 5 × 5 | 5 × 5 to 10 × 10 | 10 × 10 to 15 × 15 | 15 × 15 to 20 × 20 |
| Day side | 32929 | 65684 | 97931 | 130564 | 161343 | 301381 | 426879 | 527194 |
| | | 32755 | 32247 | 32633 | 30779 | 140038 | 125498 | 100315 |
| Night side | 32651 | 65121 | 97154 | 128345 | 158571 | 297114 | 420918 | 520465 |
| | | 32470 | 32033 | 31191 | 30226 | 138543 | 123804 | 99547 |

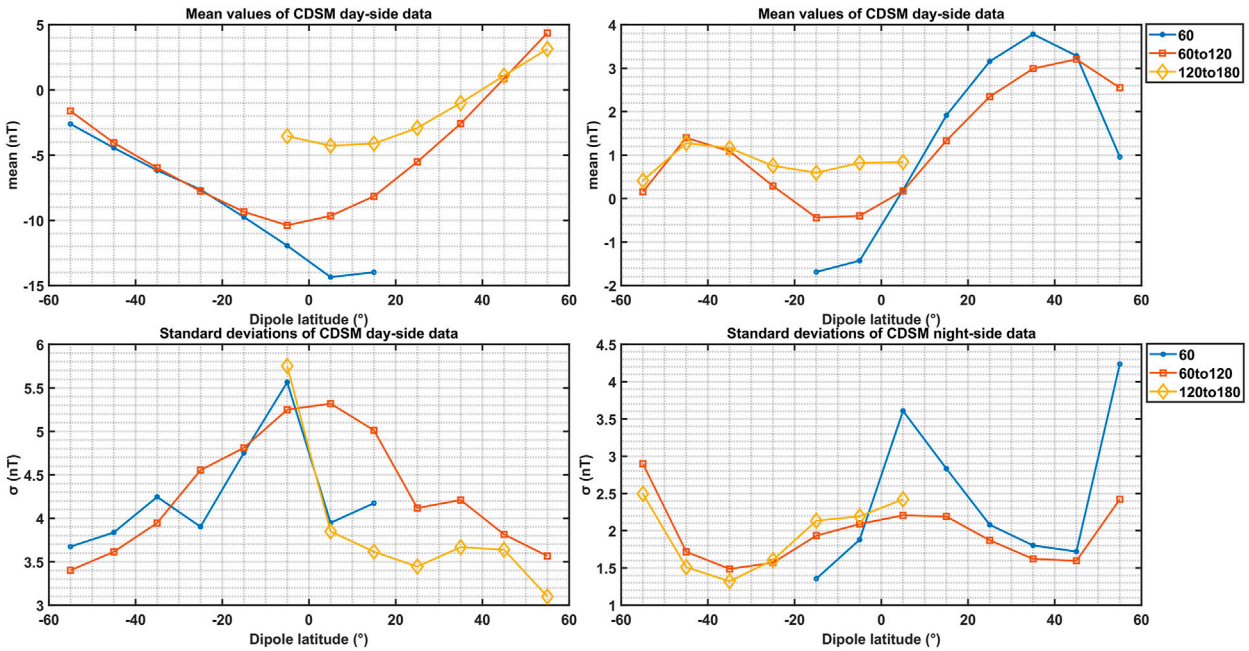


**FIGURE 10 |** Statistical results of mean values and standard deviations of $\Delta F$ from 2 September 2019 to 29 September 2019 with a spatial distance of 10°×10° and at increasing, non-overlapping time intervals of 60, 120, and 180 min.

side, and dataset size of 120–180 min is 80983 on the day side and 76455 on the night side.

As shown in the aforementioned figure, the statistical results of mean values and standard deviations of $\Delta F$ for different non-overlapping datasets appear to have similar trends, and the difference in mean values and standard deviations is not obvious.

Due to the orbital configuration of the satellites, sometimes the increase of a time window or spatial range did not allow to include additional data and cover all the latitude ranges, as can be seen in **Figures 9**, **10**, where not all the various curves are completely distributed across all latitude ranges.

As the spatial–temporal scale was amplified, the suitable data volume generally had an increasing trend. But, the statistical analysis results seem similar with different non-overlapping datasets. It can be inferred that the selection of different spatial–temporal scale standards has no obvious influence on the statistical results, which means that the results are not sensitive to the change in time interval and spatial distance.

It is necessary to choose a scale with both time interval and spatial distance in order to select sufficient data to accomplish a comparison analysis of consistency. As for the research process, the data size and workload need to be considered. To ensure that the computation is convenient for the implementation of subsequent analysis, an appropriate time interval (180 min) and an appropriate spatial scale (5° × 5°) was adopted, and proper data size can be derived to reveal the actual situation of the in-orbit data. The restriction of the Kp index and data flag parameters should also be applied. It can be seen in these aforementioned curves that there are discrepancies in the results of different dipole latitude ranges and between the day-side and night-side, so the analysis and results discussion can focus on middle-latitude data on the night side, which are less disturbed and more credible. For long-term comparison, data from 2019 to 2020 were acquired, selected, and analyzed. It is to be noted that 2019 was during the solar minimum; therefore, the comparison results are credible.

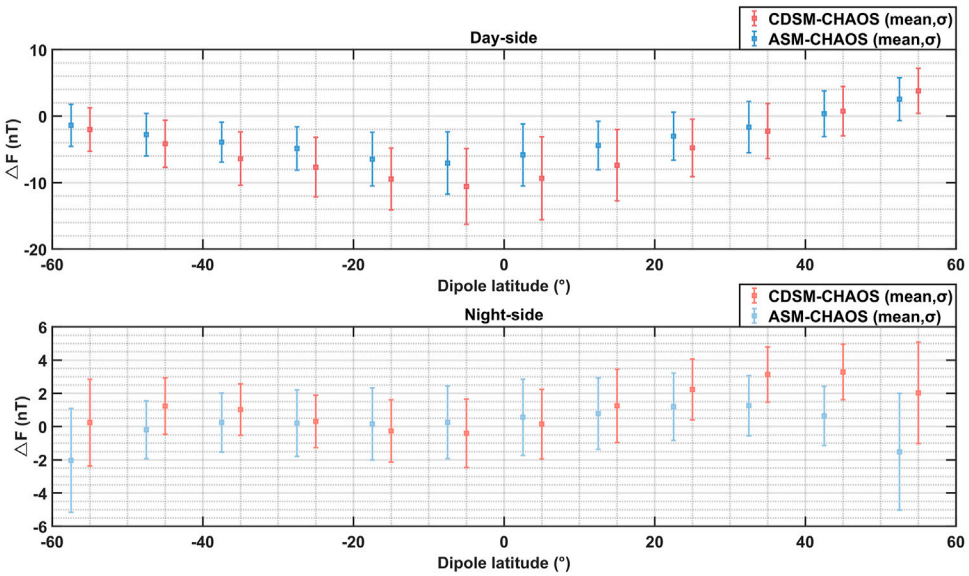


**FIGURE 11 |** Error bars of $\Delta F$ of the CDSM and ASM using selected data from August 25 to 29 September 2019 (the error bars of Swarm Alpha have been shifted 2.5° horizontally to the left in order to allow a visual comparison).

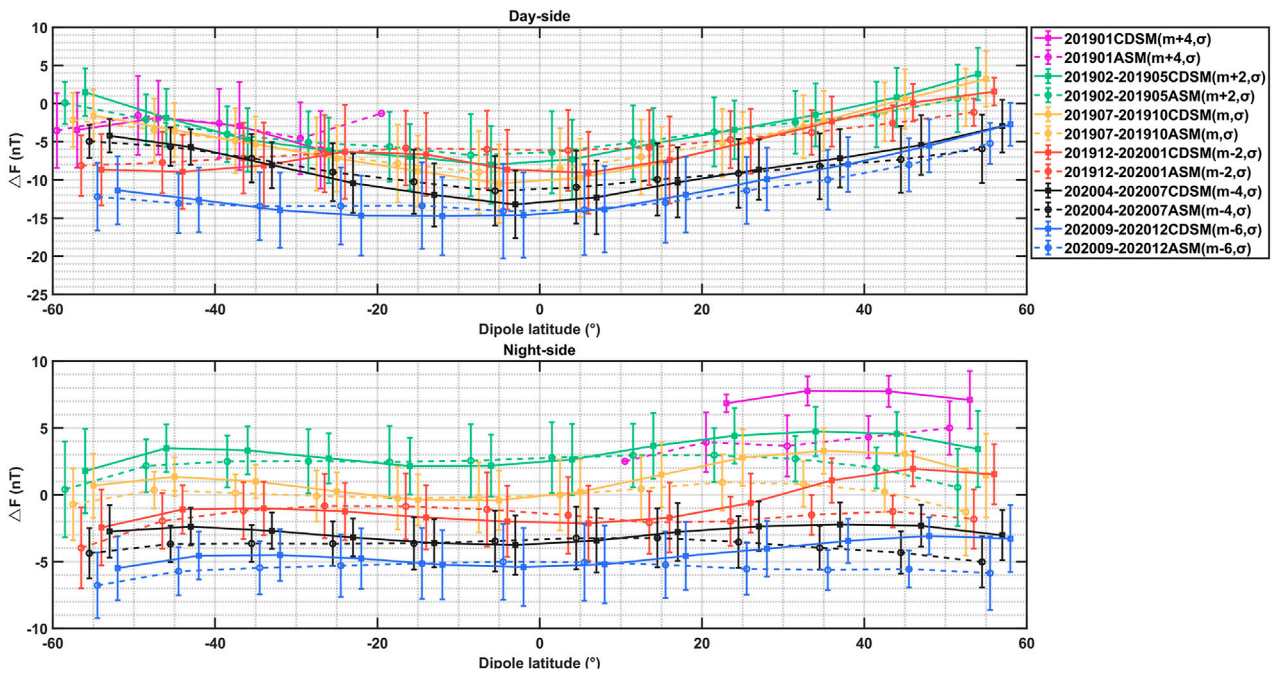


**FIGURE 12 |** Mean value and standard deviation analysis of $\Delta F$ along the dipole latitude in different periods (the error bars of CSES in these six periods in chronological order have been shifted +4nT, +2nT, 0nT, −2nT, −4nT, −6nT in vertical direction and −2°, −1°, 0°, +1°, +2°, +3° in horizontal direction, and those of Swarm Bravo have been shifted +4nT, +2nT, 0nT, −2nT, −4nT, −6nT in vertical direction and −4.5°, −3.5°, −2.5°, −1.5°, −0.5°, +0.5° in horizontal direction, in order to allow a visual comparison, as labeled in the Figure legend).

## 3.4 Application to the Swarm Alpha satellite

In order to verify the applicability and effectiveness of the data screening methods and the approach of using models to compare data from different satellites, the same analysis process was also applied to the scalar magnetic field data of Swarm Alpha. Mean value and standard deviation analysis

**TABLE 2 |** Results of data in dipole latitude range of -40° to -30° and 30° to 40° on the night side.

| Periods | Magnetometer | -40° to -30° | | 30° to 40° | |
|---|---|---|---|---|---|
| | | m | σ | m | σ |
| 201901 | CDSM | | | 3.77 | 1.09 |
| | ASM | | | -0.35 | 2.29 |
| 201902–201905 | CDSM | 1.32 | 1.80 | 2.73 | 1.85 |
| | ASM | 0.49 | 1.94 | 0.68 | 1.70 |
| 201907–201910 | CDSM | 0.99 | 1.24 | 3.29 | 1.72 |
| | ASM | 0.13 | 1.39 | 0.80 | 1.70 |
| 201912–202001 | CDSM | 0.98 | 2.00 | 3.07 | 1.67 |
| | ASM | 0.80 | 2.12 | 0.49 | 1.49 |
| 202004–202007 | CDSM | 1.31 | 1.36 | 1.78 | 1.64 |
| | ASM | 0.36 | 1.38 | 0.03 | 1.63 |
| 202009–202012 | CDSM | 1.49 | 1.94 | 2.55 | 1.66 |
| | ASM | 0.53 | 1.99 | 0.37 | 1.50 |

using scalar magnetic field data of CSES and Swarm Alpha from August to September 2019 was completed. **Figure 11** shows the results of selected data using the criterion of time interval being 180 min and spatial distance being 5°×5°, distributed from August 25 to 29 September 2019. The dataset size used in the figure is 244337 and 242416 for the CDSM on the day side and night side and 308306 and 300724 for Swarm Alpha ASM on the day side and night side.

It can be seen that the mean values and standard deviations of the CDSM and Swarm Alpha ASM show similar variation trends, meaning that the data of CDSM onboard CSES and ASM onboard Swarm Alpha have good consistency with each other. The results show that the methods are also applicable and effective for similar data comparison studies between other satellites. In this study, the analysis of long-term data mainly focuses on CSES and Swarm Bravo satellites.

## 3.5 Analysis for the Long-Term In-Orbit Data

Adopting the time interval (180 min) and the spatial scale (5° × 5°), the long-term in-orbit data of CDSM and Swarm Bravo ASM from 2019 to 2020 were analyzed. After the data screening process, there were six periods with a significant amount of data satisfying the selection criteria, consisting of January 2019, February to May 2019, July to October 2019, December 2019 to January 2020, April to July 2020, and September to December 2020. The statistical results of these periods are shown as error bars in **Figure 12**.

The quantitative results of dipole latitude range of -40° to -30° and 30° to 40° on the night side are shown in **Table 2**.

It is shown that in all these periods, the in-orbit data of both the CDSM and ASM agree with the CHAOS model value; thus, the inference can be drawn that they are relatively consistent with each other. Subtraction using the mean values of both the CDSM and ASM was carried out in **Figure 13**.

Analogously, the night-side data show great consistency with the model value. The CHAOS model is generated using the observation data from satellites including Swarm and optimized for the night side, which may explain the reason why the results for Swarm Bravo on the night side seem more accurate. Also, the distribution patterns have a similar trend with dipole latitude in different periods, indicating that both payloads are in stable operation and the quality of their data is stable overtime.

Using all the selected data of January 2019, February to May 2019, July to October 2019, December 2019 to January 2020, April to July 2020, and September to December 2020 after screening, statistical analysis was performed. As the CHAOS model is optimized for the night side and there may be solar illumination influencing the day-side data, only the night-side data were analyzed. Statistics were calculated in terms of date, and the mean value of every single day was calculated using $\Delta F$ of every data point within the 3 sigma criterion range. The results of the CDSM and ASM are shown in **Figure 14**.

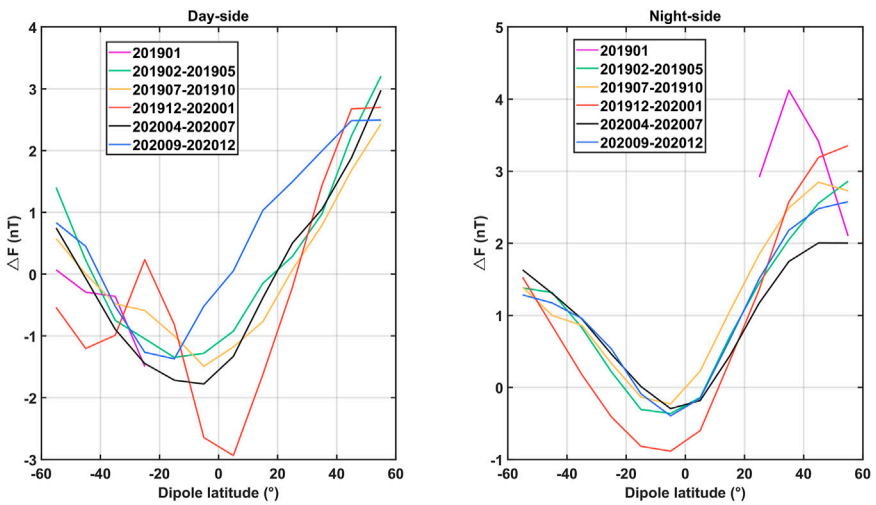


**FIGURE 13 |** Results of subtraction using the mean values of the CDSM and ASM $\Delta F$ in different periods.

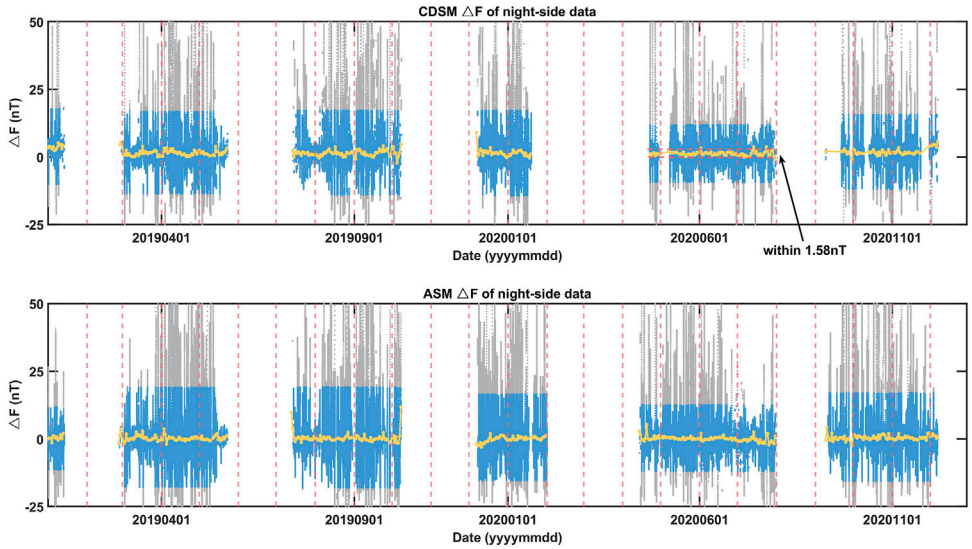


**FIGURE 14 |** Statistical results of the difference between the CDSM/ASM and CHAOS using selected data from 2019 to 2020 (gray points represent the $\Delta F$ of every data point excluded by the 3 sigma criterion, blue points represent the $\Delta F$ of points restricted with the 3 sigma criterion in night-side orbits, and yellow points represent the average daily $\Delta F$ of night-side data points restricted with 3 sigma criterion).

As shown in these different colors, the 3 sigma criterion filtered the outliers effectively, which can reduce the influence of ionospheric perturbation and make the results more reliable. The daily mean values show a relatively stable trend in the long term for both the CDSM and ASM. The variation of most CDSM daily mean values during the period of April to July 2020 is within 1.58 nT. Some average daily $\Delta F$ appear to be a little bit large because there were just few data distributed at high latitude region on this day and they may not represent the whole real situation. It can be seen that in general, the data of the CDSM and ASM were consistent with each other and maintained long-term stability.

## 4 CONCLUSION

The CSES and Swarm satellites have similar altitudes and payloads, both operating well in orbit for a relatively long period. To carry out the cross comparison analysis, the condition was applied that their time interval and spatial distance are close enough to perform the consistency analysis. After setting the standards and data screening, the data which meet our requirements were acquired. As the data of the CDSM and ASM are not exactly identical in the parameters such as geographic longitude and latitude, altitude, and UTC time, the CHAOS-7.8 model was used to calculate the model value and realize the indirect comparison analysis. Then, the difference between the in-orbit data and model value was visualized in some statistical approaches.

In this study, the data screening methods are studied and described. The scales of spatial distance were used to limit the difference between the longitudes and latitudes of the CDSM and ASM, and the scales of the time interval are used to limit the difference between the UTC time of the CDSM and ASM. Several spatial–temporal scales were set up, with spatial distances ranging from $1^\circ \times 1^\circ$ to $20^\circ \times 20^\circ$ and time intervals varying from 30 min to 180 min. Data were selected for quiet periods with Kp lower than 2+ and the data flags were examined. The results of the comparison of different scales showed that the selection of spatial–temporal scales has no obvious influence on the final results. But the data size and workload need to be considered. To ensure that the computation is convenient for the implementation of subsequent analysis and the dataset size is statistically representative, an appropriate time interval (180 min) and an appropriate spatial scale ($5^\circ \times 5^\circ$) can be adopted, and the statistical results can reflect the data quality in the long-term detection.

Applying this method, the short-term data comparison analysis for CDSM of CSES and ASM of both Swarm Alpha and Bravo in August and September, 2019, and the long-term data comparison analysis of the CDSM and Swarm Bravo ASM from 2019 to 2020 were realized. The conclusion in this study well supports the conclusion of (Pollinger et al., 2020). According to the results of the night-side orbit data, both scalar magnetic field data are in good agreement with the CHAOS model and are relatively consistent and stable. It can be inferred that the scalar magnetic field detection payloads of the two satellites have maintained long-term stability in orbit and obtained high-quality data.

## DATA AVAILABILITY STATEMENT

Publicly available datasets were analyzed in this study. The CSES datasets for this study are available at https://leos.ac.cn/#/home. The Swarm datasets for this study are available at https://earth.esa.int/eogateway/missions/swarm/data. The CHAOS-7 model is publicly available at https://www.spacecenter.dk/files/magnetic-models/CHAOS-7/index.html. The Kp index data can be obtained at http://wdc.kugi.kyoto-u.ac.jp/wdc/Sec3.html.

## AUTHOR CONTRIBUTIONS

JZ and BC carried out the data analysis. YT, YM, and BZ contributed to the development of the methodology. AP, XZ, and YY contributed to the analysis of CDSM data. XG, YZ, JW, and LL contributed to the discussion of the results. WM, RL, ZZ, and XS provided comments on the discussion of the results. All authors read and approved the final manuscript.

## FUNDING

This article is supported by the National Key Research and Development Program of China from the Ministry of Science and Technology of the People´s Republic of China (MOST) (grant no. 2018YFC1503501) and the NSFC (grant no. 41904147). Work of PA, MW, and LR was supported by the Austrian Space Applications Programme (Grant No. 873688).

## ACKNOWLEDGMENTS

This work made use of the data from the CSES mission, a project funded by the China National Space Administration (CNSA) and the National Institute of Natural Hazards, Ministry of Emergency Management of China (NINH). The authors gratefully acknowledge support from CSES teams for providing CDSM data and ESA Swarm teams for providing ASM data for long-term analysis.

## REFERENCES

Alken, P., Thébault, E., Beggan, C. D., Amit, H., Aubert, J., Baerenzung, J., et al. (2021). International Geomagnetic Reference Field: the Thirteenth Generation. *Earth, Planets Space* 73 (1). doi:10.1186/s40623-020-01288-x10.1186/s40623-020-01281-4

Cheng, B., Zhou, B., Magnes, W., Lammegger, R., Pollinger, A., Ellmeier, M., et al. (2015). "Performance of the Engineering Model of the CSES High Precision Magnetometer," in *2015 IEEE SENSORS*, 1–4. doi:10.1109/icsens.2015.7370679

Cheng, B., Zhou, B., Magnes, W., Lammegger, R., and Pollinger, A. (2018). High Precision Magnetometer for Geomagnetic Exploration Onboard of the China Seismo-Electromagnetic Satellite. *Sci. China Technol. Sci.* 61 (5), 659–668. doi:10.1007/s11431-018-9247-6

Finlay, C. C., Kloss, C., Olsen, N., Hammer, M. D., Tøffner-Clausen, L., Grayver, A., et al. (2020). The CHAOS-7 Geomagnetic Field Model and Observed Changes in the South Atlantic Anomaly. *Earth Planets Space* 72 (1), 156. doi:10.1186/s40623-020-01252-9

Finlay, C. C., Olsen, N., and Tøffner-Clausen, L. (2015). DTU Candidate Field Models for IGRF-12 and the CHAOS-5 Geomagnetic Field Model. *Earth Planet Sp.* 67 (1). doi:10.1186/s40623-015-0274-3

Fratter, I., Léger, J.-M., Bertrand, F., Jager, T., Hulot, G., Brocco, L., et al. (2016). Swarm Absolute Scalar Magnetometers First In-Orbit Results. *Acta Astronaut.* 121, 76–87. doi:10.1016/j.actaastro.2015.12.025

Matzka, J., Bronkalla, O., Tornow, K., Elger, K., and Stolle, C. (2021). *Geomagnetic Kp Index. V. 1.0*. Potsdam, Germany: GFZ Data Services. doi:10.5880/Kp.0001

National Institute of Natural Hazards Ministry of Emergency Management of China (2020). *China Seismo-Electromagnetic Satellite (ZH-1(01)) the L2/2A Data Product Description[S]*.

National Space Institute Technical University of Denmark (2019). *Swarm Level 1b Product Definition[S]*. Kongens Lyngby, Denmark: SW-RS-DSC-SY-0007. Issue 5.23.

Olsen, N., and Floberghagen, R. (2018). Exploring Geospace from Space: the Swarm Satellite Constellation Mission. *Space Res. Today* 203, 61–71. doi:10.1016/j.srt.2018.11.017

Olsen, N., Lühr, H., Sabaka, T. J., Mandea, M., Rother, M., Tøffner-Clausen, L., et al. (2006). CHAOS-a Model of the Earth's Magnetic Field Derived from CHAMP, Ørsted, and SAC-C Magnetic Satellite Data. *Geophys. J. Int.* 166 (1), 67–75. doi:10.1111/j.1365-246X.2006.02959.x

Pollinger, A., Amtmann, C., Betzler, A., Cheng, B., Ellmeier, M., Hagen, C., et al. (2020). In-orbit Results of the Coupled Dark State Magnetometer Aboard the China Seismo-Electromagnetic Satellite. *Geosci. Instrum. Method. Data Syst.* 9 (2), 275–291. doi:10.5194/gi-9-275-2020

Shen, X., Zhang, X., Yuan, S., Wang, L., Cao, J., Huang, J., et al. (2018). The State-Of-The-Art of the China Seismo-Electromagnetic Satellite Mission. *Sci. China Technol. Sci.* 61 (5), 634–642. doi:10.1007/s11431-018-9242-0

Yang, Y., Hulot, G., Vigneron, P., Shen, X., Zhima, Z., Zhou, B., et al. (2021). The CSES Global Geomagnetic Field Model (CGGM): an IGRF-type Global Geomagnetic Field Model Based on Data from the China Seismo-Electromagnetic Satellite. *Earth Planets Space* 73 (1). doi:10.1186/s40623-020-01316-w

Zhou, B., Cheng, B., Gou, X., Li, L., Zhang, Y., Wang, J., et al. (2019). First In-Orbit Results of the Vector Magnetic Field Measurement of the High Precision Magnetometer Onboard the China Seismo-Electromagnetic Satellite. *Earth Planets Space* 71 (1). doi:10.1186/s40623-019-1098-3

**Conflict of Interest:** Authors MY and ZX are employed by DFH Satellite Co. Ltd.

The remaining authors declare that the research was conducted in the absence of any commercial or financial relationships that could be construed as a potential conflict of interest.

**Publisher's Note:** All claims expressed in this article are solely those of the authors and do not necessarily represent those of their affiliated organizations, or those of the publisher, the editors, and the reviewers. Any product that may be evaluated in this article, or claim that may be made by its manufacturer, is not guaranteed or endorsed by the publisher.

frontiers | Frontiers in Earth Science

ORIGINAL RESEARCH
published: 13 July 2022
doi: 10.3389/feart.2022.933083

# Evaluation of BER for the EHF Communication System Serving Sharp-Coned Reentry Vehicles

*Xiaocui Yang*[1], *Kai Yuan*[2], *Yuhao Wang*[2]* *and Yiwen Liu*[2]

[1]School of Resources and Environment, Nanchang University, Nanchang, China, [2]School of Information Engineering, Nanchang University, Nanchang, China

"Communication blackout" could lead to severe risks to reentry vehicles. Previous studies have shown that EHF (extremely high frequency) communication is a potential solution to the "communications blackout" and was mostly used for blunt-coned vehicles. EHF communication with sharp-coned vehicles was rarely concerned before. In the present study, the propagation characteristics of the modulated EHF signals in a time-varying plasma sheath covering sharp-coned vehicles were studied numerically. The plasma sheath was obtained by solving a hypersonic fluid dynamics model. The signals propagation model is developed based on geometric optical theories. The carrier frequencies concerned in the present study are the "atmospheric window" frequencies, which are 94, 140, and 225 GHz, respectively. Based on the signal propagation characteristics, the EHF communication system was modeled. The modulation modes concerned in the present study are the 2ASK, 2PSK, and 2FSK, respectively. The results show that 1) the transmission coefficient of EHF signals in the side channel of the plasma sheath of the sharp-coned reentry vehicle increases with carrier frequency, 2) the gap between different channels at specific carrier frequency decreases with time, 3) the phase shift tends to be stable as the carrier frequency increases, and 4) the bit error rate (BER) varies with time and is affected by the location of the onboard antenna, carrier frequency, and modulation mode. The study shows that, in order to achieve good BER performance for the EHF communication system, 2PSK modulation of the signal at 140 GHz is recommended, and the onboard antenna is suggested to be installed on the wall and close to the bottom of the sharp-coned vehicle.

**Keywords: extremely high frequency (EHF), plasma sheath, sharp-coned vehicle, reentry, BER**

OPEN ACCESS

***Edited by:***
*Chao Xiong,*
*Wuhan University, China*

***Reviewed by:***
*Weihua Luo,*
*South-Central University for Nationalities, China*
*Yuhua Zou,*
*Guilin University of Electronic Technology, China*

***Correspondence:**
*Yuhao Wang*
*wangyuhao@ncu.edu.cn*

***Specialty section:***
*This article was submitted to Environmental Informatics and Remote Sensing, a section of the journal Frontiers in Earth Science*

***Received:*** *30 April 2022*
***Accepted:*** *07 June 2022*
***Published:*** *13 July 2022*

***Citation:***
*Yang X, Yuan K, Wang Y and Liu Y (2022) Evaluation of BER for the EHF Communication System Serving Sharp-Coned Reentry Vehicles. Front. Earth Sci. 10:933083. doi: 10.3389/feart.2022.933083*

## 1 INTRODUCTION

Due to aerodynamic heating, the neutral gas surrounding the hypersonic vehicle in near space could be ionized. As a result, a weakly ionized gas layer called plasma sheath is formed. The plasma sheath covers the entire vehicle. The plasma sheath absorbs, reflects, and scatters the communication signals, and eventually, the communication is interrupted (Gillman et al., 2010; Starkey 2015). The attenuation of the signals in the plasma sheath decreases rapidly as the carrier frequency increases (Starkey, 2003; Yuan et al., 2018a). The electron density in the plasma sheath can reach $10^{20}$ $m^{-3}$, and the corresponding cut-off frequency is 89 GHz. Electromagnetic (EM) waves with frequencies higher than 89 GHz can penetrate the plasma sheath. The extremely high-frequency (EHF) band is from

30 to 300 GHz. Therefore, it is feasible to use the EHF-band communication system to effectively mitigate the communication "blackout."

Many scholars have studied the propagation characteristics of EHF signals in the plasma sheath of a reentry vehicle. Tang et al. (2019) studied the relationship between the attenuation of the EHF signal in plasma sheath and the speed of the vehicle. The study by Rao et al. (2021) found that the reflectivity and transmittance of EHF waves are affected by the frequency of the incident wave, the electron density of the plasma, and the radius of the colliding particles, etc. Zhao et al. (2022a) found that the gain, lobe width, and lobe direction of 0.14 THz phased array antenna is affected by the weakly ionized plasma of the reentry vehicle. Yang et al. (2022a) found that the attenuation of the EHF signals decreases and the phase shift fluctuates more severely with an increase in the angle between the tail channel and the tail of the vehicle.

On the other hand, Wei et al. (2019) pointed out that the BER changes with the evolution of the plasma sheath. In Wei's work, the plasma parameters measured in the RAMC-II reentry experiment are used to study their effect on the BER of the evolved plasma sheath. The relevant frequencies are 1.575, 2.3, 4.0, 8.4, 32, and 100 GHz. According to this study, NC-MFSK ($M \geq 8$) modulation is recommended for communication systems serving reentry vehicles. Liu et al. (2020) studied the influence of dynamic plasma sheath on the BER of two typical modulation signals of BPSK and NC-MFSK under the action of the external magnetic field. The results show that the NC-8FSK has a better performance than BPSK, followed by NC-4FSK and NC-2FSK. According to the study by Yang et al. (2022b), the suggested modulation modes are 2PSK and 4QAM at the carrier frequency of 140 GHz, which could lead to smaller and more stable BER for the EHF communication system utilized by reentry vehicles.

Although there are many studies on the propagation of EHF waves in the plasma sheath of a blunt-coned reentry vehicle, the plasma sheath covering the sharp-coned reentry vehicle is rarely studied. The sharp-coned and blunt-coned reentry vehicles represent ballistic missiles and reentry capsules respectively. The blunt-coned reentry vehicle has been studied for a long time, and its channel characteristics have been relatively clear. Tang et al. (2021) studied the electron density, collision frequency of different channels on the side of the plasma sheath of the sharp-coned reentry vehicle and the propagation characteristics of EHF wave in the plasma sheath of the sharp-coned reentry vehicle, analyzed and compared its characteristics with that of plasma sheath of a blunt-coned reentry vehicle, analyzed the mechanism of wave energy loss, found that the signal attenuation mechanism of sharp-coned reentry vehicle is different from that of a blunt-coned reentry vehicle. Compared with the effect of a sharp-coned plasma sheath on a 0.14 THz array antenna, the blunt-coned plasma sheath refracts the radiation direction of the antenna, resulting in the deterioration of communication quality in the expected direction (Zhao et al., 2022b). The difference in attenuation mechanism between sharp-coned and blunt-coned reentry vehicles will inevitably lead to their different communication performance. However, the influence of plasma sheath on carrier phase shift and the evolution characteristics of plasma sheath are not considered in the literature on sharp-coned reentry vehicles. Without external disturbance, the plasma sheath has natural evolution characteristics, so the channel conditions will inevitably change with time, and then the performance of the communication system will also change with time. Therefore, the time-varying characteristics of EHF channels in the plasma sheath of sharp-coned reentry vehicles is an unavoidable problem in the design of a reentry communication system for ballistic missiles.

All signals propagating in the plasma sheath are modulated. The quality of communication performance is not only related to signal attenuation, but also to phase shift influenced by the plasma sheath (Shi et al., 2012). The plasma sheath of the reentry vehicle is time-varying (He et al., 2014). The time scale of plasma sheath change can be less than 1 ms (Yuan et al., 2018b). The carrier period is much smaller than the time scale of plasma sheath evolution when the communication system works in the EHF band. Therefore, it is worth studying how the BER changes with time without external disturbance. In the reference "Yang et al. (2022b)," the flight object is a blunt-coned vehicle, yet in the present work, the object is a sharp-coned vehicle. Previous work has revealed that the structures of blunt-coned plasma sheaths and sharp-coned plasma sheaths are quite different. Also, the mechanics of EHF signal attenuations are different in the two types of plasma sheaths. As the result, the SNR for the received signals differs. According to our previous works, the BER performance significantly depends on the SNR. Thus, the BER performances for identical modulation modes in sharp-coned plasma sheath are different from that in blunt-coned plasma sheath. In addition, the plasma sheath is inhomogeneous (Ouyang et al., 2020). Therefore, the location of the onboard antenna will make an important contribution to the conditions of the EHF communication channel in the plasma sheath.

The present study mainly focused on the BER of the EHF communication system serving sharp-coned reentry vehicles. The evolution of the plasma sheath was solved with a numerical hypersonic hydrodynamic model. The whole evolution cycle is 1 ms. The typical modulation modes concerned in the present study were 2ASK, 2PSK, and NC-2FSK. The carrier frequencies involved are "atmospheric windows" of 94, 140, and 225 GHz in the EHF band, respectively. The influence on the BER of EHF signals of antenna location, carrier frequency, and modulation method in the plasma sheath of a sharp-coned reentry vehicle will be investigated.

## 2 PROPAGATION CHARACTERISTICS OF EXTREMELY HIGH-FREQUENCY WAVES IN THE SHARP-CONED PLASMA SHEATH

In order to study the propagation characteristics of EHF waves in the plasma sheath of a sharp-coned reentry vehicle, the plasma sheath was modeled based on fluid theory. The evolution of the plasma sheath in 1 ms was simulated under the conditions of specific atmospheric temperature, atmospheric mass density,

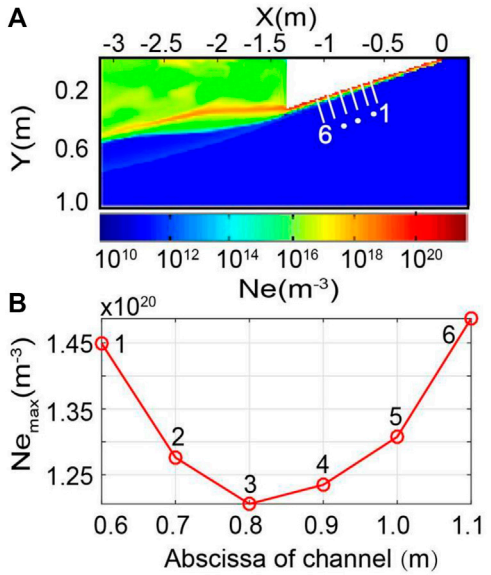


**FIGURE 1 | (A)** Schematic diagram of side channels of plasma sheath of a sharp-coned reentry vehicle, **(B)** Maximum electron density of each channel at $t$ = 1 ms.

flight speed, and angle of attack (AOA). The model used here is the same as the literature (Tang et al., 2021). The length and the bottom size of the sharp-coned are 1.295 and 0.6667 m, respectively. The angle of attack is 0°. The atmospheric mass density was $1.65 \times 10^{-1}$ kg/m$^3$, which corresponds to the atmospheric mass density at the altitude of 30 km in middle latitudes. The temperature was 215 K. The flight speed of the vehicle is 6,550 m/s (Yuan et al., 2017). A hydrodynamic model was employed to simulate the plasma sheaths.

**Figure 1** shows the electron density distribution of the plasma sheath of the sharp-coned reentry vehicle and the maximum electron density curves of the selected six channels at $t$ = 1 ms. The white short lines in **Figure 1A** indicate the side channels to be analyzed, which are marked as 1, 2, 3, 4, 5, and 6. The ends of the channels close to the vehicle are the locations of the antennas. The abscissas of the six antenna locations are 0.6, 0.7, 0.8, 0.9, 1, and 1.1 m, respectively. The color axis represents the electron density. **Figure 1B** shows the maximum electron density of the six channels in **Figure 1A** at 1 ms. It can be seen from the figure that the maximum electron densities of different channels are different at a specific time. The electron density of channel 3 is the smallest and that of channel 6 is the largest, which reflects the spatial heterogeneity of the plasma sheath of the sharp-coned reentry vehicle.

The wavelength of the EHF wave is smaller than the spatial scale of inhomogeneity in the plasma sheath. Therefore, the propagation of the EHF wave in the plasma sheath can be studied as the propagation of the EM wave in one-dimensional inhomogeneous collisional plasma. In this article, the propagation of EHF waves in plasma sheath was studied by using the one-dimensional scattering matrix method (SMM). The SMM method is a common calculation method for geometrical optics analysis in the frequency domain. It deduces the propagation and reflection coefficients based on the wave impedance of each layer of medium. The reflection term caused by impedance jump is also considered. Therefore, it is suitable for the medium with drastic changes in EM characteristic gradient and the approximate calculation of radio wave propagation in inhomogeneous plasma sheath.

In this article, it is assumed that the signal is vertically incident. The plasma slab is divided into n thin layers, as shown in **Figure 2**. Each thin layer is regarded as a homogeneous layer. The wave travels from free space (neutral atmosphere in this model) along a certain path to the plasma sheath until it reaches the antenna on the surface of the vehicle. In **Figure 2**, the region I is the free space corresponding to the blue area in **Figure 1A**, region II is the plasma slab corresponding to the part of the plasma sheath in the selected channel in **Figure 1A**, and Region III is the free space where the antenna is located corresponding to the onboard antenna of the vehicle in **Figure 1A**. The scattering matrix is calculated as the same as that in the literature (Hu et al., 1999). The transmission coefficient and phase shift of different channels at different times are calculated by the SMM method, and finally, time-varying curves of the transmission coefficient and phase shift of different channels are obtained.

**Figure 3** illustrates the transmission coefficient and phase shift. Panels A, B, and C show signal attenuation for carrier frequencies of 94, 140, and 225 GHz, respectively. The evolution of the plasma sheath of the sharp-coned reentry vehicle under certain conditions starts from the plasma generation on the top of the vehicle until it envelops the entire vehicle. The simulation lasts for 1 ms. If it continues to evolve, the overall plasma sheath changes little. The time on the abscissa of **Figure 3** starts from 0.3 ms when the entire plasma is basically formed and ends at 1 ms, which is relatively stable at the end.

When the carrier frequency is 94 GHz, as shown in **Figure 3A**, the transmission coefficients of channels (1–3) near the tip are always lower than 0.2. The transmission coefficients of channels (4–6) close to the tail are significantly higher than those of channels (1–3) in the early stage of the whole evolution period, and the transmission coefficient increases as the channel move back. In the later stage of evolution, the transmission coefficients of channels 3 and 4 in the middle are higher than that of channels close to the tip and tail, and the transmission coefficient of channel 3 is the largest.

When the carrier frequency is 140 GHz, as shown in **Figure 3B**, the transmission coefficients of the six channels are always greater than 0.5. The transmission coefficient of channel 6 near the tail is higher than that of channels 1–5 in the early stage


**FIGURE 2 |** Schematic diagram of SMM.

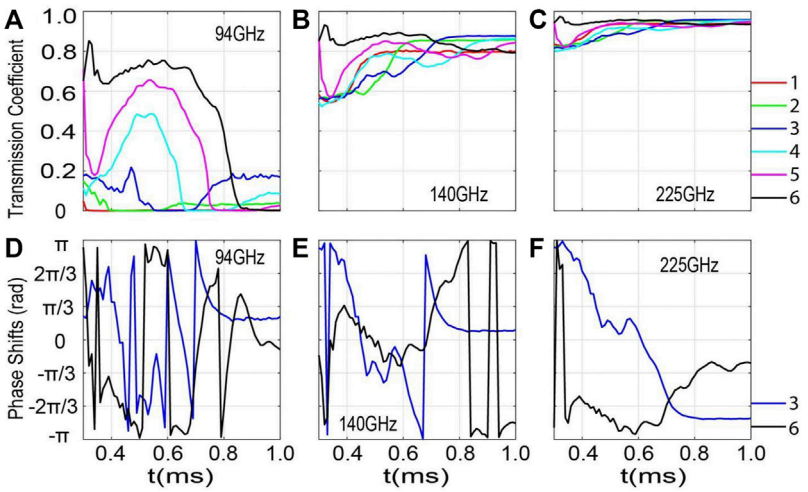


**FIGURE 3 |** Temporal variation of transmission coefficient **(A–C)** and phase shift **(D–F)** of EHF signals in the side plasma sheath channels of a sharp-coned reentry vehicle. The corresponding carrier frequencies from left to right are 94, 140, and 225 GHz respectively. Different channels are represented by curves of different colors [as shown on the right side of **(C)**].

of the whole evolution period, and the transmission coefficient is larger as the channel closer to the tail. In the later stage of evolution, the transmission coefficient of channel 3 is the largest, but the transmission coefficients of all channels are not much different, about 0.8.

When the carrier frequency is 225 GHz, as shown in **Figure 3C**, the transmission coefficients of the six channels are always greater than 0.75. The transmission coefficient of channel 6 near the tail is higher than that of channels 1–5 in the early period of plasma sheath evolution. In the later stage of evolution, the transmission coefficient of channel 3 is the largest, and the transmission coefficient of all channels is about 0.95, the difference is very small.

It can be seen from **Figures 3A–C** that the gap of transmission coefficients of different channels decreases with time at a specific carrier frequency. In general, the transmission coefficient becomes larger in the same channel as the carrier frequency increases. The reason is that the plasma sheath is a dispersive lossy medium. For the vertical incident signal, the polarization loss is zero. The absorption caused by the collision of free electrons with neutral particles becomes the main mechanism for the energy loss of EHF signals. The total absorption rate depends on the electron density, collision frequency, and wave frequency (Chen et al., 2016). High frequencies are less absorbed than low frequencies (Ouyang et al., 2021). In addition, the transmission coefficient of channel 6 is the largest in the early stage and the transmission coefficient of channel 3 is the largest in the later stage. The following section will focus on the propagation characteristics of EHF signals in channels 3 and 6.

The temporal variation of the phase shifts of the EHF signals at the frequencies of 94, 140, and 225 GHz are shown in **Figures 3D–F** respectively. Since the phase shifts of each channel fluctuate significantly at a specific carrier frequency, it is messy to draw all of them. Here, only the temporal variations of phase shifts in channels 3 and 6 are shown. The vertical axis in the figure is from $-\pi$ to $\pi$, which covers the entire phase cycle. It can be clearly seen from **Figures 3D–F** that the lower the frequency, the more drastic the phase shift changes over time. As the carrier frequency increases, the change of phase shift tends to be stable. When the carrier frequency is 225 GHz, the amplitude of phase shift change is less than one cycle during the whole evolution period. It should be noted that the phase shift is measured in the range from $-\pi$ to $\pi$ since it is not necessary to account for the full period ambiguity in the current modulation and demodulation problem. Once the phase changes from a value less than $\pi$ to a value greater than $\pi$, it appears to drop sharply in **Figures 3D–F**, although it is still a continuous change. The temporal variation of the phase shift is caused by the temporal variation of the wavelength in the plasma sheath. The plasma sheath is a dispersive medium, and according to geometric optics theory, the refractive index of the plasma sheath for EHF waves depends on the electron density, electron collision frequency, and wave frequency. Therefore, the wavelength of EHF in the plasma sheath is significantly different from that in a vacuum or neutral atmosphere. In other words, the time-varying in homogeneous plasma sheath causes the wavelength of the propagating EHF signal to vary with time during propagation. Therefore, changes in wavelength cause the measured phase shift to change over time.

## 3 THE BIT ERROR RATE

The BER of EHF wireless communication of sharp-coned reentry vehicles is affected by the spatiotemporal change of plasma sheath. This effect will be studied numerically in this section. According to **Section 2**, the transmission coefficient of channel 6 near the tail is the largest in the early stage, while that of channel 3 is the largest in the later stage. Therefore, in this section, channels 3 and 6 will be selected to study the propagation characteristics of EHF signals. Since the

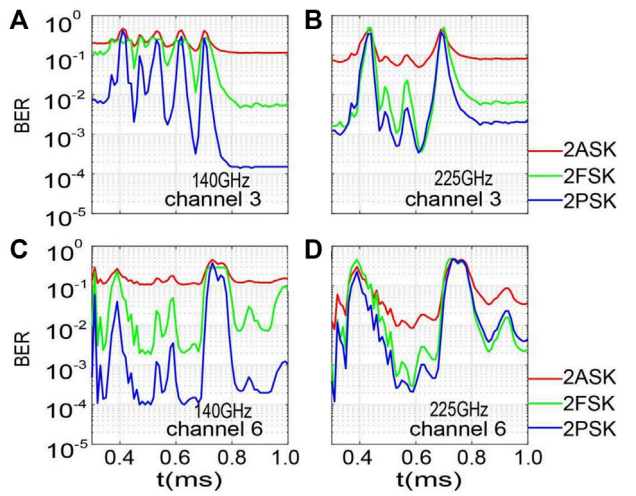


**FIGURE 4 |** The time-varying BER of EHF signals with different modulation methods in the side channels 3 **(A,B)** and 6 **(C,D)** of the plasma sheath of a sharp-coned reentry vehicle. Left panels are results of 140 GHz, and right panels are results of 225 GHz.

transmission coefficients of the six channels are relatively low in the later stage when the carrier frequency is 94 GHz, only the carrier frequencies of 140 and 225 GHz are selected in this section. In addition, the influence of antenna position and different modulation methods on BER is analyzed by Monte Carlo Simulation. The modulation modes are 2ASK, 2FSK, and 2PSK respectively.

The communication simulation system in this article includes a signal source module, modulation module, plasma sheath module, additive white Gaussian noise (AWGN) module, demodulation module, and BER statistics module. In the simulation communication system, the signal source generates random binary signals. The binary signals are modulated in the modulation module. Then, they are transferred to the plasma sheath module which causes amplitude attenuation and phase shift. After that, Gaussian white noise is added to them by the AWGN module, the noise-mixed signals are transmitted to the demodulation module, and the demodulated signals are transmitted to the BER statistics module for BER statistics. In order to compare the BER performance of various modulation methods, the AWGN module is set to the same. The power of the signal transmitter is set to 1 mW. The carrier amplitude is set to $\sqrt{0.002}$.

**Figure 4** shows the time-varying curves of BER of EHF signals with different modulation modes in side channels 3 and 6 of the plasma sheath of a sharp-coned reentry vehicle.

As can be seen from **Figure 4**, if 2ASK modulation is adopted, the minimum BER magnitude of channels 3 and 6 is $10^{-1}$ when the carrier frequency is 140 GHz. However, the BER of channel 6 reaches the magnitude of $10^{-1}$ more time, so the BER performance is relatively better. When the carrier frequency is 225 GHz, the minimum BER magnitude of channel 3 is between $10^{-1}$ and $10^{-2}$, and the BER of channel 6 can reach the magnitude of $10^{-2}$, so the BER performance of channel 6 is obviously better than that of channel 3. When channel 6 and 225 GHz carrier frequencies are selected, BER performance can reach the best.

If 2FSK modulation is adopted, when the central carrier frequency is 140 GHz, the BER of channels 3 and 6 can reach the magnitude between $10^{-2}$ and $10^{-3}$, but the BER performance of channel 6 is obviously better on the whole. When the central carrier frequency is 225 GHz, the BER of channels 3 and 6 can reach the magnitude between $10^{-3}$ and $10^{-4}$, and the BER performance of channel 6 is slightly better than that of channel 3. The BER performance is better when channel 6 is adopted and with a central carrier frequency of 225 GHz.

If 2PSK modulation is used, when the carrier frequency is 140 GHz, the BER of channel 3 can reach the magnitude between $10^{-3}$ and $10^{-4}$, but the BER of channel 6 can reach the magnitude of $10^{-4}$, and the performance is relatively better. When the carrier frequency is 225 GHz, the BER of channels 3 and 6 can reach the magnitude between $10^{-3}$ and $10^{-4}$. However, the time when the BER is less than $10^{-3}$ in channel 6 is more, the BER performance is relatively better. In the same channel, the BER performance is better when the carrier frequency is 140 GHz. Better BER performance can be obtained by combining 140 GHz carrier frequency with channel 6.

In a word, 2ASK has the worst BER performance and 2PSK has the best BER performance under the specific channel and carrier frequency. Overall, 2PSK modulation combined with 140 GHz carrier frequency and channel 6 can achieve the best BER performance.

## 4 DISCUSSION

According to **Section 2**, the transmission coefficient of EHF signals in the side channel of the plasma sheath of a sharp-coned reentry vehicle increases with carrier frequency, while the gap between different channels at specific carrier frequency decreases with time. In addition, the transmission coefficient of channel 6 near the bottom of the vehicle is the largest in the early stage, while the transmission coefficient of channel 3 in the middle of the vehicle is the largest in the later stage.

In **Figure 3**, the transmission coefficient at 225 GHz is obviously higher than 140 GHz, particularly for channel 3, yet the BER of channel 3 at 225 GHz in **Figure 4** is not significantly higher than 140 GHz. The reason is that the BER performance depends on not only the signal strength or SNR but also the phase shift of the carrier waves. The wavelengths of 225 GHz are much shorter than that of 140 GHz. Hence the phase for the signals at 225 GHz varies more frequently during the signal transmission process than that at 140 GHz. In other words, the phase of signals at 225 GHz could be less stable than that at 140 GHz. Hence, although the signals at 225 GHz suffer less attenuation in the plasma sheath, it is not a sufficient guarantee to achieve better BER performance.

According to the numerical simulation in **Section 3**, the 2PSK modulation with a carrier frequency of 140 GHz and channel 6 can achieve the best BER performance. Under specific channel and carrier frequency, the BER performance of 2ASK is the worst and that of 2PSK is the best.

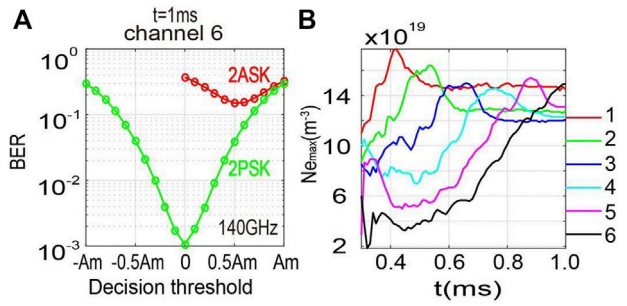


**FIGURE 5 | (A)** The BER of the EHF signals at different decision thresholds in the side channel 6 of the plasma sheath of sharp-coned reentry vehicle at a specific time ($t$ = 1 ms), where Am represents the amplitude of the signal; **(B)** The time-varying curves of the maximum electron density of the side channels (1–6).

**Figure 5** shows the BER of the EHF signals at different decision thresholds in the side channel 6 of the plasma sheath of the sharp-coned reentry vehicle at a specific time ($t$ = 1 ms), and the curves of the maximum electron density of the side channels 1–6 of the plasma sheath of the sharp-coned reentry vehicle.

As can be seen from **Figure 5A**, the optimal decision threshold of the 2PSK system is 0. The optimal threshold of 2PSK is independent of the amplitude, but the optimal threshold of 2ASK is half of the amplitude. Therefore, in the time-varying fading channel, the BER of 2ASK is relatively high, while the BER of 2PSK is relatively low.

It can be seen from **Figure 5B** that the maximum electron density of the side channels 1–6 of the plasma sheath of the sharp-coned reentry vehicle varies with time, so the transmission coefficient and phase shift of the EHF signals are time-varying. Furthermore, the BER is affected by the transmission coefficient and the phase shift is also time-varying.

In general, the maximum electron density of the side channel of the plasma sheath of the sharp-coned reentry vehicle becomes lower from channel 1 to channel 6. The maximum electron density of channel 1 is always in the magnitude of $10^{20}$ $m^{-3}$, while the maximum electron density of channel 6 is the lowest in a long time, and the variation range is the largest, from about $2 \times 10^{19}$ $m^{-3}$ to $1.5 \times 10^{20}$ $m^{-3}$. At the end of evolution, the maximum electron density of channel 3 is the lowest. As electron density is a key parameter affecting the transmission coefficient in plasma sheath, the transmission coefficient decreases with the electron density increasing. Therefore, in the early stage, the transmission coefficient of channel 6 is the largest and the BER is relatively smaller in channel 6, and in the later stage of evolution, the transmission coefficient of channel 3 is the largest and the BER is relatively smaller in channel 3.

According to **Figure 3**, in channel 6, the transmission coefficient is basically greater than 0.8 when the carrier frequency is 140 GHz. Once the carrier frequency is 225 GHz, the transmission coefficient is basically above 0.9. The transmission coefficients at the two carrier frequencies have little difference in channel 6. According to **Figure 4**, when the 2PSK modulation is adopted, the BER of 140 GHz is smaller than that of 225 GHz. It should be concerned that signals at 225 GHz suffer greater attenuation in a neutral atmosphere than that at 140 GHz. Thus, 140 GHz is recommended to be the operating frequency for the EHF communication system serving sharp-coned reentry vehicles.

## 5 CONCLUSION

In this article, the effects of spatiotemporal heterogeneity of plasma sheath of the sharp-coned reentry vehicle on the transmission coefficient and phase shift of EHF signals are studied. It is found that the transmission coefficient of EHF signal in the plasma sheath side channels of sharp-coned reentry vehicle increases with the increase of carrier frequency, the transmission coefficient gap between different channels decreases with time at a specific carrier frequency, and the phase shift tends to be stable with the increase of carrier frequency. The BER performance of EHF signals modulated by 2ASK, 2FSK, and 2PSK in the plasma sheath of a sharp-coned reentry vehicle is numerically studied. The influence of the decision threshold on BER is discussed, and the reason for the time-varying of BER is discussed according to the time-varying curves of the maximum electron density of the six channels. The electron density distribution of different channels affects the transmission coefficient and phase shift and further affects the BER. The study found that the EHF communication system with 2PSK modulation, 140 GHz carrier, and antenna installed on the side wall and close to the bottom of the vehicle can reduce the BER for sharp-coned reentry vehicles. This study reveals the propagation characteristics and BER performance of EHF signals in the plasma sheath of a sharp-coned reentry vehicle, which can provide a valuable reference for the design of EHF communication systems for sharp-coned reentry vehicles.

## DATA AVAILABILITY STATEMENT

The raw data supporting the conclusion of this article will be made available by the authors, without undue reservation.

## AUTHOR CONTRIBUTIONS

All authors listed have made a substantial, direct, and intellectual contribution to the work and approved it for publication.

## ACKNOWLEDGMENTS

The authors acknowledge the support from the National Natural Science Foundation of China (Grant No. 61861031).

## REFERENCES


Chen, J., Yuan, K., Shen, L., Deng, X., Hong, L., and Yao, M. (2016). Studies of Terahertz Wave Propagation in Realistic Reentry Plasma Sheath. *Pier* 157, 21–29. doi:10.2528/pier16061202

Gillman, E. D., Foster, J. E., and Blankson, I. M. (2010). *Review of Leading Approaches for Mitigating Hypersonic Vehicle Communications Blackout and a Method of Ceramic Particulate Injection* via *Cathode Spot Arcs for Blackout Mitigation*. NASA/TM-2010-216220. Washington, DC: NASA.

He, G., Zhan, Y., Ge, N., Pei, Y., Wu, B., and Zhao, Y. (2014). Channel Characterization and Finite-State Markov Channel Modeling for Time-Varying Plasma Sheath Surrounding Hypersonic Vehicles. *Pier* 145, 299–308. doi:10.2528/pier14031104

Hu, B. J., Wei, G., and Lai, S. L. (1999). Smm Analysis of Reflection, Absorption, and Transmission from Nonuniform Magnetized Plasma Slab. *IEEE Trans. Plasma Sci.* 27, 1131–1136. doi:10.1109/27.782293

Liu, J.-F., Ma, H.-Y., Jiao, Z.-H., Bai, G.-H., Fang, Y., Yi, Y.-M., et al. (2020). Effects of Dynamic Plasma Sheath on Electromagnetic Wave Propagation and Bit Error Rate under External Magnetic Field. *IEEE Trans. Plasma Sci.* 48, 2706–2714. doi:10.1109/tps.2020.3006955

Ouyang, W., Deng, W., and Wu, Z. (2020). Impact of Half-Angles on the Transmission of Terahertz Wave in Inhomogeneous Plasma Sheath. *IEEE Trans. Plasma Sci.* 48, 4029–4036. doi:10.1109/tps.2020.3029837

Ouyang, W., Jin, T., Wu, Z., and Deng, W. (2021). Study of Terahertz Wave Propagation in Realistic Plasma Sheath for the Whole Reentry Process. *IEEE Trans. Plasma Sci.* 49, 460–465. doi:10.1109/tps.2020.3042220

Rao, Q., Xu, G., Wang, P., and Zheng, Z. (2021). Study on the Propagation Characteristics of Terahertz Waves in Dusty Plasma with a Ceramic Substrate by the Scattering Matrix Method. *Sensors* 21, 263. doi:10.3390/s21010263

Shi, L., Guo, B., Liu, Y., and Li, J. (2012). Characteristic of Plasma Sheath Channel and its Effect on Communication. *Pier* 123, 321–336. doi:10.2528/pier11110201

Starkey, R. (2003). "EM Wave/magnetoactive Plasma Sheath Interaction for Hypersonic Vehicle Telemetry Blackout Analysis," in 34th AIAA Plasmadynamics and Lasers Conference, Orlando, United States, June 23–26, 4167.

Starkey, R. P. (2015). Hypersonic Vehicle Telemetry Blackout Analysis. *J. Spacecr. Rockets* 52, 426–438. doi:10.2514/1.a32051

Tang, R., Mao, M., Yuan, K., Wang, Y., and Deng, X. (2019). A Terahertz Signal Propagation Model in Hypersonic Plasma Sheath with Different Flight Speed. *Phys. Plasmas* 26, 043509. doi:10.1063/1.5091676

Tang, R., Xiong, Z., Yuan, K., Mao, M., Wang, Y., and Deng, X. (2021). Ehf Wave Propagation in the Plasma Sheath Enveloping Sharp-Coned Hypersonic Vehicle. *Antennas Wirel. Propag. Lett.* 20, 978–982. doi:10.1109/lawp.2021.3068575

Wei, H., Liu, Y., Shi, L., Yao, B., and Li, X. (2019). Bit Error Rate and Channel Capacity Performance of Telemetry Modulation Methods under Typical Reentry Plasma Sheath Channel. *IEEE Trans. Plasma Sci.* 47, 4950–4960. doi:10.1109/TPS.2019.2942606

Yang, X., Yuan, K., Wang, Y., Liu, Y., and Xiong, J. (2022a). Propagation Characteristics of Modulated Ehf Signal in the Wake Region of Plasma Sheath. *Aerospace* 9, 194. doi:10.3390/aerospace9040194

Yang, X., Yuan, K., Wang, Y., and Mao, M. (2022b). Numerical Modeling on the Bit Error Rate of Ehf Communication in Time-Varying Hypersonic Plasma Sheath. *AIP Adv.* 12, 045318. doi:10.1063/5.0087974

Yuan, K., Wang, Y., Shen, L., Yao, M., Deng, X., Zhou, F., et al. (2017). Sub-thz Signals'propagation Model in Hypersonic Plasma Sheath under Different Atmospheric Conditions. *Sci. China Inf. Sci.* 60, 1–11. doi:10.1007/s11432-017-9232-8

Yuan, K., Chen, J., Shen, L., Deng, X., Yao, M., and Hong, L. (2018a). Impact of Reentry Speed on the Transmission of Obliquely Incident Thz Waves in Realistic Plasma Sheaths. *IEEE Trans. Plasma Sci.* 46, 373–378. doi:10.1109/TPS.2017.2788201

Yuan, K., Shen, L., Yao, M., Deng, X., Chen, Z., and Hong, L. (2018b). Studies on the Transmission of Sub-thz Waves in Magnetized Inhomogeneous Plasma Sheath. *Phys. Plasmas* 25, 013302. doi:10.1063/1.5021363

Zhao, Z., Bai, B., Yuan, K., Tang, R., Xiong, J., and Wang, K. (2022a). Effect of Terahertz Antenna Radiation in Hypersonic Plasma Sheaths with Different Vehicle Shapes. *Appl. Sci.* 12, 1811. doi:10.3390/app12041811

Zhao, Z., Yuan, K., Tang, R., Lin, H., and Deng, X. (2022b). Theoretical Study on the Impacts of Plasmas Enveloping Reentry Vehicles on the Radiation Performance of Terahertz Array Antenna. *IEEE Trans. Plasma Sci.* 50, 517–524. doi:10.1109/tps.2022.3144483


**Conflict of Interest:** The authors declare that the research was conducted in the absence of any commercial or financial relationships that could be construed as a potential conflict of interest.

# Frontiers in Earth Science

**Investigates the processes operating within the major spheres of our planet**

Advances our understanding across the earth sciences, providing a theoretical background for better use of our planet's resources and equipping us to face major environmental challenges.

---

## Discover the latest Research Topics

See more →


**Frontiers**

Avenue du Tribunal-Fédéral 34
1005 Lausanne, Switzerland
frontiersin.org

**Contact us**

+41 (0)21 510 17 00
frontiersin.org/about/contact